Crystalline and amorphous cobalt-based metal oxides for water oxidation reaction – structure, composition, morphology and electrochemical performance

Sreena Thekkoot

A Dissertation submitted to the Faculty of Graduate Studies
in partial fulfilment of the requirements for the degree of Doctor of Philosophy

GRADUATE PROGRAM IN CHEMISTRY
YORK UNIVERSITY
TORONTO, ONTARIO
FEBURUARY 2024

Abstract

We synthesized Cu, Ni, and Fe-substituted cobalt-based amorphous materials (CoO_x, $CuCo_2O_x$, $Ni_{0.5}Cu_{0.5}Co_2O_x$, $Fe_{0.1}Cu_{0.9}Co_2O_x$, and $Fe_{0.1}Ni_{0.9}Co_2O_x$) by thermal decomposition method using near-infrared lamp. Fourier Transformed Infrared spectroscopy (FTIR) was used to check the progress of the reaction during the synthesis. These materials were characterized by scanning electron microscopy (SEM), energy dispersive X-ray spectroscopy (EDX), X-ray diffraction (XRD), transmission electron microscopy (TEM), high-resolution transmission electron microscopy (HR-TEM) and X-ray photoelectron spectroscopy (XPS). We also prepared $Cu_xCo_{3-x}O_4$ ($0 \leq x \leq 1$), $Ni_xCu_{1-x}Co_2O_4$ ($0 \leq x \leq 0.75$) and $Fe_yCu_{x-y}Co_xO_4$ (x=1, 1.5 and y = 0.1, 0.15) by thermal decomposition method. Surface area measurements were performed using cyclic voltammetry (CV) and electrochemical impedance spectroscopy (EIS). The catalytic activity of spinel oxides and amorphous metal oxides for oxygen evolution reaction (OER) was analyzed by CV, while kinetic studies were carried out using a rotating disc electrode (RDE).

TEM and HR-TEM analysis were performed on polarized and nonpolarized $CuCo_2O_4$. The study clearly indicates that the as-prepared $CuCo_2O_4$ possesses a higher degree of crystallization compared to the polarized sample. The crystallite size of the sample measured by TEM and XRD analysis is very similar.

The XRD analysis confirmed the formation of an amorphous phase while the EDX analysis shows a fairly good agreement with the stoichiometric composition. The double-layer capacitance of amorphous and crystalline/spinel oxides measured by CV and EIS showed a good agreement. Surface area measurements indicate that the incorporation of Cu and Ni increased the surface area of amorphous and crystalline samples. The incorporation of Fe increased the surface area of the amorphous samples, while an opposite trend was observed in the case of spinel oxides. XPS analysis indicates that the surface of both amorphous and crystalline samples contains different species and the metal ions exist in different oxidation states.

Catalytic activity was measured as a function of geometric and real surface area. Both amorphous and spinel oxides were found to be active for OER. However, when corrected for real surface area, spinel oxides provided much higher current density compared to amorphous samples. Our study indicates that spinel oxides outperform amorphous samples for OER.

Acknowledgment

This research work would not have been possible without the direct or indirect support of many individuals. It is my pleasure to express my gratitude to those who made this work possible.

I am extremely grateful to Almighty god for your blessings and for helping me to complete my research work successfully. I am deeply thankful to my supervisor Prof. Sylvie Morin for giving me an opportunity to be a part of her research group and for all her guidance and supervision throughout my research work. Her in-depth knowledge and expertise in research techniques and methods motivated and helped me grow into the confident and knowledgeable scientist I am today. I am extremely grateful to you for teaching me the 'Advanced Electrochemistry' course which helped me to advance in my research more easily. I really appreciate your kindness and incredible support.

I am incredibly grateful to Prof. Rene Fournier and Prof. Chris Caputo for being part of my research committee and for their guidance, support, and outstanding feedback. Their valuable comments and discussions helped me to improve my research work.

I would like to also express my sincere thanks to the lab technicians Michelle Barton and Ha B. Au for helping me with the FTIR analysis of my samples during the COVID pandemic.

I would like to thank my colleagues Rehana Islam, Bibisomaia Rezaee, Dinithi Rajaguru, Tian Jiayue, and Owen Gray for their support during my research work. I would like to extend my deepest gratitude to Magdalena Jaklewicz at York University, Faculty of Science, Imaging Facility for SEM and EDX measurements and analysis; Victoria Jarvis, MAX Diffraction Facility, for XRD measurements and X-ray diffraction pattern analysis; Dr. Zeynel Bayindir, Biointerfaces Institute, for XPS measurements; and Wajdi Alnoush and Dr. Drew Higgins from the Canadian Centre of Electron Microscopy, for TEM measurements, McMaster University, Hamilton, ON, Canada. I would like to thank Dr. Mark Biesinger for XPS measurements of our samples at Kratos Axis supra Spectrometer (Surface Science Western, London) and for instructing a short course on X-ray photoelectron spectroscopy analysis which greatly helped me to improve the data analysis and interpretation.

I would like to sincerely thank my friend Nimisha Sharma for providing me valuable information regarding research programs and your support has been truly incredible. I would like

to thank all my teachers for inspiring me and shaping my future with your knowledge and guidance. I will always be grateful to you in my life.

I would never have been able to complete my research work without my family's incredible support. I would like to dedicate my thesis to my family. I am extremely grateful to my parents and my sisters for your unconditional love and support throughout my life, you have always been in my heart. I would like to thank my husband, Raju Thekkoot for his support and help throughout my research work. I wouldn't be able to complete my research work without your help. I would like to give my special thanks to my kids (Ronit and Rohin) for making my life more valuable and enjoyable.

Finally, I would like to thank the Natural Science and Engineering Research Council (NSERC) of Canada and York University for the support through the Discovery Grant program (RGPIN-2016-05321) and Minor Research Grant, respectively awarded to Prof. Morin to support this research.

Publications and presentations

Some of the work described in this thesis has already been published or submitted and other parts are in preparation.

1. S. Thekkoot, R. Islam, and S. Morin, Improved oxygen evolution reaction performance with addition of Fe to form $Fe_yCu_{x-y}Co_{3-x}O_4$ and $Fe_yNi_{x-y}Co_{3-x}O_4$ (x = 0.5, 1 and y = 0.1, 0.15) spinel oxides, Electrochim. Acta 378 (2021) 138116
2. S. Thekkoot, R. Islam, O Gray, and S. Morin 'Efficiency of nanostructured $Cu_xCo_{3-x}O_4$ and $Ni_xCu_{1-x}Co_2O_4$ electrodes as electrocatalysts for oxygen evolution reaction – revisited', Electrochim. Acta, 471 (2023) 143339
3. S. Thekkoot, B. Rezaee, D. Rajaguru, T. Jiayue, O. Gray, Sylvie Morin, Transition metal oxides for oxygen evolution reaction: A comparative study between amorphous and crystalline materials, Manuscript in preparation**.**
4. B. Rezaee, S. Thekkoot, D. Rajaguru, T. Jiayue, O. Gray, Sylvie Morin, Systematic study of effect of iron in mixed transition metal spinel oxides as oxygen evolution electrocatalysts -electrochemistry and material properties, manuscript in preparation

My research work was presented at various conferences and symposia

1. S. Thekkoot, B. Rezaee, O. Gray, T. Jiayue, R. Islam, S. Morin, A comparative study between the properties of amorphous and crystalline transition 65th International Conference on Analytical Sciences and Spectroscopy (ICASS) meeting. Ottawa, July 2023
2. S. Thekkoot, B. Rezaee, O. Gray, T. Jiayue, R. Islam, S. Morin, Surface structure and electrochemical activity of Fe, Cu, and Ni substituted cobalt spinel oxide catalysts for efficient water splitting, 3rd Commonwealth Chemistry Posters, September 2022
3. S. Thekkoot, R. Islam, S. Morin, Fe, Cu and Ni substituted cobalt spinel oxide catalysts for efficient water splitting; Investigating the surface structure and activity, ISE 29th Topical Meeting-Energy and water: electrochemistry in securing the sustainable society development, April 2021
4. S. Thekkoot, R. Islam, B. Rezaee, S. Morin, Cobalt-based transition metal oxide thin films as efficient water oxidation electrocatalysts, IUPAC | CCCE; Solving Global Challenges with Chemistry, August 2021
5. S. Thekkoot, R. Islam, S. Morin, Cobalt based transition spinel oxide thin films as efficient water oxidation electrocatalysts, CBGRC (Chemistry and Biochemistry Graduate Student Research) online event, November 2021.
6. S. Thekkoot, B. Rezaee, R. Islam and S. Morin, Properties and surface chemistry of nanostructured electroactive materials, 11th Nano Ontario Conference and Exhibition (virtual), Toronto, Canada, November, 2021
7. S. Thekkoot, R. Islam, S. Morin, Nanostructured mixed transition metal spinel oxide thin films as efficient electrocatalysts – composition, structure and properties ISE (International society of Electrochemistry) meeting Belgrade, September 2020
8. S. Thekkoot, R. Islam, S. Morin, Nanostructured mixed transition metal spinel oxide thin films as efficient electrocatalysts – composition, structure and properties, 237th ECS meeting, May 2020 (meeting was canceled due to COVID -19, The abstract was published later as conference proceedings).

Table of contents

List of Tables

List of Figures

List of Abbreviations

A	Electrode surface area
a	Lattice parameter
b	Tafel slope
BSEs	Backscattered electrons
C_{dl}	Double layer capacitance
C_d	Differential capacitance
C_ϕ	Pseudo-capacitance
D	Diffusion coefficient ($cm^{-2}s^{-1}$)
d_{hkl}	Spacing between the atomic planes
E	Applied potential
E_{anode}	Equilibrium potential of anode
$E_{cathode}$	Equilibrium potential of cathode
E^0_{cell}	Equilibrium potentials of the cell
E_{pa}	Potential at which anodic current density is maximum
E_{pc}	Potential at which cathodic current density is maximum.
ESCA	Electrochemical active surface area of the electrode
Do_2	Molecular O_2 diffusion coefficient
F	Faraday constant
HER	Hydrogen evolution reaction
IHL	Inner Helmholtz layer
i	Current
i_o	Exchange current density
NHE	Normal hydrogen electrode
n	Number of electrons transferred
OER	Oxygen evolution reaction (OER)
OHL	Outer Helmholtz layer
R	Ideal gas constant
R_F	Roughness factor
R_s	Solution resistance
R_{ct}	Charge transfer resistance

R_{ϕ}	Faradaic resistance
R_{cell}	Electrical resistance of the cell
SCE	Saturated calomel electrode
SEs	Secondary electrons
T	Temperature in Kelvin
Z	Impedance
$dC_{(x,t)}/d_x$	Concentration gradient
$J_{(x,t)}$	Flux, rate of mass transport
j_{cap}	Cathodic current density
α_a	Transfer coefficient
β	Symmetry factor
f	Frequency
λ	Wavelength of the incident wave
ω	Radial frequency
ϕ	Phase shift
δ	Diffusion layer thickness
ν	Kinematic viscosity of the solution
ΔG	Free energy change
η	Overpotential

Chapter 1. Introduction

1.1. Introduction – electrocatalysts for water oxidation reaction

Today, most of our energy needs are met by the consumption of fossil fuels such as coal, natural gas, and petroleum. The overuse of natural resources, such as petroleum and coal has caused significant adverse environmental effects. In addition, energy insecurity has become a major crisis, causing international war, civil war, labour disputes, and environmental damage due to continuous fuel extraction and pollution arising from its combustion [1, 2]. Global warming is another serious threat that we are facing and it has already resulted in widespread impact across the world. The negative impacts of global climate change have been felt by most countries around the world and there have been efforts to develop and sign protocols and agreements on the development and deployment of clean technologies. More than a hundred countries are aiming to meet net zero emissions and are targeting to control the increase of temperature below 2 °C and 1.5 °C above preindustrial levels [3, 4]. The Kyoto Protocol has requested the control of six greenhouse gases, such as carbon dioxide, hydrofluorocarbons, methane, nitrous oxide, perfluorocarbons, and sulfur hexafluoride [2]. Greenhouse gases absorb and reradiate infrared radiation causing an increase in temperature. Global warming causes heat stress and diseases, increasing the intensity of tropical storms, the acidity of oceans, the melting of glaciers, and rising sea levels. This damages ecosystems, and animal habitats, causes the alteration of viable agriculture, and changes the timing and magnitude of rain and water supply [3]. It also increases the frequency and severity of forest fires, hurricanes, flooding, heat waves, and droughts [4]. More than 60% of the greenhouse gas content in the earth's atmosphere results from carbon dioxide, which is mainly generated due to human activities [2].

The concentration of carbon dioxide has increased by 30% in the atmosphere since 1950. Scientists believe that CO_2 controls the amount of water vapor in the atmosphere. Doubling or halving the CO_2 will increase or decrease the temperature by 3.8 ºC or -3.6 ºC, respectively [5]. Figure 1.1 shows the concentration of CO_2 through history, a significant increase of CO_2 can be observed in this graph around 1950. It is important to address global warming as quickly as possible because stabilizing the current increase in temperature requires an approximate reduction of 80% of greenhouse gas emissions [3]. Currently, many countries are undergoing a transition to clean and renewable energy sources to reduce air pollution and hence global warming. To reduce the severe impact of global climate change, a strong framework of policies

and economic incentives is urgent to accelerate the transition from fossil fuel to sustainable energy sources [6].

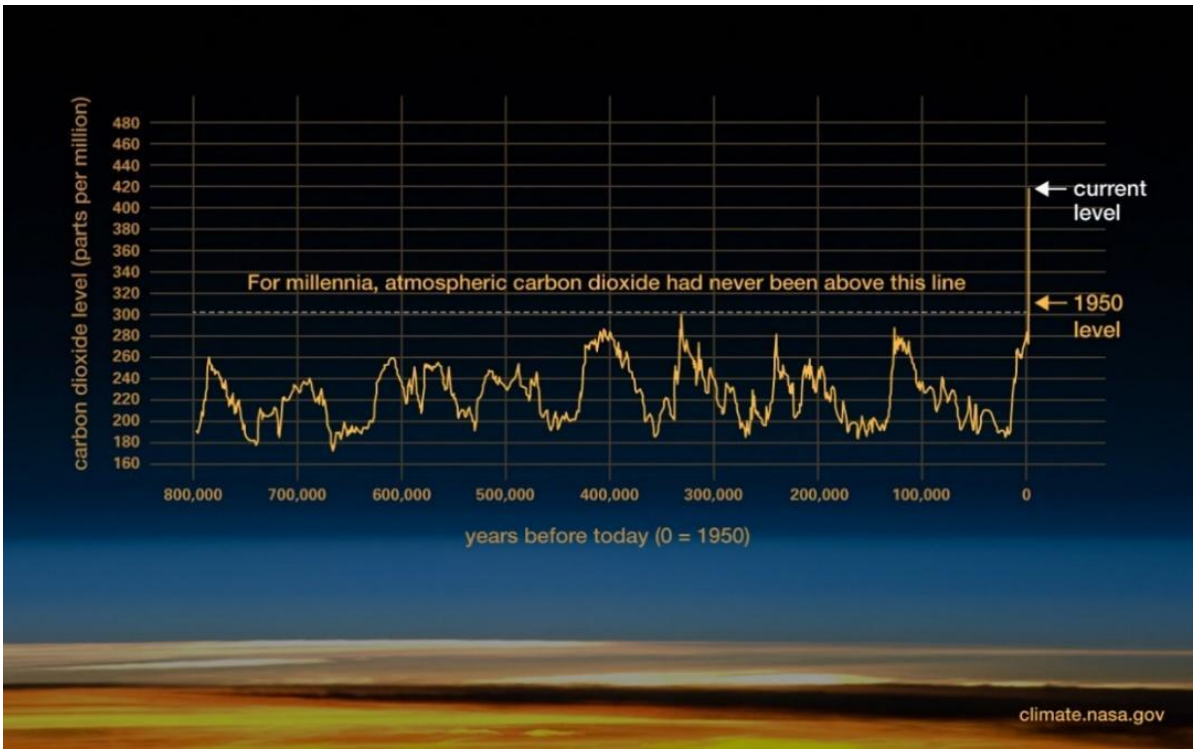

Figure 1.1. Concentration of carbon dioxide level in the atmosphere, reproduced from reference [5] with permission.

1.2. Hydrogen economy

In many countries meeting the net-zero emission targets means moving away from burning fossil fuel and establishing hydrogen gas as the fuel of the future. Hydrogen is an important component in the production of ammonia, methanol, petroleum products, and many other chemicals and materials [7]. Most of the hydrogen gas used in the industrial sector is currently produced by steam reforming of fossil hydrocarbon (mainly methane), causing atmospheric pollution as it produces CO_2. While moving towards a hydrogen economy poses great challenges, many countries including Canada have developed hydrogen strategies [8]. Canada is strategizing a clean hydrogen economy under the Clean Energy Ministerial (CEM) committee with the aim of widespread hydrogen technology deployment. This approach would help to decarbonize and provide great solutions to climate change while improving air quality. In addition, the demand for hydrogen gas is increasing significantly, and under this strategy, Canada will be able to provide about 24% of global energy demand by 2050. Canada is expected

to be the large-scale exporter of hydrogen in this growing market. A strong hydrogen economy could bring financial, environmental, and health benefits to Canadians [9]. Availability of hydrogen infrastructure, such as storage and transportation from the site of production to end users, pipeline networks, and deep water ports is also required to establish a hydrogen economy in Canada [9]. With the growing environmental concerns and adverse health effects, favorable government policies can drive a hydrogen economy, and industrial growth in this sector.

Electrochemical technology is at the center of hydrogen strategies as it offers the cleanest way of producing hydrogen gas through water splitting. Utilizing clean energy sources such as solar energy and wind energy, green and sustainable production of hydrogen can be achieved. Water electrolysis can provide highly pure hydrogen (99.9%) and high efficiency can be achieved when recombined with oxygen in a fuel cell to produce energy [10, 11]. Currently, the transportation sector is one of the major sources of pollution; with minimal environmental impact, fuel cells can be used in the transportation sector [11, 12]. Sustainable hydrogen production and its applications are shown in Figure 1.2.

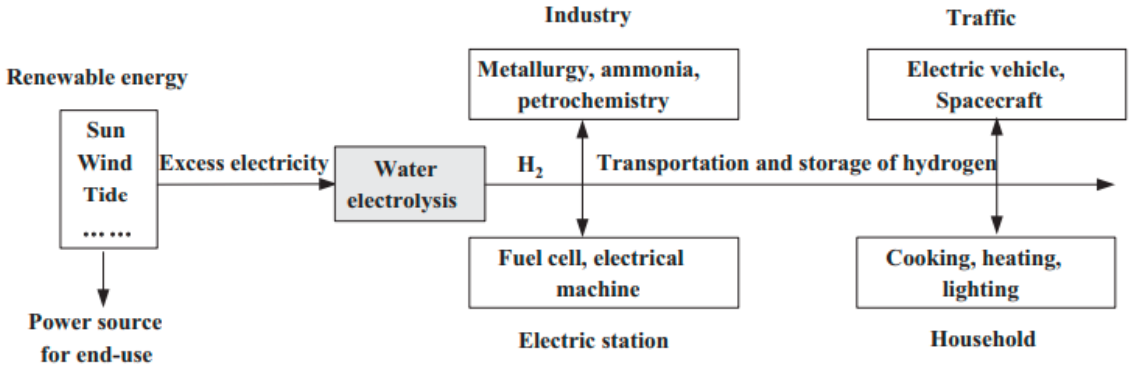

Figure 1.2. Sustainable production and application of energy. Reprinted from reference [13] with permission.

1.3. Water electrolysis – Hydrogen evolution reaction (HER) and oxygen evolution reaction (OER)

The first water electrolysis was conducted by J. R. Deiman and A. P. Troostwijk in 1789 using electricity from an electrostatic machine discharged on gold electrodes in water. Later J Ritter performed real water electrolysis and collected oxygen and hydrogen. However, industrial

application of water electrolysis started at the end of the 19th century due to various technical reasons [7]. Water electrolysis is a clean and promising technology for hydrogen production [14]

$2H_2O \rightarrow O_2 + 2H_2$ (1.1)

Water is a thermodynamically highly stable substance in nature and the conversion of water to H_2 and O_2 is thermodynamically unfavorable. The splitting of water at room temperature is negligible, nearly 10^{-7} mol/L, pure water is a very poor conductor of electricity. Hence, an acid or base is required to improve the conductivity and to facilitate the water electrolysis process [15].

Water electrolysis involves two half-reactions, the hydrogen evolution reaction (HER) at the cathode and the oxygen evolution reaction (OER) at the anode of the electrolytic cell. In an alkaline solution, oxidation of the hydroxyl group leads to the formation of two water molecules and one oxygen molecule with the same number of electrons being lost.

$4OH^- \rightarrow O_2 + 2H_2O\ (l) + 4e^-$ $E^0 = 0.40$ V vs. NHE (1.2)

$2H_2O\ (l) + 4e^- \rightarrow 2H_2\ (g) + 4OH^-$ $E^0 = -0.83$ V vs. NHE (1.3)

The overall equilibrium cell potential for the reaction is 1.23V (at 25 ºC and 1 atm). The equilibrium voltage represents the minimum voltage required for water electrolysis, which is the equilibrium potential difference between the respective anode and cathode ($E_{anode} - E_{cathode}$). In reality, the equilibrium potential is not enough to perform the water electrolysis due to the rate of the electrode reactions being very slow at ambient conditions. The generation of molecular oxygen through water splitting is associated with a high overpotential due to the four proton-electron coupled processes associated with this reaction. Although water electrolysis is a sustainable way of producing highly pure hydrogen gas, the energy cost of this electrochemical process is high, mainly due to the high overpotential associated with OER [13, 16].

Then, an additional potential is necessary to promote the water electrolysis process. This additional potential is known as the overpotential (η). This overpotential is also required to drive the ionic migration process against the resistances offered by the circuit and electrochemical cell. This causes a potential drop, iR_{cell}, where i is current and R_{cell} is the sum of the electrical resistance of the cell. Thus, the total overpotential is the sum of the overpotentials of HER and OER, electrolyte concentration difference, and bubble formation [17]

$E_{cell} = E_{anode} - E_{cathode} + \Sigma\eta + iR_{cell}$ (1.4)

OER occurs at the anode side of the electrolyzer. The OER involves multi-steps, among which some of the reactions are very fast, closer to their equilibrium potentials, while other reactions are inherently slow requiring an overpotential of $\eta = E\text{-}E^0$. The rate of electron transfer depends on the applied potential (E). The schematic diagram of water electrolysis is shown in Figure 1.3 [16, 18, 19].

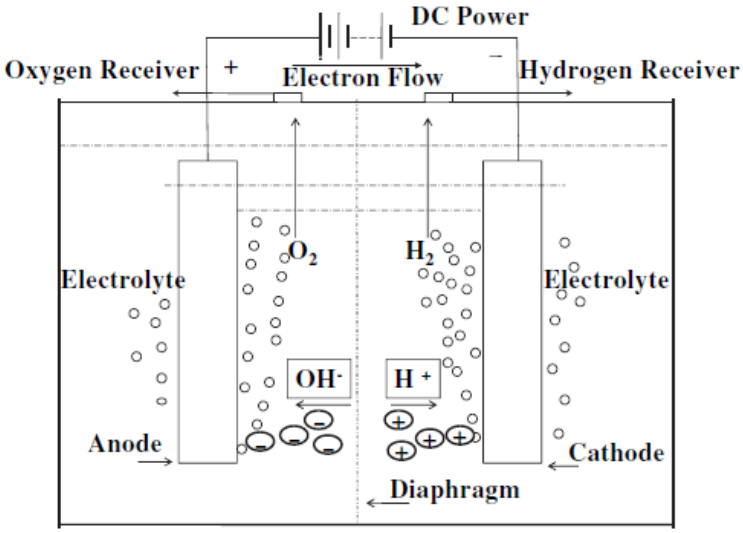

Figure 1.3. A schematic diagram of a basic water electrolysis system. Reprinted from reference [17] with permission.

Matsumoto *et al* proposed different mechanisms for OER in acidic and alkaline media. In alkaline media, the reaction initiates with the adsorption of the hydroxyl group on the active site of the electrode, which is represented by 'M', followed by several intermediate steps involved in the OER. One of the most recognized mechanisms of OER in alkaline media is shown in Figure 1.4. The proton-electron coupled steps involve MO and MOH as intermediate steps. Most of the proposed mechanisms show these intermediate steps [20, 21]. The nucleophilic attack of the hydroxyl group on MO results in the formation of a hydroperoxide intermediate, M-OOH. Followed by a proton-coupled electron transfer resulting in the generation of oxygen molecules, the active site will be regenerated. Thus, the water oxidation reaction involves four protons and four electrons in different steps and hence this process requires high potential (1.23 V).

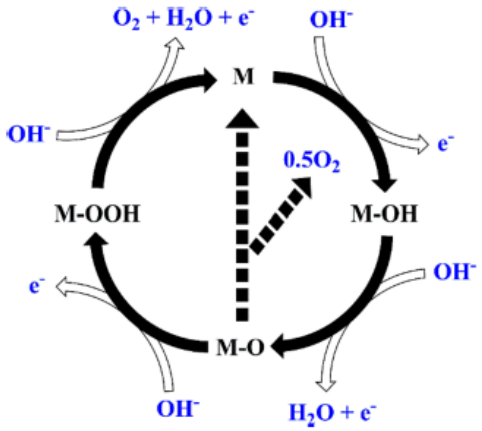

Figure 1.4. A general oxygen evolution reaction mechanism, M represents the active site. Reprinted from reference [21] with permission.

1.4. Double layer Capacitance (C_{dl}) measurement

Knowledge of the real surface area is crucial to comparing the electrocatalytic properties of different catalysts prepared by the same or different methods or catalysts from different laboratories. The surface area measured by electrochemical methods is also known as the electrochemical active surface area of the electrode (ESCA). The catalytic properties are not physically meaningful unless they are normalized by the electrochemical active surface area of the electrode (ESCA) [22]. Hence the double-layer capacitance (C_{dl}) measurements have a remarkable role in deciding the activity trend of the electrodes; ESCA is directly correlated to the double-layer capacitance of the electrode. The double-layer depends on the applied potential as it is formed in response to the large field developing at the electrode-electrolyte interface. The electrical double layer is localized over the molecular dimensions at the electrode-electrolyte interphase [23].

The structure of the double layer is shown in Figure 1.5. Generally, the charge on the electrode surface is balanced by the countercharge (opposite charge) of the same magnitude on the solution side of the interface. The solution side of the double layer can be understood based on well-accepted models. The ions present near the electrode surface are comparatively more ordered and this region is called the inner Helmholtz layer (IHL). In this region, ions can be specifically physisorbed or chemisorbed on the electrode surface. The solvated ions can only reach the surface from a certain distance, in this case, this process is purely electrostatic and

these ions are nonspecifically adsorbed. The locus of centers of these nearest solvated ions is called the outer Helmholtz layer (OHL) [23, 24].

The formation of a double layer at the interphase is a non-faradaic process; it is analogous to charging a capacitor. The electrical double layer which arises from charge separation between electrode and electrolyte is localized over molecular dimensions causing a potential gradient across the interface. The system behaves as having two capacitances in series, the compact layer and the diffuse layer, which leads to the capacitive behavior. Measuring the double-layer capacitance of the sample allows us to calculate the electrochemically active surface area of the electrode materials [17, 23, 24, 25]

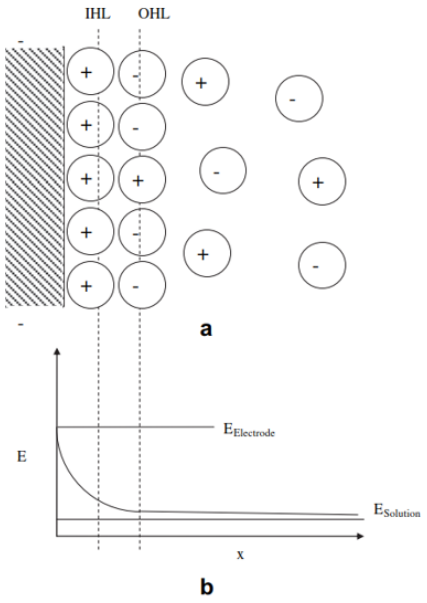

Figure 1.5. A schematic diagram of the electric double layer and potential distribution near the electrode surface. Reprinted from reference [17] with permission.

The charging current exists due to the formation of double-layer capacitance developed as a result of applied potential. This current is often much lower in magnitude than the faradaic currents and it can be neglected by using linear polarization methods such as the Tafel slope. Section 1.5 will focus on electrode kinetics theory and methods.

1.5. Theory of Kinetics of the OER and Tafel slope

Kinetic parameters such as overpotential and Tafel slope are used to evaluate the performance of the electrocatalysts. The water electrolysis process initiates when a cell potential larger than E^0_{cell} is applied. However, the rate of hydrogen and oxygen produced will greatly depend on the kinetics of two electrode reactions, which depends on the type of electrocatalyst used in the water electrolysis process. The function of an electrocatalyst in water electrolysis is to facilitate the electrochemical reaction by reducing the activation energy of the reaction without undergoing any change by itself. The reactant adsorbs on the surface of the electrode forming an adsorbed intermediate and the electrocatalysts facilitate the charge transfer process with a lower activation energy barrier [23, 26, 27].

The rate of reaction is characterized by the current density obtained during the reaction which depends firstly on the nature of the surface active sites and applied potential. When the surface area of the electrode reaction is considered,

Rate of electrolysis = i/nFA (1.5)

i is the current density, n is the stoichiometric number of electrons transferred during the reaction and F is the Faraday constant 96485 C mol^{-1}. To obtain a substantial amount of current, high overpotential is required. A faster increase of current density with a small applied potential is desired. The current density i and overpotential η can be described using the Butler-Volmer equation. When the solution is stirred, the surface concentrations do not differ appreciably from the bulk values. The overpotential and current density are related by equation (1.5).

$$i = i_o[\exp(\alpha_a nF\eta/RT) + \exp(\alpha_c nF\eta/RT)] \quad (1.6)$$

Under high anodic conditions or at large positive overpotentials, the overall current density is mainly attributed to the anodic component, cathodic contribution is negligible.

$$i \approx i_o \exp(\alpha_a nF\eta/RT) \quad (1.7)$$

where i_o is the exchange current density, α_a is the transfer coefficient, a measure of the symmetry of the energy barrier, n is the number of electrons transferred, F is the Faraday constant, R is the ideal gas constant, and T is the temperature. Higher exchange current density is always desirable so that lower overpotential is necessary. By translating the Tafel equation to logarithm function form, $\log (i) = \log (i_o) + \eta/b$ (1.8)

$b = 2.303RT/\alpha F$ (1.9)

where b is called the Tafel slope. A lower Tafel slope indicates a faster increase of current density with a smaller overpotential and is an indication of a good electrocatalyst. The Tafel slope is often used to compare the catalytic activity of catalysts [23, 26, 27].

The OER is a multi-electron transfer process and is kinetically much slower than the HER, which leads to a higher overpotential making the overall water-splitting process very inefficient. To reduce the overpotential and increase the efficiency of the OER process, highly efficient electrocatalysts are necessary [28]. Numerous research efforts have been devoted to overcoming the kinetic barrier with a lower energy demand achieving inexpensive, highly durable, and sustainable electrocatalysts. An overview of various electrocatalysts developed for OER is given below in section 1.6.

1.6. Overview of different types of materials used for the OER

The water electrolysis process is a 200-year-old technology. However, its contribution to the total hydrogen production is very small (nearly 4%) compared to other methods and it is limited to small-scale applications. Hydrogen possesses the advantages of high purity and availability. However, large-scale production of hydrogen using water electrolysis requires development in different areas including energy efficiency, durability, operability, portability, and reduction in installation and operation costs [23]. In this framework, designing highly efficient electrocatalysts can play a crucial role in the development of sustainable energy systems. As this work aims to design highly efficient electrocatalysts for OER, understanding the history of the development of electrocatalysts is very important. It provides the knowledge and significance of their role and opens up the possibilities of investigating alternative promising catalysts for OER.

1.6.1. Noble metals and metal oxides:

To achieve high performance of the electrolytic cell, the electrode materials should possess good corrosion resistance, good conductivity, high catalytic properties, and low cost. In addition, properties such as high surface area and minimization of gas bubble formation would further enhance materials performance towards water electrolysis [27, 29]. Initially, pure Ru and Ir gained a lot of attention as OER catalysts. Pt and Pd were also found to be active catalysts for OER but displayed lower performances compared to Ir and Ru. However, these metals were unstable due to their dissolution in acidic and alkaline media which hindered their practical

applicability [28, 30]. Later, the metal oxides of Ru and Ir were found to possess higher catalytic activities. This discovery led to a huge impact on large electrolytic industries, IrO_2 and RuO_2 are found to be the state of art materials for OER [29, 30]

The choice of electrocatalysts is always a compromise between catalytic activity, stability, and cost of the materials. RuO_2 displays slightly higher catalytic activity compared to IrO_2. However, IrO_2 possesses higher stability in acidic and alkaline environments and can sustain high anodic potential conditions [28,30]. The remarkable activity of these compounds is well established by many research groups [30, 31, 32, 33]. These compounds possess high conductivity due to their rutile structure [32, 34, 35]. OER involves the adsorption and desorption of intermediates such as *OH, *O and *OOH, weaker adsorption of these intermediates will not result in efficient electron transfer. Meanwhile, strong adsorption will prevent the release of catalyzed products [36]. Researchers often use M-OH bond strength and free energy change ($\Delta G_{O*} - \Delta G_{HO*}$) as descriptors which allow us to understand the trends in the OER activity of the materials. The catalysts that possess equal energy barriers for the adsorption and desorption of the intermediates will possess the highest catalytic activity for OER. When the adsorption of the O is strong, the OH does not easily form *OOH with the catalyst. On the other hand, if the adsorption is weak, *OH does not form easily. A suitable catalyst-oxygen bond strength reduces the overpotential for OER and thus a lower thermodynamic energy barrier can be achieved. A volcano plot has been proposed based on Sabatier's principle [37]. The most active catalyst is positioned at the top of the volcano plot (see Figure 1.6a) and b)).

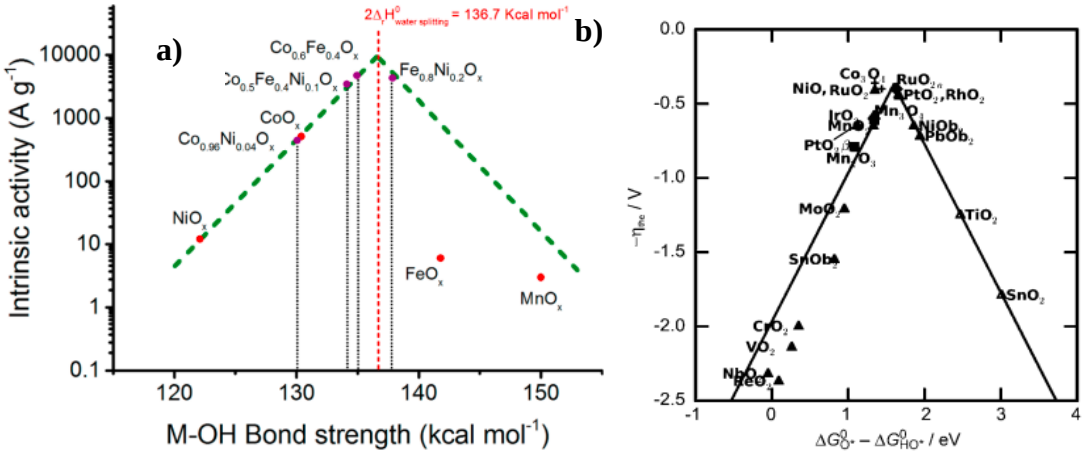

Figure 1.6. Volcano plot showing a) the intrinsic activities of transition metal (oxy)hydroxides vs M−OH bond strength reprinted with permission from reference [37] b) the overpotential for OER Gibb's free energy change. Reprinted from reference [31] with permission.

Thus, designing a highly active catalyst involves finding the materials with optimal binding energy with intermediates. IrO_2 and RuO_2 possess optimal binding energy with OER intermediates and are placed near the top of the volcano curve. In addition, kinetic studies indicate that both IrO_2 and RuO_2 possess lower Tafel slopes, indicating the fast kinetics of OER for materials [33].

Since these noble metal-based catalysts increase the cost of production of hydrogen, the application of nanosized metal or metal oxide catalysts enhanced the practical applicability of hydrogen production [38]. Nanomaterials reduce the amount of electrocatalysts required for the OER process. Nanosized materials play an important role in energy conversion and energy technologies as they possess large surface area, long durability, and excellent catalytic activity [39]. The electrocatalytic activity of these materials is remarkably superior to corresponding metals or metal oxides.

Although Ir and Ru-based catalysts are highly performing electrocatalysts, these catalysts are expensive and rare which prevents their practical application in large-scale production of hydrogen. The use of noble metals or metal oxides increases the cost of hydrogen production. Hence, large-scale production of hydrogen requires the cost of the water electrolysis process to be reduced. This motivated researchers to search for cheaper and more efficient electrocatalysts that are stable and earth-abundant.

1.6.2. Earth-abundant transition metals

Transition metal oxides are potential electrocatalysts for OER due to their low cost, good corrosion resistance, and abundance. In addition, the multivalent oxidation states of transition metals make them attractive candidates for OER [40]. Transition metals such as Ni, Cu, Co, and Fe have gained a lot of attention due to their high abundance, good catalytic activity, and stability in alkaline media [19, 21, 27]. The studies about these materials date back to more than a half-century. Early studies used mainly bulk oxides or electrochemically deposited films. Even though much effort has been made into the development of transition metal oxide catalysts, this field remains very active as further improvements in OER catalysis are sought. The advances in

nanoscience and nanotechnology allowed us to synthesize a wide range of metal oxides with controlled composition, morphology, size, structure, and surface area so that highly efficient materials can be developed. Different types of transition metal-based electrocatalysts were reported as potential candidates for OER. Among these, spinel oxides, layered hydroxides, perovskites, amorphous metal oxides, sulfides, and phosphides have gained a lot of attention due to their high catalytic activity and stability in alkaline medium, and have the potential to replace highly efficient noble metal-based electrocatalysts [25, 28, 41, 42].

1.6.3. Spinel oxides

Spinel oxides are an interesting class of compounds and have emerged as a cheaper alternative to noble metal oxide electrocatalysts in alkaline media for OER. Spinels form a large family and can include one or more metal atoms. Spinel oxides are crystallized in a face-centered cubic close-packed structure of oxygen anions with a space group of *Fd3m*. It consists of 8 formula units with 64 tetrahedral sites and 32 octahedral sites, where $1/8^{th}$ of the tetrahedral positions (8*a*) and half of the octahedral positions (16*d*) are occupied by metal ions. Spinel oxides have a general formula AB_2O_4, where cation A has a typical charge of 2+ and cation B has a typical charge of 3+ [43, 44]. Spinel oxides of the type Co_3O_4, Fe_3O_4, and MnO_2 have been widely studied. Depending on the site occupancy of the cation, spinels can be categorized as normal or inverse spinels. In a normal spinel structure, metal cation A occupies the tetrahedral sites and B occupies the octahedral sites of the spinel structure, while for the inverse spinel structure, A and half of B occupy the octahedral sites and half of B occupies the tetrahedral sites of the spinel lattice (structure of spinel oxide is shown in Figure 1.7) [45, 46]. Spinel oxides demonstrated excellent intrinsic, catalytic, magnetic, optical, and electrical properties making these class of compounds suitable for many applications [19, 47, 48, 49, 50]. Generally, spinel oxides possess good conductivity due to the electron/hole hopping between different oxidation states. Spinel oxides of different metal oxides have been reported and attracted great interest due to their notable catalytic properties. Among these, cobalt oxides showed remarkably high catalytic properties for OER and are highly stable in alkaline medium [46, 51].

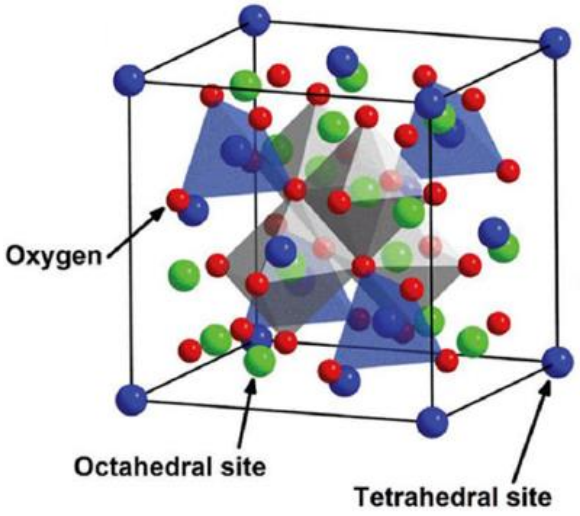

Figure 1.7. Crystal structure of a typical spinel. Reprinted from reference [52] with permission.

Various synthesis procedures have been adopted to synthesize nanostructured and mesoporous cobalt oxide materials to obtain high surface area, which is one of the strategies to achieve lower overpotential [51, 53]. Enhanced catalytic activity has also been achieved by introducing metal cations such as Fe, Cu, Ni, Mn, and Zn in the cobalt spinel lattice. Doping is a very common and highly efficient approach to achieve desirable properties such as high conductivity, better catalytic activity, and stability. Researchers have explored binary and ternary cobalt spinel oxides for OER [45, 48, 49, 54, 55]. Non-metals such as nitrogen and carbon-doped cobalt oxides have also gained a lot of attention due to their high catalytic activity for OER [56, 57].

Several reports indicate that the oxidation state and site occupancy of metal cations in spinel structure plays an important role in their activity towards OER (Co^{2+}, Co^{3+} or Co^{4+}), they act as active sites for adsorption of intermediates in the OER process [54, 58]. In a normal spinel structure, Co^{2+} occupies tetrahedral sites, and Co^{3+} occupies octahedral sites [46]. In general, cations in octahedral (Oh) sites are more oxidized than metal cations occupying tetrahedral (Td) sites. Deviation from normal spinel structure is also reported [55, 59]. Studies indicate that Zn replaces only Co^{2+} at the tetrahedral sites and hence $ZnCo_2O_4$ achieves a normal spinel structure, while, Cu and Ni preferentially occupy the octahedral sites yielding inverse spinel structure [48, 54, 57, 59].

Zang *et al.* reported efficient copper-modified cobalt oxide, with a low overpotential of 342 mV at 10.0 mA cm^{-2} for OER. They hypothesized that cobalt becomes more electron-withdrawing in nature in the presence of Cu^{2+}, which facilitates the oxidative addition of water to cobalt sites, the authors link this step to the observed enhanced OER activity [60]. The o*perando* analysis by electrochemical impedance spectroscopy and X-ray absorption spectroscopy (XAS) showed that Co^{2+} (Td) is the active site for the formation of CoOOH, which mediates water oxidation [61]. Song *et al.* performed cyclic voltammetry (CV), X-ray photoelectron spectroscopy (XPS), and Raman measurements on Ni/Mn substituted Co_3O_4. These studies revealed that oxidation of Co^{3+} to Co^{4+} is crucial for OER performance. The substitution of electronegative elements such as Ni and Mn facilitates the oxidation of Co^{3+} to Co^{4+}, enhancing the OER activity [62]. Several earlier studies proposed the formation of CoOOH on the surface of Co_3O_4, during water oxidation in alkaline media [60, 61, 63]. Recently, Magnussen *et al.* studied the potential dependent restructuring of Co_3O_4 surface using *operando* X-ray scattering. They identified the formation of a $CoO_x(OH)_y$ skin layer at ≈ 300 mV negative of the onset of OER. In the OER region, the oxidation state of Co further increases from Co^{3+} to Co^{4+} but only a small amount of Co^{4+} is detected [64]

Co, Ni, Mn, and Cu substituted Fe_3O_4 have also been widely studied, and observed enhanced catalytic activity upon substitution of metal cations [65, 66]. Li *et al* have prepared transition metal substituted ferrite nanofibers (NF) [MFe_2O_4, M= Co, Ni, Cu, and Mn], and observed improved catalytic activity for OER and H_2O_2 reduction in alkaline solution. The activity towards OER follows the order of $CoFe_2O_4$ NFs > $CuFe_2O_4$ NFs > $NiFe_2O_4$ NFs > $MnFe_2O_4$ NFs > Fe_2O_3 NFs [66]. Recently, ternary spinel oxides have also gained attention, as the right combination of metals in a spinel lattice is an excellent option to improve the performance of catalysts for OER. Lee *et al.* have prepared a series of Co-Cu-Zn ternary oxide-coated electrodes, which had high catalytic activity for the OER [67]. Lu *et al.* studied the catalytic activity of $M_{0.1}Ni_{0.9}Co_2O_4$ (M = Mn, Fe, Cu, Zn) and found that $Fe_{0.1}Ni_{0.9}Co_2O_4$ provided the highest catalytic activity. The high performance of this composition was attributed to the higher Co^{2+} to Co^{3+} and lower Ni^{2+} to Ni^{3+} ratios observed in Fe-doped $NiCo_2O_4$ [68]. Yan *et al.* synthesized ternary mixed metal spinel oxides, $Fe_xNi_{1-x}Co_2O_4$ (x = 0, 0.1, 0.25, 0.5, 0.75, 0.9, 1), and observed that $Fe_{0.5}Ni_{0.5}Co_2O_4$ exhibited the highest electrocatalytic activity with a

lower overpotential of 350 mV at 10 mA cm^{-2}. In addition, of the series of materials studied, $Fe_{0.5}Ni_{0.5}Co_2O_4$ displayed the smallest Tafel slope value of 27 mV dec^{-1} [69].

1.6.4. Cobalt-based layered hydroxides

Layered hydroxides are another promising class of transition metal oxide electrocatalysts for the OER. Layered hydroxides have great affinity to aqueous electrolytes and the layered structure of hydroxides provides high surface area and hence more active sites available for the OER. Great research efforts have been made to develop highly active layered double hydroxide catalysts. The general formula of this compound is $[M_2^{2+}M^{3+}(OH)_6](X^{n-})_{1/n}.\ yH_2O$. An LDH consists of anions or water molecules in the interlayer space. Where M^{2+} (M = Mg, Ca, Mn, Fe, Co, Ni, Cu, or Zn), and M^{3+} (M = Al, Mn, Fe, Co, or Ni) makes the metal layer positive and to compensate for this positive charge, anions such as Cl^-, Br^-, CO^{3-}, NO^{3-}or SO_4^{2-} are intercalated into the interlayer space [65]. Cobalt/iron-based hydroxides have shown excellent catalytic activity for OER [51, 65]. Zhuang *et al* prepared iron cobalt oxide nanosheets with large specific surface area and abundant oxygen vacancies. They have achieved a lower overpotential of 350 mV for OER and a Tafel slope of 36.8 mV/dec, which indicates the high catalytic activity of these materials [70]. Zou *et al* proved that Zn-Co LDH is a promising electrocatalyst for OER. Co-Mn LDH was also demonstrated to be an excellent catalyst for OER and found to possess lower overpotential compared to their corresponding monometallic hydroxides or metal oxides [71]. Similarly, NiCo and NiFe hydroxides were also reported to be excellent catalysts for OER [72].

1.6.5. Perovskite oxides

Perovskites are highly active electrocatalysts for OER. Perovskite materials are generally studied in alkaline media as they are more stable in this media compared to acid media [73]. Perovskites have a general formula of ABO_3, where A is an alkaline and rare-earth metal atom. Transition metal atom B occupies the center of the octahedral site which is connected by corners. Transition metals in perovskite usually accept the +3 or +4 oxidation state depending on the oxidation state of A. The catalytic activity of perovskite can be modified by different strategies. Changes in the oxidation state of cations or anions or creating oxygen vacancies in the lattice can change the conductivity and catalytic activity of perovskites. Doping of A site, B site, or co-doping can modify the electronic properties, crystal structure, and morphology of the compound [73, 74]. For example, substituting a cation with a cation of lower valence increases conductivity

by introducing unoccupied electronic states. Shen *et al* observed high catalytic activity when Sr was substituted for La in $LaFeO_3$. This improved catalytic activity was linked to the presence of Fe^{4+} which created a hole in the conduction band facilitating charge transfer rate [75]. Doping B site in perovskite is also an effective strategy to alter the performance of the material for OER. Doping at the B site can promote the adsorption of intermediates at the surface of catalysts. Kim *et al* prepared $La_{0.2}Sr_{0.8}Co_{1-x}Fe_xO_{3-\delta}$ and $Ba_{0.5}Sr_{0.5}Co_{1-x}Fe_xO_{3-\delta}$ with x = 0 and 0.2, by flame spray synthesis and they observed that Fe incorporation enhanced the catalytic activity and stability of the perovskite materials significantly [76]. Among various perovskite compositions reported, $Ba_{0.5}Sr_{0.5}Co_{0.8}Fe_{0.2}O_{3-\delta}$ is one of the best-performing quaternary compositions and its intrinsic OER catalytic activity was one order magnitude higher than state-of-the-art material IrO_2. The high performance of this composition was attributed to the e_g occupancy of 3d electron; at an e_g occupancy close to unity high covalency of transition metal-oxygen bonds is expected [77].

1.6.6. Amorphous metal oxides

Recently, amorphous materials have emerged as promising catalysts for water oxidation. The high activity of amorphous metal oxides was attributed to the presence of abundant active sites. Both single and multimetal amorphous oxides have been reported. Cobalt and nickel-based amorphous metal oxides are of great interest to researchers [78, 79, 80]. S. Trudel *et al* prepared amorphous quaternary Ba-Sr-Co-Fe oxide (BACF) and showed excellent catalytic activity towards OER. They found that photochemical decomposition is a suitable method to synthesize quaternary amorphous metal oxides with controlled compositions. This amorphous BACF film showed a lower Tafel slope and higher current density compared to their corresponding crystalline materials. This high catalytic activity was attributed to the presence of a large number of coordinately unsaturated surface metal sites available for the OER and the single-phase nature of the amorphous materials [80]. C.P. Berlinguette *et al* demonstrated that amorphous iron oxide shows superior catalytic activity than hematite, while α-$Fe_{100-y-z}Co_yNi_zO_x$ possessed a comparable catalytic activity to those of noble metal oxide catalysts for OER [81]. M. Driess *et al* synthesized amorphous and crystalline materials by facile solvothermal route by controlling the crystallinity of the samples by changing the solvent and reaction time. They found that amorphous cobalt iron oxide showed superior catalytic activity compared to crystalline material under photochemical and electrochemical water oxidation and water reduction reactions [79].

A. Irshad and N. Munichandraiah developed an extremely catalytically active amorphous Iridium-phosphate (Ir-Pi) by electrodeposition on carbon paper electrode from neutral phosphate buffer solution containing Ir^{3+} ions, which possessed high activity for the OER and showed an overpotential as low as 220 mV in phosphate buffer (pH=7) solution. This catalyst exhibited superior catalytic activity compared to state-of-the-art materials such as IrO_2 and Co-Pi catalysts in terms of current density and onset potential [82].

Xiao *et al* reported that cobalt iron bimetallic phytate nanostructures possess a low overpotential of 278 mV in 1M KOH and provided a current density of 10 mA cm^{-2} with a lower Tafel slope of 34 mV dec^{-1} [83]. Liardet *et al* developed cobalt vanadium oxide by facile hydrothermal route and was designed based on the volcano plot of metal-OH bond strength and activity. These materials achieved a current density of 10 mA cm^{-2} at an overpotential of 254 mV with a Tafel slope of only 35 mV dec^{-1} [84]. Thus, several studies have reported the high catalytic activity of amorphous materials for the OER and are found to be stable for electrochemical reactions. Amorphous materials have a more disordered structure and the active site for the OER is found to be (oxy)hydroxides according to many studies. These (oxy)hydroxides play an important role in the OER reaction. The amorphous materials easily transform to hydroxides and possibly, the reason for the high activity of these materials. These materials are found to be promising electrocatalysts for the OER [85, 86].

Multimetal systems show remarkable catalytic properties for the OER compared to single metal systems. Along with compositional flexibility, nanostructured materials, and thin film deposition techniques further enhanced the catalytic properties of these materials. Even though significant efforts have been made to design highly efficient electrocatalysts, noble metals, and metal oxides are still extensively used in industry due to their high performance and stability in acid and alkaline media. A systematic study of the relation between structure, composition, and properties of the materials allows for the identification of descriptors that correlate with materials' efficiency towards OER, which is crucial to designing highly efficient electrocatalysts. The surface characterization techniques along with other characterization methods enable a deeper understanding of the materials' properties at the atomic scale and ultimately the tailoring of improved transition metal oxide electrocatalysts.

1.7. Techniques used for the characterization of electrodes

1.7.1. Scanning electron Microscopy (SEM)

Scanning electron microscopy is a very useful technique in material chemistry and examines the microscopic structure of the materials and provides information about the surface morphology of the materials. Due to the large depth of field of SEM, images have a three-dimensional appearance and have great application in material chemistry [87].

1.7.1.1. Instrumentation

SEM has an electron gun and a series of electromagnetic lenses and apertures. The electron beam from the electron gun is condensed to a fine probe and scans the surface of the materials. A field emission gun is also used in advanced SEM due to its high beam brightness. The two condenser lenses reduce the cross-over diameter of the electron beam and the objective lens focuses this beam as a probe with a diameter of nanometer scale. The probe moves over the surface of the sample and along the line and displaces to a position next, and a rectangular raster is generated. The detector collects the electrons emitted from the sample surface and amplifies and reconstructs the image. The two pairs of electromagnetic coils control the deflection system of SEM. The aperture in SEM is mainly used to control the divergence of the electron beam in the optical path. The Structure of an SEM instrument is shown in Figure 1.8.

An SEM can provide an image magnification of about 20× to greater than 100,000×. Everhart–Thornley (E–T) detector is commonly used in SEM. Two types of electron signals are generated when high-energy electron beams hit the surface of samples, inelastic scattering produces secondary electrons (SEs) and elastic scattering produces backscattered electrons (BSEs). Secondary electrons achieve topographic contrast, while BSEs are useful signals for elemental composition contrast. SEs can emit only from a volume near the sample surface with a depth of 5 – 50 nm even though they generate in the whole pear-shaped zone and have an energy level of several electron volts. Meanwhile, BSEs can escape from a depth of 50 – 300 nm due to their higher energy (energy level close to that of incident electrons) [87, 88]. In Figure 1.9, the interaction zone of electrons and sample atoms below the sample surface is shown. The SEM instrument used for the analysis of our samples is shown in Figure 1.10.

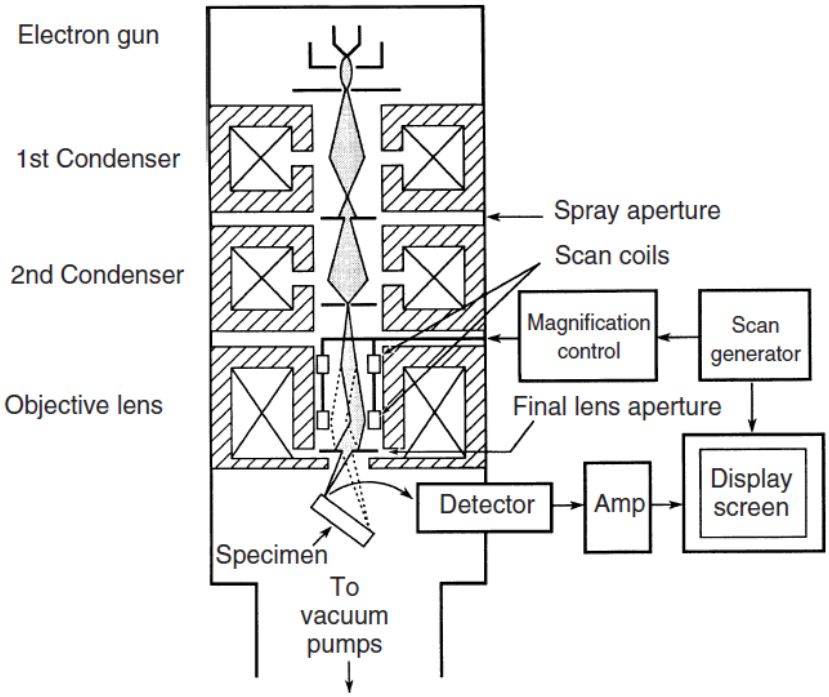

Figure 1.8. Structure of a scanning electron microscope. Reprinted from [87] with permission

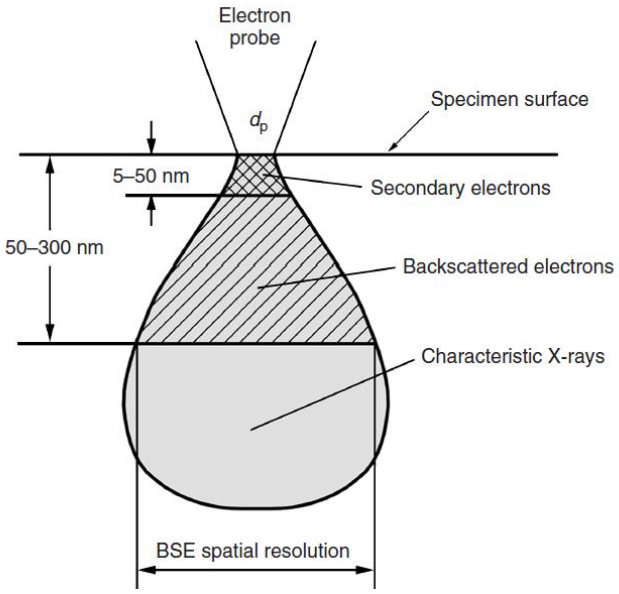

Figure 1.9. Interaction zone of electrons and sample atoms below the sample surface. Reprinted from [87] with permission.

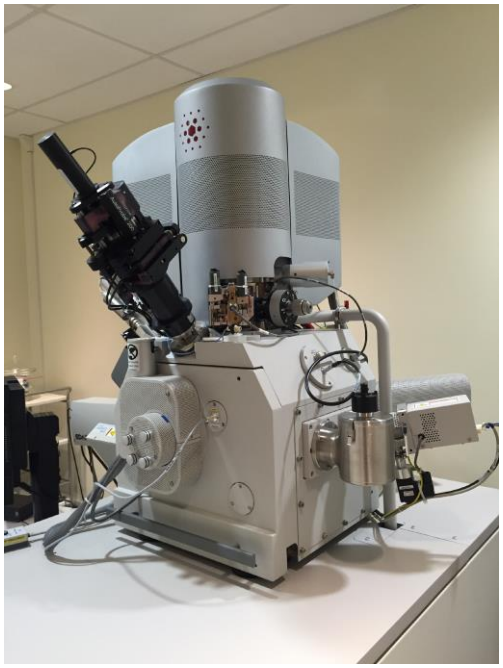

Figure 1.10. Scanning electron microscope (SEM), SEM FEI, QUANTA 3D PEG used for the analysis of our prepared samples.

1.7.2. Energy Dispersive X-ray spectroscopy (EDX)

EDX analysis is an effective tool for identifying elements present in the sample using characteristic X-rays emitted from the sample. It also quantifies the chemical elements so that the composition of the materials can be identified [87].

Each element has a unique set of characteristic peaks in its electromagnetic spectrum. Upon the interaction of X-ray with the sample, electrons in the inner shell of atoms excite the outer shell creating a hole. When the electron from a higher energy shell fills this hole, the energy is released in the form of an X-ray. The energy difference between the high-energy shell and the inner energy shell generates characteristic X-rays. This characteristic X-ray is well-defined and dependent on the atomic number of each element. The excitation of characteristic X-rays is shown in Figure 1.11. The chemical elements can be identified either by the wavelength of X-rays as in X-ray wavelength dispersive spectroscopy (WDS) or using their X-ray energy as in Energy dispersive X-ray spectroscopy (EDX). The peak position indicates the type of elements, and from the intensity of peaks, the quantity of each element present in the sample can be identified. This allows us to determine the composition of the material. Several characteristic X-rays are emitted depending on the number of shells and the atomic number of atoms. These

characteristic X-rays are denoted as Kα, Kβ, etc., depending on the energy of the shell they are emitted from [87, 88].

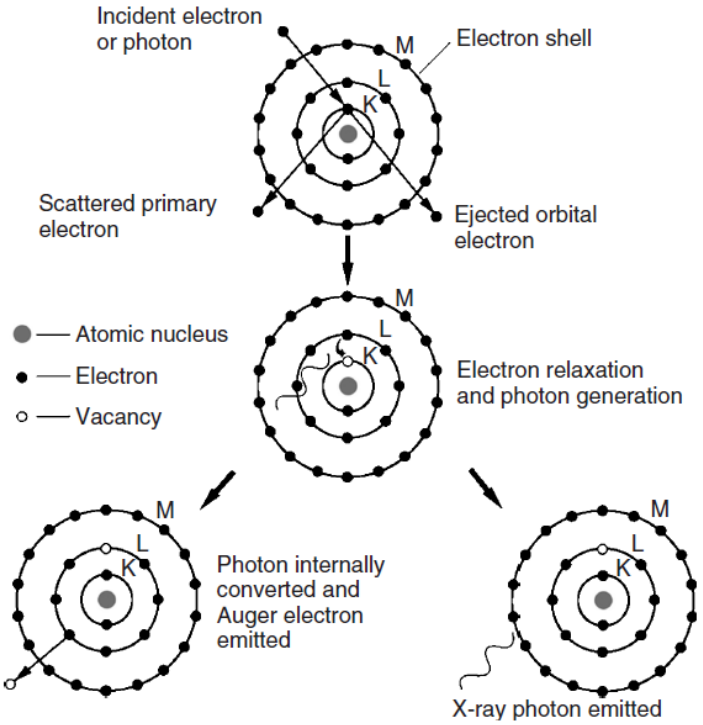

Figure 1.11. Excitation of a characteristic X-ray photon or an Auger electron by high energy X-ray photon or electron. Reprinted from [87] with permission.

1.7.2.1. Instrumentation

The Si(Li) is the most commonly used detector in energy dispersive X-ray spectroscope. This detector contains a small cylinder of P-type silicon and lithium in the form of a Si(Li) diode. The detector generates the electron-hole pairs depending on the intensity of X-ray photons they receive from the sample. The higher the X-ray photon energy, the more electron-hole pairs are formed. These electron-hole pairs are swept from the detector diode and a preamplifier collects this charge to produce an output electrical pulse, whose voltage amplitude is directly proportional to the X-ray photon energy. An EDX spectrum is a plot of the intensity of characteristic X-ray lines vs. X-ray energy range [87, 88]. The main components of the energy-

dispersive X-ray spectroscope are shown in Figure 1.12.

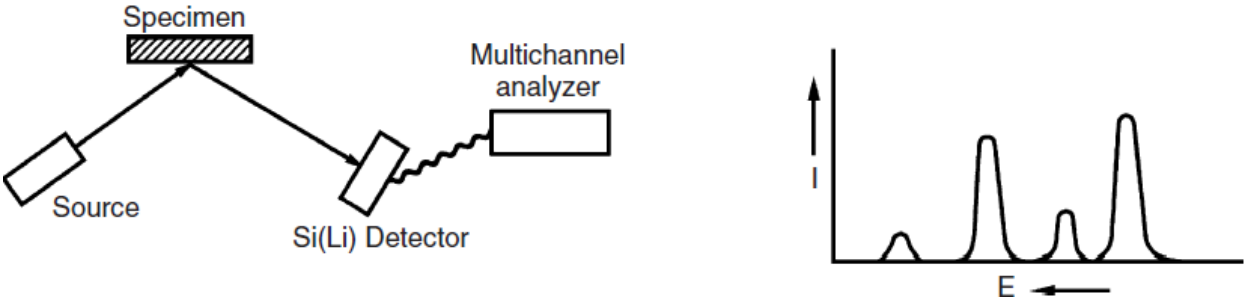

Figure 1.12. Main components of Energy dispersive X-ray spectroscope. Reprinted from [87] with permission.

1.7.3. X-ray diffraction (XRD)

X-ray diffraction is a highly efficient technique and is widely used for characterizing the crystal structure of materials. The X-ray diffraction method usually requires monochromatic X-ray radiation. X-rays are high-energy electromagnetic radiation and are produced in an X-ray tube (see Figure 1.13). The electrons are accelerated by a high-voltage field and collide on a metal target. The rapid deceleration of these electrons causes the kinetic energy of electrons to be converted to X-ray radiation. An X-ray tube generates continuous X-rays with a sharp intensity maximum, called characteristic X-rays. This characteristic X-ray is filtered out from other radiations and is used for the X-ray diffraction method [87, 89].

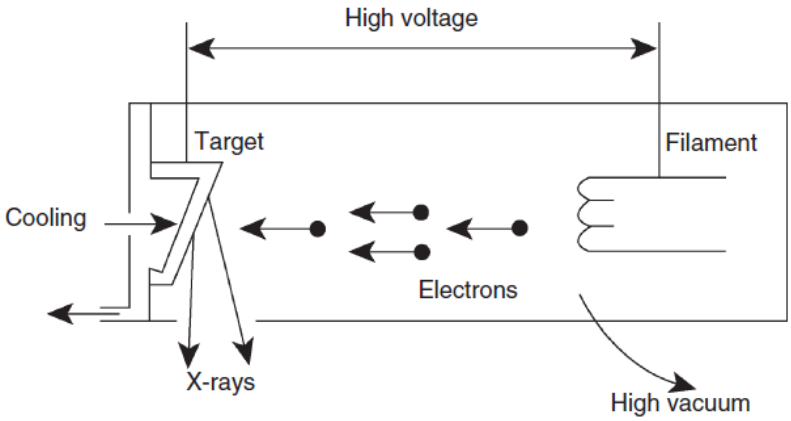

Figure 1.13. Structure of X-ray tube. Reprinted from [87] with permission.

Crystalline materials consist of regular arrays of atoms or ions having an interatomic spacing of the order of 100 pm. When an X-ray beam incident on a crystalline material at an angle θ, the reflection occurs only when the following condition of constructive interference is fulfilled.

$n\lambda = 2d_{hkl}\sin\theta$ (1.10)

This is known as Bragg's equation, where λ is the wavelength of the incident wave, n is an integer and d is the distance between the lattice planes. The spacing between the atomic planes (d_{hkl}) of a crystal can be calculated by knowing the incident angle at which constructive interference occurs and the wavelength (λ) of the incident beam [87, 90]. Bragg diffraction by crystal planes is shown in Figure 1.14.

Knowing the d spacing of crystallographic planes, the lattice parameter of a cubic crystal (a) can be calculated using the formula,

$a = d\,(h^2 + k^2 + l^2)^{1/2}$ (1.11)

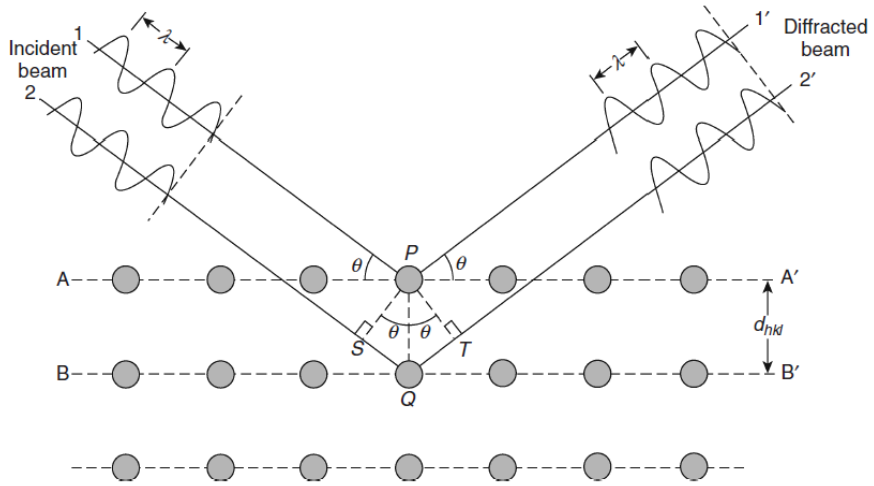

Figure 1.14. Bragg diffraction by crystal planes. Reprinted from [87] with permission.

1.7.3.1. Instrumentation

The X-ray diffraction instrument is called X-ray diffractometer. The **g**eometric arrangement of the X-ray diffractometer is shown in Figure 1.15. X-ray is generated in a cathode ray tube. X-ray radiation which passes through the Soller slits that collimate the X-ray beam and strike the specimen. X-rays that are diffracted from the sample pass through the monochromatic filter. This arrangement would help to filter out wavelengths other than K*α* radiation and to reduce background radiation originating from the sample. The relative movements of the X-ray tube, sample, and detector allow recording the X-ray spectrum in a range of 2θ. The diffractometer records the intensity, and the peaks located at different 2θ give the fingerprint for a crystalline material. The diffraction spectrum is a plot of diffraction intensity vs angle 2θ. Each

peak indicates the diffraction from certain crystallographic planes. Comparing this spectrum to that of the standard spectrum allows us to identify the type of crystalline material or crystalline phase of the sample [87].

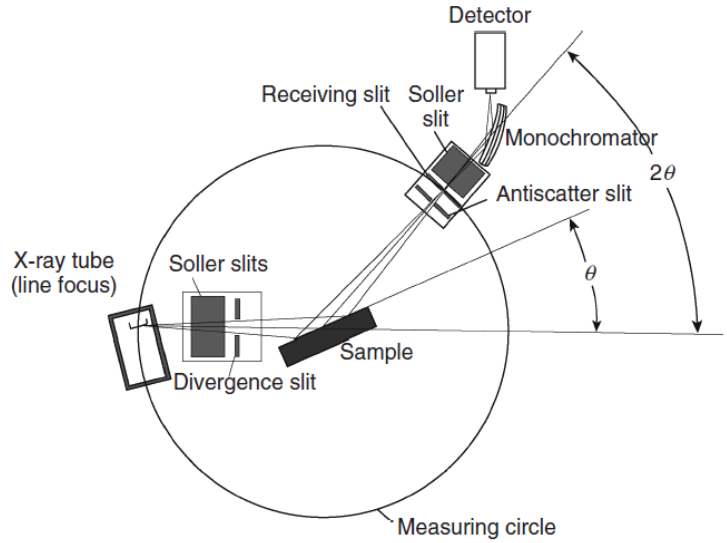

Figure 1.15. Geometric arrangement of X-ray diffractometer. Reprinted from [87] with permission.

1.7.4. X-ray photoelectron spectroscopy (XPS)

X-ray photoelectron spectroscopy (XPS) is a highly useful technique for studying the surface structure and composition of materials. This technique was developed by Kai Siegbahn's research group at Uppsala University, Sweden, and won the Nobel Prize in 1981. This technique is also known as Electron spectroscopy for chemical analysis (ESCA) which provides information about the chemical state of elements and the composition of materials at the surface [91].

1.7.4.1. Instrumentation

XPS analysis is performed in an ultra-high vacuum of the order of 10^{-8} Pa as it is very sensitive to surface contamination. The monochromatic X-ray source is used for XPS analysis. The thermionic emission of electrons from tungsten filament is used as a source of X-rays for XPS analysis. These high energy electrons are accelerated to a water-cooled anode and cause ejection of electrons from the core-shell of the atom, followed by, these elements relaxing by emitting characteristic X-rays. Generally, Al or Mg is deposited onto the anode giving Al and Mg Kα X-rays of energies 1253.6 eV and 1486.6 eV respectively. An electron energy analyzer

(or hemispherical analyzer) disperses the electrons based on the kinetic energy of the electron [87, 91]. A schematic diagram of the hemispherical analyzer is shown in Figure 1.16.

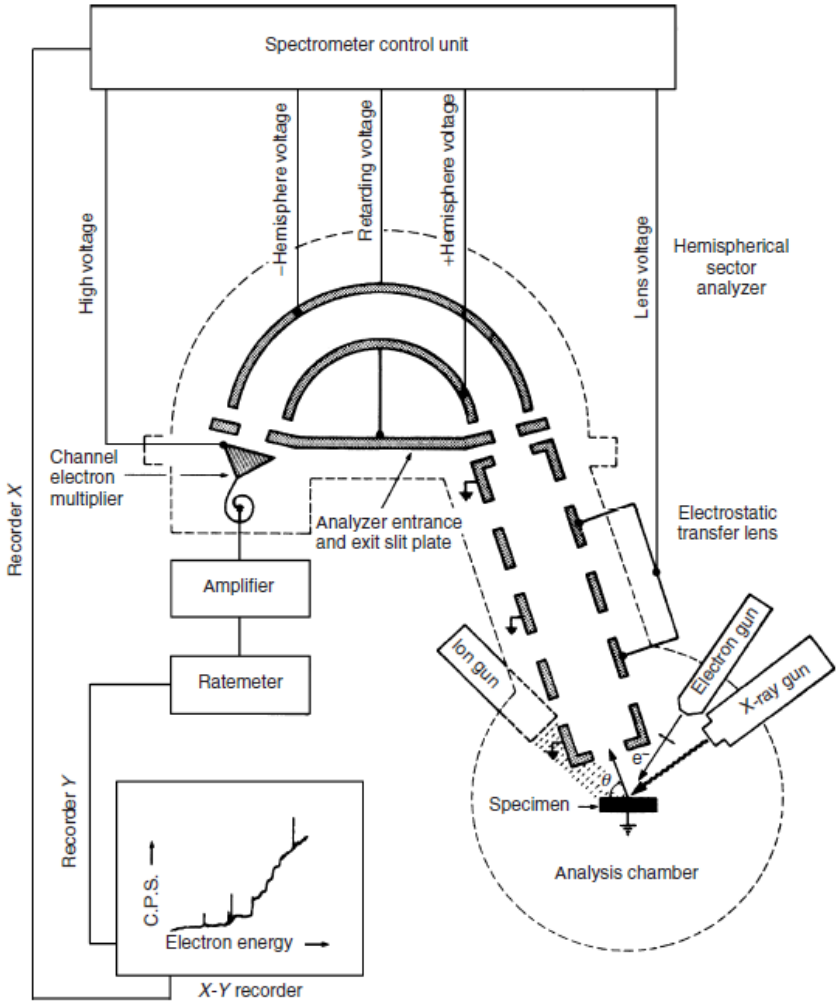

Figure 1.16. Schematic representation of electron energy analyzer. Reprinted from [87] with permission.

The hemispherical analyzer has a conducting inner and outer hemisphere with input and output slit. The two concentric hemispheres will be given different potentials and this applied potential generates a median equipotential surface. The potential along the median surface is called the pass energy of a concentric hemispherical analyzer. The kinetic energy of the sample is reduced by the lens system (called pass energy) before entering the slit of the hemispherical analyzer. The electrons entering at the slit are deflected by the electric field between the two hemispheres so that only the electrons traveling at a pass energy of $E_p = eV_p$ will follow a path given by mean radius will reach the detector. Thus, the device disperses the electrons based on

the kinetic energy of the electron. The detector measures the position and intensity of the emitted photoelectron. An XPS spectrum is a plot of the intensity versus kinetic energy or binding energy of the electrons [87].

1.7.5. Fourier transformed Infrared spectroscopy

The infrared region of the spectrum ranges from 12,800 to 10 cm^{-1}. It is conventionally divided into near, mid, and far infrared radiation. Infrared spectroscopy deals with infrared absorption, emission, and reflection spectra of molecular species and is used to identify chemical substances or functional groups. Absorption of infrared radiation causes the transition of a molecule from one rotational or vibrational level to another one. To absorb infrared radiation by a molecule, the molecule should undergo a net change in dipole moment. The dipole moment is determined by the distance between the charges and their charge difference. Absorption of IR radiation occurs when the frequency of IR radiation matches the natural frequency of the molecule. The molecule absorbs frequencies that are characteristic of its structure. Analyzing the IR spectrum gives abundant structural information about the molecule. The vibrational and rotational levels are quantized for molecules. For most molecules, the energy difference between the vibrational levels corresponds to the mid-infrared region. The energy required to cause a change in rotational level is lower (100 cm^{-1} or less) [92]. FTIR spectroscope (Nicolet 6700 FTIR) used for the analysis of our sample is shown in Figure 1.17.

Figure 1.17. FTIR spectrometer (Nicolet 6700 FTIR) was used for the analysis of samples.

1.7.5.1. Instrumentation

Figure 1.18 shows the schematic diagram of the arrangement of components in a typical infrared spectrophotometer. The instrument consists of an inert solid which is heated electrically to a temperature between 1500 K and 2200 K, the heated solid material emits infrared radiation. The radiation from the source is split into two beams, half of the beam passes through the sample cell and another half passes through the reference cell. The reference beam then passes through the attenuator and then to the chopper. The chopper consists of a motor-driven disc that reflects the reference beam and transmits the sample beam into the monochromator. The alternating beams fall on the transducer and convert them to an electrical signal. The signal is amplified and passed to the synchronous rectifier. The current from the rectifier is filtered and further amplified [92].

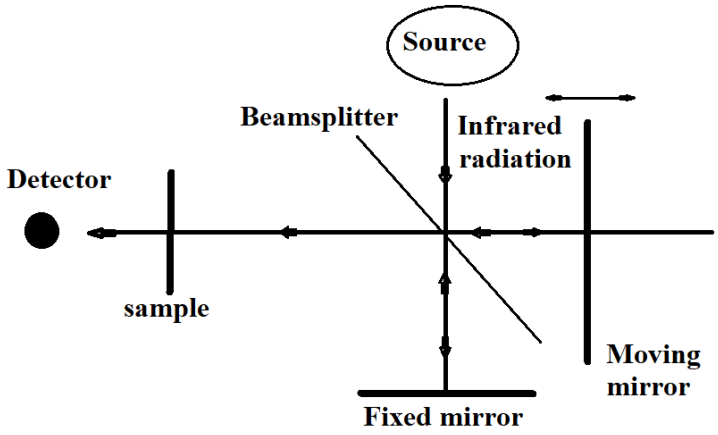

Figure 1.18. Schematic diagram of the arrangement of components in a typical interferometer in FTIR [87]

1.7.6. Transmission electron microscopy (TEM)

Transmission electron microscopy is a highly useful technique to visualize small structures and can reveal details at the atomic scale. It provides much higher magnification and resolution relative to a light microscope. This high resolution is due to the short wavelength of the electrons used in TEM which allows us to see the ultrafine details of the sample. The main difference between TEM and light microscopy is that in TEM, the electrons are used for illumination instead of visible light, and instead of glass lenses, electromagnetic lenses are used. Also, a vacuum environment is required in TEM.

1.7.6.1. Instrumentation

The transmission electron microscope includes a light source, condenser lens, specimen stage, objective lens, and projector lens as shown in Figure 1.19. In TEM, the electron gun generates a high-energy electron beam. The electrons emitted from a cathode are accelerated by high voltage and produce a high-energy beam. All lenses in an electron microscope are electromagnetic. The electron beam passes through the lenses and is focused and deflected by magnetic lenses. TEM has two or more condenser lenses to demagnify the electron beam emitted from the electron gun and control the beam diameter. The TEM possesses three lenses to ensure magnification - objective lens, intermediate lens, and projector lens. The aperture of the microscope is a piece of metal with a small hole at the center which limits the light scattering. The specimen is mounted on a specimen holder (specimen stage), usually mounted on a 3 mm disc of copper [87].

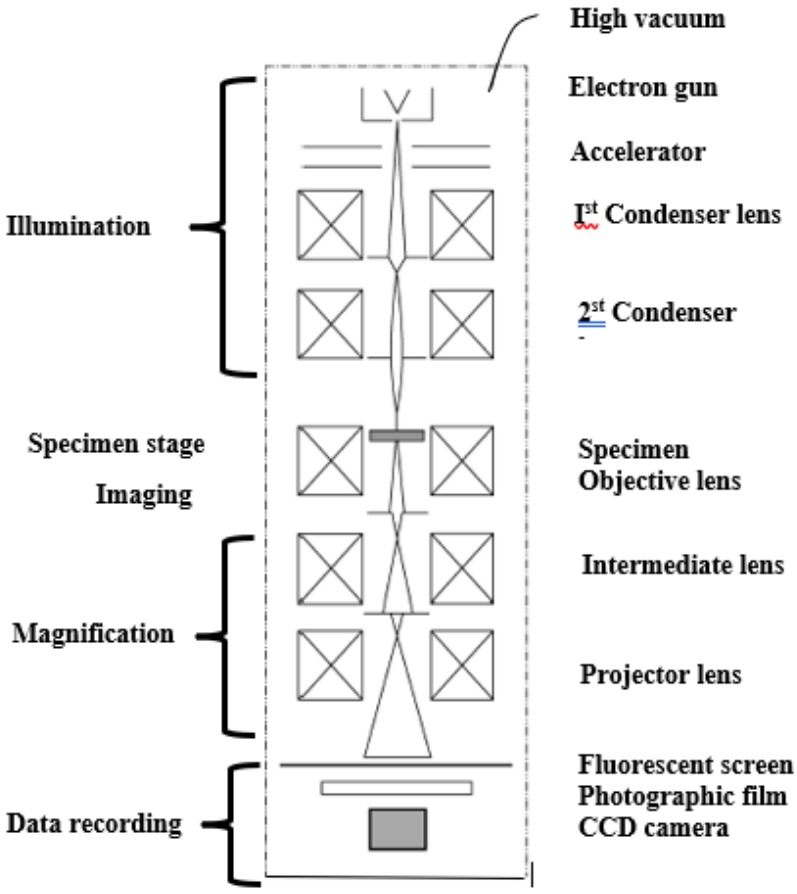

Figure 1.19. Structure of Transmission electron microscope and optical path. Reprinted from the reference [87]

1.8. Electrochemical measurements

1.8.1. Cyclic voltammetry

Cyclic voltammetry is a widely used technique to study the electrode process. The current response of a stationary electrode is plotted as a function of potential in an unstirred solution and the direction of scan is reversed at switching potentials. It provides rapid information about the location of redox potentials of electroactive species. A potential sweep results in the oxidation and reduction of active species, capacitive current due to the double layer charging, and adsorption of species depending on the potential applied. Cyclic voltammetry can be used to study the mechanisms of electrochemical reactions and identification of species present in the solution. The faradaic current depends on the kinetics of electron transfer and the rate at which redox species diffuse to the surface. A typical shape of a cyclic voltammogram is shown in Figure 1.20, which possesses an anodic peak, where oxidation of the analyte occurs, and a corresponding cathodic peak, where reduction occurs. E_{pa} represents the potential at which anodic current density is maximum and E_{pc} is the potential at which cathodic current density is maximum. n is the number of electrons transferred during the redox reaction [92, 93, 94]

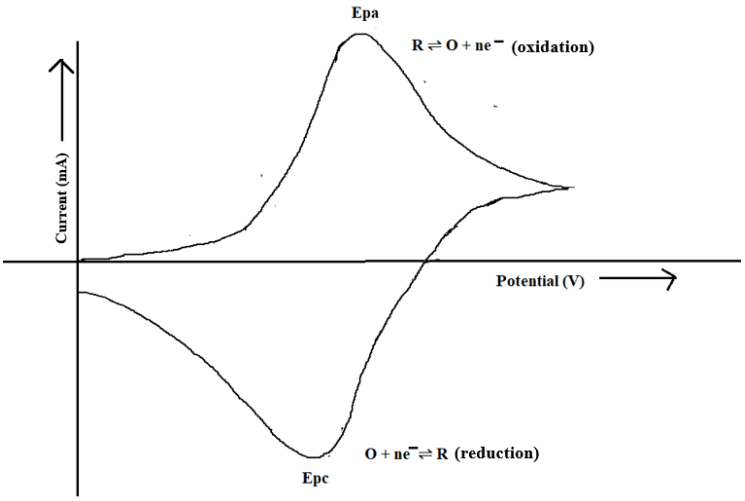

Figure 1.20. Schematic diagram of typical cyclic voltammogram

In an unstirred solution, the reaction occurring at the surface creates a concentration gradient which in turn creates a diffusion flux. According to Fick's first law, the rate of diffusion is directly proportional to the concentration gradient [93].

$$J_{(x,t)} = DdC_{(x,t)}/d_x \qquad (1.12)$$

where J is the flux, rate of mass transport (unit is mol cm^{-2} s^{-1})

D is the diffusion coefficient (cm^{-2} s^{-1})

$dC_{(x,t)}/d_x$ is the concentration gradient at a distance x and time t

The current (i) produced during the electrochemical reaction is directly proportional to the flux and surface area.

$i = -nFAJ$ (1.13)

1.8.1.1. Instrumentation

A three-electrode system is used for performing cyclic voltammetry (see Figure 1.21). A working electrode, reference electrode, and counter electrode. The electrochemical cell consists of an electrolyte with electroactive species. A potentiostat applies a potential between the working electrode and the reference electrode and measures the current between the counter electrode and the working electrode. Reference electrode provides a stable potential. The most commonly used reference electrodes are silver/silver chloride (Ag/AgCl) electrodes and saturated calomel electrodes (SCE) [92, 94]. The experimental set of cyclic voltammetry is given in Figure 1.22.

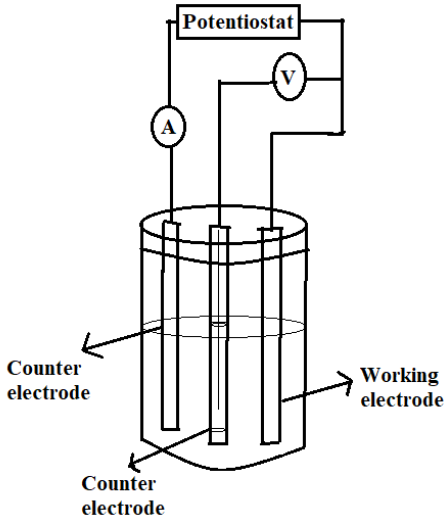

Figure 1.21. Three-electrode system for cyclic voltammetry experiment [94]

Figure 1.22. Cyclic voltammetry experimental setup used for the analysis of samples

1.8.2. Impedance spectroscopy

Oliver Heaviside put forward the concept of impedance and later A.E. Kennelly and C.P. Steinmetz developed this in terms of vector diagrams and complex numbers. Later Randles and Warburg developed an equivalent circuit modeling approach to represent the impedance data. Impedance spectroscopy measures impedance over a range of frequencies and provides the possibility of separating various phenomena associated with the electrode-electrolyte interface. It is highly useful to characterize energy storage units, material testing, corrosion and coatings, and inductive, capacitive, and conductive sensors. When an electric field V(t) is applied current I(t) is obtained [95].

According to Ohm's law, resistance is the ratio of input voltage and output current.

$R = V/I$ (1.14)

This equation is limited to an ideal resistor and the resistance is independent of AC frequency. The ideal resistor can be replaced by an ideal capacitor or inductor. The AC current and voltage signals through an ideal capacitor are completely out of phase, where the current follows the voltage. Impedance is the complex resistance encountered as the current passes through the circuit constituted of resistors, capacitors, and inductors. In Figure 1.23, sinusoidal voltage input V at a single frequency f and current response I in an impedance experiment are shown.

When the ac signal with small perturbation dV is given, the corresponding response perturbation dI occurs. As the perturbation dV is small, the corresponding response dI will be linear.

The voltage signal V(t) is expressed as a function of time.

$V(t) = V_A \sin(\omega t)$ (1.15)

ω is the radial frequency and is expressed in radian/second.

$\omega = 2\pi f$ (1.16)

f is the frequency and is expressed in Hertz.

In a linear or pseudo-linear system, the current response to sinusoidal voltage will be a sinusoid at the same frequency but with a shifted phase (ϕ).

The resulting current $I(t) = I_A \sin(\omega t + \phi)$ (1.17)

The complex impedance of the system analogous to Ohm's law is,

Impedance $(Z) = V\sin(\omega t)/I_A\sin(\omega t + \phi)$ (1.18)

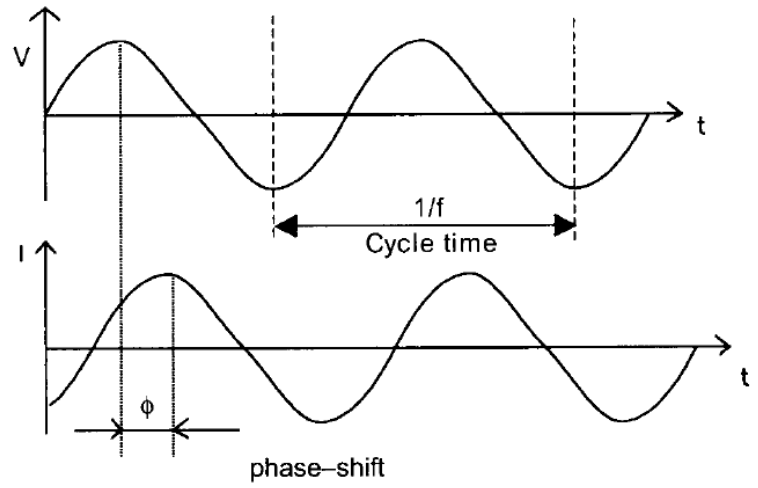

Figure 1.23. Sinusoidal voltage input V at a single frequency f and current response I in an impedance experiment. Reprinted from the reference [95] with permission.

1.8.3. Rotating disc experiments (RDE)

The theory of mass transport at the rotating disc electrode was developed by Benjamin Levich. The steady-state laminar flow conditions near a rotating disc electrode provide information about the electrode kinetics and this technique has been used by many electroanalytical chemists. RDE can be used in the electrodeposition process and characterization of thin films. RDE provides efficient and reproducible mass transport so that analytical

measurements can be done with high sensitivity and precision. The fluid near the adjacent layer develops a radial velocity that moves away from the disc center and is replenished soon due to the rotation of the solution, which means, RDE always gives fresh solution from the bulk. Under these conditions, the thickness of the diffusion layer decreases. The rate at which material arrives on the surface of the electrode increases with increasing electrode angular velocity. The diffusion layer thickness (δ) decreases with increase of angular velocity [93].

$$\delta = 1.61 D^{1/3} \omega^{-1/2} \nu^{1/6} \qquad (1.19)$$

The limiting current (for a reversible system) is thus proportional to the square root of the angular velocity, as described by the Levich equation,

$$i_l = 0.62nFA\, D{o_2}^{1/3} \omega^{1/2} \nu^{1/6} \qquad (1.20)$$

n is the number of electrons transferred during the reaction. F is Faraday constant (96485 C mol^{-1}). A is the electrode surface area in cm^2 (0.196 cm^2). Do_2 is the molecular O_2 diffusion coefficient (1.9 *10^{-5} cm^2 s^{-1} in 0.1 M KOH) and ν is the kinematic viscosity of the solution (0.01 cm^2 s^{-1} at 298 K).

1.8.3.1. Instrumentation

The rotating disc electrode (RDE) is positioned vertically in the shaft of a controllable speed motor, which can be rotated at different angular velocities ($\omega = 2\pi f$), where f is the rotation speed in rpm [3]. It comprises of glassy carbon electrode attached to the shaft of a controllable speed motor. A three-electrode arrangement is used for the electrochemical measurements. The ink is deposited on this glassy carbon disc, which serves as the working electrode. This glassy carbon electrode is immersed in the electrolyte [111]. The rotating disc electrode used for the kinetic measurements of our sample is shown in Figure 1.24.

Figure 1.24. Rotating disc electrode used for the kinetic measurements

1.9. Thesis objectives

Electrocatalysts generally increase the rate and selectivity of electrochemical reactions, reduce the energy demand, and play an important role in the sustainable development of clean energy technologies. A material science approach (Figure 1.25) has been used to identify the materials' characteristics that yield highly efficient electrocatalysts for the OER. The structure of materials is greatly influenced by the method employed in the process of the raw materials, and in turn the materials' structure dictates its electronic, redox and electrocatalytic properties.

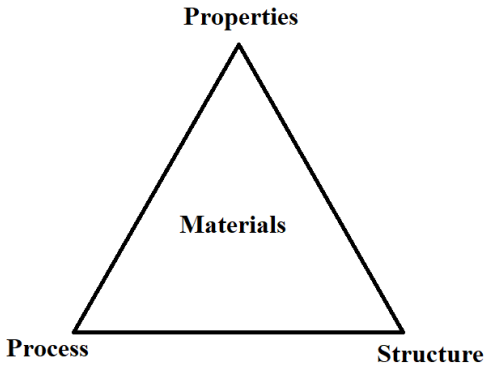

Figure 1.25. Material science approach triangle

As discussed in section 1.5.3., the spinel oxide structure is highly tunable and is a promising class of materials as OER catalysts. Different site occupancies and multiple valences make them good hosts for many different types of metals in their structure, which provide immense possibilities for designing efficient catalysts. Suitable doping of the materials is one of the effective strategies that have a prominent effect on the electronic and chemical properties of these materials. Cobalt-based spinel oxides are potential electrocatalysts for OER due to their excellent electric and catalytic properties, and their controllable composition, structure, and morphology. In our previous work, we synthesized Fe, Ni, and Cu substituted cobalt spinel oxides and identified them as active compositions for OER [48, 49]. This work aims to reprepare these spinel oxides, and study their surface composition, and identify, quantify, and understand the metal cationic species occupied in specific sites using XPS. A systematic overview of surface composition, active site occupation of metal ions, and structural properties would help to understand the underlying reasons for the performance of samples and can guide the development of novel efficient spinel compounds.

Amorphous metal oxides are another class of compounds that recently gained a lot of attention due to their high catalytic activity. A large number of coordinatively unsaturated sites and the highly defective nature of amorphous materials make it a potential candidate for OER. The objective of this work will also include synthesizing the crystalline counterpart of cobalt-based amorphous materials, both binary and ternary metal oxides will be prepared using the thermal decomposition method. Amorphous ternary metal oxides have not been much reported. These materials will be characterized using several analytical techniques such as scanning electron microscopy (SEM), energy dispersive X-ray spectroscopy (EDX), X-ray diffraction

(XRD), X-ray photoelectron spectroscopy (XPS), transmission electron microscopy (TEM) and electrochemical experiments such as cyclic voltammetry (CV) and electrochemical impedance spectroscopy (EIS).

Hence the main goals of this work are a) to understand how binary and ternary cobalt-based spinel oxide's surface structure and composition are related to their electrochemical redox and electrocatalytic properties; b) to investigate if a crystalline structure, such as those of binary and ternary spinel oxides is critical to the electrocatalytic behavior towards the OER; c) to investigate the double-layer capacitance of the crystalline and amorphous samples by cyclic voltammetry and further verify using impedance measurements; d) to investigate the underlying kinetics and mechanism of the catalyzed OER reactions of various spinel oxides and amorphous metal oxides using a rotating disc electrode (RDE); e) to investigate the correlation between various material properties evaluated using different characterization techniques and their catalytic activity for OER.

1.10. Outline of Thesis

The thesis is presented in seven chapters. Chapter 1 is an overview of the potential use of hydrogen gas as a renewable energy source and the production of hydrogen through water electrolysis. The thermodynamics and kinetics of the OER are explained in Chapter 1. Chapter 1 also presents an overview of the OER electrocatalyst design and the state-of-the-art materials studied today for water electrolysis. This chapter also explains the principle and instrumentation of the techniques used to study the characterization of the materials studied in this thesis.

Chapter 2 discusses the spinel oxide's and amorphous transition metal oxide's synthesis procedures employed in this work. It also gives experimental details pertaining to the materials characterization techniques such as sample preparation and analysis conditions.

Chapter 3 presents the materials characterization results, namely scanning electron microscopy (SEM), energy dispersive X-ray spectroscopy (EDX), X-ray diffraction (XRD), and transmission electron microscopy (TEM). This Chapter also compares the material properties of amorphous and crystalline samples. In Chapter 4, the surface characterization of crystalline and amorphous materials using X-ray photoelectron spectroscopy (XPS) is presented and discussed.

Chapter 5 reports the electrochemical properties of amorphous and crystalline samples, including double-layer characterization, OER electrode kinetics, and redox properties. A

comparison of the properties of amorphous and crystalline materials is also discussed in this Chapter. In Chapter 6, the structural, physical, and electrochemical properties of amorphous and crystalline materials will be compared and property correlations will be explored. Chapter 7 states the main conclusions of this research and its achievements.

1.11. References

[1] M. Z. Jacobson, A. K. V. Krauland, S. J. Coughlin, E. Dukas, A. J. H. Nelson, F. C. Palmer, K. R. Rasmussen, Low-cost solutions to global warming, air pollution, and energy insecurity for 145 countries, Energy Environ. Sci., 15 (2022) 3343 - 3359

[2] A. Mujtaba, P. K. Jena, F. V. Bekun, P. K. Sahu, Symmetric and asymmetric impact of economic growth, capital formation, renewable and non-renewable energy consumption on the environment in OECD countries, Renew. Sust. Energ. Rev. 160 (2022) 112300

[3] M. Z. Jacobson, Review of solutions to global warming, air pollution, and energy security, Energy Environ. Sci., 2 (2009) 148–173

[4] K. C. Nadeau, I. Agache, M. Jutel, I. Annesi Maesano, M. Akdis, V. Sampath, G. d'Amato, L. Cecchi, C. Traidl-Hoffmann, C. A. Akdis, Climate change: A call to action for the United Nations. In Allergy: European Journal of Allergy and Clinical Immunology, 77, 4 (2021) 1087–1090

[5] Global Climate Change: Evidence. (2008, June 15). Retrieved January 15, 2023, from http://climate.nasa.gov/evidence/

[6] J. Yu, Y. M. Tang, K. Y. Chau, R. Nazar, S. Ali, W. Iqbal, Role of solar-based renewable energy in mitigating CO_2 emissions: Evidence from quantile-on-quantile estimation. J. Renewable Energy, 182 (2022) 216 – 226

[7] S. A. Grigoriev, V. N. Fateev, D. G. Bessarabov, P. Millet, (2020). Current status, research trends, and challenges in water electrolysis science and technology. Int. J. Hydrogen Energy, 45, 49 (2020), 26036 – 26058.

[8] H. Gao, S. Liu, Y. Li, E. Conte, Y. Cao, A critical review of spinel structured iron-cobalt oxides based materials for electrochemical energy storage and conversion. J. Energies 10, 11 (2017) 1787

[9] Hydrogen strategy for Canada : seizing the opportunities for hydrogen : a call to action [2020], Natural Resources Canada. (n.d.).

[10] Green Hydrogen Market Size, Share & Trends Analysis Report By Technology (PEM Electrolyzer, Alkaline Electrolyzer), By Application (Power Generation, Transportation), By Distribution Channel, By Region, And Segment Forecasts, 2022 – 2030, Retrieved January 15, 2023, https://www.grandviewresearch.com/industry-analysis/green-hydrogen-market

[11] F. Safizadeh, E. Ghali, G. Houlachi, Electrocatalysis developments for hydrogen evolution reaction in alkaline solutions - A Review. Int. J. Hydrogen Energy, 40, 1 (2015) 256 - 274
[[12] A. G. Olabi, M. A. Abdelkareem, Renewable energy and climate change. Renewable Sustainable Energy Rev., 158 (2022) 112111
[13] M. Wang, Z. Wang, X. Gong, Z. Guo, The intensification technologies to water electrolysis for hydrogen production - A review. In Renewable Sustainable Energy Rev. 29 (2014) 573 - 588
[14] M. Plevova, M., J. Hnat, K. Bouzek, Electrocatalysts for the oxygen evolution reaction in alkaline and neutral media. A comparative review. J. Power Sources, 507 (2021) 230072
[15] M. Rashid, M. K. Al Mesfer, H. Naseem, M. Danish, Hydrogen Production by Water Electrolysis: A Review of Alkaline Water Electrolysis, PEM Water Electrolysis and High Temperature Water Electrolysis, In International Journal of Engineering and Advanced Technology 3 (2015) 80 - 93
[16] M. Gong, H. Dai. A mini review of NiFe-based materials as highly active oxygen evolution reaction electrocatalysts. Nano Research 8, 1,(2015) 23 - 39
[17] K. Zeng, K, D. Zhang, Recent progress in alkaline water electrolysis for hydrogen production and applications. Progress in Energy and Combustion Science 36, 3, (2010) 307 - 326
[18] H. Ding, H. Liu, W. Chu, C. Wu, Y. Xie, Structural Transformation of Heterogeneous Materials for Electrocatalytic Oxygen Evolution Reaction. In Chem. Rev, 121, 21 (2021)13174 - 13212
[19] L. Trotochaud, S. W. Boettcher, Precise oxygen evolution catalysts: Status and opportunities. Scr. Mater.,74 (2014), 25–32
[20] Y. Matsumoto, E. Sato, Electrocatalytic properties of transition metal oxides for oxygen evolution Reaction, J. Mat. Chem. Phy., 14(1986) 397 - 426
[21] F. Song, L. Bai, A. Moysiadou, S. Lee, C. Hu, L. Liardet, X. Hu, Transition metal oxides as electrocatalysts for the oxygen evolution reaction in alkaline solutions: an application-inspired renaissance, J. Am. Chem. Soc., 140 (2018) 7748 - 7759
[22] S. Trasatti, O. A. Petrii, Real surface area measurements in electrochemistry, J. Electroanal. Chem. 327 (1992) 353 - 376
[23] D. M. F. Santos, C. A. C. Sequeira, J. L. Figueiredo, Hydrogen production by alkaline water electrolysis. Quim. Nova, 36, 8 (2013) 1176 - 1193

24] A. J. Bard, L. R. Faulkner, Eletcrochemical methods-Fundamentals and applications, 2nd ed.; New York,2001

[25] C. C. L. McCrory, S. Jung, J. C. Peters, T. F. Jaramillo, Benchmarking heterogeneous electrocatalysts for the oxygen evolution reaction. J. Am. Chem. Soc. 135, 45 (2013) 16977 - 16987.

[26] N. T. Suen, S. F. Hung, Q. Quan, N. Zhang, Y. J. Xu, H. M. Chen, Electrocatalysis for the oxygen evolution reaction: Recent development and future perspectives. In Chem. Soc. Rev. 46, 2 (2017) 337–365

[27] E. Fabbri, A. Habereder, K. Waltar, R. Kotz, T. J. Schmidt, Developments and perspectives of oxide-based catalysts for the oxygen evolution reaction. Catal. Sci. Technol. 4, 11 (2014) 3800 - 3821

[28] , M. A. Khan, H. Zhao, W. Zou, Z. Chen, W. Cao, J. Fang, J. Xu, L. Zhang, J. Zhang,. Recent Progresses in Electrocatalysts for Water Electrolysis, Electrochemical Energy Reviews 1, 4 (2018) 483 - 530

[29] S. Trasatti S. Electrocatalysis in the anodic evolution of oxygen and chlorine, J. Electrochim. Acta 29, 11 (1984) 1503 - 1512

[30] S. Cherevko, S. Geiger, O. Kasian, N. Kulyk, J. P. Grote, A. Savan, B. R. Shrestha, S. Merzlikin, B. Breitbach, A. Ludwig, K. J. J. Mayrhofer, Oxygen and hydrogen evolution reactions on Ru, RuO_2, Ir, and IrO_2 thin film electrodes in acidic and alkaline electrolytes: A comparative study on activity and stability. Catalysis Today, 262 (2016) 170 - 180.

[31] I. C. man, H. Y. Su, F. C. Vallejo, H. A. Hansen, J. I. Martinez, N. G. Inoglu, J. Kitchin, T. F. Jaramillo, J. K. Nørskov, J. Rossmeisl, Universality in Oxygen Evolution Electrocatalysis on Oxide Surfaces, ChemCatChem 3 (2011) 1159 - 1165

[32] T. Audichon, T. W Napporn, C. Canaff, C. Morais, C. Comminges, K. B. Kokoh, IrO_2 coated on RuO_2 as efficient and stable electroactive nanocatalysts for electrochemical water splitting. J. Phys. Chem. C, 120, 5 (2016) 2562 - 2573.

[33] C.Wang, L. Jin, H. Shang, H. Xu, Y. Shiraishi, Y. Du, Advances in engineering RuO_2 electrocatalysts towards oxygen evolution reaction. Chinese Chemical Letters, 32, 7 (2021) 2108 - 2116.

[34] R. Kotz, S. Stuck), Stabilization of RuO_2 and IrO_2 for anodic oxygen evolution in acid media, J. Electrochim. Acta, 31, 10 (1986) 1311 – 1316

[35] K. A. Stoerzinger, L. Qiao, M. D. Biegalski, Y. Shao-Horn, Y. Orientation-dependent oxygen evolution activities of rutile IrO_2 and RuO_2. J. Phys. Chem. Lett., 5, 10 (2014)1636 - 1641.
[36] W. Zhang, L. Cui, J. Liu, Recent advances in cobalt-based electrocatalysts for hydrogen and oxygen evolution reactions, J. Alloys Compd. 821 (2020) 153542
[37] C. G. Morales-Guio, L. Liardet, X. Hu, (2016). Oxidatively electrodeposited thin-film transition metal (oxy)hydroxides as oxygen evolution catalysts. J. Am. Chem. Soc. 138 (28), (2016) 8946 - 8957.
[38] S. Anwar, F. Khan, Y. Zhang, A. Djire, Recent development in electrocatalysts for hydrogen production through water electrolysis. Int. J. Hydrogen Energy, 46, 63 (2021) 32284 - 32317.
[39] R. Ramachandran, T. W. Chen, P. Veerakumar, G. Anushya, S. M. Chen, R. Kannan, V. Mariyappan, S. Chitra, N. Ponmurugaraj, M. Boominathan, M. Recent development and challenges in fuel cells and water electrolyzer reactions: an overview. In RSC Advances 12, 43, (2022) 28227 - 28244.
[40] J. Song, C. Wei, Z. F. Huang, C. Liu, L. Zeng, X. Wang, Z. J. Xu,. A review on fundamentals for designing oxygen evolution electrocatalysts. In Chem. Soc. Rev. 49, 7 (2020) 2196 - 2214
[41] A. Buttler, H. Spliethoff, Current status of water electrolysis for energy storage, grid balancing and sector coupling via power-to-gas and power-to-liquids: A review. J. Renew. Sust. Energ. Rev., 82 (2018) 2440 - 2454
[42] M. D. Koninck, S. C. Poirier, B. Marsan, $Cu_xCo_{3-x}O_4$ used as bifunctional catalyst: Physiochemical properties and electrochemical characterization for oxygen evolution reaction, J. Electrochem. Soc., 153 (2006) 1, A2103 - A2110
[43] C. Wolverton, K. C. Hass, Phase stability and structure of spinel-based transition aluminas, Physical Review B, 63, 2 (2001) 24102
[44] H. L. Andersen, M. Saura-Múzquiz, C. Granados-Miralles, E. Canevet, N. Lock, M. Christensen, Crystalline and magnetic structure-property relationship in spinel ferrite nanoparticles. Nanoscale, 10, 31 (2018) 14902 - 14914.

[45] L. Zhang, Q. Fan, K. Li, S. Zhang, X. Ma, First-row transition metal oxide oxygen evolution electrocatalysts: regulation strategies and mechanistic understandings. Sustain. Energy Fuels 4, 11 (2020) 5417 - 5432

[46] S. Trasatti, G. Lodi. Electrodes of Conductive Metallic Oxides, Part A-B; Elsevier Science Publishers: Amsterdam, The Netherlands, 1980/1981.

[47] B. M. Hunter, H. B. Gray, A. M. Muller, Earth-abundant heterogeneous water oxidation catalysts. Chem. Rev. 116, 22 (2016) 14120 - 14136

[48] S. Thekkoot, R. Islam, S. Morin. "Improved oxygen evolution reaction performance with addition of Fe to form $Fe_yCu_{x-y}Co_{3-x}O_4$ and $Fe_yNi_{x-y}Co_{3-x}O_4$ (x= 0.5, 1 and y= 0.1, 0.15) spinel oxides." Electrochimica Acta 378 (2021) 138116.

[49] S. Thekkoot, R. Islam, O. Gray, S. Morin. "Efficiency of nanostructured $Cu_xCo_{3-x}O_4$ and $Ni_xCu_{1-x}Co_2O_4$ electrodes as electrocatalysts for the oxygen evolution reaction–revisited." Electrochimica Acta 471 (2023) 143339.

[50] F. Zerarga, A. Bouhemadou, R. Khenata, S. Bin-Omran,. Structural, electronic and optical properties of spinel oxides $ZnAl_2O_4$, $ZnGa_2O_4$ and $ZnIn_2O_4$. Solid State Sciences, 13, 8 (2011), 1638 - 1648.

[51] J. Wang, W. Cui, Q. Liu, Z. Xing, A. M. Asiri, X. Sun,. Recent Progress in Cobalt-Based Heterogeneous Catalysts for Electrochemical Water Splitting. Adv. Mater. 28, 2 (2016), 215 - 230.

[52] Y. Li, Q. Li, H. Wang, L. Zhang, D. P. Wilkinson, J. Zhang, Recent progresses in oxygen reduction reaction electrocatalysts for electrochemical energy applications, Electrochemical Energy Reviews 2 (2019) 518 - 538

[53] A. J. Esswein, Mcmurdo, P. N.Ross, A. T. Bell, T. D. Tilley, Size-dependent activity of Co_3O_4 nanoparticle anodes for alkaline water electrolysis, J. Phys. Chem. C, 113, 33 (2009), 15068 - 15072.

[54] H. Osgood, S. V. Devaguptapu, H. Xu, J. Cho, G. Wu, Transition metal (Fe, Co, Ni, and Mn) oxides for oxygen reduction and evolution bifunctional catalysts in alkaline media, Nano Today 11, 5 (2016) 601 - 625.

[55] J. Jacob, M. A. Khadar, (2010). Investigation of mixed spinel structure of nanostructured nickel ferrite, J. Appl. Phys., 107, (2010) 114310

[56] Y. J. Wang, H. Fan, A. Ignaszak, , L. Zhang, S. Shao, D. P. Wilkinson, J. Zhang, Compositing doped-carbon with metals, non-metals, metal oxides, metal nitrides and other materials to form bifunctional electrocatalysts to enhance metal-air battery oxygen reduction and evolution reactions, J. Chemical Engineering 348, (2018) 416 - 437.
[57] Z. Q. Liu, H. Cheng, N. Li, T. Y. Ma, Y. Z. Su, $ZnCo_2O_4$ Quantum dots anchored on nitrogen-doped carbon nanotubes as reversible oxygen reduction/evolution electrocatalysts. J. Adv. Mater. 19 (2016) 3777 - 3784
[58] X. He, F. Yin, G. Li, (2015). A Co/metal-organic-framework bifunctional electrocatalyst: The effect of the surface cobalt oxidation state on oxygen evolution/reduction reactions in an alkaline electrolyte. Int. J. Hydrogen Energy, 40, 31 (2015), 9713 - 9722.
[59] B. Chi, H. Lin, J. Li, (2008). Cations distribution of $Cu_xCo_{3-x}O_4$ and its electrocatalytic activities for oxygen evolution reaction. Int. J. Hydrogen Energy, 33,18 (2008) 4763 - 4768.
[60] Y. Zhang, X. Zhou, F. Zhang, T. Tian, Y. Ding, H. Gao, Design and synthesis of Cu modified cobalt oxides with hollow polyhedral nanocages as efficient electrocatalytic and photocatalytic water oxidation catalyst, J. Catal., 352 (2017) 246 - 255
[61] H.Y. Wang, S.F. Hung, H. Y. Chen, T.S. Chan, H. M. Chen, B. Liu, In operando identification of geometrical-site-dependent water oxidation activity of spinel Co_3O_4, J. Am. Chem. Soc., 138 (2016) 36 - 39
[62] W. Song, Z. Ren, S. Y. Chen, Y. Meng, S. Biswas, P. Nandi, H. A. Elsen, P. X. Gao, S. L. Suib, Ni and Mn promoted mesoporous Co_3O_4: A stable bifunctional catalyst with surface-structure-dependent activity for oxygen reduction reaction and oxygen evolution reaction, ACS Appl. Mater. Interfaces, 8 (2016) 20802 - 20813
[63] T. Wiegmann, I. Pacheco, F. Reikowski, J. Stettner, C. Qiu, M. Bouvier, M. Bertram, F. Faisal, O. Brummel, J. Libuda, J. Drnec, P. Allongue, F. Maroun, O. M. Magnussen, Operando Identification of the Reversible Skin Layer on Co_3O_4 as a Three-dimensional reaction zone for oxygen evolution, ACS Catal, 12 (2022) 3256 - 3268
[64] F. Reikowski, F. Maroun, I. Pacheco, T. Wiegmann, P. Allongue, J. Stettner, O. M. Magnussen, Operando surface X-ray diffraction studies of structurally defined Co_3O_4 and CoOOH thin films during oxygen evolution, ACS Catal., 9, (2019) 3811 - 3821
[65] J. S. Kim, B. Kim, H. Kim, K. Kang, (2018). Recent progress on multimetal oxide catalysts for the oxygen evolution reaction, Adv. Energy Mater.,8, 11 (2018) 1702774

[66] M. Li, Y. Xiong, X. Liu, X. Bo, Y. Zhang, C. Han, L. Guo, (2015). Facile synthesis of electrospun MFe_2O_4 (M = Co, Ni, Cu, Mn) spinel nanofibers with excellent electrocatalytic properties for oxygen evolution and hydrogen peroxide reduction, Nanoscale, 7, 19 (2015) 8920 - 8930
[67] Y. S. Lee, C. C. Hu, T. C. Wen, Oxygen evolution on Co-Cu-Zn ternary spinel oxide-coated electrodes in alkaline solution: Integration of statistical, electrochemical, and textural approaches, J. Electrochem. Soc. 143, 4, (1996) 1218
[68] Y. T. Lu, Y. J. Chien, C. F. Liu, T. H. You and C. C. Hu, Active site-engineered bifunctional electrocatalysts of ternary spinel oxides, $M_{0.1}Ni_{0.9}Co_2O_4$ (M: Mn, Fe, Cu, Zn) for the Air Electrode of Rechargeable Zinc-Air Batteries, J. Mater. Chem. A, 5 (2017) 21016
[69] K. L Yan, X. Shang, Z. Li, B. Dong, X. Li, W. K. Gao, J. Q. Chi, Y. M. Chai, C. G. Liu, Ternary mixed metal Fe-doped $NiCo_2O_4$ nanowires as efficient electrocatalysts for oxygen evolution reaction, J. Appl. Surf. Sci. 416 (2017) 371 - 378
[70] L. Zhuang, L. Ge, Y. Yang, M. Li, Y. Jia, X. Yao, Z. Zhu, (2017). Ultrathin iron-cobalt oxide nanosheets with abundant oxygen vacancies for the oxygen evolution reaction. Adv. Mater., 29, 17 (2017) 1606793
[71] X. Zou, A. Goswami, T. Asefa, Efficient noble metal-free (electro)catalysis of water and alcohol oxidations by zinc-cobalt layered double hydroxide. J. Am. Chem. Soc., 135, 46 (2013), 17242 - 17245
[72] F. Dionigi, Z. Zeng, I. Sinev, T. Merzdorf, S. Deshpande, M. B. Lopez, S. Kunze, I. Zegkinoglou, H. Sarodnik, D. Fan, A. Bergmann, J. Drnec, J. F. Araujo, M. Gliech, D. Teschner, J. Zhu, W. X. Li, J. Greeley, B. R. Cuenya, P. Strasser, 2020). In-situ structure and catalytic mechanism of NiFe and CoFe layered double hydroxides during oxygen evolution. Nat. Commun. 11, 1 (2020) 2522.
[73] Deeksha, P. Kour, I. Ahmed, Sunny, S. K. Sharma, K. Yadav, Y. K. Mishra, Transition metal-based perovskite oxides: emerging electrocatalysts for oxygen evolution reaction. ChemCatChem., 15, 6 (2023) 1-32
[74] D. Liu, P. Zhou, H. Bai, H. Ai, X. Du, M. Chen, D. Liu, W. F. Ip, K. H. Lo, C. T. Kwok, S. Chen, S. Wang, G. Xing, X. Wang, H. Pan, (2021). Development of Perovskite Oxide-Based Electrocatalysts for Oxygen Evolution Reaction. In Small, 17, 43 (2021) 2101605

[75] Z. Shen, Y. Zhuang, W. Li, X. Huang, F. E. Oropeza, E. J. M. Hensen, J. P. Hofmann, M. Cui, A. Tadich, D. Qi, J. Cheng, J. Li, K. H. L. Zhang, Increased activity in the oxygen evolution reaction by Fe^{4+} induced hole states in perovskite $La_{1-x}Sr_xFeO_3$. J. Mater. Chem. A, 8, 8, (2020) 4407 - 4415

[76] B. J. Kim, E. Fabbri, D. F. Abbott, X. Cheng, A. H. Clark, M. Nachtegaal, M. Borlaf, I. E. Castelli, T. Graule, T. J. Schmidt, Functional role of Fe-doping in Co-based perovskite oxide catalysts for oxygen evolution reaction. J. Am.Chem. Soc., 141, 13 (2019) 5231 - 5240

[77] J. Suntivich, K. J.May, H. A. Gasteiger, J. B. Goodenough, Y. Shao-Horn, A Perovskite oxide optimized for oxygen evolution catalysis from molecular orbital principles, Science 334 (2011) 1383 - 1385

[78] W. D. Chemelewski, H. C. Lee, J. F. Lin, A. J. Bard, C. B. Mullins, Amorphous FeOOH oxygen evolution reaction catalyst for photoelectrochemical water splitting. J. Am. Chem. Soc., 136, 7 (2014) 2843–2850.

[79] A. Indra, P. W. Menezes, N. R. Sahraie, A. Bergmann, C. Das, M. Tallarida, D. Schmeiber, P. Strasser, M. Driess, (2014). Unification of catalytic water oxidation and oxygen reduction reactions: Amorphous beat crystalline cobalt iron oxides. J. Am. Chem. Soc. 136, 50 (2014), 17530 - 17536

[80] C. Zhang, C. P. Berlinguette, S. Trudel, (2016). Water oxidation catalysis: An amorphous quaternary Ba-Sr-Co-Fe oxide as a promising electrocatalyst for the oxygen-evolution reaction. Chem. Commun., 52, 7 (2016) 1513 -1516

[81] R. D. L. Smith, M. S. Prevot, R. D. Fagan, Z. Zhang, P. A. Sedach, M. K. J. Siu, S. Trudel,C. P. Berlinguette, Photochemical Route for Accessing Amorphous Metal Oxide Materials for Water Oxidation Catalysis, Science 340 (2013) 60 - 63

[82] A. Irshad, N. Munichandraiah, (2015). High catalytic activity of amorphous Ir-Pi for oxygen evolution reaction. ACS Appl. Mater. Interfaces, 7, 29 (2015) 15765 - 15776

[83] Y. Zhang, T. Gao, Z. Jin, X. Chen, D. Xiao, (2016). A robust water oxidation electrocatalyst from amorphous cobalt-iron bimetallic phytate nanostructures. J. Mater. Chem. A, 4(41), 15888 - 15895

[84] L. Liardet, X. Hu, Amorphous cobalt vanadium oxide as a highly active electrocatalyst for oxygen evolution. ACS Catalysis, 8, 1 (2018), 644 - 650

[85] L. Trotochaud, J. K. Ranney, K. N. Williams, S. W. Boettcher, (2012). Solution-cast metal oxide thin film electrocatalysts for oxygen evolution. J. Am. Chem. Soc., 134, 41(2012) 17253 - 17261
[86] D. Xu, M. B. Stevens, Y. Rui, G. DeLuca, S. W. Boettcher, E. Reichmanis, Y. Li, Q. Zhang, H. Wang, (2018). The role of Cr doping in Ni–Fe oxide/(oxy)hydroxide electrocatalysts for oxygen evolution. Electrochim. Acta, 265 (2018), 10–18.
[87] Y. Leng, Materials characterization: Introduction to microscopic and spectroscopic methods; John Wiley & Sons: Asia, 2008
[88] J. I. Goldstein, D. E. Newbury, D. C. Joy, C. E. Lyman, P. Echlin, E. Lifshin, L. Sawyer, J. R. Michael, Scanning electron microscopy and X-ray microanalysis, 3rd ed.; Kluwer Academic/Plenum Publishers: New York, 2003.
[89] B. D. Cullity, S. R. Stock, Elements of X-ray diffraction, 3rd ed; Prentice hall: Upper Saddle River, 2001
[90] L. Smart, E. Moore, Solid State Chemistry – An Introduction, 2nd ed; CRC press, Boca Raton, 2012
[91] G. C. Smith, Surface analysis by electron spectroscopy, Plenum Press NewYork and London, 1994
[92] D. A. Skoog, F. J. Holler, T. A. Nieman, Principles of instrumental analysis 5th edition, Harcourt Brace college Publishers
[93] J. Wang, Analytical Chemistry, 3rd edition, John and Wiley Sons INC. , Publication, 2006.
[94] N. Elgrishi, K. J. Rountree, B. D. McCarthy, E. S. Rountree, T. T. Eisenhart, J. L. Dempsey, A Practical Beginner's Guide to Cyclic Voltammetry. Journal of Chemical Education, 95, 2 (2018), 197.
[95] V. F. Lvovich, Impedance Spectroscopy: Applications to Electrochemical and Dielectric Phenomena, 2012, John Wiley and Sons, Hoboken New Jersy

Chapter 2. Synthesis of Materials and characterization

2.1. Introduction

Preparation methods greatly influence the physicochemical and electrochemical properties of the electrocatalysts. Different methods such as thermal decomposition [1,2, 3], coprecipitation [4, 5], sol-gel [6, 7], spray pyrolysis[8, 9], and electrodeposition methods [10] have been widely used to synthesize cobalt spinel oxides. Among these methods, the thermal decomposition method is known for synthesizing highly stable materials with higher incorporation of other metal cations in the cobalt spinel oxide [1, 2, 11, 12].

In this work $Cu_xCo_{3-x}O_4$ ($0 \leq x \geq 1$), $Ni_xCu_{1-x}Co_2O_4$ ($0 \leq x \leq 0.75$) $Fe_yNi_{x-y}Co_{3-x}O_4$ ($x = 0.5, 1$), ($y = 0.1, 0.15$) were reprepared to perform kinetic measurements and X-ray photoelectron spectroscopy (XPS) analysis. In our previous work, we evaluated the surface area of the electrodes using cyclic voltammetry, which allowed us to normalize the current density obtained from each sample by the real surface area of the electrode. This allows us to compare the catalytic activity of different samples without the difference in their surface area influencing the data. Different methods have been proposed to measure the surface area of the electrodes and have been shown to be valid to normalize the experimental data, including cyclic voltammetry [13]. Measuring surface area using an electrochemical method is also known as electrochemically active surface area (ESCA). Some people still question the physical meaning of the surface area values obtained using these methods. Hence in this work the double-layer capacitance of $Cu_xCo_{3-x}O_4$ ($0 \leq x \geq 1$) and $Ni_xCu_{1-x}Co_2O_4$ ($0 \leq x \leq 0.75$) were also verified using differential capacitance and electrochemical impedance spectroscopy (EIS) measurements. The double-layer capacitance is a quantitative measurement of the surface area of the sample as the surface area is accessible to electrolyte ions. This requires choosing a potential window where there is no faradaic charge transfer occurring [13]. We have also synthesized and characterized amorphous cobalt oxide samples (CoO_x, $CuCo_2O_x$, $Ni_{0.5}Cu_{0.5}Co_2O_x$, $Fe_{0.1}Cu_{0.9}Co_2O_x$, and $Fe_{0.1}Ni_{0.9}Co_2O_x$) and studied their electrocatalytic properties for OER. For amorphous materials, the number of oxygen atoms in the stoichiometric formula is denoted by x.

2.2. Experimental

2.2.1. Synthesis of cobalt-based spinel oxides

2.2.1.1. Reagents and materials - All chemicals purchased were of analytical grade and were used without any further purification. Cobalt nitrate hexahydrate ($Co(NO_3)_2.6H_2O$), copper nitrate trihydrate ($Cu(NO_3)_2.3H_2O$), nickel nitrate hexahydrate ($Ni(NO_3)_2.6H_2O$), iron nitrate nonahydrate ($Fe(NO_3)_3.9H_2O$), isopropanol, KOH and Triton X-100 were purchased from Sigma Aldrich. The reagent water (Millipore water) used in this work was from Millipore, Milli-Q Synthesis A10 filtered through a 0.22 μm pore size Millipore system.

2.2.1.2. Synthesis of $Cu_xCo_{3-x}O_4$ ($0 \leq x \geq 1$), $Ni_xCu_{1-x}Co_2O_4$ ($0 \leq x \leq 0.75$) $Fe_yNi_{x-y}Co_{3-x}O_4$ (x = 0.5, 1 and y = 0.1, 0.15)

The individual salt precursor solutions were prepared by dissolving $Co(NO_3)_2.6H_2O$ (A.C.S Sigma Aldrich, ≥ 98%), $Cu(NO_3)_2.3H_2O$ (Sigma Aldrich, 99.0% - 100.5%) and $Ni(NO_3)_2{\cdot}6H_2O$ (Sigma Aldrich, ≥ 98.5%) and $Fe(NO_3)_3.9H_2O$ [A.C.S Sigma Aldrich ≥ 98%] in a (3:1) ratio solvent mixture of isopropanol and ultrapure water (Millipore, Milli-Q Synthesis A10). These nitrate salt solutions were mixed in an appropriate molar ratio to produce $Cu_xCo_{3-x}O_4$ with x = 0, 0.25, 0.5, 0.75, 1 and $Ni_xCu_{1-x}Co_2O_4$ with x = 0.25, 0.5, 0.75, 0.9, 1 and $Fe_yNi_{x-y}Co_{3-x}O_4$, x = 0.5, 1 and y = 0.1, 0.15 to prepare a 0.3 M solution. 10 μL of Triton X-100 was added to 5 mL 0.3 M solution to decrease the surface tension of the liquid film when the samples were prepared. Typically, 15 μL of the nitrate salt solution was deposited on a ca. 1.5 cm x 1.5 cm piece of clean fluorine-doped tin oxide coated transparent conductive glass (FTO glass). The solvent was evaporated by heating the samples at 60ºC, followed by the films were heated at 300ºC for ten minutes (Lindberg BF51732BC) ($Fe_y(Cu/Ni)_{x-y}Co_{3-x}O_4$ was heated at 400 ºC for 10 minutes). Multiple oxide layers (typically five layers) were deposited by repeating this procedure, and a final annealing step was carried out at 300ºC for one hour ($Fe_y(Cu/Ni)_{x-y}Co_{3-x}O_4$ was annealed at 400 ºC for 2 hours) [1, 3]. The amount of material deposited was obtained by comparing the mass change of the sample before deposition and after annealing.

2.2.2. Synthesis of amorphous cobalt-based metal oxides

2.2.2.1.Reagents and materials - All chemicals were analytical reagent grade and used without additional purification. Cobalt (II) 2-ethylhexanoate, nickel (II) 2-ethylhexanoate, iron (III) 2-ethylhexanoate, and copper (II) 2-ethylhexanoate were used to prepare the salt precursors.

Hexane was used as the solvent. Copper (II) 2-ethylhexanoate was dissolved in ethanol as the solubility of this salt was lower in hexane.

2.2.2.2. Preparation of CoO_x, $CuCo_2O_x$, $Ni_{0.5}Cu_{0.5}Co_2O_x$, $Fe_{0.1}Cu_{0.9}Co_2O_x$ and $Fe_{0.1}Ni_{0.9}Co_2O_x$

Salt precursors were prepared by dissolving cobalt (II) 2-ethylhexanoate (65 wt. % in mineral spirits, Sigma Aldrich), nickel (II) 2-ethylhexanoate (78% w/w in ethylhexanoic acid, Sigma Aldrich), and iron (III) 2-ethylhexanoate (50% in mineral spirit – Alfa Aesar) in hexane to obtain a stock solution concentration of 0.5M for each. Copper (II) 2-ethylhexanoate (Sigma Aldrich) was dissolved in ethanol. These solutions were mixed in an appropriate molar ratio to obtain the desired concentration of 0.5 M and were deposited onto a (2 cm x 1.5 cm) piece of previously sonicated fluorine-doped tin oxide transparent conductive glass (FTO glass, Pilkington) using a micropipette and placed under the 150 W near Infrared light heat lamp for 30 minutes. 3 layers were deposited on FTO glass using a similar procedure [12, 14]. The oxide loading ranged between 0.95 mg to 1.18 mg.

2.2.3. Characterization of samples

The surface morphology and composition of the prepared films were examined by scanning electron microscope (SEM), SEM FEI, QUANTA 3D PEG, and energy dispersive X-ray spectroscope (EDX), EDAX GENESIS, respectively, located in the Imaging Facility at York University, Toronto. The *Everhart-Thornley Detector* was used to detect the secondary electrons deflected from the sample. The Octane Elect Plus Detector was used to detect the backscattered electrons and a high energy of 20kV was applied for the analysis. For SEM and EDX analysis, the samples were deposited (3 layers) on FTO glass (ca. 1.5 cm x 1.5 cm).

X-ray diffraction patterns of $Cu_xCo_{3-x}O_4$ electrodes were acquired at the PXRD facility, University of Toronto. They were recorded with an X-ray diffractometer (Bruker AXS D2 phaser) using Cu Kα radiation of 0.15418 nm. Ni filter has been used to eliminate Cu Kβ radiation. High-resolution Solid State Lynxeye XE has been used as a detector and the Rietveld method was utilized for data refinement. Infrared spectra were obtained using the FTIR instrument (Thermo Nicolet 6700 FTIR)) located at York University.

The crystal structure of amorphous samples was characterized by X-ray diffraction technique (Bruker D8 DISCOVER DAVINCI DESIGN diffractometer) using Co Kα radiation of ((λ = 1.79026 Å). A high-resolution Vantec 500 – MikroGap TM technology has been used

as a detector. The data was collected with DIFFRAC.Measurement centre Version 3.0 software and the unit cell refinements were carried out using Topas Version 4.0 software, located in the X-ray diffraction facility at McMaster University. The samples for XRD analysis were deposited on FTO conductive glass (ca. 1.5 cm x 1.5 cm).

The XPS analysis was performed with a PHI Quantera SXM located at McMaster-Biointerfaces (McMaster University, Hamilton, Ontario) using a monochromatic Al Kα X-ray source (1486.6 eV). Crystalline and amorphous samples were deposited on FTO glass (ca. 1 cm x 1 cm). The instrument base pressure was 1×10^{-9} Torr. High-resolution spectra were obtained using an analysis area of approximately 8×10^{3} μm^2 and a pass energy of 26 eV with a step size of 0.1 eV.

The X-ray photoelectron spectroscopy (XPS) analysis of Fe containing spinel oxides was performed with a Kratos Axis supra Spectrometer (Surface Science Western, London) using a monochromatic Ag L(alpha) X-ray monochromatic source (2984.2 eV). The instrument work function was calibrated to give an Au $4f_{7/2}$ metallic gold binding energy (BE) of 83.95 eV. Instrument base pressure was 8×10^{-10} Torr. High-resolution spectra were obtained from an analysis area of approximately 300 × 700 μm and a pass energy of 20 eV, with a step size of 0.1 eV and 60-second sweep intervals.

Spectra from samples have been charge corrected using adventitious C 1s of binding energy 284.8 eV. A Shirley background was applied to the entire 2p peak and a mixed Gaussian/Lorentzian (70:30) was used to fit the peaks of the data for all the samples**.** The peak energies were given to an accuracy of ± 0.2 eV. Peak areas were normalized by using appropriate atomic sensitivity factors.

2.2.4. Electrochemical measurements

Cyclic voltammetry studies were carried out at room temperature in 1M KOH solution, using VoltaLab 80 (PGZ402 potentiostat and Voltamaster 4 software). A standard three-electrode setup was used with the sample as the working electrode, saturated calomel electrode (SCE) as a reference electrode, and platinum wire as the counter electrode. The sample is placed at the bottom of the Teflon cell, which is machined with a 0.98 ± 0.01cm^2 opening to ensure a constant surface area is exposed to the electrolyte. For cyclic voltammetry measurements, the samples were deposited on FTO glass.

The electrochemical surface area of the $Cu_xCo_{3-x}O_4$ and $Ni_{1-x}Cu_xCo_2O_4$ electrodes was determined from double-layer charging curves via cyclic voltammetry in 1M KOH solution. Cyclic voltammograms were recorded in a narrow potential range of –50 mV to 50 mV (vs. SCE) at different scan rates (10 mV s^{-1} to 100 mV s^{-1}). The redox properties and the electrocatalytic activity of the electrodes for the OER were analyzed by recording CVs at a scan rate of 10 mV s^{-1} and 50 mV s^{-1} respectively.

The double-layer capacitance of the samples was also measured by EIS with a Voltalab 80 using (PGZ402 potentiostat and Voltamaster 4 software). The measurements were carried out at room temperature at 0 V vs SCE in 1M KOH using the experimental setup mentioned above. A frequency range of 0.1 Hz to 100 kHz with a potential perturbation of ±10 mV. The impedance data were fitted using EC-Lab V10.40 software.

Finally, the differential capacitance of the samples was measured at every 50 mV in a potential range of 0 to 400 mV at a frequency of 200 Hz. The measurements were carried out at room temperature in 1M KOH using the experimental setup mentioned above.

Rotating disc experiments were carried out using Pine Research Wave Driver 200 potentiostat and Pine instrument company MSRX speed control. Aftermath 1.6.1020 version was used for data analysis. The samples were deposited on glassy carbon, a platinum mesh was used as the counter electrode, and a saturated calomel electrode (SCE) as the reference electrode. The sample preparation reported in reference 15 was employed. The nitrate salt solutions (section 2.2) were mixed in an appropriate molar ratio to produce the corresponding spinel oxides. The solutions were then transferred to a crucible where the solvent was evaporated and the salt mixture was dried. $Cu_xCo_{3-x}O_4$ and $Ni_xCu_{1-x}Co_2O_4$ were annealed at 300ºC for one hour and $Fe_yCu_{x-y}Co_{3-x}O_4$ and $Fe_yNi_{x-y}Co_{3-x}O_4$ were annealed at 400ºC for two hours. The powder obtained was ground and 12 mg of the sample was mixed with Vulcan XC-72R (Cabot), carbon powder is a conductive filler and provides a high surface area to the catalyst. To this mixture, 280 µl of isopropanol, 280 µl of water and 140 µl of Nafion were added. Nafion is added as a binder. The solution was stirred very well and deposited on the glassy carbon disc (0.196 cm^2), and dried [15, 16]. The kinetics measurements were performed in a 0.1 M KOH electrolyte. The electrode was rotated at different speeds (500, 1000, 1500, 2000, 2500 and 3000 rpms) to generate the data for the Koutechy-Levich plots. The Tafel plot was acquired at a rotation speed of 3000 rpm. The electrolyte was purged with argon gas during the measurements.

2.3. References

[1] S. Thekkoot, R. Islam, S. Morin, Improved oxygen evolution reaction performance with addition of Fe to form $Fe_yCu_{x-y}Co_{3-x}O_4$ and $Fe_yNi_{x-y}Co_{3-x}O_4$ (x = 0.5, 1 and y = 0.1, 0.15) spinel oxides, Electrochim. Acta, 378 (2021) 138116

[2] A. L. Rosa-Toro, R. Berenguer, C. Quijada, F. Montilla, E. Morallon, J. L. Vazquez, Preparation and characterization of copper-doped cobalt oxide Electrodes, J. Phys. Chem. B., 110 (2006) 24021 - 24029

[3] B. Marsan, N. Fradette, G. Beaudoin, Physico chemical and electrochemical properties of $CuCo_2O_4$ electrodes prepared by thermal decomposition for oxygen evolution, J. Electrochem. Soc., 139, 7 (1992) 1889 - 1896

[4] J. P. Singh, R. N. Singh, New active spinel-type $M_xCo_{3-x}O_4$ films for electro-catalysis of oxygen evolution, J. New Mat. Electrochem. Systems, 3 (2000) 131 - 139

[5] X. Yang, X. Wnag, Z. Zhang, Electrochemical properties of submicron cobalt ferrite spinel through a co-precipitation method, J. Cryst. Growth 277 (2005) 467 - 470

[6] R.N. Singh, J.P. Pandey, N.K. Singh, B. Lal, P. Chartier, J.-F. Koenig, Sol-gel derived spinel $M_xCo_{3-x}O_4$ (M = Ni, Cu; $0 \leq x \leq 1$) films and oxygen evolution, Electrochim. Acta, 45 (2000) 1911 - 1919

[7] P. Lavela, J. L. Tirado, C. V. Abarca, Sol–gel preparation of cobalt manganese mixed oxides for their use as electrode materials in lithium cells, J. Electrochim. Acta 52 (2007) 7986 - 7995

[8] J. L. Gautier, E. Trollund, E. Rios, P. Nkeng, G. Poillerat, Characterization of thin $CuCo_2O_4$ films prepared by chemical spray pyrolysis. Study of their electrochemical stability by ex situ spectroscopic analysis, J. Electroanal. Chem. 428 (1997) 47 - 56

[9] A. Louardi, A. Rmili, F. Ouachtari, A. Bouaoud, B. Elidrissi, H. Erguig, Characterization of cobalt oxide thin films prepared by a facile spray pyrolysis technique using perfume atomizer, J. Alloys Compd. 509 (2011) 9183 - 9189

[10] X. H. Xia, J. P. Tu, J. Zhang, J. Y. Xiang, X. L. Wang, and X. B. Zhao, Cobalt Oxide Ordered Bowl-Like Array Films Prepared by Electrodeposition through Monolayer Polystyrene Sphere Template and Electrochromic Properties, ACS Appl Mater interfaces, 2, 1 (2010) 186 - 192

[11] I. Nikolov, R. Darkaoui, E. Zhecheva, R. Stoyanova, N. Dimitrov, T. Vitanov, Electrocatalytic activity of spinel related cobaltites $M_xCo_{3-x}O_4$ (M = Li, Ni, Cu) in the oxygen evolution reaction, J. Electroanal. Chem., 429 (1997) 157 -168
[12] D. A.Salvatore, K. E. Dettelbach, J. R. Hudkins, C. P. Berlinguette, Near-infrared-driven decomposition of metal precursors yields amorphous electrocatalytic films. Science Advances, 1, 2 (2015) 1400215
[13] C. Wei, S. Sun, D. Mandler, X. Wang, S. Z. Qiao, Z. J. Xu, Approaches for measuring the surface areas of metal oxide electrocatalysts for determining their intrinsic electrocatalytic activity, Chem. Soc. Rev., 48 (2019) 2518 - 2534
[14] D. Xu, M. B. Stevens, Y. Rui, G. DeLuca, S. W. Boettcher, E. Reichmanis, Y. Li, Q. Zhang, H. Wang, (2018). The role of Cr doping in Ni–Fe oxide/(oxy)hydroxide electrocatalysts for oxygen evolution. Electrochimica Acta, 265 (2018), 10 -18.
[15] A. D. Pauric, E. B. Easton, B. J. MacLean, (2010). Fe-N/C oxygen Reduction catalysts prepared by surface functionalization of carbon black with 5,6-diamino,1-10-phenanthroline. ECS Transactions, 28, 23 (2010), 55 - 62.
[16] F. Luo, S. Liao, D. Chen, Platinum catalysts supported on Nafion functionalized carbon black for fuel cell application, J. of Energy Chem. 22 (2013) 87 - 92

Chapter 3. Material Characterization

3.1 Introduction

As described in section 1.8. (Chapter 1), a materials science approach was taken in this work. Material characterization is an important aspect of this approach. Understanding the fundamental structure, composition, and physicochemical properties are important as these are some of the controlling factors that establish guidelines for achieving desired properties for highly efficient and stable electrocatalysts for OER. The thermal decomposition method was used for the synthesis of electrocatalysts. The detailed preparation method of spinel oxides and amorphous metal oxides is given in section 2.2. of Chapter 2. The material properties of various transition metal oxide compositions were studied by different characterization techniques. In this Chapter, the crystallite size of $Cu_xCo_{3-x}O_4$ ($0 \leq x \leq 1$) and $Ni_{1-x}Cu_xCo_2O_4$ ($0 \leq x \leq 0.75$), and TEM results of $CuCo_2O_4$ will be reported. Also, I will report and discuss SEM, EDX and XRD characterization results for amorphous samples such as CoO_x, $CuCo_2O_x$, $Ni_{0.5}Cu_{0.5}Co_2O_x$, $Fe_yCu_{x-y}Co_{3-x}O_x$ and $Fe_yNi_{x-y}Co_{3-x}O_x$ ($x = 1, 0.5$ and $y = 0.1, 0.15$).

3.2. Transition metal spinel oxides

3.2.1. Crystallite size determination of spinel oxides

In Prof. Morin's group, cobalt-based spinel oxides $Cu_xCo_{3-x}O_4$ ($0 \leq x \leq 1$), $Ni_{1-x}Cu_xCo_2O_4$ ($0 \leq x \leq 0.75$), $Fe_yCu_{x-y}Co_{3-x}O_4$ and $Fe_yNi_{x-y}Co_{3-x}O_4$ ($x = 1, 0.5$ and $y = 0.1, 0.15$) were prepared by the thermal decomposition method. The structure and composition of the samples were studied by EDX and XRD respectively [1, 2]. The EDX analysis indicated that compositions have a good correlation between the stoichiometric and EDX composition, while XRD analysis revealed that all the compositions were crystallized mainly in spinel structure [1, 2]. Using the X-ray diffraction analysis data, the average crystallite size of the samples was evaluated. The crystallite size was determined from the broadening of the spinel peak using the Debye- Scherrer's equation [3]:

$$T = 0.9\,\lambda/B\cos\theta \qquad (1)$$

where λ is the X-ray wavelength and B is the full width at half maximum (radians) of the most intense peak (311), which includes the correction for the broadening of the peak. The crystallite size of $Cu_xCo_{3-x}O_4$ and $Ni_{1-x}Cu_xCo_2O_4$ samples are given in Tables 1 and 2, respectively. For $Cu_xCo_{3-x}O_4$, we observed a decrease in crystallite size with an increase in copper content in the samples. For $Ni_{1-x}Cu_xCo_2O_4$, the crystallite size of samples does not

change significantly with composition. According to the X-ray diffraction analysis, the average crystallite diameter of $Cu_xCo_{3-x}O_4$ varies from 3.5 nm to 9.9 nm, while that of $Ni_xCu_{1-x}Co_2O_4$ ranges from 3.3 to 5.7 nm.

Table 3.1. The lattice parameter and crystallite size of $Cu_xCo_{3-x}O_4$ electrodes prepared by the thermal decomposition method.

Composition	Lattice parameter (Å)	Crystallite size (nm)
Co_3O_4	8.084 ± 0.003 [1]	9.9 ± 0.7
$Cu_{0.25}Co_{2.75}O_4$	8.099 ± 0.002 [1]	6.6 ± 0.4
$Cu_{0.5}Co_{2.5}O_4$	8.106 ± 0.003 [1]	6.1± 0.2
$Cu_{0.75}Co_{2.25}O_4$	8.108 ± 0.003 [1]	5.6 ± 0.4
$CuCo_2O_4$	8.114 ± 0.009 [1]	3.5 ± 0.5

Table 3.2. The lattice parameter and crystallite size of $Ni_xCu_{1-x}Co_{3-x}O_4$ electrodes prepared by the thermal decomposition method.

Composition	Lattice parameter (Å)	Crystallite size (nm)
$NiCo_2O_4$	8.1260 ±0.0004 [2]	4.4 ± 0.5
$Ni_{0.9}Cu_{0.1}Co_2O_4$	8.1240 ± 0.0003 [2]	4.3 ± 0.6
$Ni_{0.75}Cu_{0.25}Co_2O_4$	8.1205 ± 0.0004 [2]	4.4 ± 0.5
$Ni_{0.5}Cu_{0.5}Co_2O_4$	8.1202 ± 0.0004 [2]	5.7 ± 0.3
$Ni_{0.25}Cu_{0.75}Co_2O_4$	8.1222 ± 0.0006 [2]	3.3 ± 0.6

From Table 3.1, we can see that for $Cu_xCo_{3-x}O_4$ electrodes, the crystallite size decreases with an increase in the lattice parameter. This could be attributed to the presence of the secondary metal in the crystal lattice, causing lattice stress and strain, and/or differences in nucleation and growth kinetics with the composition of the solid solution [4, 5]. The particle size

of our materials can influence their electronic properties and hence the catalytic activity of the materials [6, 7].

3.2.2. Transmission Electron Microscopy (TEM) and High-Resolution Transmission Electron Microscopy (HR-TEM) of $CuCo_2O_4$

Transmission electron microscopy (TEM) and high-resolution transmission electron microscopy (HR-TEM) analysis were performed on nonpolarized (as prepared sample) and polarized (CV performed on the sample) $CuCo_2O_4$ samples to investigate the microscopic crystal structure of $CuCo_2O_4$ and to study the effect of polarization on the structure of the sample. Figure 3.1a) confirms that the as-prepared $CuCo_2O_4$ is composed of spherical-shaped grains and crystallite's size ranging from ~ 5-8 nm. After polarization, the size of the grains slightly decreased as shown in Figure 3.1d). In Figure 3.1 b) and e) HR-TEM images of non-polarized and polarized $CuCo_2O_4$ respectively are given (more HR-TEM images can be found in Figure A1.1). The HR-TEM image clearly indicates that the as-prepared $CuCo_2O_4$ possesses a higher degree of crystallization than polarized samples. Crystalline samples possess well-resolved lattice fringes which are absent in amorphous samples. Compared to the polarized $CuCo_2O_4$, crystallites and lattice fringes are more visible in non-polarized samples.

From Figure 3.1b) and e), we can see that the lateral sizes and 2D characteristics of the crystalline samples were affected by polarization. In addition, both crystalline and amorphous phases coexist in $CuCo_2O_4$. Lattice fringes are not very distinct throughout the sample. This feature is more significant in Figure 3.1e), indicating that the amorphous nature of the material increases after polarization. A lower temperature used for our sample preparation could be a reason for the coexistence of both crystalline and amorphous phases in our sample, annealing temperature influences the structure and morphology of materials [8]. Some studies indicate that the coexistence of amorphous and crystalline phases enhanced the catalytic activity for OER, where it incorporates the highly defective and high density of coordinatively unsaturated atoms of the amorphous phase, and the atomic and electronic structural features of the crystalline phase. [9, 10, 11].

In nonpolarized $CuCo_2O_4$, where lattice fringes are more resolved (Figure 3.1b), the lattice fringe spacings range from 0.206 nm to 0.252 nm corresponding to the (311) facet of the cubic phase of spinel. The diffraction rings in the SAED pattern confirm the polycrystalline nature of our materials (Figures 3.1c) and 3.1f)). The SAED patterns do not show sharp and well-defined

spots for both polarized and nonpolarized samples as expected for crystalline materials. This further confirms the coexistence of crystalline and amorphous phases. Figure 3.1b) reveals that the small crystalline grains are interspersed within some amorphous phase. In Figure 3.1e) the rings are more diffused than observed in Figure 3.1b); the polarization increases the amorphization of the sample.

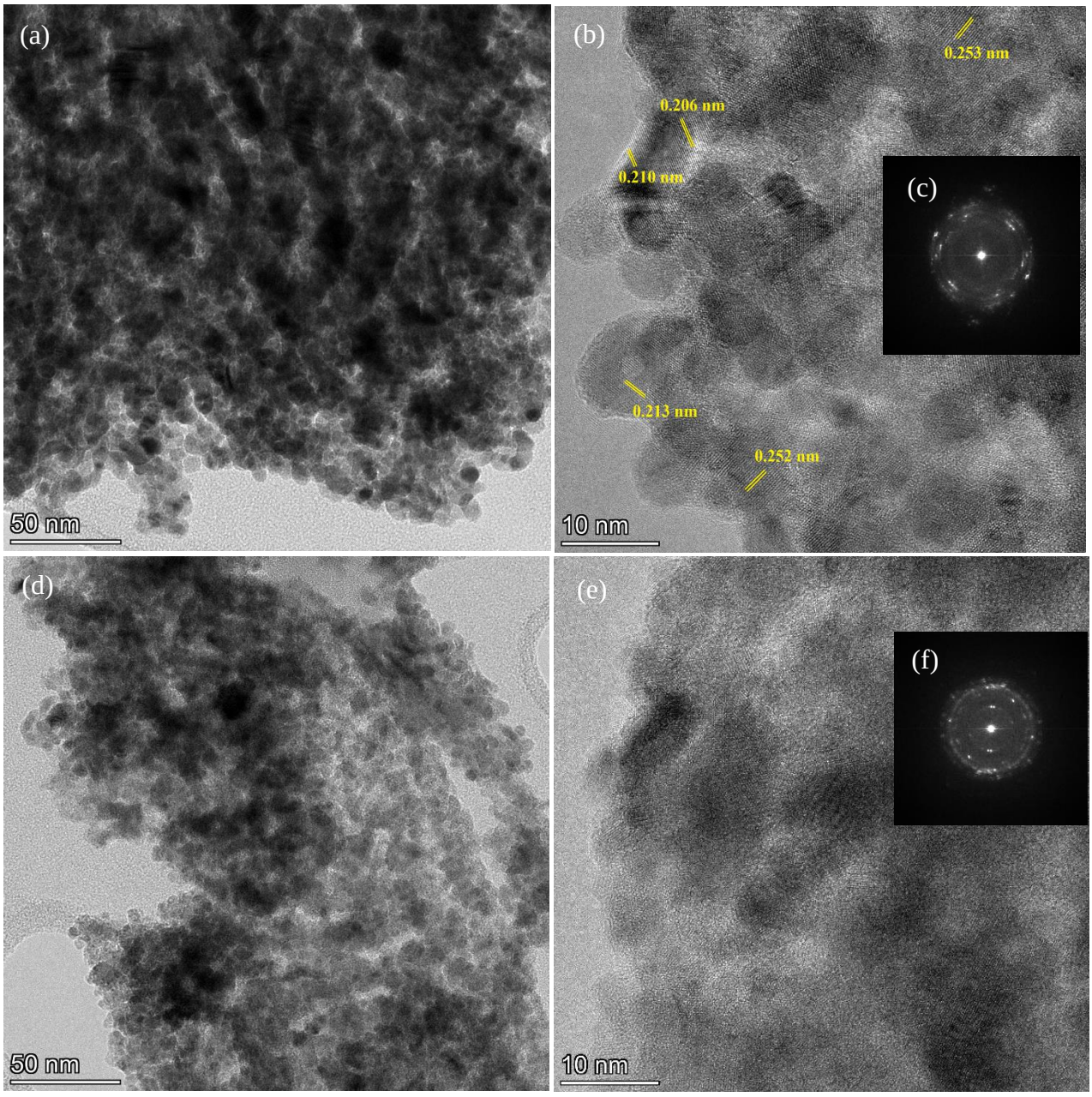

Figure 3.1. TEM, HR-TEM images and SAED patterns of (a-c) non-polarized $CuCo_2O_4$ (d-f) polarized $CuCo_2O_4$ respectively.

3.3. Amorphous transition metal oxides

3.3.1 Optimization of the reaction conditions

Infrared spectroscopy is a very useful technique for the identification of materials and functional groups. In our study we have used FTIR to investigate the progress of the reaction during the preparation of amorphous metal oxides. We have synthesized CoO_x, $CuCo_2O_x$, $Ni_{0.5}Cu_{0.5}Co_2O_x$, $Fe_{0.1}Cu_{0.9}Co_2O_x$, and $Fe_{0.1}Ni_{0.9}Co_2O_x$ on FTO glass. For that Cu, Ni, Co and Fe - 2-ethyl hexanoate organic reagents were mixed in the appropriate molar ratio and deposited on FTO glass [12, 13]. Since we have used organic reagents to synthesize amorphous metal oxide compositions, it is necessary to confirm the bands associated with these organic reagents are completely removed and metal oxide is formed. The samples were heated under the IR lamp to obtain amorphous metal oxides [12, 13]. When each layer was heated under an IR lamp for 30 minutes (3 layers were deposited), the bands associated with the C-H and C-O bonds completely disappeared. In Figure 3.2, the infrared spectrum of copper 2 ethyl hexanoate (precursor) before annealing and that of amorphous metal oxide film obtained after annealing is given, which reveals the complete removal of organic functional groups from the sample. FTIR spectra of other samples can be found in the Appendix from Figure A1. 2 a) to d).

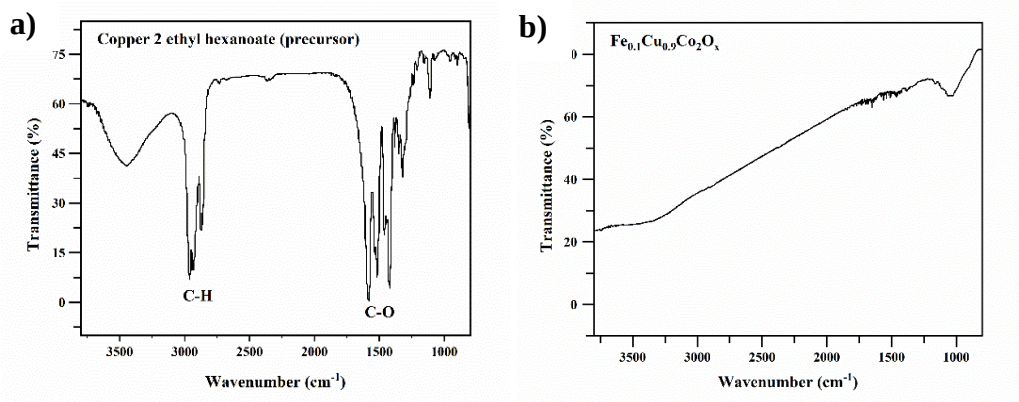

Figure 3.2. FTIR spectra of a) copper 2 ethyl hexanoate (precursor) b) $Fe_{0.1}Ni_{0.9}Co_2O_4$

3.3.2. Confirmation of amorphous phase

X-ray diffraction was used to study the amorphous nature of the prepared samples. The precursor solution was deposited on fluorine-doped tin oxide conductive glass (FTO). Initially, we used lower temperatures to prepare amorphous samples. For that, CoO_x and $Fe_{0.1}Cu_{0.9}Co_2O_x$ were deposited on FTO glass and annealed at 220°C and 240°C for one hour using Lindberg

BF51732BC furnace. The resulting X-ray diffraction pattern indicated the formation of both amorphous and crystalline phases in the sample. At higher temperature (240°C), the intensity of the peaks was more intense. We could not achieve amorphous materials by annealing the samples in the furnace.

Then we deposited the thin films of samples on FTO glass and annealed them using the near-infrared lamp. Each layer was heated for 30 minutes under an IR lamp (3 layers were deposited). The X-ray diffraction patterns of CoO_x, $CuCo_2O_x$, $Ni_{0.5}Cu_{0.5}Co_2O_x$, $Fe_{0.1}Cu_{0.9}Co_2O_x$, and $Fe_{0.1}Ni_{0.9}Co_2O_x$ are given in Figure 3.3. The CoO_x possessed a nanocrystalline structure with peaks corresponding to spinel structure. In Figure 3.4, XRD patterns of CoO_x and $CuCo_2O_x$ are shown separately. The XRD pattern of CoO_x (Figure 3.4b) clearly shows very small peaks associated with spinel oxide structure, indicating the formation of nanocrystalline spinel oxide. However, the X-ray diffraction pattern of other samples shows only the peaks corresponding to FTO. This confirms the formation of an amorphous phase for copper, nickel, or iron-substituted cobalt oxide samples. CoO_x crystallizes more readily than other metal-substituted cobalt oxide compositions. In our previous work, we observed that the crystallinity or intensity of the peaks decreased with the substitution of other metals in the cobalt oxide spinel oxide [1]. To further confirm the amorphous nature of the samples and to exclude the overlap of peaks from FTO glass, one of the amorphous samples, $Fe_{0.1}Ni_{0.9}Co_2O_x$ was deposited on normal glass and performed X-ray diffraction analysis. No peaks were observed in the XRD pattern of the sample (Figure A1. 3), indicating that the sample is amorphous.

Bai *et al* also reported similar results. They prepared $FeCoNiO_x$, $FeCoO_x$ and CoO_x by aqueous sol-gel techniques. The X-ray diffraction analysis showed that CoO_x possessed well-defined peaks of cubic crystalline structure, while $FeCoNiO_x$ displayed amorphous nature when prepared under similar conditions [14].

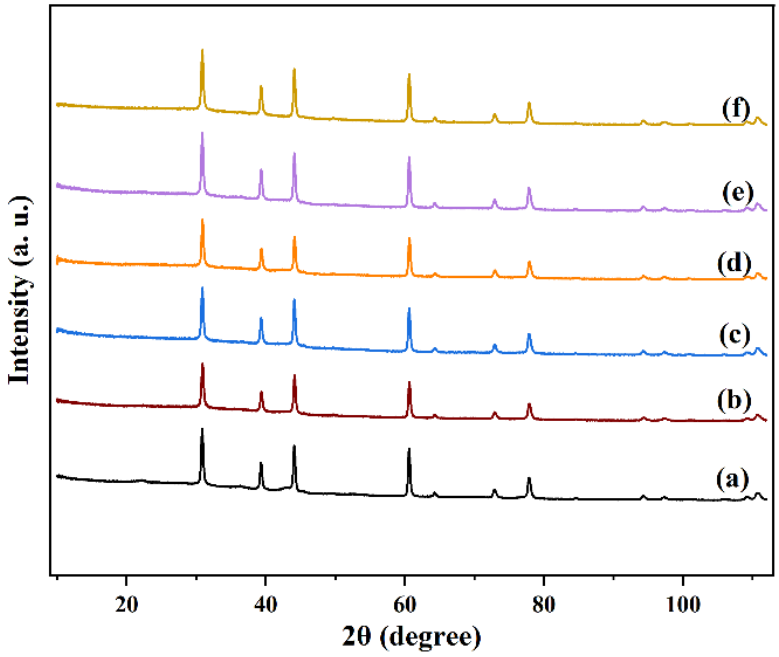

Figure 3.3. X-ray diffraction pattern of (a) CoO_x, (b) $CuCo_2O_x$, (c) $Ni_{0.5}Cu_{0.5}Co_2O_4$, (d) $Fe_{0.1}Cu_{0.9}Co_2O_4$, (e) $Fe_{0.1}Ni_{0.9}Co_2O_4$ and (f) FTO coated glass. Samples a) to e) were prepared on fluorine-doped tin oxide conductive glass (FTO).

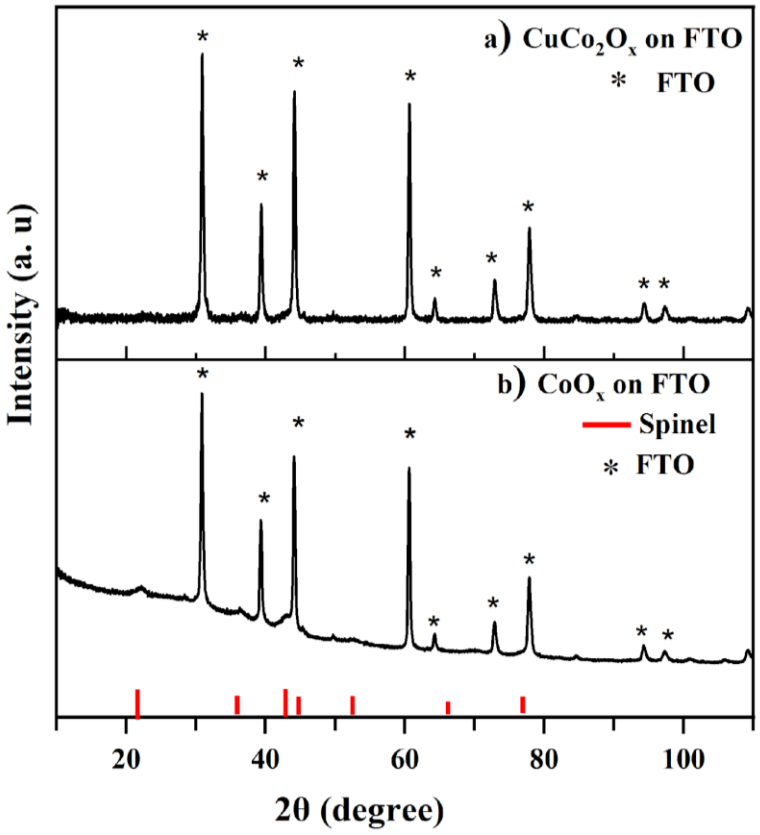

Figure 3.4. X-ray diffraction patterns of a) $CuCo_2O_x$ and b) CoO_x deposited on FTO glass. Peaks for FTO glass are indicated by a star and spinel standard peaks for Co_3O_4 are indicated by red lines b).

3.3.3 Amorphous Sample Compositions

Energy dispersive X-ray analysis (EDX) was used for elemental analysis and to study the bulk composition of the amorphous materials. The EDX analysis confirms that the samples contain all elements as expected according to their composition. In addition, we have observed a small peak for carbon could be due to the adventitious carbon. Since we have deposited thin films of samples on FTO glass, we have also observed strong peaks for the tin in the EDX spectra for all samples. The EDX spectrum of $Ni_{0.5}Cu_{0.5}Co_2O_x$ is shown in Figure 3.5, which displays characteristic peaks of Ni, Cu, Co, and oxygen along with Sn and carbon (the EDX spectra of $CuCo_2O_x$ and $Fe_{0.1}Ni_{0.9}Co_2O_x$ can be found in Figure A1. 4 a) and b) respectively).

The composition of the samples was evaluated from the quantification of elements obtained from EDX analysis. The EDX composition of the amorphous samples and that of spinel oxides obtained from previous work is given in Table 3.3, which indicates that the composition of all samples obtained from EDX analysis is close to the stoichiometric composition. To calculate the error in the homogeneity of the prepared samples, the EDX spectrum was taken from different areas of the samples and quantified the amount of each element in the sample. The standard deviation in the atomic percentage was calculated for various elements in the sample and the relative error ranges from 1% to 7%. Since we have used a lower temperature for the synthesis, the incorporation of Sn in the metal oxide films can be neglected. Ling *et al* detected Sn in their samples prepared on FTO glass only when the samples were annealed at or above 650 ºC [15].

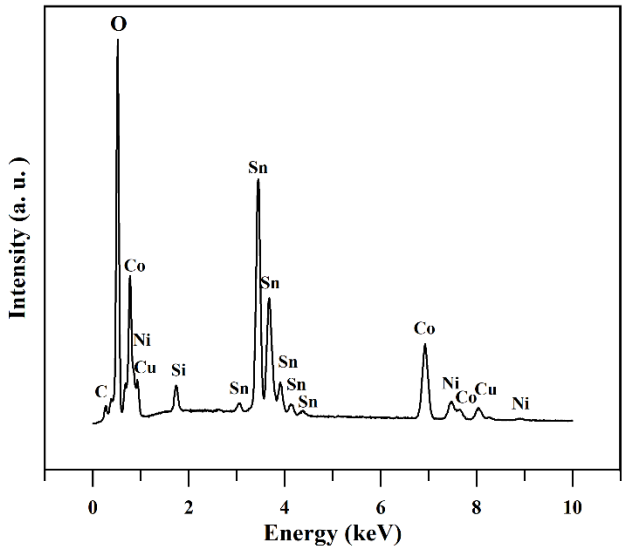

Figure 3.5. The Energy dispersive X-ray spectra of $Ni_{0.5}Cu_{0.5}Co_2O_x$. The EDX spectra of other samples were given in the supplementary file.

Table 3.3. The EDX composition of amorphous metal oxides and spinel oxides

Stoichiometric composition	EDX amorphous sample composition	EDX spinel sample composition
$CuCo_2O_{x\ or\ 4}$	$Cu_{0.95}Co_{2.05}O_x$	$Cu_{1.34}Co_{1.65}O_4$ [1]
$Ni_{0.5}Cu_{0.5}Co_2O_{x\ or\ 4}$	$Ni_{0.53}Cu_{0.44}Co_{2.03}O_x$	$Ni_{0.57}Cu_{0.87}Co_{1.57}O_4$ [2]
$Fe_{0.1}Cu_{0.9}Co_2O_{x\ or\ 4}$	$Fe_{0.14}Cu_{0.80}Co_{2.06}O_x$	$Fe_xCu_{1.08}Co_{1.92}O_4$ [2]
$Fe_{0.1}Ni_{0.9}Co_2O_{x\ or\ 4}$	$Fe_{0.09}Ni_{1.09}Co_{1.81}O_x$	$Fe_xNi_{0.63}Co_{2.37}O_4$ [2]

3.3.4 Amorphous sample morphology

The surface morphology of the samples was analyzed by scanning electron microscopy. The SEM picture of CoO_x, $CuCo_2O_x$ and $Ni_{0.5}Cu_{0.5}Co_2O_x$ at 100,000x magnification is given in Figure 3.6 a) to c), and the SEM pictures of their corresponding crystalline counterparts are given in Figure 3.6 d) to f). Unlike the crystalline samples, the surface of all amorphous samples appears very smooth and compact, no grains have been formed as we observed in their corresponding spinel oxides prepared by the thermal decomposition method, which would possibly support the formation of the amorphous phase. Meanwhile, the surface of spinel oxides

is made of very small grains (a few nanometers in size) that appear spherical. They assemble to form various mesoscopic and microscopic features. For Co_3O_4 (Figure 3.6a), these nanostructures assemble to form larger features (ca. 1 μm in diameter). As the Cu substitution increased, the appearance of these features changed, the surface appeared more homogeneous, and displayed high porosity (Figure 3.6e). Most $Ni_{1-x}Cu_xCo_2O_4$ samples have a much smoother and compact morphology with uniform material distribution with the exception of a few cracks. SEM micrographs of $Ni_{0.5}Cu_{0.5}Co_2O_4$ samples are displayed in Figure 3.6f). Unlike amorphous metal oxides, the spinel oxides were annealed at a higher temperature (300°C) [1, 2]. The SEM pictures of CoO_x, $CuCo_2O_x$, and $Ni_{0.5}Cu_{0.5}Co_2O_x$ on FTO glass at lower magnification (10,000×) are given in Figure A1. 5.

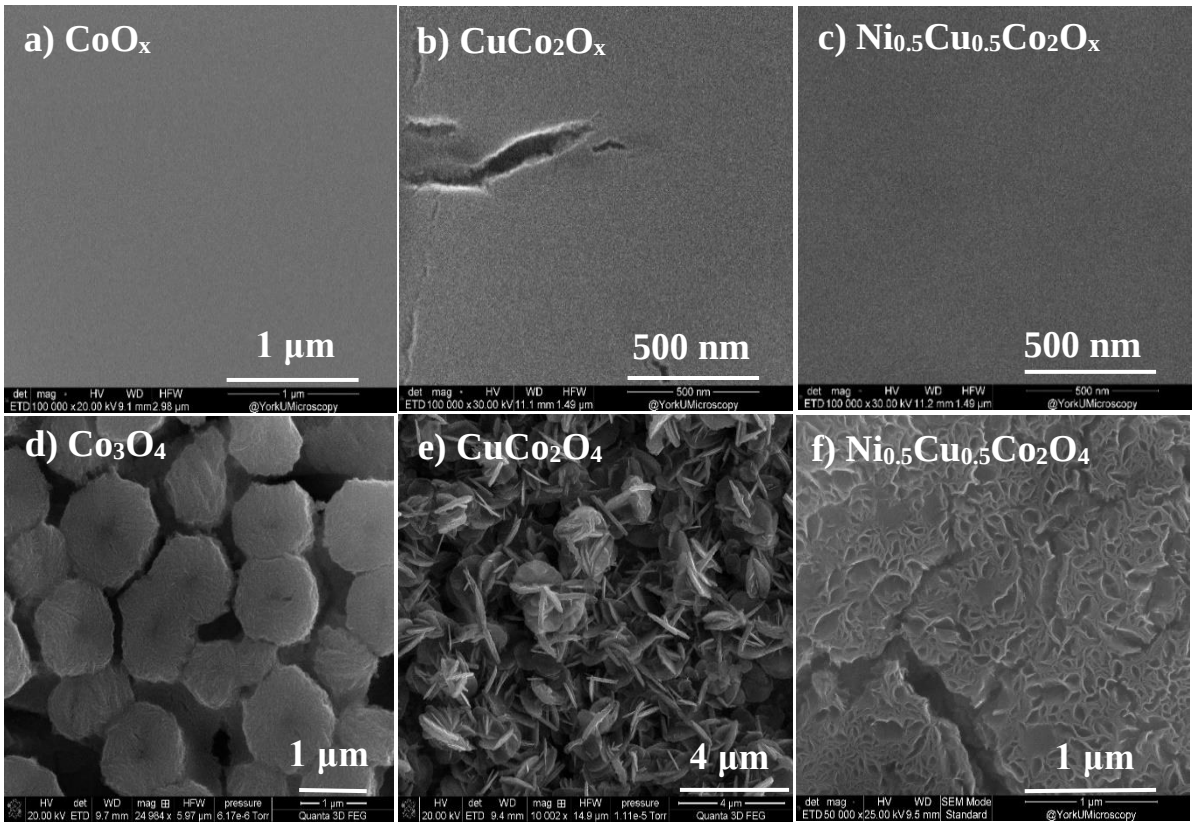

Figure 3.6. SEM micrographs of (a) CoO_x (b) $CuCo_2O_x$ (c) $Ni_{0.5}Cu_{0.5}Co_2O_x$ (d) Co_3O_4 (e) $CuCo_2O_4$ (f) $Ni_{0.5}Cu_{0.5}Co_2O_4$ (deposited on fluorine-doped tin oxide conductive glass (FTO). Samples a), b) and c) have a magnification of 100,000× d) c.a. 25,000× e) 10,000× and f) 50,000×

3.4. References

[1] S. Thekkoot, S. Morin (2016) " Nanostructured mixed transition metal spinel oxide as efficient electrocatalysts" MSc. Thesis (Chemistry), York University.

[2] R. Islam, S. Morin (2019), "Performance of nanostructured ternary metal spinel oxide as efficient electrocatalysts" M.Sc. Thesis (Chemistry), York University

[3] L. Smart, E. Moore, Solid State Chemistry – An Introduction, 2nd ed; CRC press, Boca Raton, 2012.

[4] H. Ghayour, M. Abdellahi, J. Power Technol. A brief review of the effect of grain size variation on the electrical properties of $BaTiO_3$-based ceramics, 292 (2016) 84 - 93

[5] A.I.Y. Tok, S.W. Du, F.Y.C. Boey, W.K. Chong, J. Mater. Sci. Eng. A, Hydrothermal synthesis and characterization of rare earth doped ceria nanoparticles 466 (2007) 223 - 229

[6] D. Prieur, W. Bonani, K. Popa, O. Walter, K. W. Kriegsman, M. H. Engelhard, X. Guo, R. Eloirdi, T. Gouder, A. Beck, T. Vitova, A. C. Scheinost, K. Kvashnina, P. Martin, Size dependence of lattice parameter and electronic structure in CeO_2 nanoparticles, J. Inorg. Chem. 59 (2020) 5760 - 5767

[7] K. Chakrapani, G. Bendt, H. Hajiyani, I. Schwarzrock,T. Lunkenbein, S. Salamon, J. Landers, H. Wende, R. Schlçgl, R. Pentcheva, M. Behrens, S. Schulz, Role of composition and size of cobalt ferrite nanocrystals in the oxygen evolution reaction, ChemCatChem., 9 (2017) 2988 - 2995

[8] M. M. Viana, N. D. S. Mohallem, D. R. Miquita, K. Balzuweit, E. Silva-Pinto, Preparation of amorphous and crystalline Ag/TiO_2 nanocomposite thin films. Appl. Surf. Sci., 265, (2013) 130 - 136

[9] Z. Guo, Y. Pang, H. Xie, G. He, I. P. Parkin, and G. L. Chai, "Phosphorus-doped $CuCo_2O_4$ oxide with partial amorphous phase as a robust electrocatalyst for the oxygen evolution reaction," J. ChemElectroChem, 8, 1 (2021) 135 -141

[10] M. Jiang, J. Li, J. Li, Y. Zhao, L. Pan, Q. Cao, D. Wang, Y. Du, Two-dimensional bimetallic phosphide ultrathin nanosheets as non-noble electrocatalysts for a highly efficient oxygen evolution reaction, Nanoscale, 11 (2019) 9654 - 9660

[11] X. Zhang, J. Zhang, B. Xu, K. Wang, X. W. Sun, Synergistic effects in biphasic nanostructured electrocatalyst: Crystalline core versus amorphous shell. Nano Energy, 41, (2017) 788 - 797

[12] D. A. Salvatore, K. E. Dettelbach, J. R. Hudkins, C. P. Berlinguette, Near-infrared-driven decomposition of metal precursors yields amorphous electrocatalytic films. Science Advances, 1, 2 (2015) 1400215
[13] D. Xu, M. B. Stevens, Y. Rui, G. DeLuca, S. W. Boettcher, E. Reichmanis, Y. Li, Q. Zhang, H. Wang, The role of Cr doping in Ni–Fe oxide/(oxy)hydroxide electrocatalysts for oxygen evolution. Electrochim. Acta, 265 (2018) 10–18.
[14] L. Bai, X. Wen, J. Guan, Amorphous Fe-Co-Ni oxide for oxygen evolution reaction. Materials Today Energy, 12 (2019) 311 - 317.
[15] Y. Ling, G. Wang, D. A. Wheeler, J. Z. Zhang, Y. Li, Sn-doped hematite nanostructures for photoelectrochemical water splitting. Nano Letters, 11, 5 (2011) 2119 - 2125

Chapter 4. Transition metal oxide surface composition determination by X-ray Photoelectron Spectroscopy analysis

4. 1. Introduction

EDX and XRD analyses provide the composition and structure of the bulk of the electrodes respectively, while X-ray photoelectron spectroscopy (XPS) provides information about the surface structure and composition of the electrodes. Surface chemistry has significant importance in electrochemistry as the electrode reactions happen on the surface of the electrodes [1, 2]. Hence, the catalytic properties of the electrodes are influenced by the surface chemistry of the electrode. XPS analysis allows us to differentiate the atoms in different environments by measuring electron binding energies and identifying metal oxidation states and the presence of mixed oxides on the surface of the samples.

This technique is based on the photoelectric effect. When the sample is irradiated by an X-ray photon of energy hν, the target atom absorbs the energy, followed by a photoelectron ejected with kinetic energy (E_k),

$E_k = h\nu - E_b - \Phi$ (4.1)

where E_b is the binding energy of the electron and Φ is the work function of the electrode material. By calculating the binding energy of the electron, the elements can be identified. Two elements do not share the same set of electronic binding energies. XPS mainly focuses on electrons in the core level of atoms. In addition, the changes in the chemical environment can also be monitored by measuring the binding energies of photoelectron peaks. X-ray photoelectron spectrum is a plot of the intensity vs binding energy (or kinetic energy) of the electrons [3]. Figure 4.1 a) and b) show the photoelectron and auger electron process respectively.

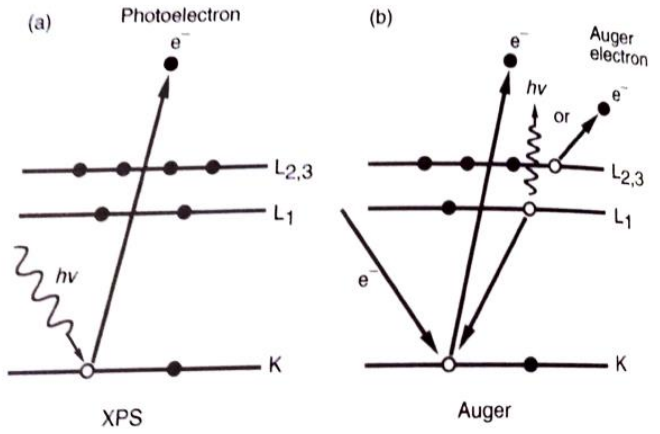

Figure 4.1. Schematic representation of a) photoelectron emission and b) auger electron emission. Reprinted from ref. [3] with permission.

XPS analysis was performed on both spinel oxides ($Cu_xCo_{3-x}O_4$ (x = 0, 1), $Ni_xCu_{1-x}Co_2O_4$ ($0 \leq x \leq 0.75$), $Fe_yCu/Ni_{x-y}Co_{3-x}O_4$ (x=0.5, 1 and y= 0.1, 0.15)) and amorphous samples (CoO_x, $CuCo_2O_x$, $Ni_{0.5}Cu_{0.5}Co_2O_x$, $Fe_{0.1}Cu_{0.9}Co_2O_x$, and $Fe_{0.1}Ni_{0.9}Co_2O_x$). The peaks were assigned based on established standard values available in the literature [4, 5, 6, 7, 8].

Both survey spectra and high-resolution spectra were recorded for each sample. The survey spectrum is a wide scan and records all the elements present in the sample so that the composition of the samples can be determined. High-resolution spectra give more detailed information about the chemical states and binding energy of electrons emitted from each element. This would allow us to study the chemical environment of elements.

The XPS analysis of the first-row transition metals and their oxides is more complicated due to their peak asymmetry, complex multiple fittings, shake-up peaks (satellite peaks), and close binding energy values of the species involved in the structure. The peaks were assigned based on established standard values available in the literature, where the difference between binding energy positions and FWHM values was constrained by referencing values published for standard samples [4, 5, 6, 7, 8]. Since the peaks are deconvoluted into photoelectron and satellite peaks corresponding to multiple species, constraining the difference between binding energy values and FWHM values provides more meaningful results. Satellite peaks are useful in characterizing the environment of metal ions, which result from the photoelectron peaks that lose energy as a result of their interaction with valence electrons [3]

For more accurate quantification and analysis, background subtraction from the spectrum is important. Shirley background was used to model this signal and perform background correction. This background was applied to the entire 2p peak of metals and the O 1s peak. The Shirley background is a commonly applied method for background correction as it gives good results when used with care and is widely adopted by many studies. The simple linear background correction depends on the operator's judgment of placing the endpoints and it may lead to loss of intensity in many cases. Tougaard is another background correction used for XPS analysis, which is difficult to apply for multicomponent samples.

A mixed Gaussian/Lorentzian (70:30) was used for fitting the XPS peaks, which provided the lowest residual standard deviation value after fitting the peaks. The peak areas were normalized using appropriate atomic sensitivity factors (R.S.F. factor). The peak energies were given to an accuracy of ± 0.1 eV. For that XPS measurements were performed at different spots of the $CuCo_2O_4$ sample.

This surface structure analysis would help us study how the copper, nickel, and iron substitution influence the elemental states and chemical environment of the cobalt oxides [9, 10]. The XPS analysis results of both cobalt-based spinel oxides and amorphous metal oxides will be presented in this chapter based on the analysis of survey spectra and high-resolution spectra. Survey spectra and high-resolution spectra of one of the amorphous and spinel oxides are shown in the discussion here. The results for the other thin film materials can be found in Appendix 2. The spectral fitting parameters, binding energy values, and percentage of various species are also included in that Appendix.

4. 2. XPS analysis of spinel oxides ($Ni_{1-x}Cu_xCo_2O_4$ ($0 \leq x \leq 0.75$), $Cu_xCo_{3-x}O_4$ ($x = 0, 1$), $Fe_yCu/Ni_{x-y}Co_{3-x}O_4$ ($x=0.5, 1$ and $y= 0.1, 0.15$))

4.2.1 The detailed XPS analysis of $Ni_{0.5}Cu_{0.5}Co_2O_4$

The survey spectra of $Ni_{1-x}Cu_xCo_2O_4$ and $Cu_xCo_{3-x}O_4$ indicate that the surface of the electrodes is free of contaminants except for carbon. However, the survey spectra of $Fe_yCu_{x-y}Co_{3-x}O_4$ and $Fe_yNi_{x-y}Co_{3-x}O_4$ show a trace amount of sodium, chlorine, and sulfur. The survey spectrum of $Ni_{0.5}Cu_{0.5}Co_2O_4$ is shown the Figure 4.2 and that of $Fe_yCu/Ni_{x-y}Co_{3-x}O_4$ ($x = 0.5, 1$ and $y = 0.1, 0.15$) are given in Appendix from Figure A2. 1.

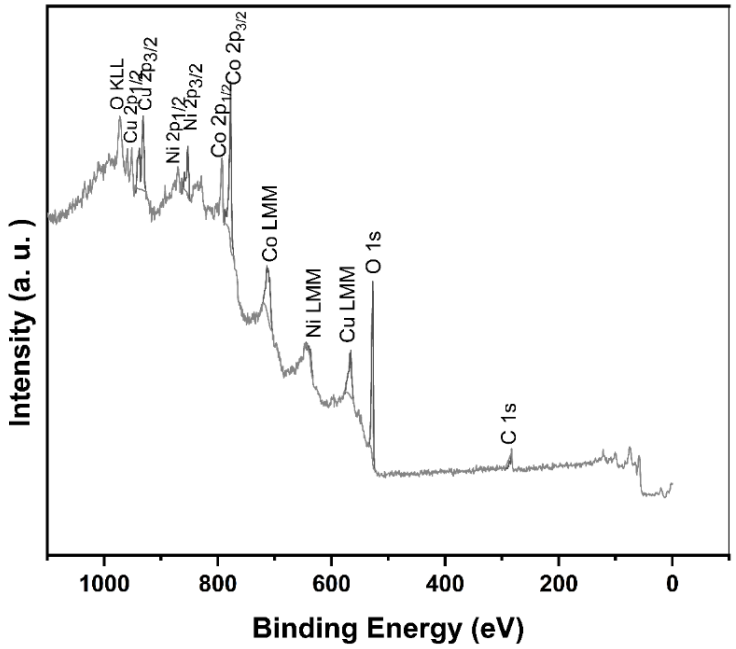

Figure 4.2. The survey spectrum of $Ni_{0.5}Cu_{0.5}Co_2O_4$ electrode

The core level spectra of Co $2p_{3/2}$, Cu $2p_{3/2}$, Ni $2p_{3/2}$ Fe $2p_{3/2}$ and O 1s were chosen for the analysis as they are the most intense photoelectron peaks so that detailed information can be derived. Comparing the peak shape and binding energy of the high-resolution spectrum of elements to that of standard samples, the oxide composition can be derived. The peaks were deconvoluted into component peaks corresponding to photoelectron peaks and satellite peaks of various species. For the quantification of the species, both photoelectron peaks and satellite peaks of high-resolution spectra were used. The metal 2p peaks have been split into $2p_{3/2}$ and $2p_{1/2}$, $2p_{3/2}$ is more intense and hence used for the analysis and quantification.

The XPS line shapes of all the metal cations and oxygen anions were similar to the spectra reported in the literature [4, 5, 7, 8]. The high-resolution spectra of all samples contain mixed valences of transition metal cations. The high-resolution spectrum of $Ni_{0.5}Cu_{0.5}Co_2O_4$ is shown in Figure 4.3 and that of other samples is given in Appendix 2, from Figure A2.2a to Figure A2. 12c. The Co $2p_{3/2}$ peak analysis (Figure 4.3a) indicates that cobalt exists as Co^{2+} and Co^{3+} ions in cobalt-based samples. The Co $2p_{3/2}$ region is curve fitted with two photoelectron peaks and three satellite peaks for spinel structure. The deconvoluted peaks of both $Co(OH)_2$ and CoOOH possess two photoelectrons and two satellite peaks. CoOOH peak possesses weak

satellite peaks; in general, Co^{3+} has weak satellite peaks, while Co^{2+} is always associated with well-known satellite peaks. This helps to distinguish between Co^{2+} and Co^{3+} metal cations in the composition. $Co(OH)_2$ has strong satellite peaks at the high binding energy side [11].

Binding energies and full width at half maximum (FWHM) of all peaks of $Ni_{0.5}Cu_{0.5}Co_2O_4$ are given in Table 4.1. The spinel structure constitutes two deconvoluted photoelectron peaks and three satellite peaks. The photoelectron peaks positioned at the lower binding energy side, 779.4 eV and 780.7 eV, were attributed to Co^{3+} and Co^{2+} respectively in the spinel structure. The three-satellite peaks were located at higher binding energy, 782.0 eV, 785.0 eV, and 789.3 eV, indicating the presence of mixed valences of cobalt in the sample [7, 12]. Marsan *et al* assigned the satellite peak at 785.2 eV to the paramagnetic Co^{2+} and the peak at 790.1 was indexed to the Co^{3+} cation [7]. Karmakar *et al* attributed the presence of a weak satellite peak at 788.8 eV to the octahedral occupancy of the Co^{3+} ion in the spinel structure [12]. Xu *et al* assigned the satellite peak centered at 786 eV to the Co^{2+} oxidation state [13]. Amri *et al* observed minor curve-fitting satellite peaks at 783.9 eV and 787.0 eV, which were assigned to the Co^{2+} ion in the spinel structure [14]. Based on the literature, it is difficult to separate the contribution of Co^{2+} and Co^{3+} in the satellite peaks, however, these satellite peaks are mainly the result of paramagnetic Co^{2+} ions.

XPS analysis of Cu 2p high-resolution spectra of all samples showed that copper also exists in different oxidation states, Cu^{1+} and Cu^{2+}. The Cu 2p spectrum of $Ni_{0.5}Cu_{0.5}Co_2O_4$ is shown in Figure 4.3b. The peak observed at 932.2 eV was assigned to the Cu^{1+} ion in Td site of the spinel and the peak at 933.4 eV was ascribed to Cu^{2+} occupying the Oh site, while the peak at 936.5 eV corresponds to Cu^{2+} ions at Td site [7, 15]. This explains the lower Co^{2+} to Co^{3+} ratio of copper-substituted cobalt spinel oxide; Cu^{1+} might be replacing the Co^{2+} in the Td site. The formation of Cu^{1+} could be due to the reduction of Cu^{2+} by X-ray irradiation [12]. The Cu $2p_{3/2}$ peak exhibits intense satellite peaks at high binding energy positions and is likely to be associated with paramagnetic Cu^{2+} ions [7, 12]. In this work, the peaks having lower binding energy, in the range of 932.1 – 932.4 eV, were indexed to Cu^{1+}, while the peaks observed in the range of 933.4 – 934.0 eV were attributed to Cu^{2+} in the octahedral site and the peaks at 936.5 – 936.8 eV were assigned to Cu^{2+} in the tetrahedral site of the spinel structure. The two satellite peaks in the range of 940.2 – 940.3 eV and 943.0 - 943.5 eV could be associated with the paramagnetic Cu^{2+} cations [7, 9].

XPS studies on copper-containing spinel oxides also report similar results. Costa *et al* observed similar peaks in their spectra, the peak situated at 932.7 eV was assigned to Cu^{1+}, while the peaks at 933.9 eV and 935. 8 eV were assigned to Cu^{2+} at octahedral and tetrahedral sites respectively [8]. Zhang *et al* observed a peak at 933.9 eV and two intense satellite peaks at 940.6 eV and 943.2 eV, which were indexed to the Cu^{2+} cation [16]. Amri *et al* observed a peak at 931. 2 eV for the copper-cobalt oxide thin films and was assigned to octahedral Cu^{1+}, and the peak at 932. 8 eV was ascribed to tetrahedral Cu^{1+}. The peak at 933.8 eV was assigned to the octahedral Cu^{2+}. The strong satellite peaks at 940.7 eV and 943.2 eV correspond to the paramagnetic Cu^{2+} ion [17].

The Ni 2p spectrum of $Ni_{0.5}Cu_{0.5}Co_2O_4$ is shown in Figure 4.3c. Ni $2p_{3/2}$ peak analysis indicates that Ni^{2+} and Ni^{3+} ions are present on the surface of the sample. The peaks centered at 854.2 eV and 855.7 eV indicate the existence of Ni^{2+} ion and Ni^{3+} ions respectively in the spinel structure. The corresponding satellite peaks were located at 861.5 eV, 863.6 eV, and 867.1 eV which indicates the presence of paramagnetic Ni^{2+} and Ni^{3+} ions [15, 18]. Lu *et al* have reported two satellite peaks at 861.2 eV and 879.7 eV which were attributed to the existence of mixed-valence states of Ni in the sample [15]. Various studies indicate that both Ni^{2+} and Ni^{3+} mainly occupy the octahedral site, while cobalt is occupying both octahedral and tetrahedral sites [2, 19]. We have observed a higher amount of Ni^{3+} cations for all compositions. Marco *et al* have performed X-ray powder diffraction (XRD), X-ray absorption spectroscopy (EXAFS and XANES), and X-ray photoelectron spectroscopy (XPS) on $NiCo_2O_4$ and found that both Ni^{2+} and Ni^{3+} ions will only occupy the octahedral site [2].

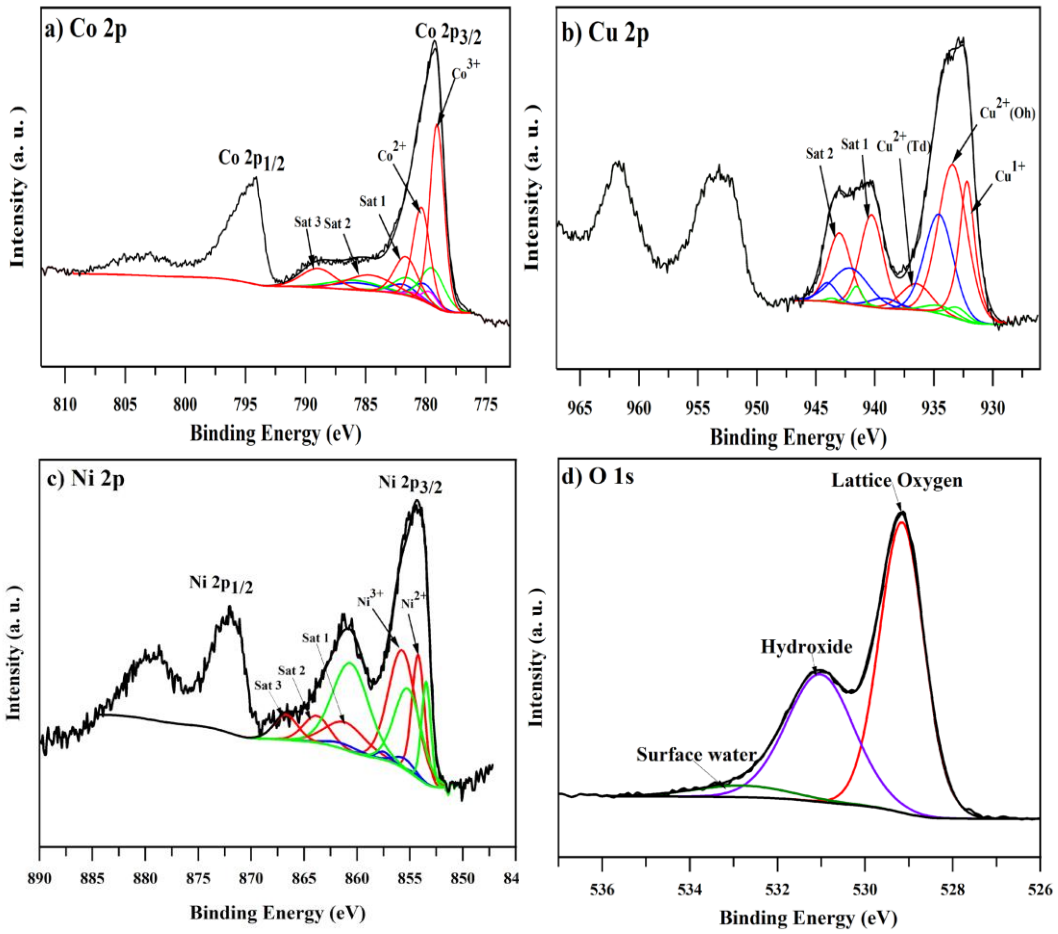

Figure 4.3. XPS core-level spectra of a) $Co2p_{3/2}$, b) Cu $2p_{3/2}$ c) Ni $2p_{3/2}$ d) O 1s of $Ni_{0.5}Cu_{0.5}Co_2O_4$. XPS spectra of other compositions can be found in Appendix 2, from Figure A2.2a to Figure A2. 12c .

The high-resolution spectra of O 1s were recorded for all spinel oxides and were deconvoluted into three peaks. O 1s of all the electrodes possessed similar XPS line shapes. The O1s spectrum of $Ni_{0.5}Cu_{0.5}Co_2O_4$ is shown in Figure 4.3d. The peak at 529.1 eV corresponds to the metal-oxygen bond in the lattice of spinel oxides, which occupies approximately 30% of the total area of the peak. The second peak positioned at a binding energy of 531.0 eV could be due to the hydroxide or defective sites within the oxide crystal. The analysis of all metal peaks indicates that a significant amount of metal hydroxides have been formed on the surface of the samples, hence the peak positioned at 531.0 eV could be mainly due to the oxygen in the form of hydroxide. A third small peak at a high binding energy of 532.8 eV might be due to the adsorbed

water [12, 13]. The percentage of oxygen-containing species involved in the spinel oxides is given in Table A2.1.

Table 4.1. Spectral fitting parameters of Co 2p, Cu 2p, Ni 2p and O1s for $Ni_{0.5}Cu_{0.5}Co_2O_4$ electrode

		Peak - 1	FWHM	Peak 2	FWHM	Peak 3	FWHM	Peak 4	FWHM	Peak 5	FWHM
Co 2p	CoO	779.4	2.30	781.5	2.30	784.9	2.40	785.9	5.00		
	$Co(OH)_2$	780.1	2.20	781.9	2.60	785.7	4.70	790.1	2.30		
	CoOOH	779.7	1.45	781.0	1.50	782.7	1.47	789.7	3.25		
	Co-Spinel	779.1	1.40	780.4	1.65	781.7	2.25	784.7	4.40	789.0	3.30
Cu 2p	Cu_2O	932.2	1.56								
	CuO	933.0	2.07	934.4	3.05	940.4	1.03	941.6	1.13	943.6	1.17
	$Cu(OH)_2$	934.6	2.85	939.2	2.80	942.10	3.66	944.0	1.76		
	Cu – spinel	933.4	2.91	936.5	3.00	943.0	2.26	940.3	2.27		
Ni 2p	NiO	853.5	1.01	855.2	3.00	860.6	4.00				
	$Ni(OH)_2$	854.7	1.50	855.5	0.94	860.1	1.20	861.3	1.42		
	Ni-spinel	854.2	1.40	855.7	3.10	861.1	4.41	863.8	2.90	866.7	2.60
O1s		529.1	1.21	531.0	1.82	532.8	2.60				

4.2.2. Detailed XPS analysis of $Fe_{0.1}Cu_{0.9}Co_2O_4$

The high-resolution spectra of Co 2p, Cu 2p, Fe 2p, and O1s of $Fe_{0.1}Cu_{0.9}Co_2O_4$ are shown in Figure 4.4, the peak shapes are similar to that reported in the literature [4, 5, 6, 7, 8]. From the spectrum, we can see that all the metal ions in this composition exist in different oxidation states as observed in the case of $Ni_{0.5}Cu_{0.5}Co_2O_4$. The Co 2p spectrum of $Fe_{0.1}Cu_{0.9}Co_2O_4$ is shown in Figure 4.4a. The Co $2p_{3/2}$ spinel peak was deconvoluted into five

peaks: two photoelectron peaks and three satellite peaks. The peak centered at lower binding energy of 779.4 eV was assigned to Co^{3+} and that positioned at 780.7 eV corresponds to the Co^{2+} in the spinel structure. The presence of satellite peaks indicates the presence of mixed valence states of the cobalt in the spinel structure [7, 8]. The Co^{2+} to Co^{3+} ratio is found to be 0.74 which is lower than that observed for Co_3O_4.

The high-resolution spectrum of Cu 2p of $Fe_{0.1}Cu_{0.9}Co_2O_4$ is shown in Figure 4.4b. Cu $2p_{3/2}$ spinel peak also indicates the existence of different oxidation states of copper in the spinel structure. Cu^{1+} is expected to occupy the Td site of the spinel, while Cu^{2+} occupies both the Td and Oh sites, even though Cu^{2+} preferentially occupies the Oh site. The peak deconvoluted at 932.5 eV was attributed to the Cu^{1+} ion (in Cu_2O). The peaks at 934.0 eV and 936.6 eV indicate the presence of Cu^{2+} in Oh and Td sites, respectively. The two intense satellite peaks show the existence of paramagnetic Cu^{2+} in the sample [7, 8]. Marsan *et al* reported the existence of octahedral Cu^{3+} ions located at 937.1 eV in the XPS spectra of the $CuCo_2O_4$ sample. However, they observed that the binding energy (peak position) changed with the deconvolution parameters. When the Gaussian/Lorentzian ratio changed, this peak shifted to lower binding energy, which corresponds to the tetrahedral Cu^{2+}. Thus, the possibility of having both cations - Cu^{3+} on the Oh site and Cu^{2+} in the Td site cannot be excluded [7]. In addition, Cu^{1+} could arise from the reduction of Cu^{2+} by X-ray irradiation [12]. In our study, high-resolution peaks for Cu were acquired first to minimize this artifact.

Co LMM (at 713 eV) and Ni LMM (at 712 eV) peaks have significant overlap with the Fe 2p peak when spectra were recorded with Al Kα radiation [20, 21, 22]. To exclude these overlaps, Fe-containing spinel oxide samples were analyzed using Ag Lα radiation. $Fe_yNi_{x-y}Co_{3-x}O_4$ electrodes did not show the characteristic peaks of Fe, while $Fe_yCu_{x-y}Co_{3-x}O_4$ electrodes showed Fe 2p spectrum with negligible intensity (see Figure 4.4c). This indicates that in our samples, the amount of surface Fe atoms was too low to be detected in the XPS spectra. XPS analysis of Fe $2p_{3/2}$ indicates the presence of various phases such as Fe_2O_3, Fe_3O_4 and FeOOH. Fe^{2+} and Fe^{3+} ions are detected, the peak at 709.2 eV was attributed to Fe^{2+} and the peak at 710.2 was assigned to Fe^{3+} ions in the spinel structure with four satellite peaks at higher binding energy, 711.2 eV, 712.3 eV, 713.4 eV and 714.5 eV [4, 15, 23]. Due to the negligible peak intensity, the error associated with the analysis could be very large. Lu *et al* reported the co-existence of the Fe^{2+} and Fe^{3+} in a $Fe_{0.1}Ni_{0.9}Co_2O_4$ spinel [15].

Kouotou *et al* have performed XPS analysis on cobalt ferrite spinel oxides ($Co_{2.1}Fe_{0.9}O_4$) and observed that Fe is mainly in a 3+ oxidation state. They observed a peak at 710.6 eV and 723.3 eV with a small satellite structure at 734 eV [24]. Whereas Kashyap *et al* found that Fe exists as Fe^{2+} and Fe^{3+} oxidation states in cobalt ferrites, they obtained a Fe^{2+}/Fe^{3+} ratio of 1.68 and 1.11 for $CoFe_2O_4$ and Co_2FeO_4 respectively [25]. Zou *et al* prepared $CoFe_2O_4$ spinel oxide powder and observed that Fe is in a 3+ oxidation state, where the peak at 710.65 eV and 724.23 eV was attributed to the presence of Fe^{3+} in the octahedral site, while the peak positioned at 713.26 eV and 725.36 eV was assigned to the Fe^{3+} in a tetrahedral site of spinel oxide. They also found that Fe^{3+} is mainly in octahedral sites (70%) [26]. Depending on the composition, the oxidation state and the site occupancy of cations are different. However, based on XPS spectra, it is difficult to assign the site occupancy of Fe^{2+} or Fe^{3+} ions.

XPS line shapes and binding energy positions of the O 1s spectrum of all Fe-containing samples are similar. The O1s spectrum of $Fe_{0.1}Cu_{0.9}Co_2O_4$ is shown in Figure 4.2d. The analysis of the O 1s spectrum indicates that the main peak is composed of three peaks. The first peak was located at 529.7 eV. This peak was attributed to the lattice oxygen. The second peak, located at 531.3 eV in the O 1s spectra was attributed to the adsorbed oxygen-containing species such as hydroxides or defective sites in the oxide crystal. Our XPS analysis indicates the formation of a significant amount of metal hydroxides on the surface of the electrodes. The third peak located at 533.3 eV was assigned to the surface bonded water molecule, present in very small amounts [6, 7].

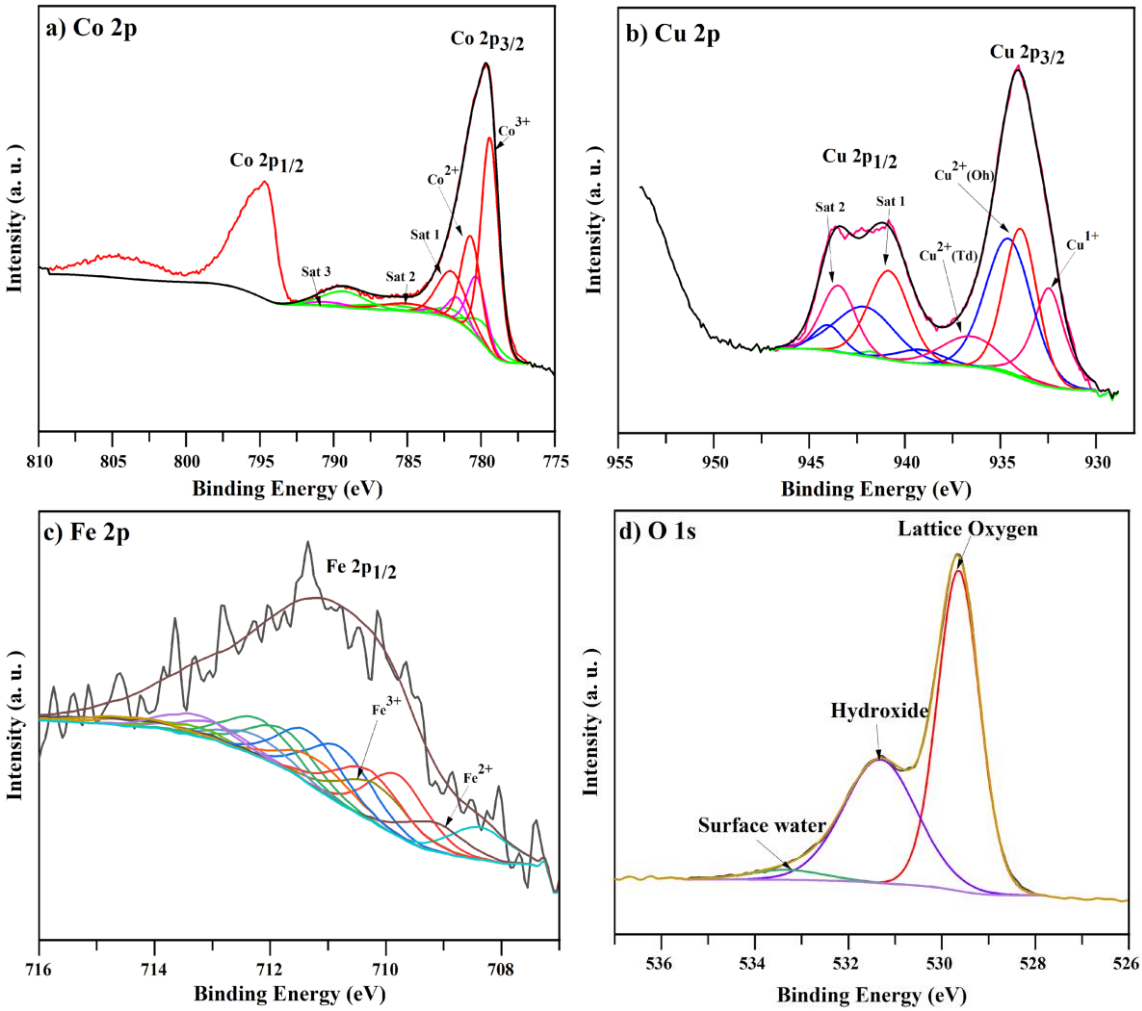

Figure 4.4. XPS core level spectra of a) Co2$p_{3/2}$, b) Cu 2$p_{3/2}$ c) Fe 2$p_{3/2}$ d) O 1s of $Fe_{0.1}Cu_{0.9}Co_2O_4$

4.2.3. Summary of XPS analysis results for binary and ternary co-based spinel oxides

Even though XRD analysis confirmed the formation of spinel oxide in our samples, different metal oxide species have been detected in XPS analysis. The high-resolution spectra of the Co 2$p_{3/2}$ peak indicate the presence of CoO, $Co(OH)_2$ and CoOOH phases along with cobalt in the spinel structure. The percentage of metals incorporated in each species calculated from high-resolution spectra is given in Table 4.2. Cobalt in spinel oxide is found to be the major phase for all samples and ranges from 60 – 73.6%, while 6.0 – 20.3% CoO is formed on the

surface of these electrodes. CoOOH and $Co(OH)_2$ species have been formed up to 18.2% and 18.9% respectively for different samples.

The XPS analysis of the Cu $2p_{3/2}$ peak indicates that copper is mainly incorporated in the spinel phase, while other phases such as CuO and $Cu(OH)_2$ were also detected. The deconvoluted spectra of the Ni $2p_{3/2}$ peak reveal that 33.3% - 58.8% of the peak area constitutes NiO in different samples. Ni is also incorporated in spinel and $Ni(OH)_2$ species. The studies indicate that Ni ions tend to migrate within the crystal structures and Ni^{3+} ions reduce to Ni^{2+} creating the NiO phase during the high-temperature treatment, which decreases the reversibility and affects the catalytic properties of the electrode [10]. It is observed that a significant amount of metal hydroxides has been formed on the surface of all the samples.

Table 4.2. The percentage of different species formed on the surface of electrodes evaluated from the high-resolution spectrum of $Cu_xCo_{3-x}O_4$ (x = 0, 1), $Ni_xCu_{1-x}Co_2O_4$ ($0 \leq x \leq 0.75$), $Fe_yCu/Ni_{x-y}Co_{3-x}O_4$ (x = 0.5, 1 and y = 0.1, 0.15

Peak	**Phase**	**Percentage**	**Peak**	**Phase**	**Percentage**
Co 2p	Co-Spinel	60.0 – 73.6	**Ni 2p**	Ni spinel	22.8 – 46.9
	CoOOH	2.4 – 18.2		NiO	33.3 – 58.8
	$Co(OH)_2$	0.3 – 18.9		$Ni(OH)_2$	3.1 – 26.9
	CoO	6.0 – 20.3	**O1s**	lattice oxide	44.0 – 62.8
Cu 2p	Cu - spinel	61.6-70.6		Hydroxide	32.4 – 53.1
	Cu_2O	8.5 – 19.1		Surface water	1.0 – 6.3
	CuO	4.5 – 6.8			
	$Cu(OH)_2$	7.7 – 39.1			

The overall composition of the samples obtained from XPS analysis is consistent with the stochiometric compositions employed during the sample preparation (see Table 4.3). According to the XPS analysis, most of the samples are deficient in cobalt except $Ni_{0.75}Cu_{0.25}Co_2O_4$, $Fe_{0.1}Ni_{0.9}Co_2O_4$, and $Fe_{0.15}Ni_{0.35}Co_{2.5}O_4$. Meanwhile, copper is in excess in all samples. A surface enrichment in copper has been reported previously for copper-containing spinel oxides [9]. The amount of Fe was negligible on the surface of the sample for all Fe-containing samples.

Table 4.3. The XPS composition of spinel oxide electrodes.

#	Sample	XPS Composition
1	$NiCo_2O_4$	$Ni_{1.95}Co_{1.05}O_4$
2	$Ni_{0.9}Cu_{0.1}Co_2O_4$	$Ni_{0.90}Cu_{0.24}Co_{1.83}O_4$
3	$Ni_{0.75}Cu_{0.25}Co_2O_4$	$Ni_{0.48}Cu_{0.30}Co_{2.22}O_4$
4	$Ni_{0.5}Cu_{0.5}Co_{2.24}O_4$	$Ni_{0.96}Cu_{0.72}Co_{1.33}O_4$
5	$Ni_{0.25}Cu_{0.75}Co_2O_4$	$Ni_{0.30}Cu_{0.90}Co_{1.77}O_4$
6	$CuCo_2O_4$	$Cu_{1.47}Co_{1.52}O_4$
7	$Fe_{0.1}Cu_{0.9}Co_2O_4$	$Fe_xCu_{1.08}Co_{1.92}O_4$
8	$Fe_{0.15}Cu_{0.35}Co_{2.5}O_4$	$Fe_xCu_{0.69}Co_{2.30}O_4$
9	$Fe_{0.1}Ni_{0.9}Co_2O_4$	$Fe_xNi_{0.63}Co_{2.37}O_4$

Photoelectron peaks were used for the quantification of cations. The assignment of satellite peaks is difficult as the separation of different oxidation states of metal ions is difficult. Therefore, a significant error may be associated with the quantification of cations. In the normal spinel structure, Co^{2+} occupies the tetrahedral site (Td) and Co^{3+} occupies the octahedral site (Oh) of the spinel, and possesses a Co^{2+} to Co^{3+} ratio of 0.5 for stoichiometric composition [27]. However, in our study, all spinel oxides possess a higher Co^{2+} to Co^{3+} ratio than the stoichiometric ratio. The cation ratios of elements of different oxidation states present in the spinel structure are given in Table 4.4. We have observed a Co^{2+} to Co^{3+} ratio of 0.92 for pure

cobalt oxide which possessed the highest Co^{2+} to Co^{3+} ratio compared to all other compositions. This high Co^{2+} to Co^{3+} ratio indicates that the Co^{2+} is also occupying the Oh site providing mixed-valence oxidation states of cobalt in the spinel structure. The studies indicate that the mixed-valence state of cations in the octahedral position promotes electron transfer between them with relatively low activation energy and enhances the conductivity of the materials; hence the catalytic activity increases [9, 28]. When cobalt is replaced by Ni, Cu, and Fe, the Co^{2+} to Co^{3+} ratio is significantly decreased. $NiCo_2O_4$ has a Co^{2+} to Co^{3+} ratio of 0.84 and this ratio further decreased as the copper content increased in the sample (see Table 4.4). The same trend was reported earlier by Marsan *et al*., they observed a decrease in Co^{2+} to Co^{3+} ratio when copper is added to the cobalt spinel lattice [7].

As the amount of Cu in the sample increases, the Cu^{1+} (Td)/Cu^{2+}(Oh) ratio increases (for the sample $CuCo_2O_4$, this ratio decreases), and the Cu^{2+} (Td)/Cu^{2+} (Oh) ratio decreases (for $Ni_{0.25}Cu_{0.75}Co_2O_4$ the ratio slightly increases). However, the percentage of copper in the octahedral and tetrahedral sites remains approximately the same for all of the samples, irrespective of the amount of copper added to the cobalt spinel.

Table 4.4: The cation ratio of elements in spinel oxides from high-resolution spectra

#	Sample	Co^{2+}/Co^{3+} ± 0.049	Ni^{2+}/Ni^{3+} ± 0.069	Cu^{1+}/Cu^{2+} ± 0.056	Cu^{2+}(Td)/Cu^{2+}(Oh) ± 0.019
1	$NiCo_2O_4$	0.837	0.465		
2	$Ni_{0.9}Cu_{0.1}Co_2O_4$	0.730	0.581	0.293	0.432
3	$Ni_{0.75}Cu_{0.25}Co_2O_4$	0.660	0.539	0.483	0.215
4	$Ni_{0.5}Cu_{0.5}Co_2O_4$	0.587	0.477	0.542	0.178
5	$Ni_{0.25}Cu_{0.75}Co_2O_4$	0.537	0.616	0.719	0.186
6	Co_3O_4	0.924			
7	$CuCo_2O_4$	0.546		0.665	0.120
9	$Fe_{0.1}Cu_{0.9}Co_2O_4$	0.74		0.68	0.35
10	$Fe_{0.15}Cu_{0.35}Co_{2.5}O_4$	0.68		0.40	0.34

11	$Fe_{0.1}Ni_{0.9}Co_2O_4$	0.56	0.71		
12	$Fe_{0.15}Ni_{0.35}Co_{2.5}O_4$	0.58	0.50		

A shift in the binding energy of an element is indicative of a change in the chemical state of the element in the sample. XPS analysis shows that the Co 2p peak of pure Co_3O_4 and Fe substituted spinel oxides exhibit higher binding energy than Cu and Ni substituted spinel oxides. This higher binding energy indicates that the cobalt ions (Co^{2+} and Co^{3+}) in pure cobalt oxide spinel or Fe-substituted spinel oxides are more oxidized than the Cu or/and Ni substituted spinel oxides. The binding energy of cations in the spinel structure is given in Appendix Table A2. 2.

4.3. XPS analysis of amorphous metal oxides

The curve fitting procedure used for the analysis of amorphous metal oxide is given in Chapter 2, section 2.2.3. For both amorphous and spinel oxides, a similar spectral curve fitting procedure is used. Both survey spectra and high-resolution spectra were collected for CoO_x, $CuCo_2O_x$, $Ni_{0.5}Cu_{0.5}Co_2O_x$, $Fe_{0.1}Cu_{0.9}Co_2O_x$, and $Fe_{0.1}Ni_{0.9}Co_2O_x$. The survey spectra of all samples indicate that the surface of the electrodes is free of contaminants except for a small amount of carbon. This carbon peak was used for the calibration of spectra of all samples. For the data fitting, the binding energy positions and FWHM values were constrained using the parameters of standard samples as in the case of spinel oxides [4, 5]. The metal 2p photoelectron peaks have been split into $2p_{1/2}$ and $2p_{3/2}$ as we observed in the case of corresponding crystalline materials. The $2p_{3/2}$ peak is more intense than the $2p_{1/2}$ peak, therefore, the $2p_{3/2}$ peak was used for the quantification and analysis. The core-level spectra of Co $2p_{3/2}$, Cu $2p_{3/2}$, Ni $2p_{3/2}$, and O 1s were chosen for the analysis. Since the Al Kα X-ray source (1486.6 eV) was used for the analysis Fe 2p peak overlapped with Co and Ni LMM peaks. The peak shape of Cu 2p, Ni 2p, Co 2p, and O 1s appear similar to that of crystalline materials.

The analysis of high-resolution spectra of amorphous samples indicates that different species such as metal oxides, hydroxides, and oxyhydroxides exist on the surface of the electrodes for all compositions. Each species possesses characteristic photoelectron peaks and satellite peaks, both these peaks were used for the quantification of species.

Several XPS studies mentioned the existence of hydroxides or oxyhydroxides on the surface of metal oxides [29, 30, 31]. D. L. Smith *et al* performed XPS analysis on the ternary mixture of amorphous $Fe_{40}Co_{40}Ni_{20}O_x$ and found that Fe sites exist as FeOOH, Ni as $Ni(OH)_2$, and cobalt as Co_3O_4 and $Co(OH)_2$ [29]. Berlinguette *et al* also found higher surface hydroxylation of the surface metal atoms, this trend is consistent with the XPS analysis of the first-row transition metals [30]. Kim *et al* carried out the XPS analysis on amorphous oxyhydroxide films and found that after oxygen evolution, the metal hydroxides significantly converted to metal oxyhydroxides [31].

4.3.1. Detailed XPS analysis of $Ni_{0.5}Cu_{0.5}Co_2O_x$

The high-resolution spectrum of Co 2p, Cu 2p, Ni 2p, and O1s of $Ni_{0.5}Cu_{0.5}Co_2O_x$ is shown in Figure 4.5. XPS analysis of amorphous metal oxide showed approximately similar surface structural features as that of spinel oxides. The surface contains atoms of different binding energies that can be assigned to metal oxides, hydroxides, and oxyhydroxides. The convoluted peaks of Co 2p peak indicate that species such as CoOOH, Co_3O_4, and $Co(OH)_2$ coexist on the surface of these electrodes. In spinel oxides, we observed small amounts of CoO as well. Among the deconvoluted peaks of Co 2p, the peak corresponds to the lower binding energy belonging to spinel oxide species [4, 7].

Each species possesses photoelectron peaks and satellite peaks. Peak positions and FWHM values of various species found in $Ni_{0.5}Cu_{0.5}Co_2O_x$ are given in Table 4.5. The peaks at 779.1 and 781.3 eV indicate the presence of Co^{3+} and Co^{2+} respectively in the spinel structure, and possess three satellite peaks at 781.7 eV, 784.7 eV, and 789.0 eV. Several studies have reported similar deconvoluted peaks for spinel oxides [4, 7, 8].

N. S. McIntyre *et al* have performed XPS studies on oxides and hydroxides of Ni, Co, and Cu. They observed very weak and low-intensity peaks for CoOOH, while intense satellite peaks were observed for CoO and $Co(OH)_2$ [11]. In our study, the peak positions observed for $Co(OH)_2$ are shifted to higher binding energy, where peaks at 780.2 and 782.0 eV were assigned to the photoelectron peaks of $Co(OH)_2$, and their satellite peaks were observed at 785.8 and 790.2 eV. These intense satellite peaks are due to the presence of paramagnetic Co^{2+} in $Co(OH)_2$. Gao *et al* also observed a redshift for $Co(OH)_2$ compared to Co_3O_4 indicating an increased oxidation state of Co. They observed more symmetric spectra for $Co(OH)_2$ compared to Co_3O_4, this was assigned to the single oxidation state of cobalt in $Co(OH)_2$. Meanwhile, two

nonsymmetric peaks accompanied by weak satellite peaks were assigned to the coexistence of Co^{2+} and Co^{3+} in the spinel structure. The curve-fitted peaks at 780.0 and 795.1 eV were assigned to Co^{3+}, and the peaks at 781.5 and 797.0 eV were assigned to Co^{2+} [34].

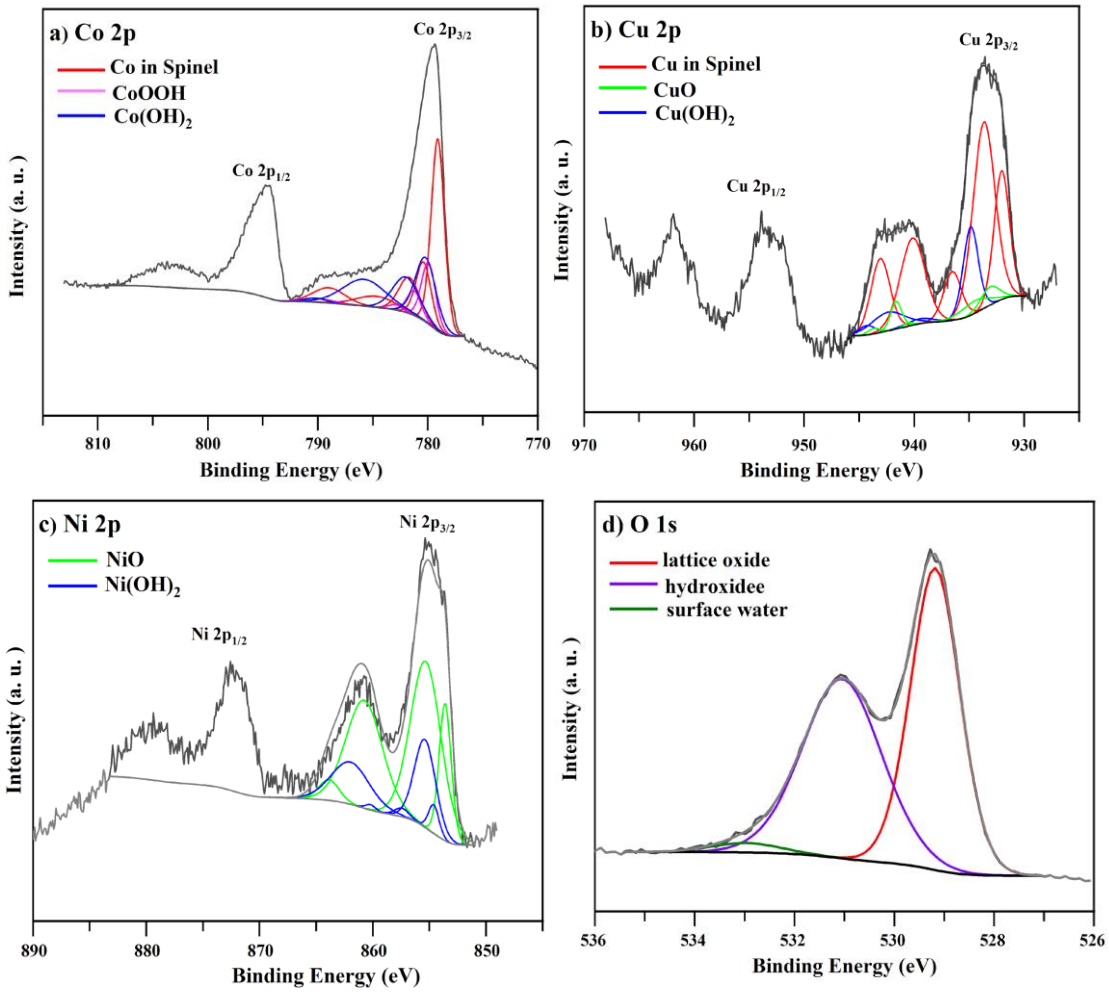

Figure 4. 5. XPS core-level spectra of a) $Co2p_{3/2}$, b) Cu $2p_{3/2}$ c) Ni $2p_{3/2}$ d) O 1s of $Ni_{0.5}Cu_{0.5}Co_2O_x$.

The core-level spectra of Ni and Cu (Figure 4.5b and Figure 4.5c respectively) also indicate that these metal ions are incorporated into different species on the surface of the $Ni_{0.5}Cu_{0.5}Co_2O_x$ electrode. A significant amount of Cu is incorporated into the spinel structure and hydroxide. A small amount of CuO is also detected on the surface. Cu 2p of spinel oxides also possesses similar features in their convoluted spectra. Cu $2p_{3/2}$ of $Ni_{0.5}Cu_{0.5}Co_2O_x$ has a deconvoluted peak at 932.0 eV which was assigned to Cu^{1+} in the tetrahedral coordination of spinel structure.

Biesinger *et al* assigned the peak at 932.18 eV for Cu (I) oxide [5]. Tavares *et al* and Marsan *et al* assigned the peak observed at 932.4 eV and 931.9 eV respectively for the Cu(I) in the tetrahedral position of the spinel structure [7, 9]. The peak that we observed at the 933. 7 eV was assigned to the paramagnetic Cu(II) at the octahedral site of the spinel structure and has two well-defined satellite peaks at 940.1 eV and 943.1 eV.

Many authors use the presence of these well-defined satellite peaks to confirm the presence of Cu^{2+} in the sample [33, 34]. A small amount of CuO phase was observed for all the amorphous samples with two photoelectron peaks and three shake-up peaks. The binding energy of Cu^{2+} of spinel and CuO phase has a small difference. The two photoelectron peaks observed at the high binding energy side, i.e. 934.9 eV and 939.5 eV were assigned to Cu^{2+} of $Co(OH)_2$ and have two corresponding satellite peaks at 942.4 and 944.3 eV. Cu^{1+} or Cu_2O does not possess satellite peaks.

Ni in $Ni_{0.5}Cu_{0.5}Co_2O_x$ is mainly incorporated into NiO and $Ni(OH)_2$ species. The corresponding crystalline sample possessed additional peaks of spinel oxide. The deconvoluted peaks of NiO are present at lower binding energy compared to $Ni(OH)_2$. Both NiO and $Ni(OH)_2$ possess two photoelectron peaks and two satellite peaks. A strong and broad satellite band above the photoelectron peaks is indicative of paramagnetic Ni^{2+} in the composition. N. S. McIntyre *et al* have studied the surface chemistry of NiO and $Ni(OH)_2$ using XPS and found them to have approximately similar peak positions for both these phases. They have observed a strong satellite band for NiO and $Ni(OH)_2$ above the principle line (photoelectron peak). According to their study, these bands are due to the presence of paramagnetic Ni ions [11].

Thus, both amorphous and spinel oxides indicate the presence of various chemical species on the surface of the electrode. However, the X-ray diffraction analysis does not indicate the existence of these phases. This indicates that the bulk structure is different from the surface for both spinel oxides and amorphous samples.

The high-resolution spectrum of O1s of $Ni_{0.5}Cu_{0.5}Co_2O_x$ is shown in Figure 4.5d. The peak is composed of mainly three component peaks. The peak at lower binding energy (529.2 eV) corresponds to lattice oxide, and the peak at 531.1 eV is associated with hydroxide or defective oxygen. As the metal ions are incorporated into a significant amount of hydroxide, this peak was assigned to hydroxide as in the case of spinel oxide. The small peak present at higher binding energy (533.0 eV) was attributed to adsorbed surface water [7, 8]. O 1s of

$Fe_{0.9}Cu_{0.9}Co_2O_x$ also contains three deconvoluted peaks, while other amorphous samples (CoO_x, $CuCo_2O_x$ and $Fe_{0.1}Cu_{0.9}Co_2O_x$) possess only two component peaks, the peak corresponds to lattice oxide and hydroxide. Surface water was not detected in these samples.

Table 4.5. Spectral fitting parameters of Co 2p, Cu 2p, Ni 2p and O1s for $Ni_{0.5}Cu_{0.5}Co_2O_x$ electrode

		Peak 1 (eV)	FWHM (eV)	Peak 2 (eV)	FWHM (eV)	Peak 3 (eV)	FWHM (eV)	Peak 4 (eV)	FWHM (eV)	Peak 5 (eV)	FWHM (eV)
Co 2p	$Co(OH)_2$	780.2	2.20	782.0	2.80	785.8	4.60	790.2	2.22		
	CoOOH	779.9	1.50	781.3	1.50	783.0	1.49	790.0	3.50		
	Co-Spinel	779.1	1.41	780.4	1.62	781.7	2.21	784.7	4.20	789.0	3.40
Cu 2p	Cu_2O	932.0	1.66								
	CuO	933.1	2.00	934.5	3.10	940.5	1.00	941.6	1.20	943.7	1.30
	$Cu(OH)_2$	934.9	1.61	939.5	2.90	942.4	3.60	944.3	1.75		
	Cu – spinel	933.7	2.35	936.5	1.90	940.1	2.65	943.1	2.04		
Ni 2p	NiO	853.6	1.26	855.3	3.20	860.8	3.80	863.9	2.10		
	$Ni(OH)_2$	854.6	1.10	855.4	2.20	860.21	1.10	862.0	4.00		
O1s		529.2	1.16	531.1	1.86	533.0	1.60				

The binding energy of metal ions obtained from the XPS analysis of amorphous materials is given in Table A2.5. From this Table, we can see that the incorporation of other metal ions such as Cu, Ni, and Fe did not influence the binding energy or the chemical state of Co^{2+} or Co^{3+} in amorphous samples. Meanwhile, the composition or the presence of other metal ions affected the binding energy of cobalt ions in spinel oxides.

4.3.2 Summary of XPS analysis of amorphous metal oxides

The surface composition of the samples was evaluated using high-resolution spectra of metal ions. The surface composition of all amorphous samples is given in Table 4.6. A fairly

good correlation exists between the stoichiometric and XPS composition of amorphous oxides. The XPS composition of amorphous samples indicates that cobalt is found in excess compared to the stoichiometric composition, while spinel oxides possessed a deficiency of cobalt on the surface of the electrode. We found an enrichment of copper on the surface of spinel oxides, while amorphous metal oxides possess either a deficiency or a similar composition as that of stoichiometric composition, Ni has a close agreement with the stoichiometric composition. Different preparation methods might have affected the surface compositions.

Table 4.6. The XPS composition of amorphous metal oxides

Stoichiometric composition	XPS composition (amorphous)
$CuCo_2O_x$	$Cu_{0.64}Co_{2.36}O_x$
$Ni_{0.5}Cu_{0.5}Co_2O_x$	$Ni_{0.58}Cu_{0.5}Co_{1.91}O_x$
$Fe_{0.1}Cu_{0.9}Co_2O_x$	$Fe_xCu_{0.82}Co_{2.18}O_x$
$Fe_{0.1}Ni_{0.9}Co_2O_x$	$Fe_xNi_{0.77}Co_{2.23}O_x$

The amorphous sample's surface contains different species as in the case of crystalline materials/spinel oxides. The amount of cobalt incorporated in the spinel phase ranges from 39.9% to 70.8% while CoOOH and $Co(OH)_2$ formed up to 31.2 and 34.9% respectively in different amorphous samples (see Table A2. 3). The percentage of different species formed on the surface of $Ni_{0.5}Cu_{0.5}Co_2O_x$ and its analogous crystalline counterpart is given in Table 4.7. From Table 4.7, we can see that a significant amount of metal hydroxides have been formed on the surface of $Ni_{0.5}Cu_{0.5}Co_2O_x$. This is also evident from the O 1s peak of all compositions, where a large amount of oxygen has been incorporated into hydroxide species (see Table A2.4). The percentage of each component of the O 1s peak of all the compositions is given in Table A2. 5. The XPS line shape of the O 1s peak is not significantly changed with sample composition, spinel oxides also displayed a similar peak shape.

Table 4.7. The percentage of various species present at the surface of $Ni_{0.5}Cu_{0.5}Co_2O_x$

Peak	Phase	Amorphous (%)	Spinel (%)	Peak	Phase	Amorphous (%)	Spinel (%)
Co 2p	Co-Spinel	50.8	69.6	Ni 2p	Ni-spinel		46.9
	CoOOH	14.3	3.2				
	$Co(OH)_2$	34.9	11.1		$Ni(OH)_2$	16.3	3.9
	CoO		16.0		NiO	83.7	49.1
Cu 2p	Cu - spinel	75.8	67.2	O 1s	Metal oxide	50.2	57.2
					Hydroxide	47.7	37.9
	$Cu(OH)_2$	16.2	28.3		Surface water	2.1	4.9
	CuO	8.0	4.5				

The cation ratios evaluated from the spinel species of amorphous samples are given in Table 4.8. For CoO_x, Co^{2+} to Co^{3+} ratio is found to be 1.31; cobalt is mainly in the 2+ oxidation state. Meanwhile, other samples possessed a lower Co^{2+} to Co^{3+} ratio, where enrichment of Co^{3+} on the surface is observed. Substitution of other metal cations decreased Co^{2+} to Co^{3+} ratio. In the case of spinel oxides, all the samples possess a higher Co^{2+} to Co^{3+} ratio compared to their stoichiometric ratio (0.5), pure cobalt spinel oxide showed the highest ratio of 0.92. Cobalt is also incorporated in the $Co(OH)_2$ and CoOOH species with Co^{2+} and Co^{3+} oxidation states respectively.

Copper is mainly in 2+ oxidation state for both amorphous and spinel oxides. Since the satellite peaks are due to the presence of Cu^{2+}, for calculating the Cu^{1+} to Cu^{2+} ratio, the satellite peaks were also considered; According to the various studies, the Cu_2O does not possess satellite peaks above the photoelectron peaks [27]. While, in the case of cobalt, both Co^{3+} and Co^{2+} possess satellite peaks, even though Co^{3+} has weak satellite peaks. The contribution of peak intensity from each valence state cannot be identified from the satellite peaks. Hence, only

photoelectron peaks are considered for the calculation of the Co^{2+} to Co^{3+} ratio. This might lead to some errors in Co^{2+} to Co^{3+} ratio. Ni is not found to be incorporated into the spinel structure. Ni^{3+} was not detected in this study.

Table 4.8. The cation ratio of amorphous samples and corresponding spinel oxides.

Amorphous samples				Spinel oxides	
#	Sample	Co^{2+}/ Co^{3+}	Cu^{+}/ Cu^{2+}	Co^{2+}/ Co^{3+}	Cu^{+}/ Cu^{2+}
1	Co_3O_4	1.31	-	0.92	
2	$CuCo_2O_4$	0.38	0.18	0.55	0.22
3	$Ni_{0.5}Cu_{0.5}Co_2O_4$	0.36	0.17	0.59	0.17
4	$Fe_{0.1}Cu_{0.9}Co_2O_4$	0.46	0.30	0.74	0.15
5	$Ni_{0.9}Fe_{0.1}Co_2O_4$	0.61	-	0.56	

4.4. Comparison between XPS of analysis of crystalline and amorphous

The surface of both amorphous and crystalline materials that we have analyzed in this work contains metal atoms of different binding energies which can be assigned to different species such as metal oxides, hydroxides, and oxyhydroxides. Cobalt exists as CoOOH, Co_3O_4, and $Co(OH)_2$ on the surface of all these electrodes except for $Fe_{0.1}Cu_{0.9}Co_2O_4$, where $Co(OH)_2$ species was not detected. In spinel oxides, we observed an additional peak for CoO. In amorphous materials ($Ni_{0.5}Cu_{0.5}Co_2O_x$ and $Fe_{0.1}Ni_{0.9}Co_2O_x$), Ni is mainly incorporated into NiO and $Ni(OH)_2$ at the surface. In crystalline materials ($Ni_xCu_{1-x}Co_2O_4$ ($0 \leq x \leq 0.75$), $Fe_yNi_{x-y}Co_{3-x}O_4$ (x=0.5, 1 and y= 0.1, 0.15)), Ni is also incorporated into spinel oxides along with NiO and $Ni(OH)_2$ species. A higher amount of hydroxides or oxyhydroxides have been formed on the

surface of amorphous materials compared to spinel oxides. In spinel oxides, a significant fraction of Cu and Co have been incorporated into spinel oxide species, while Ni is mainly incorporated in NiO in Ni-containing spinel oxides. Both amorphous and spinel oxides possess similar surface species, but their abundance differs.

Another marked difference observed between these materials is their Co^{2+} to Co^{3+} ratio, all spinel oxides showed a higher Co^{2+} to Co^{3+} ratio than the stoichiometric ratio (0.5), while for amorphous materials, only CoO_x shows a higher ratio (Co^{2+}/Co^{3+} = 1.31). For other amorphous samples, this ratio is lower than 0.5, which indicates that cobalt is mainly in 3+ oxidation state. In these cases, it is possible that Co^{3+} is occupying a Td-type site.

In our study we observed a noticeable change in the electron binding energy of cobalt ions (Co^{2+} and Co^{3+}) in spinel oxide compositions, Cu and Ni substitution decreased the oxidation state of cobalt ions, while, Fe substitution increased the oxidation state of cobalt ions. Such variation in the binding energy of cobalt with the composition was not observed in the case of amorphous metal oxides. Such an extensive study of spinel and amorphous transition metal oxides using XPS has not been reported before. Other studies have indicated that a high Co^{2+}/Co^{3+} ratio as an indicator of improved electrocatalytic activity [15]. However, for our spinel oxides, the best catalysts do not always have the highest Co^{2+} to Co^{3+} ratio [35, 36].

Both amorphous and spinel oxides possess different surface species even though the bulk remains mainly a single phase (amorphous or spinel respectively) as reported by X-ray diffraction analysis. It is possible that the surface can have a significant effect on the catalytic properties of these samples. However, the contribution of the bulk cannot be ruled out. In chapters 5 and 6, the electrocatalytic activity of the samples and the correlations between various parameters observed in this study will be discussed. That would provide more insight into the composition, structure (surface and bulk), and activity interdependence of our samples.

4.5. References

[1] A. J. Bard, L. R. Faulkner, Eletrochemical methods-Fundamentals and applications, 2nd ed.; New York,2001.

[2] J. F. Marco, J. R. Gancedo, and M. Gracia, J. L. Gautier, E. Rios, F. J. Berry, Characterization of the Nickel Cobaltite, $NiCo_2O_4$, Prepared by Several Methods: An XRD, XANES, EXAFS, and XPS Study J. Solid State Chem. 153 (2000) 74.

[3] Leng, Y. Materials characterization: Introduction to microscopic and spectroscopic methods; John Wiley & Sons: Asia, 2008.

[4] M.C. Biesinger, B.P. Payne, A.P. Grosvenor, L.W.M. Lau, A.R. Gerson, R. St.C. Smart, "Resolving surface chemical states in XPS analysis of first row transition metals, oxides and hydroxides: Cr, Mn, Fe, Co and Ni", J. Appl. Surf. Sci. 257 (2011) 2717.

[5] M.C. Biesinger, L.W.M. Lau, A.R. Gerson, R. St.C. Smart, Resolving surface chemical states in XPS analysis of first row transition metals, oxides and hydroxides: Sc, Ti, V, Cu and Zn", J. Appl. Surf. Sci. 257 (2010) 887.

[6] M.C. Biesinger, B.P. Payne, L.W.M. Lau, A. R. Gerson, R. St.C. Smart, "X-ray photoelectron spectroscopic chemical state quantification of mixed nickel metal, oxide and hydroxide systems", Surf. Interface Anal. 41 (2009), 324

[7] M.D. Koninck, S.C. Poirier, B. Marsan, "$Cu_xCo_{3-x}O_4$ used as bifunctional electrocatalyst: Physiochemical properties and electrochemical characterization for the oxygen evolution reaction", J. Electrochem. Soc. 153 (2006) 1, A2103.

[8] A.C. Tavares, M.A.M. Cartaxo, M.I. da Silva Pereira, F. M. Costa, "Effect of the partial replacement of Ni or Co by Cu on the electrocatalytic activity of the $NiCo_2O_4$ spinel oxide", J. Electroanal. Chem. 464 (1999) 187.

[9] A. C. Tavares, M. A. M. Cartaxo, D. S. Pereira, F. M. Costa., Electrochemical study of spinel oxide systems with nominal compositions $Ni_{1-x}Cu_xCo_2O_4$ and $NiCo_{2-y}Cu_yO_4$, J solid state electro. Chem 5 (2001) 57.

[10] H. Osgood, S. V. Devaguptapu, H. Xu, J. Cho, G. Wu, Transition metal (Fe, Co, Ni and Mn) oxides for oxygen reduction and evolution bifunctional catalysts in alkaline media, Nano Today 11 (2016) 601.

[11] N. S. McIntyre and M. G. Cook, X-ray phototelectron studies on some oxides and hydroxides of cobalt, nickel and copper, J. Analytical Chemistry, 47, 13 (1975) 2208

[12] A. Karmakar, S. K. Srivastava, Interconnected copper cobaltite nanochains as efficient electrocatalysts for water oxidation in alkaline medium, ACS Appl. Mater. Interfaces, 9 (2017) 22378
[13] L. Xu, Q. Jiang, Z. Xiao, X. Li, J. Huo, S. Wang, L. Dai, Plasma-engraved Co_3O_4 nanosheets with oxygen vacancies and high surface area for the oxygen evolution reaction, Angew. Chem. Int. Ed. 55 (2016) 5277.
[14] A. Amri, A. Fadli, Z. T. Jiang, C. Y. Yin, M. M. Rahman, H. Widjaja, S. Herman, S. R. Yenti, M. M. Munir, G. Priyotomo, M. Iqbal, N. Frimayanti, Surface structural and solar absorptance features of nitrate-based copper cobalt oxides composite coatings: Experimental studies and molecular dynamic simulation, Ceram. Int. 44 (2018)15274.
[15] Y. T. Lu, Y. J. Chien, C. F. Liu, T. H. You and C. C. Hu, Active site-engineered bifunctional electrocatalysts of ternary spinel oxides, $M_{0.1}Ni_{0.9}Co_2O_4$ (M: Mn, Fe, Cu, Zn) for the Air Electrode of Rechargeable Zinc-Air Batteries, J. Mater. Chem. A, 5 (2017) 21016
[16] Y. Zhang, X. Zhou, F. Zhang, T. Tian, Y. Ding, H. Gao, Design and synthesis of Cu modified cobalt oxides with hollow polyhedral nanocages as efficient electrocatalytic and photocatalytic water oxidation catalyst, J. Catal., 352 (2017) 246
[17] A. Amri, X. Duan, C. Y. Yin, Z. T. Jiang, M. M. Rahman, T. Pryor, Solar absorptance of copper–cobalt oxide thin film coatings with nano-size, grain-like morphology: Optimization and synchrotron radiation XPS studies J. Appl. Surf. Sci. 275 (2013) 127.
[18] K. L Yan, X. Shang, Z. Li, B. Dong, X. Li, W. K. Gao, J. Q. Chi, Y. M. Chai, C. G. Liu, Ternary mixed metal Fe-doped $NiCo_2O_4$ nanowires as efficient electrocatalysts for oxygen evolution reaction, J. Appl. Surf. Sci. 416 (2017) 371.
[19] J. Xiao, L. Zhang, J. Peng, H. Xue, H. Yuan, L. Chen, C. Xiong, Fabrication and characterization of spinel $Ni_{0.5}Cu_{0.5}Co_2O_4$ nanoparticles as bi-functional catalysts for oxygen reduction and evolution reaction Int. J. Mod. Phys. B 33 (2019) 1940060 (1-6)
[20] R. R. Waltrovitz, G. Qian, F. Groot, J. S. Quinton, S. L. Harmer, Influence of Co:Fe:Ni ratio on cobalt Pentlandite's electronic structure and surface speciation, Miner. Eng. 190 (2022) 107935
[21] K. Elumeeva, M. A. Kazakova, D. M. Morales, D. Medina, A. Selyutin, G. Golubtsov, Y. Ivanov, V. Kuznetzov, A. Chuvilin, H. Antoni, M. Muhler, W. Schuhmann, J. Masa, (2018). Bifunctional oxygen reduction/oxygen evolution activity of mixed Fe/Co Oxide nanoparticles

with variable Fe/Co ratios supported on multiwalled carbon nanotubes. ChemSusChem, 11, 7 (2018) 1204.
[22] J. F. Moulder, W. F. Stickle, P. E. Sobol, K. D. Bomben, J. Chastain, (n.d.). Handbook of X-ray photoelectron spectroscopy A reference book of standard spectra for identification and interpretation of XPS data (1992).
[23] S. G. Mohamed, Y. Q. Tsai, C. J. Chen, Y. T. Tsai, T. F. Hung, W. S. Chang, R. S. Liu, Ternary Spinel MCo_2O_4 (M = Mn, Fe, Ni, and Zn) Porous nanorods as bifunctional cathode materials for lithium−O_2 batteries, ACS Appl. Mater. Interfaces 7 (2015) 12038.
[24] P. M. Kouotou, , H. Vieker, Z. Y. Tian, P. H. T. Ngamou, , A. El Kasmi, A. Beyer, A. Golzhauser, K. Kohse-Hoinghaus, Structure-activity relation of spinel-type Co-Fe oxides for low-temperature CO oxidation. Catalysis Science and Technology, 4, 9 (2014), 3359.
[25] V. Kashyap, A. Pandikassala, G. Singla, T. S. Khan, M. Ali Haider, C. P. Vinod, S. Kurungot, Unravelling faradaic electrochemical efficiencies over Fe/Co spinel metal oxides using surface spectroscopy and microscopy techniques. Nanoscale, 14, 42 (2022) 15928.
[26] Z. Zhou, Y. Zhang, Z. Wang, W. Wei, W. Tang, J. Shi, R. Xiong, (2008). Electronic structure studies of the spinel $CoFe_2O_4$ by X-ray photoelectron spectroscopy. Applied Surface Science, 254, 21 (2008), 6972.
[27] S. Trasatti, G. Lodi, Electrodes of Conductive Metallic Oxides, Part A-B; Elsevier Science Publishers: Amsterdam, The Netherlands, 1980/1981
[28] E. Rios, J. L. Gautier, G. Poillerat, P. Chartier, Mixed valency spinel oxides of transition metals and electrocatalysis: case of the $Mn_xCo_{3-x}O_4$ system, J. Electrochim. Acta 44 (1998) 1491.
[29] R. D. L. Smith, M. S. Prévot, R. D. Fagan, S. Trudel, C. P. Berlinguette, Water oxidation catalysis: Electrocatalytic response to metal stoichiometry in amorphous metal oxide films containing iron, cobalt and nickel, J. Am. Chem. Soc. 135 (2013) 11580.
[30] R. D. L. Smith, B. Sporinova, R. D. Fagan, S. Trudel, C. P. Berlinguette, Facile photochemical preparation of amorphous iridium oxide films for water oxidation catalysis, Chem. Mater. 26, (2014) 1654.
[31] Y. K. Kim, J. H. Kim, Y. H. Jo, J. S. Lee, Precipitating metal deposition of amorphous metal oxyhydroxide electrodes containing Ni, Fe, and Co for electrocatalytic water oxidation, ACS Catal. 9 (2019) 9650−9662

[32] P. Gao, Y. Zeng, P. Tang, Z. Wang, J. Yang, A. Hu, J. Liu, Understanding of the synergic effects and structural evolution of $Co(OH)_2$ and Co_3O_4 toward boosting electrochemical charge storage, Adv. Funct. Mater., 32 (2022) 2108644
[33] S. Poulston, P. M. Parlett, P. Stone, M. Bowker, Surface oxidation and reduction of CuO and Cu_2O studied using XPS and XAES, Surf. Interface. Anal. 24 (1996) 811.
[34] P. Velasquez, D. Leinen, J. Pascual, J. R. R. Barrado, P. Grez, H. Gomez, R. Schrebler, R. D. Rio, R. Cordova, A Chemical, morphological, and electrochemical (XPS, SEM/EDX, CV, and EIS) analysis of electrochemically modified electrode surfaces of natural chalcopyrite ($CuFeS_2$) and pyrite (FeS_2) in alkaline solutions, J. Phys. Chem. B, 109 (2005) 4977.
[35] S. Thekkoot, R. Islam, S. Morin, Improved oxygen evolution reaction performance with addition of Fe to form $Fe_yCu_{x-y}Co_{3-x}O_4$ and $Fe_yNi_{x-y}Co_{3-x}O_4$ (x = 0.5, 1 and y = 0.1, 0.15) spinel oxides, Electrochim. Acta, 378 (2021) 138116
[36] S. Thekkoot, R. Islam, O Gray, S. Morin, Efficiency of nanostructured $Cu_xCo_{3-x}O_4$ and $Ni_xCu_{1-x}Co_2O_4$ electrodes as electrocatalysts for the oxygen evolution reaction – revisited, Electrochim. Acta, 471, (2023) 143339

Chapter 5.1. Electrochemical properties - Double layer capacitance measurements on crystalline and amorphous transition metal oxides

5.1.1. Introduction

The electrochemical performance of different samples varies greatly depending on the composition, method and conditions used for the preparation of these materials. These materials possess different surface areas that greatly influence the observed electrochemical current and hence the catalytic activity. The absence of surface area-corrected electrochemical data makes it difficult to compare the material's performance with those of the literature. Hence it is crucial to normalize the current density using the real surface area of the electrode [1, 2]. It is difficult to precisely evaluate the intrinsic activity trend of different samples without measuring the real surface areas of each sample. Different methods have been adopted to measure the surface area of the samples and this topic has been reviewed recently in ref. 1. Cyclic voltammetry is an efficient technique to study the electrocatalytic activity of electrodes and can be used to determine the double-layer capacitance of the electrode interfaces [3].

As explained in Chapter 1, section 1.4, electrochemical active surface area (ESCA) is directly related to the double-layer capacitance of the electrode. Measuring the double-layer capacitance, the roughness factor can be calculated, which is the ratio of double-layer capacitance of the sample and that of the smooth surface of the electrode (60 μF cm^{-2}). Normalizing the current density by the roughness factor, the surface area effect can be excluded which allows us to compare the catalytic activity of different samples for OER [1,2, 3]. $Cu_xCo_{3-x}O_4$ and $Ni_xCu_{1-x}Co_{3-x}O_4$ were re-prepared in this work to verify the surface area of the electrode using cyclic voltammetry and EIS measurements.

The double-layer capacitance (C_{dl}) measurement of the samples has been described in detail in ref. 4. The cyclic voltammograms were recorded at room temperature in 1M KOH at different scan rates namely 10 mV s^{-1}, 20 mV s^{-1}, 40 mV s^{-1}, 60 mV s^{-1}, 80 mV s^{-1} and 100 mV s^{-1} in a narrow potential range of -0.50 mV to 50 mV vs SCE. The cathodic current density at -25 mV is plotted as a function of sweep rates. From the slope of this linear plot, the double-layer capacitance (C_{dl}) of the sample was obtained. The roughness factor (R_F) is calculated as the ratio of C_{dl} of the electrode and that of a smooth surface of the electrode, i.e. 60 μF cm^{-2}, the accepted value as reported in the literature [3, 4].

Impedance measurements were used to evaluate the capacitance of crystalline and amorphous materials. Two methods were employed a) electrochemical impedance spectroscopy (EIS) and b) differential capacitance to verify the capacitance values obtained from CV analysis. EIS analysis is an excellent method to study electrical transport characterization using resistive (real part) and capacitive (imaginary part) of the complex impedance of materials and their interface with a solution as a function of the frequency of an alternating potential perturbation. This method allows for the evaluation of the double-layer capacitance of the samples as well as for obtaining information on other components (pseudo-capacitance(s), charge transfer resistance (s), and solution resistance. A $R_s + C_{dl}/R_{ct} + C_\phi/R_\phi$ circuit model (Figure 5.1.1) has been used for fitting the experimental data of all samples where R_s is the solution resistance, C_{dl} and R_{ct} are the double-layer capacitance and charge transfer resistance. C_ϕ and R_ϕ are the pseudo-capacitance and Faradaic resistance associated with slow reaction processes. Several other circuits, such as those used in refs 5, 6, 7, 8 were tested but the fits were of poor quality with very large standard deviations associated with the circuit elements. For high surface area and porous films, both C_{dl} and C_ϕ values are expected [8]. The double-layer capacitance values obtained using CV method will be compared to those obtained by the EIS and differential capacitance. Differential capacitance is the total capacitance measured at a given potential, which is equivalent to the sum of C_{dl} and C_ϕ in series.

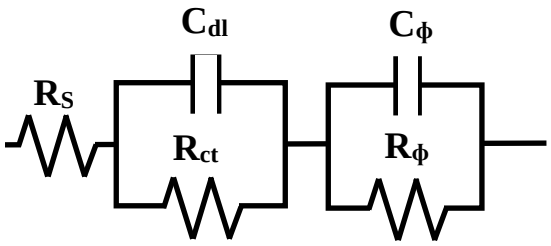

Figure 5.1.1. The Equivalent circuit model used for Nyquist plot fitting of amorphous metal oxides

5.1.2. Capacitance measurements on crystalline samples/spinel oxides

The cyclic voltammograms of Co_3O_4 and $NiCo_2O_4$ in a narrow potential range of -50 mV to 50 mV are shown in Figure 5.1.2a and Figure 5.1.2b respectively. The anodic and cathodic current densities for each electrode were found to have nearly equal magnitude at the same scan

rates, and the current density increased as the scan rate increased. The cyclic voltammograms of other samples are given in the Appendix from Figure A3.1.1 and Figure A3.1.3. The cathodic current density (j_{cap}) at -25 mV is plotted as a function of the sweep rate for the samples Co_3O_4 and $NiCo_2O_4$ is shown in Figure 5.1.3a and Figure 5.1.3b respectively, and that of other samples are given in Appendix Figure A3.1.2 and Figure A3.2.4. From the linear plot, the double-layer capacitance and roughness factor were calculated.

The roughness factor calculated from CV data is also given in Table 5.1.1. Pure cobalt oxide was found to have a lower roughness factor, the addition of Cu increased the roughness factor. The incorporation of Ni further enhanced the roughness factor or surface area of the electrode.

The Nyquist plot was obtained from EIS measurements for all the prepared spinel oxides. The Nyquist plot was fitted using the circuit model $R_s + C_{dl}/R_{ct} + C_\phi/R_\phi$. The features of the Nyquist plots are very similar for all samples, results for $Cu_{0.25}Co_{2.75}O_4$ are shown in Figure 5.1.4. The double-layer capacitance values obtained from EIS measurements are also given in Table 5.1.1, while Table 5.1.2 and Table A3.1 list the circuit parameters and standard deviation obtained from EIS measurements for all $Cu_xCo_{3-x}O_4$ and $Ni_xCu_{1-x}Co_2O_4$ samples. The double-layer capacitance values obtained from CV and EIS (Table 1) are very similar for most of our samples and well within the 18% accuracy reported. This confirms that the CV method is suitable for the determination of the roughness factor for $Cu_xCo_{3-x}O_4$ and $Ni_xCu_{1-x}Co_2O_4$ samples. In the case of $Cu_{0.25}Co_{2.75}O_4$ and $Ni_{0.5}Cu_{0.5}Co_2O_4$, the difference between C_{dl} values is greater than 20%, and in these cases, the values obtained from the CV were used to calculate the roughness factor. It is possible that material properties are affected by the high-frequency perturbation.

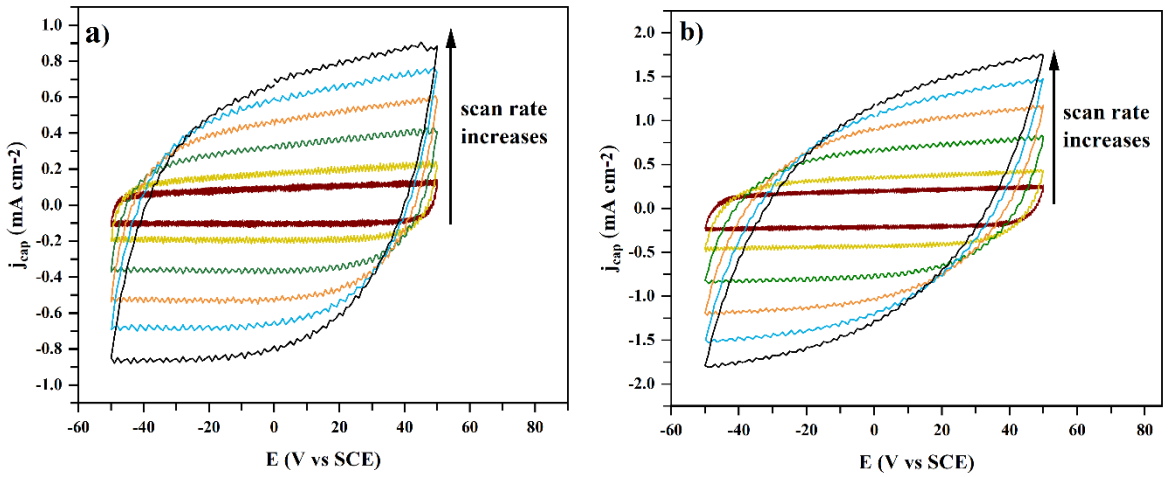

Figure 5.1.2. Cyclic voltammograms of a) Co_3O_4 and b) $NiCo_2O_4$ in 1 M KOH for scans recorded in a potential range of -50 mV to 50 mV (SCE) for sweep rates of 10, 20, 40, 60, 80 and 100 mV s^{-1}. Cyclic voltammograms for other $Cu_xCo_{3-x}O_4$ for $Ni_xCu_{1-x}Co_2O_4$ samples can be found in Figure A3.1.1. and Figure A3.1.3., respectively.

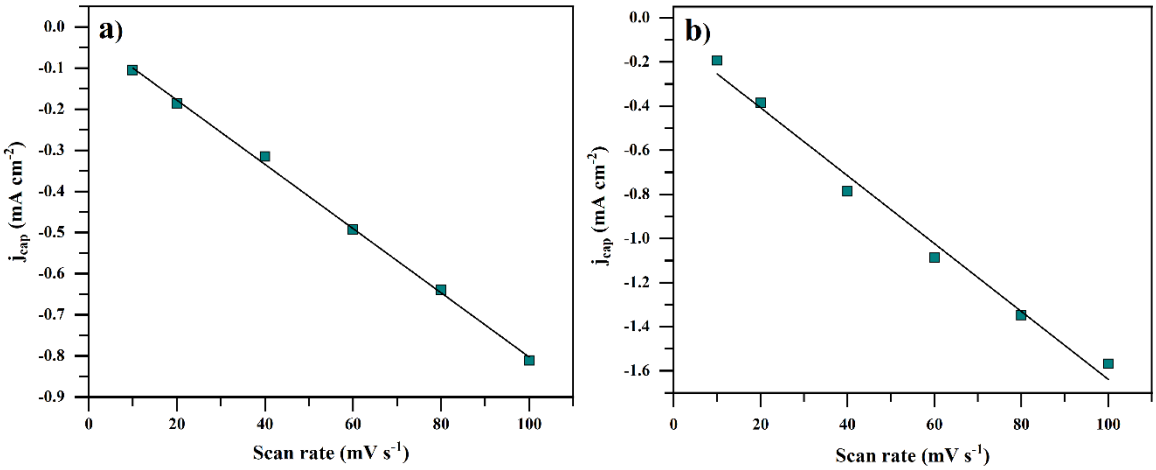

Figure 5.1.3. Graphs of the double-layer charging current density as a function of potential sweep rate (for the anodic sweep direction) for a) Co_3O_4 and b) $NiCo_2O_4$ samples in 1 M KOH. The graphs for all $Cu_xCo_{3-x}O_4$ for $Ni_xCu_{1-x}Co_2O_4$ samples can be found in Figure A3.1.2. and Figure A3.1.4., respectively.

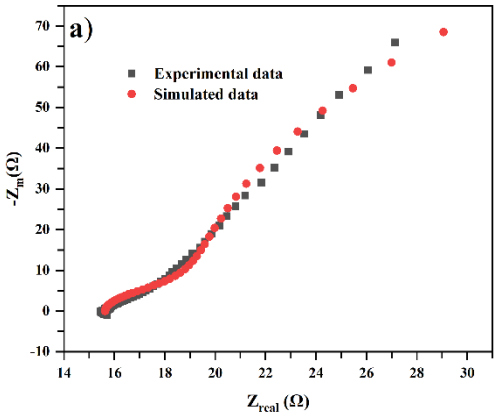

Figure 5.1.4. a) Nyquist plot for $Cu_{0.25}Co_{2.75}O_4$ measured at 0 mV in a frequency range of 0.1 Hz to 100 KHz.

Table 5.1.1. The capacitance and roughness factors of $Cu_xCo_{3-x}O_4$ and $Ni_{1-x}Cu_xCo_2O_4$ electrodes measured by CV and EIS measurements in 1 M KOH.

Composition	$C_{dl,CV}$ / mF cm^{-2} from CV	Roughness factor (R_F) from CV	$C_{dl,EIS}$ / mF cm^{-2} from EIS
Co_3O_4	7.8 ± 0.3	130 ± 14	6.5 ± 1.1
$Cu_{0.25}Co_{2.75}O_4$	8.1 ± 0.2	135± 14	17.4± 3.5
$Cu_{0.5}Co_{2.5}O_4$	9.6 ± 0.4	160 ± 16	12.8± 1.7
$Cu_{0.75}Co_{2.25}O_4$	12.8 ± 0.6	213 ± 31	14.8± 2.6
$CuCo_2O_4$	9.9 ± 0.3	165 ± 22	8.9±2.0
$NiCo_2O_4$	15.4 ± 1.1	257 ± 44	17.8±2.9
$Ni_{0.9}Cu_{0.1}Co_2O_4$	12.4 ± 0.7	207 ± 32	12.5±2.5
$Ni_{0.75}Cu_{0.25}Co_2O_4$	14.3 ± 1.0	238 ± 40	18.7±2.8

$Ni_{0.5}Cu_{0.5}Co_2O_4$	14.6 ± 1.8	243 ± 54	28.5±4.4
$Ni_{0.25}Cu_{0.75}Co_2O_4$	12.0 ± 1.0	200 ± 22	14.1±3.0

The differential capacitance (C_d) corresponds to the total capacitance was also measured for our samples. The C_d at 0 V versus SCE in 1 M KOH is given in Table 5.1.2. C_{total} can also be calculated using our EIS data. For capacitances in series,

$1/C_{total} = 1/C_{dl} + 1/C_\phi$

Using the C_{dl} and C_ϕ values obtained from the fitting of Nyquist plot, C_{total} values were calculated (C_{dl}, C_ϕ and C_{total} values are given in Table 5.1.2). We obtained good agreement between C_{total} and C_d values when the two capacitances (C_{dl} and C_ϕ) are arranged in series in the equivalent circuit. A parallel arrangement of the two capacitances in the equivalent circuit resulted in a large difference between C_{total} and C_d. This observation ($1/C_{dl} + 1/C_\phi \approx 1/C_d$) further supports the choice of the equivalent circuit to fit our EIS data [8]

Table 5.1.2. The capacitance of $Cu_xCo_{3-x}O_4$ and $Ni_xCu_{1-x}Co_2O_4$ electrodes obtained from Nyquist plot and differential capacitance measurements

sample	$C_{dl,EIS}$ / mF cm^{-2}	C_ϕ / mF cm^{-2}	C_{total} / mF cm^{-2}	Differential capacitance (C_d) / mF cm^{-2}
Co_3O_4	6.5 ± 1.1	8.5 ± 0.1	3.68 ± 0.46	2.6 ± 0.2
$Cu_{0.25}Co_{2.75}O_4$	17.4 ± 3.5	14.6 ± 0.3	7.9 ± 1.1	5.0 ± 0.2
$Cu_{0.5}Co_{2.5}O_4$	12.8 ± 1.7	10.7 ± 0.2	5.8 ± 0.6	4.0 ± 0.2
$Cu_{0.75}Co_{2.25}O_4$	14.8 ± 2.6	15.2 ± 0.2	7.5 ± 1.0	5.4 ± 0.4
$CuCo_2O_4$	8.9 ± 2.0	11.3 ± 0.2	5.0 ± 0.9	3.7 ± 0.1
$NiCo_2O_4$	17.8 ± 2.9	22.7 ± 3.3	10.0 ± 1.8	5.8 ± 0.3
$Ni_{0.9}Cu_{0.1}Co_2O_4$	12.5 ± 2.5	14.4 ± 0.2	6.7 ± 3.0	4.0 ± 0.6
$Ni_{0.75}Cu_{0.25}\ Co_2O_4$	18.7 ± 2.8	18.9 ± 0.6	9.4 ± 1.0	5.6 ± 0.3

$Ni_{0.5}Cu_{0.5}Co_2O_4$	28.5 ± 4.4	21.6 ± 0.2	12.3 ± 1.1	6.9 ± 0.6
$Ni_{0.25}Cu_{0.75}Co_2O_4$	14.1 ± 3.0	17.1 ± 3.7	7.7 ± 2.3	5.4 ± 0.1

Introduction of copper and nickel into the cobalt spinel oxide tends to increase the C_{dl} of the sample which can be associated with an increase of the roughness of the spinel oxide. SEM analysis supports this observation, Cu substituted cobalt oxides appear more porous than pure cobalt oxide. The addition of nickel further increased the roughness factor for some of the samples, although the SEM images of Ni-containing samples display a rather smooth surface. However, higher-resolution images show that the film surface consists of very small particles. The increase of the roughness factor with the incorporation of Cu or Ni was reported in other studies [9, 10]. Singh *et al.* observed a high roughness factor for $M_xCo_{3-x}O_4$ (M = Ni, Cu) using sol-gel method [11]. The high roughness factor indicates that the material possesses a larger surface area and may lead to a larger number of active sites on the surface being available for the catalytic process.

5.1.3. Capacitance measurements on amorphous metal oxides

The double-layer capacitance and roughness factor of amorphous metal oxides were also evaluated using cyclic voltammetry and EIS measurements using the procedure explained in section 5.1.1. The double-layer capacitance and the roughness factor of each electrode are given in Table 5.1.3. CoO_x possessed the lowest roughness factor, the incorporation of other metal cations into the cobalt oxide lattice increased the roughness factor/surface area of the samples. $Fe_{0.1}Ni_{0.9}Co_2O_x$ possessed a higher roughness factor compared to other samples. For both amorphous and spinel oxides, the incorporation of Cu and Ni increased the surface area of the samples. However, the Fe substitution showed a contradictory effect. When Fe substitution increased the surface area of amorphous oxides, an opposite trend was observed for spinel oxides, where Fe incorporation resulted in a decreased surface area of the electrode. For example, $Fe_{0.1}Ni_{0.9}Co_2O_4$ spinel oxides possessed a roughness factor of 85 ± 12 [12], while $Fe_{0.1}Ni_{0.9}Co_2O_x$ possessed a roughness value of 333 ± 61. Thus, for the same compositions, different surface area is possible. This could be due to the difference in the synthesis procedure of these metal oxides [12, 13, 14].

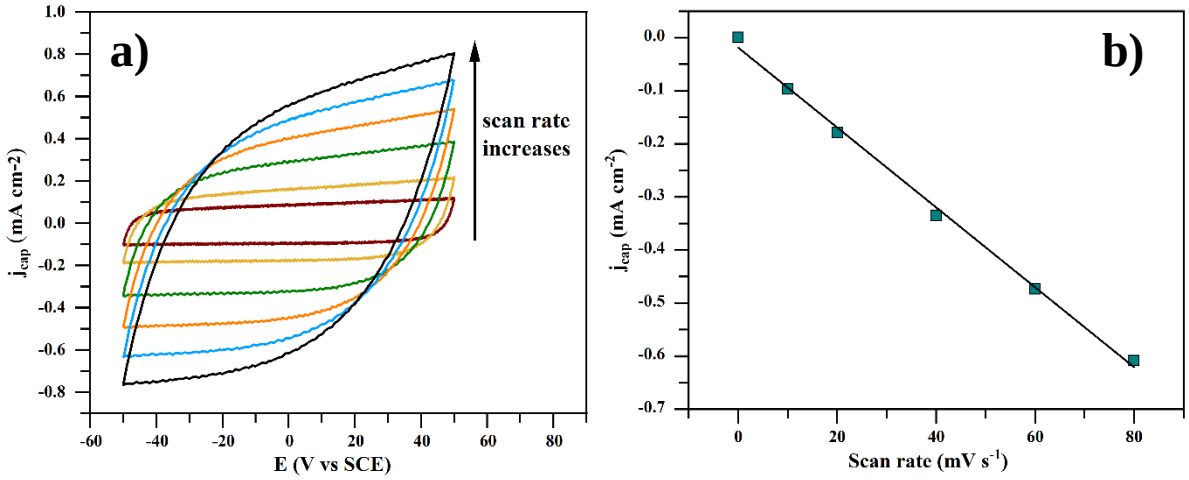

Figure 5.1.5. Cyclic voltammogram of the CoO_x electrode in 1M KOH for scans recorded in a potential range of -50 mV to 50 mV (SCE) for sweep rates of 10, 20, 40, 60 and 80 mV s^{-1} and b) Graphs of the double-layer charging current density at -25mV as a function of potential sweeps towards negative potentials for CoO_x electrode.

Table 5.1.3. The capacitance and roughness factors of amorphous metal oxides measured by CV and EIS measurements in 1 M KOH

Sample	C_{dl} /mF cm^{-2} from CV	Roughness factor
CoO_x	6.7 ± 0.2	112 ± 14
$CuCo_2O_x$	9.5 ± 0.5	158 ± 23
$Nu_{0.5}Cu_{0.5}Co_2O_x$	12.1± 0.3	202 ± 24
$Fe_{0.1}Cu_{0.9}Co_2O_x$	12.3 ± 0.8	205 ± 15
$Fe_{0.1}Ni_{0.9}Co_2O_x$	20.0 ± 1.7	333 ± 61
$Fe_{0.5}Co_{2.5}O_x$	12.8 ± 1.0	213 ± 37
$Fe_{0.5}Cu_{0.5}Co_2O_x$	11.3 ± 0.8	188 ± 31

To further verify the double-layer capacitance of the samples evaluated from cyclic voltammetry, we have performed EIS analysis. The details of EIS analysis are given in section

5.1.1. Double-layer capacitance and pseudo capacitances were evaluated by fitting the Nyquist plot using an $R_s + C_{dl}/R_{ct} + C_\phi/R_\phi$ circuit model, a similar equivalent circuit used for fitting the Nyquist plot obtained from EIS measurements. The circuit parameters are described in Section 5.1.1. Nyquist plot is given in Figure 5.1.6. The double-layer capacitance measured from cyclic voltammetry and EIS measurements are given in Table 5.1.4 and from this Table, we can see that C_{dl} values obtained from CV and EIS measurements are very close for all samples. Therefore, both these methods (CV and EIS) are suitable for evaluating the surface area of amorphous samples as that of crystalline materials.

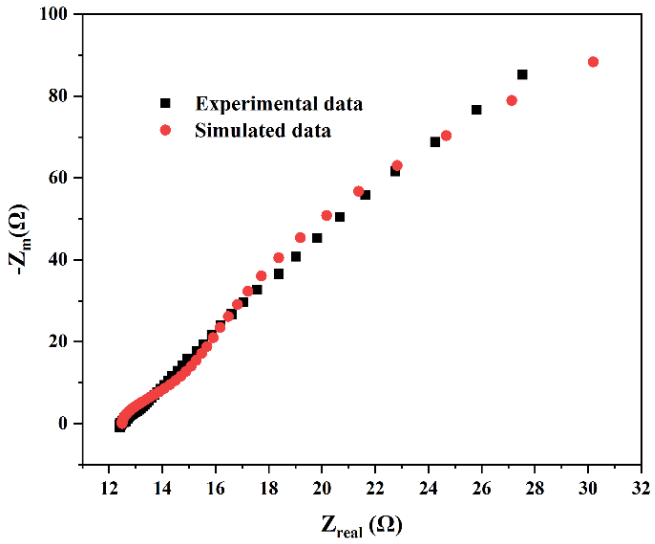

Figure 5.1.6. Nyquist plot for $CuCo_2O_x$ measured at 0 mV in a frequency range of 0.1 Hz to 100 KHz.

Table 5.1.4. Capacitance values measured by CV and EIS measurements

sample	C_{dl} /mF cm^{-2} from CV	(C_{dl}) (mF cm^{-2}) from EIS	C_{dl} /mF cm^{-2} from CV for corresponding spinel oxides
CoO_x	6.7 ± 0.2	9.6 ± 0.2	7.8 ± 0.3
$CuCo_2O_x$	9.5 ± 0.5	12.5± 0.3	9.9 ± 0.3
$Nu_{0.5}Cu_{0.5}Co_2O_x$	12.1± 0.3	13±0.4	14.6 ± 1.8

$Fe_{0.1}Cu_{0.9}Co_2O_x$	12.3 ± 0.8	11.6±0.2	4.7 ± 0.4
$Fe_{0.1}Ni_{0.9}Co_2O_x$	20.0±1.7	24.0±0.2	5.3 ± 0.6

The differential capacitance (C_d) of the samples was also measured to confirm the data obtained from CV and EIS measurements. The differential capacitance measured for all amorphous samples at 0 mV vs. SCE is given in Table 5.1.5. The sum of the capacitances (C_{dl} and C_ϕ) obtained from EIS measurements was calculated using the equation $1/C_{total} = 1/C_{dl} + 1/C_\phi$, C_{dl}, C_ϕ and C_{total} are given in Table 5.1.5. Even though there are some discrepancies between C_{total} and C_d, a series arrangement of capacitances provided better agreement between C_{total} and C_{dl} values than having a circuit model with a parallel arrangement of capacitances. This verifies the selection of the circuit model used for the Nyquist plot fitting of amorphous materials.

Table 5.1.5. The Capacitance of amorphous metal oxides obtained from the Nyquist plot, and differential capacitance measurements

sample	C_{dl} / mF cm^{-2}	C_ϕ / mF cm^{-2}	C_{total} / mF cm^{-2}	Differential capacitance (C_d) mF cm^{-2}
CoO_x	6.7 ± 0.2	2.3 ± 0.7	1.9 ± 0.9	1.1 ± 0.3
$CuCo_2O_x$	9.5 ± 0.5	29.6 ± 3.0	8.9 ± 3.8	10.7 ±1
$Ni_{0.5}Cu_{0.5}Co_2O_x$	12.1± 0.3	13.2 ± 0.4	6.5 ± 0.7	2.1 ± 0.5
$Fe_{0.1}Cu_{0.9}Co_2O_x$	12.3 ± 0.8	18.1 ± 0.8	7.1 ± 1.6	4.6 ± 0.1
$Fe_{0.1}Ni_{0.9}Co_2O_x$	20.0 ± 1.7	25.5 ± 3	12.3 ± 4.7	7.1 ± 0.2

Thus, electrochemical measurements such as CV and EIS are reasonable techniques to measure the electrochemically active surface area of the electrode. Even though the double-layer capacitance measurements are affected by electrode potential, surface structure, and electrolytes, these methods are found to be more suitable for our materials. Both these methods provided

comparable double-layer capacitance values for spinel oxides and amorphous metal oxides. In Chapter 5.2, the roughness factor obtained from cyclic voltammetry analysis will be used for normalizing the current density obtained from spinel oxides and amorphous metal oxides, so that the intrinsic catalytic activity of the materials can be compared.

5.1.4. References

[1] C. Wei, S. Sun, D. Mandler, X. Wang, S. Z. Qiao, Z. J. Xu, Approaches for measuring the surface areas of metal oxide electrocatalysts for determining their intrinsic electrocatalytic activity, Chem. Soc. Rev., 48 (2019) 2518

[2] S. Trasatti, O. A. Petrii, Real surface area measurements in electrochemistry, J. Electroanalchem. 327 (1992) 353

[3] B. Marsan, N. Fradette, G. Beaudoin, (1992). Physicochemical and electrochemical properties of $CuCo_2O_4$ electrodes prepared by thermal decomposition for oxygen evolution. J. Electrochem. Soc., 139, 7 (1992) 1889.

[4] S. Thekkoot, R. Islam, O Gray, S. Morin, Efficiency of nanostructured $Cu_xCo_{3-x}O_4$ and $Ni_xCu_{1-x}Co_2O_4$ electrodes as electrocatalysts for the oxygen evolution reaction – revisited, Electrochim. Acta, 471 (2023) 143339

[5] H. A. Bandal, A. R. Jadhav, A. H. Tamboli, H. Kim, Bimetallic iron cobalt oxide self-supported on Ni-Foam: An efficient bifunctional electrocatalyst for oxygen and hydrogen evolution reaction, Eletcrochim Acta, 249 (2017) 253

[6] A. Rebekah, E. A. Kumar, C. Viswanathan, N. Ponpandian, Effect of cation substitution in $MnCo_2O_4$ spinel anchored over rGO for enhancing the electrocatalytic activity towards oxygen evolution reaction (OER), Int. J. Hydrog. Energy, 45 (2020) 6391

[7] J. Qiao, F. Song, J. Hu, D. Huo, J. Yuan, J. Shen, L. Niu, A. Wang, Mesoporous spinel NiFe oxide cubes as advanced electrocatalysts for oxygen evolution, Int. J. Hydrog. Energy, 44 (2019) 16368

[8] B. E. Conway, V. I. Birss, I. Wojtowicz, The role and utilization of pseudocapacitance for energy storage by supercapacitors, J. Power Sources, 66 (1997)1-14

[9] Q. Zhang, Z. D. Wei, C. Liu, X. Liu, X. Q. Qi, S. G. Chen, W. Ding, Y. Ma, F. Shi, Y.M. Zhou, Copper-doped cobalt oxide electrodes for oxygen evolution reaction prepared by magnetron sputtering, Int. J. Hydrog. Energy, 37 (2012) 822

[10] W. Jin, J. Chen, Z. Wu, G. Maduraiveeran, Encapsulated spinel $Cu_XCo_{3-X}O_4$ in carbon nanotubes as efficient and stable oxygen electrocatalysts, Int. J. Hydrog. Energy, 44 (2019) 11421.

[11] R.N. Singh, J.P. Pandey, N.K. Singh, B. Lal, P. Chartier, J.-F. Koenig, Sol-gel derived spinel $M_xCo_{3-x}O_4$ (M = Ni, Cu; $0 \leq x \leq 1$) films and oxygen evolution, Electrochim. Acta, 45 (2000) 1911
[12] S. Thekkoot, R. Islam, S. Morin, Improved oxygen evolution reaction performance with addition of Fe to form $Fe_yCu_{x-y}Co_{3-x}O_4$ and $Fe_yNi_{x-y}Co_{3-x}O_4$ (x = 0.5, 1 and y = 0.1, 0.15) spinel oxides, Electrochim. Acta, 378 (2021) 138116
[13] S. Thekkoot, B. Rezaee, D. Rajaguru, J. Tian, O. Gray, S. Morin, Transition metal oxides for oxygen evolution reaction: A comparative study between amorphous and crystalline materials, Manuscript in preparation.
[14] A. Vu , Y. Qian , A. Stein, Porous electrode materials for lithium-ion batteries – How to prepare them and what makes them special, Adv. Energy Mater. 2 (2012) 1056.

Chapter 5.2. Electrochemical properties – Catalytic activity of crystalline and amorphous transition metal oxides towards the OER and OER kinetics

5.2.1. Introduction

Alkaline water electrolysis has been studied extensively over centuries but the cost of hydrogen production has been prohibitive until recently. Hence, there is much knowledge regarding OER kinetics. Nowadays, much of the OER research is centered on finding suitable electrocatalysts/electrode materials to reduce the cost and increase the energy output of water electrolysis. Good electrochemical performance indicates a low thermodynamic barrier (described in Chapter 1, section 1.6.1), fast kinetics, and abundance of surface reactive intermediates [1, 2]. Different compositions and resulting surface structures can induce changes in the rate-determining steps and hence overall kinetics of the reaction [3]. Cyclic voltammetry is a highly efficient technique to measure the catalytic activity of the electrodes. In this work, cyclic voltammetry has been used to analyze the catalytic activity of the crystalline and amorphous samples prepared in our lab.

When the solution is unstirred during a voltammetry experiment, the diffusion-controlled mass transfer dominates. For electrochemical techniques in which the electrode moves with respect to the solution such as rotating disc electrode experiments, the rate of mass transfer at the surface of the electrode is larger than diffusion alone so that the relative contribution of mass transfer to the electron transfer kinetics due to diffusion is smaller [4]. In our study, the kinetics of spinel oxides and amorphous metal oxides were performed using a rotating disc experiment (RDE).

The Koutecky–Levich (K-L) equation correlates the measured electric current produced at the electrode due to an electrochemical reaction and the mass transport of reactants. K-L plots can be used to derive the kinetic current at different rotation rates.

$$1/I_d = 1/I_k + 1/I_{dl} = 1/nFAkc_{O_2}b + 1/0.62nFAD_{O_2}^{2/3}\nu^{-1/6}c_{O_2}b\omega^{1/2} = 1/I_k + 1/B\omega^{1/2} \quad (5.2.1.)$$

where I_k and I_{dl} correspond to kinetic and diffusion-limited current respectively, n is the number of electrons transferred during the reaction, F is the Faraday constant (96485C mol^{-1}), A is the electrode surface area in cm^2 (0.196 cm^2), D_{O_2} is molecular O_2 diffusion coefficient (1.9 ×

10^{-5} cm^2 s^{-1} in 0.1 M KOH), ν is the kinematic viscosity of the solution (0.01 cm^2 s^{-1} at 298 K), c_{O_2} is the bulk concentration of molecular oxygen at 295 K (1.17×10^{-6} mol cm^{-3} in 0.1 M KOH) and ω is the angular rotation speed in rad s^{-1}. A plot of disc current versus $\omega^{1/2}$ provides a straight line. The kinetic current is calculated from the intercept, while the slope of the straight line gives the constant B [4, 5, 6].

The Tafel plot (described in chapter 1, section 1.5) is an important measurement used to evaluate the catalytic activity of the electrodes and can give valuable information about the mechanism and rate-determining step of the reaction under study [7]. In practice, a higher overpotential is required to achieve a significant amount of current density. A faster increase of current density with a smaller overpotential is desired. The Tafel slope is a very useful parameter to study this correlation as it is a function of overpotential vs current density and is often used to compare the catalytic activity of the electrocatalysts. A lower Tafel slope is an indication of better catalytic activity of the material. In this work, the Tafel plot is recorded with linear sweep voltammetry (LSV) using the rotating disc experiment (details are given in Chapter 2, section 2.2.4.).

5.2.2. Catalytic activity of spinel oxides

The electrocatalytic activity of $Cu_xCo_{3-x}O_4$ and $Ni_xCu_{1-x}Co_{3-x}O_4$ electrodes for OER was analyzed using cyclic voltammetry (CV). CVs were carried out at room temperature in 1 M KOH at a scan rate of 50 mV s^{-1} in a potential region of -0.1 V to 1 V. The cyclic voltammograms of $Cu_xCo_{3-x}O_4$ and $Ni_xCu_{1-x}Co_{3-x}O_4$ are reported in Figure 5.2.1a and Figure 5.2.1b, respectively. The cyclic voltammograms show the characteristic shape; it possesses an anodic peak and a corresponding cathodic peak before the OER as expected for spinel oxides. In these CVs, the current density obtained from the unit geometric surface area (apparent current density) of the electrode is plotted as a function of potential (vs SCE). The current density increases in the positive potential region after the anodic peak of each cyclic voltammogram. The CVs of all spinel oxides display similar characteristic features, where current varies exponentially with potential (refer to equation 1.7). All Ni and Cu substituted samples possessed a higher current density compared to pure cobalt spinel oxide except for $Cu_{0.25}Co_{2.25}O_4$. This could be related to

the increased roughness or porosity of copper and nickel-substituted cobalt oxides, a higher surface area is beneficial for water oxidation as it provides more active sites for OER [8].

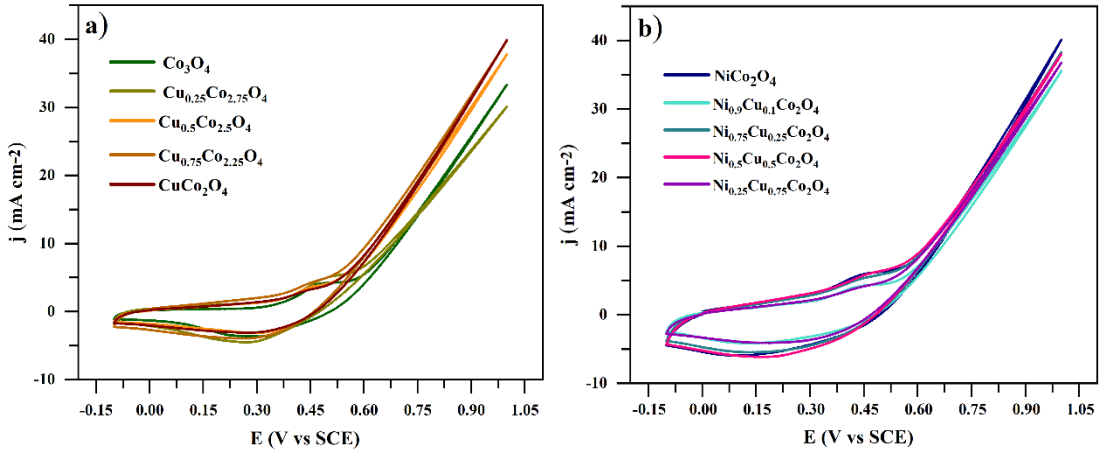

Figure 5.2.1. Cyclic voltammograms of a) $Cu_xCo_{3-x}O_4$ and b) $Ni_xCu_{1-x}Co_2O_4$ samples recorded in 1M KOH at a scan rate of 50 mV s^{-1}.

The onset potential for OER for each electrode is calculated by extrapolating the current density to the x-axis. The onset potential values of the $Cu_xCo_{3-x}O_4$ and $Ni_xCu_{1-x}Co_{3-x}O_4$ electrodes for OER are summarized in Table 5.2.1. It is clear from this Table that $NiCo_2O_4$ possesses the highest onset potential for OER followed by Co_3O_4. The addition of Cu decreased the onset potential significantly. Overall, $Ni_{0.5}Cu_{0.5}Co_2O_4$ displayed the lowest onset potential. Such a decrease in the OER overpotential for Cu substituted cobalt oxides has been reported before and is associated with an increase in the electrode materials' surface area [9, 10]. Both SEM analysis and roughness factor measurements indicate that Cu and Ni substitutions increase the surface area of the electrode. Improving the surface area is an effective strategy to achieve lower overpotential.

Wang *et al.* mentioned the importance of engineering the surface active sites and increasing the surface area to attain a lower overpotential [11]. Bothra *et al.* studied the activity of pure and Fe, Ni, and Cu-substituted cobalt oxides for the OER. They observed that 25% Cu-substituted cobalt oxides achieved the lowest onset potential compared to Fe or Ni-substituted cobalt oxides. In the case of Ni and Fe substituted cobalt oxides, Ni and Fe were found to be the active sites for water oxidation, while for Cu-substituted cobalt oxides, Co is found to be the

more favorable active site for adsorbate formation. However, the volcano plot showed that the 25% Cu doped cobalt oxide is positioned at the top of the plot providing suitable bond strength to cobalt for oxygen evolution reaction and thus, showing superior catalytic activity for OER by significantly decreasing the overpotential [12].

Table 5.2.1. The onset potential of $Cu_xCo_{3-x}O_4$ and $Ni_xCu_{1-x}Co_{3-x}O_4$ samples for OER in 1 M KOH.

Composition	Onset potential (mV)	Composition	Onset potential (mV)
Co_3O_4	536 ± 4	$NiCo_2O_4$	556± 11
$Cu_{0.25}Co_{2.75}O_4$	511 ± 11	$Ni_{0.9}Cu_{0.1}Co_2O_4$	517± 3
$Cu_{0.5}Co_{2.5}O_4$	522 ± 2	$Ni_{0.75}Cu_{0.25}Co_2O_4$	514 ± 4
$Cu_{0.75}Co_{2.25}O_4$	515 ± 2	$Ni_{0.5}Cu_{0.5}Co_2O_4$	501 ± 6
$CuCo_2O_4$	514 ± 3	$Ni_{0.25}Cu_{0.75}Co_2O_4$	514 ± 3

To exclude the contribution of surface area effect when comparing the sample's catalytic activity and to understand the role of foreign metal cations in OER, the charging current density was normalized to the unit real surface area using the roughness factor of the $Cu_xCo_{3-x}O_4$ and $Ni_xCu_{1-x}Co_2O_4$ electrodes (Figure 5.2.2a and 5.2.2b respectively). As shown in Figure 5.2.2a, among the $Cu_xCo_{3-x}O_4$ series, Co_3O_4 (x = 0) achieved the highest current density (0.26 mA cm^{-2} at 1 V) compared to other copper-containing spinel oxides. This observation reveals that the cobalt site is more active for the OER. The copper substitution may decrease the number of most catalytically active cobalt sites in the spinel lattice and thereby decrease the current density. $Cu_xCo_{3-x}O_4$ samples with x values = 0.25, 0.5, and 1 possess similar current densities. As the double-layer capacitance evaluation carries a large error [13], the roughness factor also possesses a large error as reported in Table 5.1.1 in section 5.1.2. When the error in the roughness factor is taken into consideration, Co_3O_4 and $Cu_xCo_{3-x}O_4$ samples possess similar current density. In addition, copper addition is beneficial as it lowers the onset potential of OER. $Ni_xCu_{1-x}Co_{3-x}O_4$

samples have lower current density values compared to $Cu_xCo_{3-x}O_4$ when the current density is corrected for the real surface area using the roughness factor (Figure 5.2.2b). This study clearly indicates that Ni substitution increases the apparent current density probably due to the high surface area, but does not actually contribute to the catalytic activity of the material.

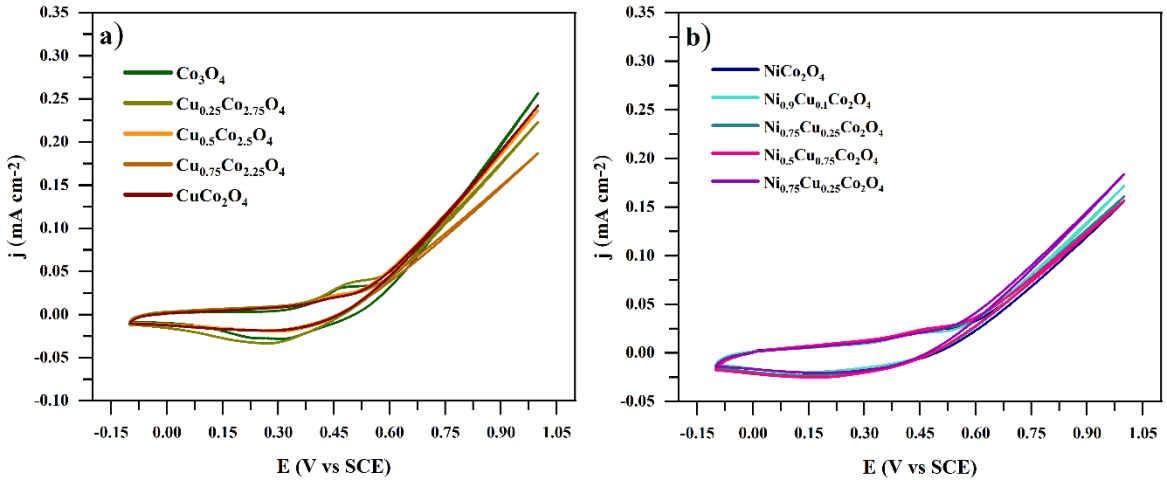

Figure 5.2.2. Cyclic voltammograms of a) $Cu_xCo_{3-x}O_4$ and b) $Ni_xCu_{1-x}Co_2O_4$ samples recorded in 1M KOH at a scan rate of 50 mV s^{-1}. The CVs are corrected for the real surface area of samples using their corresponding roughness factor.

According to XPS analysis, Co_3O_4 possesses a high Co^{2+} to Co^{3+} ratio (0.92); the stoichiometric Co^{2+} to Co^{3+} ratio is 0.5. The excess of Co^{2+} cations occupies the octahedral site of the spinel structure, which provides the mixed-valence states in the octahedral site and facilitates the charge transfer between cations, which consequently increases catalytic activity towards OER [14, 15, 16]. Moreover, Co^{2+} at the Oh site has unpaired electrons in the valence shell, whereas, Co^{3+} in the Oh site has a d^6 electronic configuration with a low spin state [14]. Hence the Co^{2+} at the Oh site could be a more active site than the Co^{3+}. Several reports mention that e_g filling is more advantageous over T_{2g} orbital filling as the e_g orbital has direct overlap with the oxygen anion [17].

$CuCo_2O_4$ possesses a Co^{2+} to Co^{3+} ratio of 0.55, which indicates that Cu^{1+} or Cu^{2+} is replacing Co^{2+} preferentially. From the XPS analysis, it is clear that Cu^{1+} and some of the Cu^{2+} ions are occupying the Td site. The Cu^{2+} that preferentially occupies the octahedral site might be replacing the Co^{2+} in the Oh site [18]. The addition of Cu and Ni provided the mixed-valence oxidation states in the octahedral site, which is expected to increase the conductivity. However, the substitution of Cu and Ni replaced the most active Co^{2+} from the Co_3O_4 which already

existed in the mixed-valence state. Meanwhile, the addition of a suitable amount of copper might optimize the bond strength of the cobalt oxygen bond and possibly provide a lower overpotential [12]. The lower activity of $Ni_{1-x}Cu_xCo_{3-x}O_4$ electrodes could be due to the presence of surface NiO content in the sample. Although Ni-containing spinel oxides show a comparatively higher Co^{2+} to Co^{3+} ratio, due to the presence of the NiO on the surface, it is not possible to predict the effect of the Co^{2+} to Co^{3+} ratio on the catalytic activity [18, 19].

Bothra *et al.* observed that even though Co_3O_4 is catalytically more active, small amounts of copper could provide suitable bond strength to cobalt for effective overlap with the adsorbate (oxygen anion), thus enhancing the catalytic activity of OER. High substitution of copper may decrease the number of catalytically active cobalt sites and possibly cause deviation from the optimal bond strength, resulting in a decrease in catalytic activity [12]. Singh *et al.* also observed a decrease in true catalytic activity for OER when cobalt is replaced with Ni and Cu in Co_3O_4 [9]. Chartier *et al.* observed that the introduction of 0.2 or 0.5 mol of Cu or Ni resulted in enhanced true catalytic activity, while higher Cu or Ni substitution did not affect the true catalytic activity [20].

Figure 5.2.3 shows the linear sweep voltammetry curves for the sample $Fe_{0.1}Cu_{0.9}Co_2O_4$ at different rotation speeds (500, 1000, 1500, 2000, 2500 and 3000 rpms) in 0.1 M KOH solution at room temperature at a scan rate of 2 mV s^{-1}. The current density increased as the rotation speed increased. As the rotation speed increases, it brings more oxygen flux to the surface of the electrode [21]. Similar results were obtained for other samples as well.

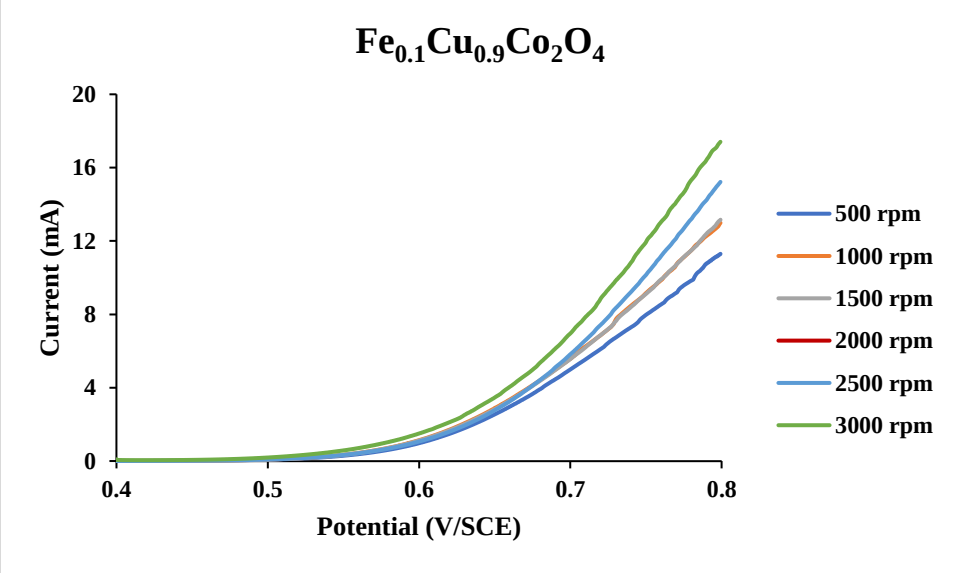

Figure 5.2.3. LSV curves of $Fe_{0.1}Cu_{0.9}Co_2O_4$ at different rotation speed in 0.1 M KOH solution.

The OER Tafel slope values were obtained for our catalysts by rotating disc experiment using 0.1 M KOH at 3000 rpm (see details in Chapter 2, section 2.2.4.). The Tafel values are given in Table 5.2.2. The Tafel plot was corrected using *iR* drop. The uncompensated solution resistance was measured using impedance spectroscopy.

As stated in equation 1.9 in chapter 1, The Tafel slope, $b = 2.303RT/\alpha F$. The charge transfer coefficient can be expressed by the following equation.

$$\alpha = n_b/v + n_r\beta \quad (5.2.2)$$

where n_b is the number of electrons transferred before the rate-determining step (RDS), v is the stoichiometric number with a typical value of 1, n_r is the number of electrons transferred during RDS and β is the symmetrical potential energy barrier factor, also known as the electrochemical Bronsted factor with a value of 0.5 - 1 [22]. In a single electron reaction, α refers to the symmetry factor β.

The Tafel plot of $Fe_{0.5}Co_{2.5}O_4$ is shown in Figure 5.2.4 and that of other spinel oxides are shown in Appendix 3.2, Figure A3.2.1.The Tafel values of spinel oxides are given in Table 5.2.2. The Tafel slopes of spinel oxides range from 71.4 mV dec^{-1} to 90.6 mV dec^{-1},which indicates that the OER mechanism is not changing significantly with composition. Fe-containing samples have comparatively lower Tafel slopes compared to Cu and Ni-substituted cobalt spinel oxides, except

$Fe_{0.1}Cu_{0.9}Co_2O_4$ (85.5 mV dec^{-1}). Similar Tafel values have been reported before in the literature for spinel oxides [10, 23, 24]. Noble metal oxides usually achieve lower Tafel slope (less than 60 mV dec^{-1}) which indicate their fast kinetics of OER [7]. Tafel slope of 60 mV dec^{-1} indicates that the rate-limiting step is a chemical reaction following the first electron transfer (where $n_r = 0$, $n_b = 1$). The Tafel slope of our samples shows a higher value, however, much lower than 120 mV dec^{-1}. A Tafel slope of 120 indicates a first-electron transfer in an electrochemical step. Also, a Tafel slope of 30 mV dec^{-1} indicates that the rate determining step is the third electron transfer step [22]. So, we believe that for our samples, it is possible that the rate-determining step is a chemical reaction followed by 1st electron transfer (reaction mechanism similar to 60 mV dec^{-1}). However, it is difficult to explain the mechanism where the Tafel slope is close to 90. According to Marcus theory, only one electron can transfer in a single elementary step, $n_r = 1$. Under this condition, β, the charge transfer coefficient will take a value between 0.5 and 1, than the accepted value of 0.5 [22, 25]. Scholz *et al* assigned a Tafel value of 60 mV dec^{-1} to the rate-determining step of O-O bond formation between M-O site and OH_{aq} adsorbed [26]. According to reference 27, O-H bond breaking is considered the rate-determining step of the reaction for the same Tafel slope. Sepulveda *et al* also suggested that a Tafel slope of 60 mV dec^{-1} corresponds to the rate-determining step of deprotonation of M-OH [28]. Nikolov *et al* performed Tafel analysis on Co_3O_4, $Cu_xCo_{3-x}O_4$, and $Ni_xCu_{1-x}Co_2O_4$ electrodes and observed a Tafel slope of 2.3RT/F (60 mVdec^{-1}). He also assigned the rate-determining step as the deprotonation of M-OH bond ($MOH + OH^- \rightarrow MO + H_2O + e^-$) [29].

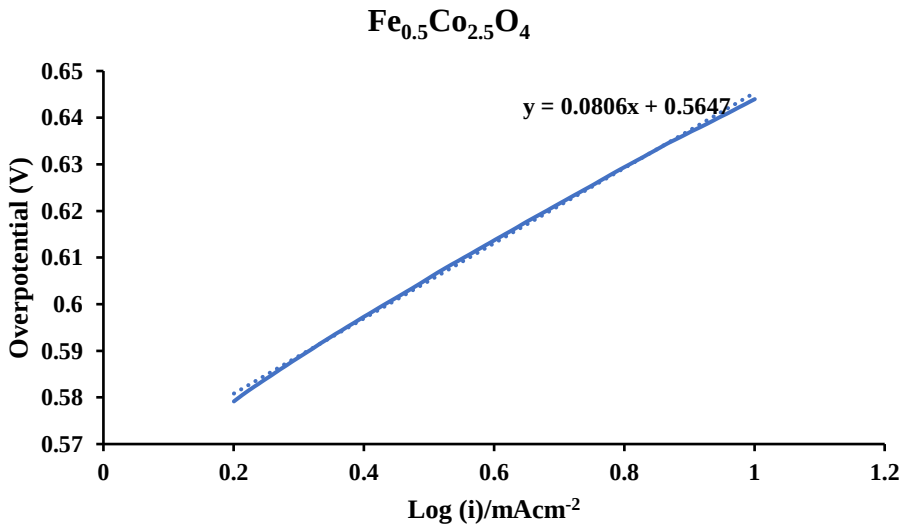

Figure 5.2.4. Tafel slope of $Fe_{0.5}Co_{2.5}O_4$ in 0.1M KOH at 3000 rpm, where the current density is corrected for ohmic drop measured by EIS

Table 5.2.2. Tafel slope of various spinel oxides obtained in 0.1 M KOH solution

Sample	Tafel slope ± 10 mV dec^{-1}
Co_3O_4	75.3
$CuCo_2O_4$	90.6
$Ni_{0.5}Cu_{0.5}Co_2O_4$	87.7
$NiCo_2O_4$	85.6
$Fe_{0.1}Cu_{0.9}Co_2O_4$	85.5
$Fe_{0.1}Ni_{0.9}Co_2O_4$	78
$Fe_{0.5}Co_{2.5}O_4$	80.6
$Fe_{0.75}Co_{2.25}O_4$	71.4
$Fe_{0.75}Cu_{0.25}Co_2O_4$	73.8
$Fe_{0.75}Ni_{0.25}Co_2O_4$	85.8

The K-L plot is given in Figure 5.2.5. The plots are linear and parallel to each other, which indicates that the electron transfer is consistent at different potentials and follows the first-order reaction kinetics [21]. The number of electrons exchanged per mole of oxygen produced during the reaction was calculated using equation 5.2.1. The number of electrons transferred, n, calculated for Co_3O_4 sample is found to be 2.5 to 6.5 at different potentials with an average of four electrons transferring during the OER reaction. Cobalt-based spinel oxide may favor a $4e^-$ transfer during the OER process.

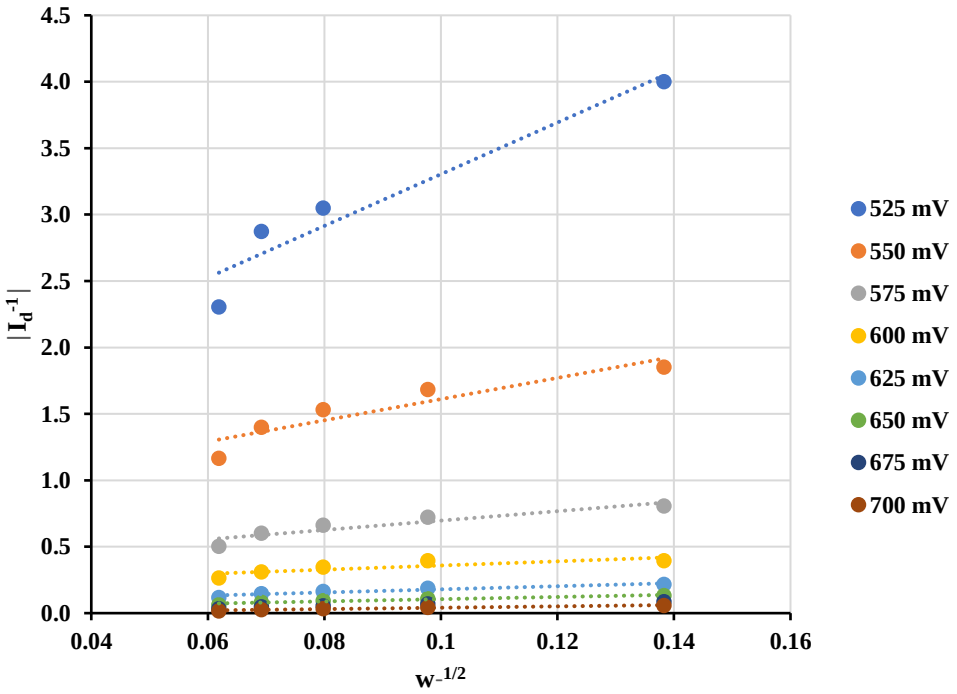

Figure 5.2.5. K-L plots of Co_3O_4 at different potentials

To evaluate the order of the OER reaction, m, and to justify the K-L plot, the following equation was used [6].

log of $|I_d| = \log |I_k| + m \log(|1-I_d/I_{dl}|)$ (5.2.3)

The slope m is calculated at different potentials. The order of the reaction, m for the sample Co_3O_4 was evaluated at three different potentials, namely, 525, 575 and 600 mV at various rotation speeds (500, 1000, 1500, 2000 and 2500 rpm) are shown in Figure 5.2.6. The analysis indicates that the order of the reaction is 1 irrespective of applied potential for the sample Co_3O_4. The same result was obtained for all the spinel oxide electrodes analyzed in this work. This confirms the first-order dependence of the OER process for spinel oxides. A reaction order of one suggests that only one hydroxyl group is participating at each active site and in each reaction step of OER including the rate-determining step [25]. Thus, with a 4 e^- transfer OER process and a reaction order of 1, the following OER mechanism can be suggested for spinel oxides, as proposed by many research groups for metal oxides under alkaline conditions. The mechanism includes some intermediates such as MO and MOOH groups. OER is a heterogeneous reaction. The electrocatalytic activity greatly depends on the interactions within

the intermediates such as MOH, MO and MOOH [22]. As explained in section 1.6.1., an optimal energy barrier for adsorption and desorption of intermediates are suitable for high catalytic activity.

$M + OH^- \rightarrow MOH + e^-$

$MOH + OH^- \rightarrow MO + H_2O + e^-$

$MO + OH^- \rightarrow MOOH + e^-$

$MOOH + OH^- \rightarrow M + O_2 + H_2O + e^-$

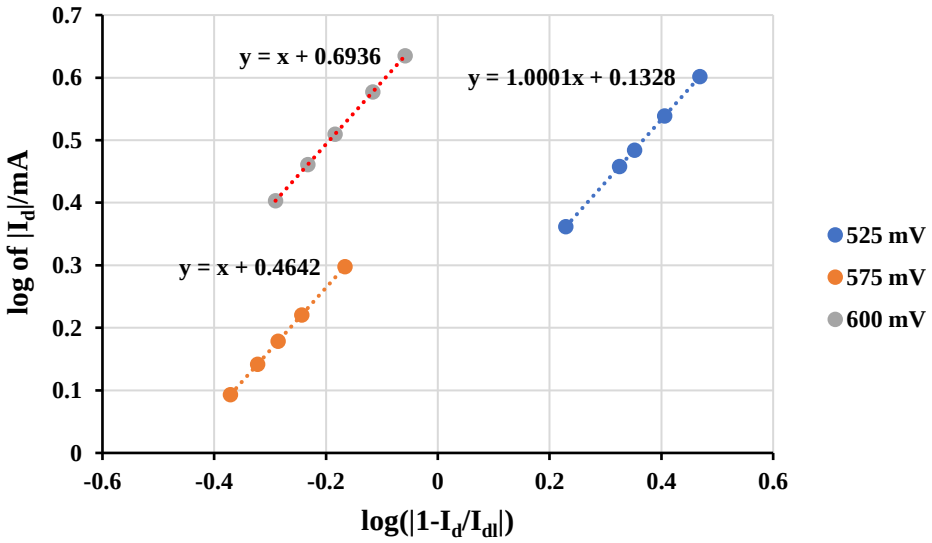

Figure 5.2.6. Evaluation of electrochemical reaction order with respect to O_2 for OER at Co_3O_4 electrode for different rotation speeds (500, 1000, 1500, 2000 and 2500 rpm) and potentials (525, 575 and 600 mV). The value of m is given by the slope of linear plots for each potential.

5.2.3. Catalytic activity of amorphous metal oxides

The catalytic activity of amorphous metal oxides was studied using cyclic voltammetry. Cyclic voltammograms were recorded at room temperature for CoO_x, $CuCo_2O_x$, $Ni_{0.5}Cu_{0.5}Co_2O_x$, $Fe_{0.1}Cu_{0.9}Co_2O_x$ and $Fe_{0.1}Ni_{0.9}Co_2O_x$ in a potential range of -100 mV -1000 mV at a scan rate of 50 mV s^{-1}. 1 M KOH was used as an electrolyte. The current density obtained from amorphous samples was reported as a function of the sample's geometric area (also called apparent current

density) and as a function of real surface area by normalizing the current density by the roughness factor of the corresponding sample.

The current density obtained from the unit geometric area is shown in Figure 5.2.7a. The CoO_x electrode possessed well-defined anodic and cathodic peaks before OER and has the characteristic shape of spinel oxides, while these peaks are absent for other samples. This could be due to the nanocrystalline spinel structure of CoO_x as indicated by X-ray diffraction analysis. The CoO_x possessed the lowest current density compared to other compositions. The Cu, Ni and Fe incorporation into the cobalt oxide increased surface area of the samples. The current density of the samples also increased with Cu, Ni, and Fe substitution in cobalt oxide. $Fe_{0.1}Ni_{0.9}Co_2O_x$ with the highest surface area possessed the highest current density. This indicates that the current density of amorphous samples is a function of the surface area of the electrode.

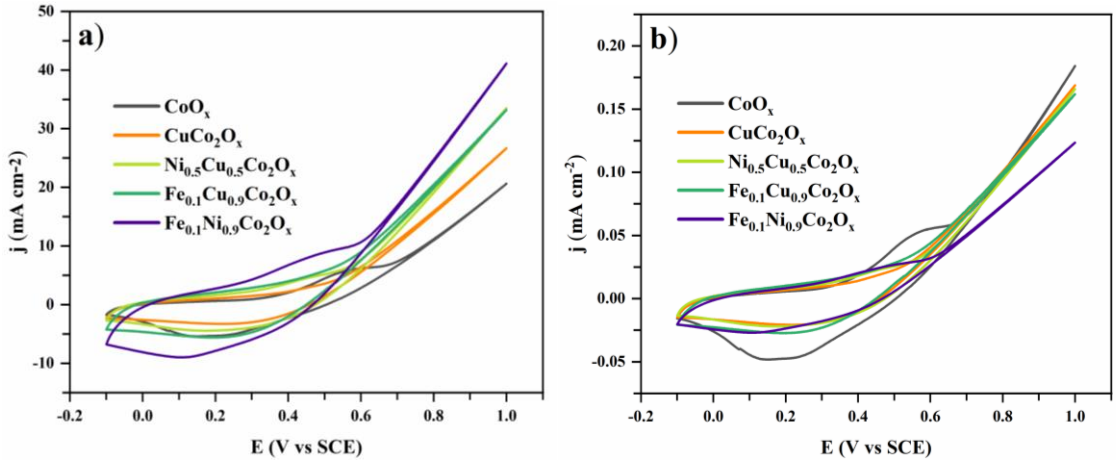

Figure 5.2.7. Cyclic voltammograms of amorphous metal oxides in 1M KOH recorded in a potential range of -0.1 V to 1.0 V (SCE) at a scan rate of 50 mV s^{-1}. a) current density normalized for geometric area b) current density normalized for sample's real surface area using the roughness factor.

When the current density was normalized to the real surface area using the roughness factor evaluated from CV, $Fe_{0.5}Cu_{0.5}Co_2O_x$ possessed the highest current density compared to other samples, while $Fe_{0.1}Ni_{0.9}Co_2O_x$ showed a lower current density. All other samples possessed similar current density (see Figure 5.2.7b). The lower activity of $Fe_{0.1}Ni_{0.9}Co_2O_x$ could be due to the presence of NiO species formed on the surface of the sample, $Fe_{0.1}Ni_{0.9}Co_2O_x$ contains a higher amount of Ni in the composition. In our previous work, $Fe_{0.1}Ni_{0.9}Co_2O_4$ spinel oxide was

found to be highly active, however, the corresponding amorphous oxide is showing a lower catalytic activity. Ni and/or Cu substitution did not significantly improve the catalytic activity when corrected for real surface area. Similar results were obtained in the case of spinel oxides, where, Co_3O_4 showed higher current density compared to Ni and/or Cu-substituted cobalt spinel oxide when normalized for real surface area [18, 19]. Since the roughness factor is associated with large error (see Table 5.1.3 in section 5.1.3), within the error, all the samples possess similar current density. Different compositions do not make a significant impact on their performance towards OER.

The onset potential is the potential at which the OER begins; a lower onset potential is a desirable property of a good catalyst. The onset potentials of amorphous metal oxides are given in Table 5.2.3. CoO_x showed the highest onset potential. Substitution of Cu, Ni, and Fe decreased the onset potential of the electrodes for OER. Fe substitution significantly lowered the onset potential of the electrodes, $Fe_{0.5}Cu_{0.5}Co_2O_x$ achieved the lowest onset potential. Several reports indicate that Fe could be the active site for the high catalytic activity [30, 31]. Burke *et al* found that the OER activity of $Co_{1-x}Fe_x(OOH)$ is 100 fold higher when $x \approx 0.6$ to 0.7 compared to $x = 0$ and observed a lower Tafel slope with Fe substitution (26 -39 mV dec^{-1}) for these compositions. Pure cobalt films possessed a Tafel slope of 62 mV dec^{-1}. They found that Fe incorporation enhances OH^- intercalation and facilitates the oxidation of $Co(OH)_2$ to CoOOH. They also observed an anodic shift of $Co^{2+/3+}$ with the incorporation of Fe in CoOOH, which indicates the strong electronic interaction of Co and Fe, thus modifying the electronic structure of the catalyst[31].

Table 5.2.3: Onset potential of amorphous and spinel oxides

Composition	Onset potential of amorphous metal oxides (mV)
Co_3O_4	556 ± 11
$CuCo_2O_4$	505 ± 3
$Ni_{0.5}Cu_{0.5}Co_2O_4$	518 ± 3

$Fe_{0.1}Cu_{0.9}Co_2O_4$	484 ± 28
$Fe_{0.1}Ni_{0.9}Co_2O_4$	499 ± 11
$Fe_{0.5}Co_{2.5}O_x$	488 ± 3
$Fe_{0.5}Cu_{0.5}Co_2O_x$	480 ± 10

In Figure 5.2.8, cyclic voltammograms of some of the spinel oxides from previous work are compared to those of amorphous metal oxide samples. The analysis indicates that spinel oxides show high catalytic activity compared to amorphous samples, at a given potential, spinel oxides possessed a higher current density compared to all amorphous metal oxides. According to XPS analysis, the surface of both amorphous and spinel oxides consists of different species, indicating a short-range order of various species or the formation of an amorphous layer on the surface of both these types of electrodes. However, a marked difference is observed in the catalytic activity of spinel oxides and corresponding amorphous metal oxides. This observation reveals that the bulk of the material also has a significant contribution towards the catalytic activity of the electrodes. Spinel oxides possess both tetrahedral and octahedral sites in their crystal structure. This allows these types of materials to accommodate different metal cations of different oxidation states and can improve the charge transfer properties and conductivity of the electrodes, which promote the catalytic activity towards OER. A long-range order of crystalline materials possibly enhances the electron transfer mechanism efficiently and hence the OER catalytic activity [32, 33]. By appropriate doping, the electronic structure of crystalline materials can be modified and the surface adsorption feature of oxygen-containing intermediates can be regulated giving rise to enhanced OER activity.

Indra *et al* showed that amorphous cobalt iron oxides outperform corresponding crystalline material when the current density is normalized by BET surface area of the electrode [34]. Koza *et al* found that both crystalline and amorphous cobalt oxides are active for OER. They obtained a Tafel slope of 49 mV dec^{-1} and an exchange current density of 2.0×10^{-10} A cm^{-2} for crystalline Co_3O_4. For amorphous cobalt oxide, they measured a Tafel slope of 36 mV dec^{-1} and an exchange current density of 5.4×10^{-12} A cm^{-2}. However, crystalline materials are found to be more stable than corresponding amorphous cobalt oxide, crystallinity and stability of the

materials were found to be the function of their annealing temperature. The samples deposited at 50 ºC to 90 ºC were found to be amorphous and those deposited above 103 ºC were found to be crystalline. Crystalline films adhere strongly to the substrate while amorphous films peeled off easily after drying [35].

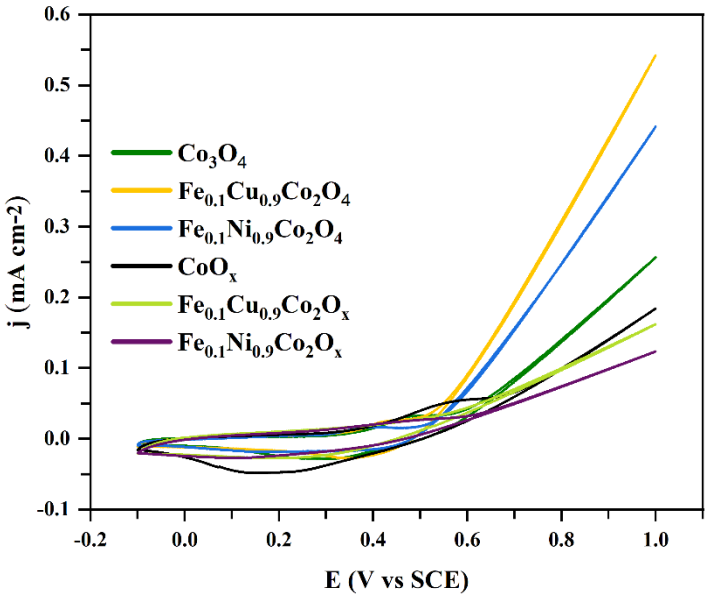

Figure 5.2.8. Cyclic voltammograms of amorphous metal oxides in 1M KOH for scans recorded in a potential range of -0.1 V to 1.0 V (SCE) at a scan rate of 50 mV s^{-1}. The current density is corrected for their real surface area using the roughness factor. CVs of $Fe_{0.1}Cu_{0.9}Co_2O_4$ and $Fe_{0.1}Ni_{0.9}Co_2O_4$ are adopted from Reference 19.

The Tafel plots of some of the amorphous samples were analyzed using the rotating disc experiment. These experiments were performed in 0.1 M KOH solution at 3000 rpm. The analysis indicates that amorphous samples have a higher Tafel slope than corresponding spinel oxides. For example, the Tafel slopes of $Fe_{0.5}Co_{2.5}O_x$ and $CuCo_2O_x$ are 301 mV dec^{-1} and 138 mV dec^{-1}, respectively. The Tafel plot of $CuCo_2O_x$ is shown in Figure 5.2.9. These higher Tafel slope values indicate slower OER kinetics of amorphous samples and proceed through a different OER mechanism [7, 34, 36, 37]. It is possible that the higher Tafel slope can be related to the electrochemical changes in the material's surface and sub-surface during OER. There is no proposed mechanism for Tafel slopes that are above 120 mV dec^{-1}.

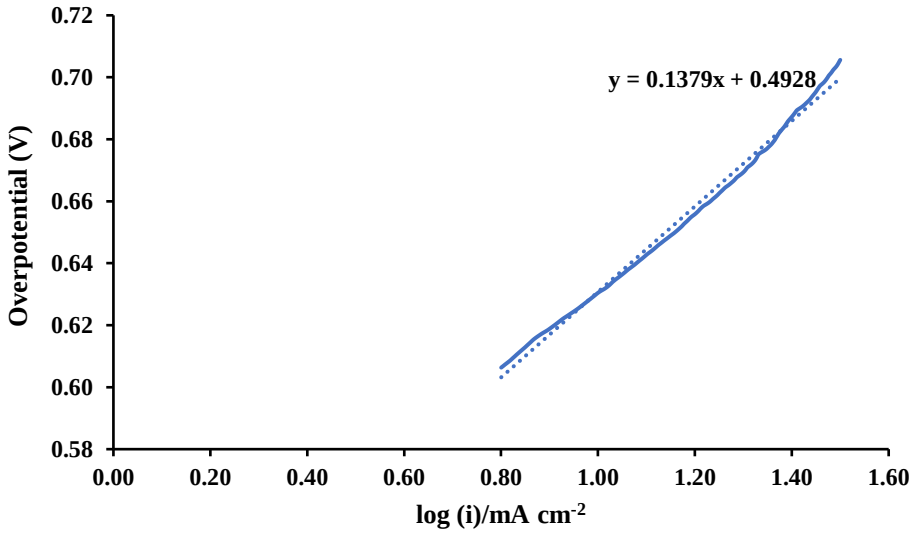

Figure 5.2.9. Tafel slope of $CuCo_2O_x$ in 0.1 M KOH solution at 3000 rpm

In Figure 5.2.10, the K–L plot of $Fe_{0.5}Co_{2.5}O_x$ performed at different rotating speeds and obtained at different potentials is given. A linear plot was obtained. Similar results were observed in the case of spinel oxides. The number of electrons is calculated at different potentials using equation 5.2.1. The number of electrons transferred varies from 2 to 6 with an average of 4 electrons during the reaction. The order of the reaction was determined from equation 5.2.3. A plot of $\log(|1-I_d/I_{dl}|)$ vs log of $|I_d|$ provided a linear plot (see Figure 5.2.11) for all potentials. Amorphous samples also have a reaction order of 1 as that of spinel oxides and therefore only one hydroxyl group is involved in each reaction step. The major difference we observed between the kinetic measurements of crystalline and amorphous metal oxides is their difference in Tafel slope, which indicates that these materials have different rate-determining steps. Crystalline materials exhibit a lower Tafel slope which implies that these materials are more active towards OER and electron transfer occurs more efficiently than corresponding amorphous materials. This observation is evident from their catalytic activity measurements. At a given potential, spinel oxides provided a higher current density than their amorphous counterparts.

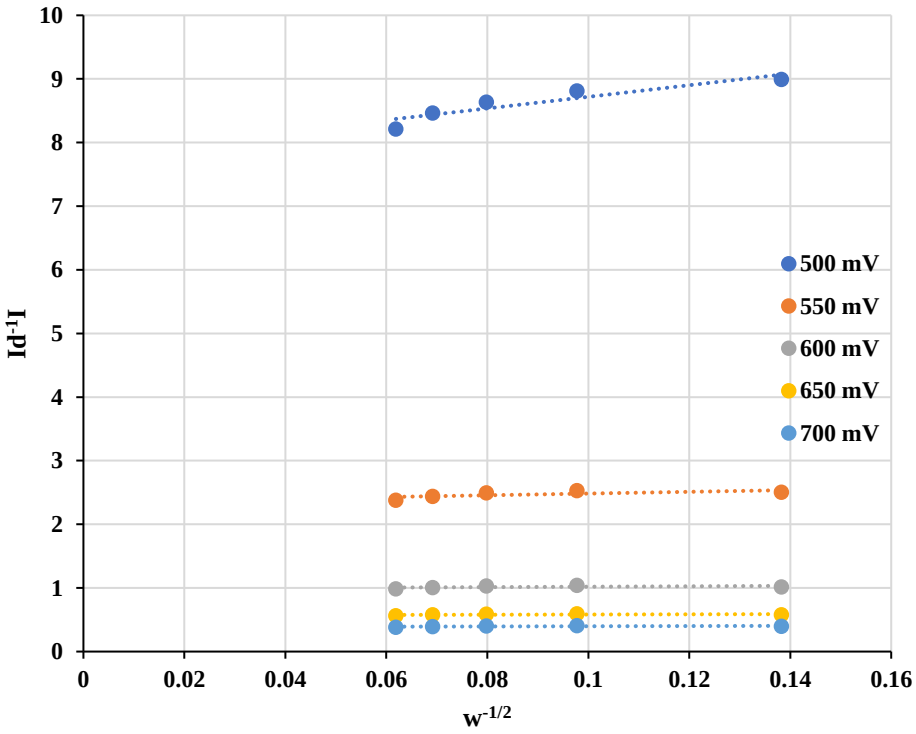

Figure 5.2.10. Koutecky–Levich K–L plots of $Fe_{0.5}Co_{2.5}O_x$

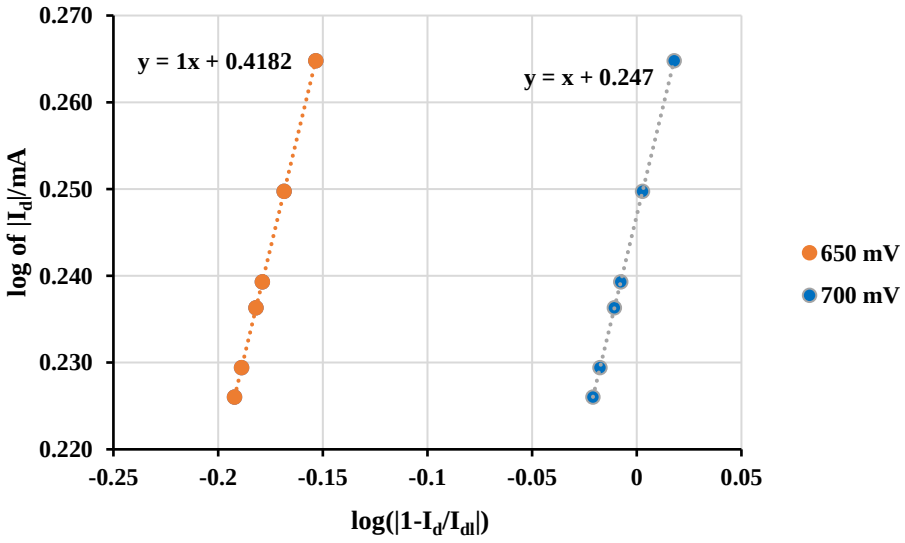

Figure 5.2.11. Evaluation of electrochemical reaction order with respect to O_2 for OER at $Fe_{0.5}Co_{2.5}O_x$ electrode for different rotation speeds (500, 1000, 1500, 2000, 2500 rpm and 300 rpm) and potentials (525, 575 and 600 mV). The value of m is given by the slope of linear plots for each potential.

The formation of cobalt oxyhydroxide layer prior to the OER was confirmed using *operando* spectroscopy techniques recently [38]. This skin layer continues to grow in the positive potential region and is found to be stable at high current densities. This layer has a significant impact on the OER kinetics and hence on the catalytic activity. Magnussen *et al* observed a lower Tafel slope for CoOOH (001) (52 mV dec^{-1}) than Co_3O_4 (111) (65 mV dec^{-1}) [38]. Studies reveal that FeOOH has low electrical conductivity, while Fe acts as an indirect active site by changing the spin or charge of other metal ions or stabilizing the active site, thereby increasing the activity towards OER [39, 40]. Xiang *et al* considered that the (Co, Fe)OOH is the active intermediate for the OER activity of $CoFe_2O_4$ [39] . Budianto *et al* proposed that the Co(Fe)-OOH layer has been formed during the OER which is very conductive and enhances the charge transfer reaction facilitating the OER process [41]. For our materials, even though Fe is not present on the surface of the samples, it facilitates the formation of an oxyhydroxy layer on the surface and improve conductivity, thereby improving OER kinetics.

Overall, our study reveals that spinel oxides outperform amorphous metal oxides for OER even though both of these types of materials possess similar surface structural features. The lower activity of amorphous materials could be the result of a lack of long-range ordered crystal structure. The long-range order of crystalline materials probably allows an effective electronic interaction between the atoms, where the doping effect would be larger than an amorphous sample [42]. In our study, Fe-substitution increased the electron binding energy of cobalt. While Cu and Ni substitution decreased the electron binding energy of cobalt in cobalt-based spinel oxides. Concurrently, Fe doping also increases the oxidation state of oxygen (meaning it is greater than -2). Consequently, these electronic and structural changes will influence the catalytic activity but the mechanism stays the same. Gao *et al* reported that the increased oxidation state of cobalt facilitates the oxidative addition of water to the catalyst, leading to an enhanced OER catalytic activity [43]. Zhang *et al* found that an increased oxidation state of cobalt significantly improved the catalytic activity of cobalt spinel oxide for OER. They have introduced cobalt vacancies in Co_3O_4 lattice and hence the oxidation state of cobalt was higher [44]. Meanwhile, this effect was negligible in the case of amorphous metal oxides.

One of the main objectives of our research is to study the correlation between the structure, composition, and catalytic activity of the materials that we employed as

electrocatalysts for OER. Scaling relations between the material's properties and their catalytic activity for OER is important and provides the scope for further improvements in the material design. In our study, we observed several correlations between various parameters and catalytic activities of our materials which will be discussed in the following chapter 6.

5.2.4. References

[1] M. Nasser, T. F. Megahed, S. Ookawara, H. Hassan, (2022). A review of water electrolysis–based systems for hydrogen production using hybrid/solar/wind energy systems. Environmental Science and Pollution Research 29, 58 (2022) 86994.

[2] S. Anwar, F. Khan, Y. Zhang, A. Djire, (2021). Recent development in electrocatalysts for hydrogen production through water electrolysis. Int. J. Hydrogen Energy, 46, 63, (2021) 32284.

[3] J. Zhang, H. B. Tao, M. Kuang, H. B. Yang, W. Cai, Q. Yan, Q. Mao, B. Liu, Advances in thermodynamic-kinetic model for analyzing the oxygen evolution reaction, ACS Catal. 10 (2020) 8597

[4] A. J. Bard, L. R. Faulkner, Eletcrochemical methods-Fundamentals and applications, 2nd ed.; New York, 2001

[5] S. Treimer, A. Tang, D. C. Johnson, A consideration of the application of Koutecký-Levich plots in the diagnoses of charge-transfer mechanisms at rotated disk electrodes. J. Electroanalysis 14, 3 (2002) 165

[6] M. de Koninck, S. C. Poirier, B. Marsan, $Cu_xCo_{3-x}O_4$ used as bifunctional electrocatalyst. J. Electrochem. Soc. 154**,** 4 (2007) A381

[7] E. Fabbri, A. Habereder, K. Waltar, R. Kotz, T. J. Schmidt, Developments and perspectives of oxide-based catalysts for the oxygen evolution reaction. Catal. Sci. Technol. 4, 11 (2014) 3800.

[8] S. Trasatti, Electrocatalysis in the anodic evolution of oxygen and chlorine, Electrochim. Acta, 29 (1984) 1503

[9] J. P. Singh, R. N. Singh, New active spinel-type $M_xCo_{3-x}O_4$ films for electro-catalysis of oxygen evolution, J. New Mat. Electrochem. Systems, 3 (2000) 131

[10] Y. Zhang, X. Zhou, F. Zhang, T. Tian, Y. Ding, H. Gao, Design and synthesis of Cu modified cobalt oxides with hollow polyhedral nanocages as efficient electrocatalytic and photocatalytic water oxidation catalyst, J. Catal., 352 (2017) 246

[11] J. Wang, W. Cui, Q. Liu, Z. Xing, A. M. Asiri, X. Sun, Recent progress in cobalt-based heterogeneous catalysts for electrochemical water splitting, Adv. Mater. 28 (2016) 215

[12] P. Bothra, S. K. Pati, Activity of water oxidation on pure and (Fe, Ni, and Cu)-substituted Co_3O_4, ACS Energy Lett., 1 (2016) 858

[13] C. Wei, S. Sun, D. Mandler, X. Wang, S. Z. Qiao, Z. J. Xu, Approaches for measuring the surface areas of metal oxide electrocatalysts for determining their intrinsic electrocatalytic activity, Chem. Soc. Rev. 48 (2019) 2518
[14] A. Eftekhari, Tuning the electrocatalysts for oxygen evolution reaction, J. Mater. Today Energy, 5 (2017) 37
[15] B. Chi, H. Lin, J. Li, Cations distribution of $Cu_xCo_{3-x}O_4$ and its electrocatalytic activities for oxygen evolution reaction, Int. J. Hydrog. Energy, 33 (2008) 4763
[16] E. Rios, J. L. Gautier, G. Poillerat, P. Chartier, Mixed valency spinel oxides of transition metals and electrocatalysis: case of the $Mn_xCo_{3-x}O_4$ system, J. Electrochim. Acta 44 (1998) 1491
[17] L. Xu, Q. Jiang, Z. Xiao, X. Li, J. Huo, S. Wang, L. Dai, Plasma-Engraved Co_3O4 Nanosheets with Oxygen Vacancies and High Surface Area for the Oxygen Evolution Reaction, Angew. Chem. Int. Ed. 55 (2016) 5277.
[18] S. Thekkoot, R. Islam, O Gray, S. Morin, Efficiency of nanostructured $Cu_xCo_{3-x}O_4$ and $Ni_xCu_{1-x}Co_2O_4$ electrodes as electrocatalysts for the oxygen evolution reaction – revisited, Electrochim. Acta, 471 (2023), 143339
[19] S. Thekkoot, R. Islam, S. Morin, Improved oxygen evolution reaction performance with addition of Fe to form $Fe_yCu_{x-y}Co_{3-x}O_4$ and $Fe_yNi_{x-y}Co_{3-x}O_4$ (x = 0.5, 1 and y = 0.1, 0.15) spinel oxides, Electrochim. Acta, 378 (2021) 138116
[20] R. N. Singh, J. P. Pandey, N. K. Singh, B. Lal, P. Chartier, J.-F. Koenig, Sol-gel derived spinel $M_xCo_{3-x}O_4$ (M = Ni, Cu; $0 \leq x \leq 1$) films and oxygen evolution, Electrochim. Acta, 45 (2000) 1911.
[21] H. Li, W. Kang, L. Wang, Q. Yue, S. Xu, H. Wang, J. Liu, Synthesis of three-dimensional flowerlike nitrogen-doped carbons by a copyrolysis route and the effect of nitrogen species on the electrocatalytic activity in oxygen reduction reaction, Carbon 54 (2013) 249.
[22] N. T. Suen, S. F. Hung, Q. Quan, N. Zhang, Y. J. Xu, H. M. Chen, Electrocatalysis for the oxygen evolution reaction: recent development and future perspectives, Chem. Soc. Rev., 46 (2017) 337.
[23] L. Yao, W. Yang, Y. Niu, J. Liu, S. Zhang, S. Wu, Z. Deng, L. Ma, C. Wang, Z. Cao, Comparison of the effects of cation and phosphorus doping in cobalt-based spinel oxides towards the oxygen evolution reaction, CrystEngComm, 23 (2021) 1849.

[24] J. P. Sing, R. N. Sing, New active spinel-type $M_xCO_{3-x}O_4$ films for electro-catalysis of oxygen evolution, J. New Mater. Electrochem. Syst., 3 (2000) 131
[25] L. Negahdar, F. Zeng, S. Palkovits, C. Broicher, R. Palkovits, Mechanistic Aspects of the Electrocatalytic Oxygen Evolution Reaction over Ni-Co Oxides, J. ChemElectroChem 6 (2019) 5588.
[26] J. Scholz, M. Risch, K. A. Stoerzinger, G. Wartner, Y. Shao-Horn, C. Jooss, Rotating Ring−Disk Electrode Study of Oxygen Evolution at a Perovskite Surface: Correlating Activity to Manganese Concentration, J. Phys. Chem. C, 120 (2016) 27746.
[27] R.G. G. Huerta, G. R. Sanchez, P.B. Balbuena, Oxygen evolution in Co-doped RuO_2 and IrO_2: Experimental and theoretical insights to diminish electrolysis overpotential, J. Power Sources, 268 (2014) 69
[28] M. A. A. Sepulveda, C. Dhital, A. Huq, L. Li, C. A. Bridges, M. P. Paranthaman, S. R Narayanan, D. J. Quesnel, D. A. Tryk, A. Manivannan, The Influence of Fe substitution in lanthanum calcium cobalt oxide on the oxygen evolution reaction in alkaline media, J. Electrochem. Soc., 163, 9 (2016) F1124.
[29] I. Nikdov, R. Darkaoui, E. Zhecheva, R. Stoyanova, N. Dimitrov, T. Vitanov, Electrocatalytic activity of spine1 related cobaltites $MCo_{3-x}O_4$ (M = Li, Ni, Cu) in the oxygen evolution reaction, J. Electroanal. Chem., 429 (1997) 157
[30] L. Bai, X. Wen, J. Guan, (2019). Amorphous Fe-Co-Ni oxide for oxygen evolution reaction. Mater. Today Energy, 12 (2019) 311.
[31] M. S. Burke, M. G. Kast, L. Trotochaud, A. M. Smith, S. W. Boettcher, Cobalt−iron (oxy)hydroxide oxygen evolution electrocatalysts: The role of structure and composition on activity, stability, and mechanism, J. Am. Chem. Soc., 137 (2015) 3638.
[32] J. S. Kim, B. Kim, H. Kim, K. Kang, (2018). Recent progress on multimetal oxide catalysts for the oxygen evolution reaction. Adv. Energy Mater. 8, 11 (2018) 1702774
[33] S. Trasatti, G. Lodi, Electrodes of Conductive Metallic Oxides, Part A-B; Elsevier Science Publishers: Amsterdam, The Netherlands, 1980/1981.
[34] A. Indra, P. W. Menezes, N. R. Sahraie, A. Bergmann, C. Das, M. Tallarida, D. Schmeiber, P. Strasser, M. Driess, Unification of catalytic water oxidation and oxygen reduction reactions: Amorphous beat crystalline cobalt iron oxides. J. .Am. Chem. Soc. 136 (2014) 17350

[35] J. A. Koza, Z. He, A. S. Miller, J. A. Switzer, Electrodeposition of crystalline Co_3O_4, A catalyst for the oxygen evolution reaction. Chem. Mater., 24, 18 (2012) 3567.
[36] C. Bocca, A. Barbucci, M. Delucchi, G. Cerisola, Nickel -cobalt oxide-coated electrodes in oxygen evolution reaction (OER) in an alkaline solution, Int. J. Hydrogen Energy 24 (1999) 21
[37] C. Hu, L. Zhang, J. Gong, Recent progress made in the mechanism comprehension and design of electrocatalysts for alkaline water electrolysis, Energy Environ. Sci. 12 (2019) 2620
[38] F. Reikowski, F. Maroun, I. Pacheco, T. Wiegmann, P. Allongue, J. Stettner, O. M. Magnussen, Operando surface X-ray diffraction studies of structurally defined Co_3O_4 and CoOOH thin films during oxygen evolution, ACS Catal., 9 (2019) 3811
[39] W. Xiang, N. Yang, X. Li, J. Linnemann, U. Hagemann, O. Ruediger, M. Heidelmann, T. Falk, M. Aramini, S. DeBeer, M. Muhler, K. Tschulik, T. Li,. 3D atomic-scale imaging of mixed Co-Fe spinel oxide nanoparticles during oxygen evolution reaction. Nat. Commun., 13, 1 (2022).
[40] X. T. Wang, T. Ouyang, L. Wang, J. H. Zhong, T. Ma, Z. Q. Liu, Redox-Inert Fe^{3+} Ions in Octahedral Sites of Co-Fe Spinel Oxides with Enhanced Oxygen Catalytic Activity for Rechargeable Zinc-Air Batteries, Angew Chem Int. Ed. 58, 38 (2019) 13291
[41] E. Budiyanto, S. Salamon, Y. Wang, H. Wende, H. Tuysuz, Phase Segregation in Cobalt Iron Oxide Nanowires toward Enhanced Oxygen Evolution Reaction Activity. JACS Au, 2, 3 (2022) 697.
[42] X. Luo, L. Zhang, M. Guo, Z. Liu, D. Wu, D. Zhen, Y. Liu, (2022). Engineering the structural defects of spinel oxide nanoneedles by doping of V for a highly efficient oxygen evolution reaction. ACS Applied Mater. Interfaces 14 (2022) 50055.
[43] Y. Zhang, X. Zhou, F. Zhang, T. Tian, Y. Ding, H. Gao, Design and synthesis of Cu modified cobalt oxides with hollow polyhedral nanocages as efficient electrocatalytic and photocatalytic water oxidation catalyst, J. Catal., 352 (2017) 246
[44] R. Zhang, Y. C. Zhang, L. Pan, G. Q. Shen, N. Mahmood, Y. H. Ma, Y. Shi, W. Jia, L. Wang, X. Zhang, Engineering cobalt defects in cobalt oxide for highly efficient electrocatalytic oxygen evolution, ACS Catal., 8 (2018) 3803

Chapter 6. Important materials science correlations for the mixed transition metal oxides

6.1. Introduction

The sluggish OER kinetics is a major contributing factor to the low efficiency of the water electrolysis process. Developing highly efficient and stable non-noble electrocatalysts for OER is of great interest to researchers as these materials can achieve improved energy conversion efficiency as well as provide materials with large surface areas that are also dimensionally stable. Designing high-efficiency electrocatalysts requires a deeper understanding of composition-structure-activity relationships [1]. The various correlations that were observed in our study will be discussed in this Chapter. Please note that each composition is represented by the same color.

6.2. Correlation between crystallite size and lattice parameter of spinel oxides

In Figure 6.1, the crystallite size of $Cu_xCo_{3-x}O_4$ electrodes is plotted as a function of the lattice parameter where the crystallite size decreases with an increase of the lattice parameter. This could be attributed to the presence of the secondary metal in the crystal lattice causing lattice stress and strain or differences in nucleation and growth kinetics with the composition of the solid solution [2, 3]. The particle size of our materials can influence their electronic properties and hence the catalytic activity of the materials [4, 5]. In our study, we observed an increase in surface area with the addition of Cu and Ni in the cobalt oxide lattice. This could be due to the decrease in particle size, SEM analysis supports this observation. We have also observed an increase in apparent current density; a large surface area provides more active sites on the surface of the sample.

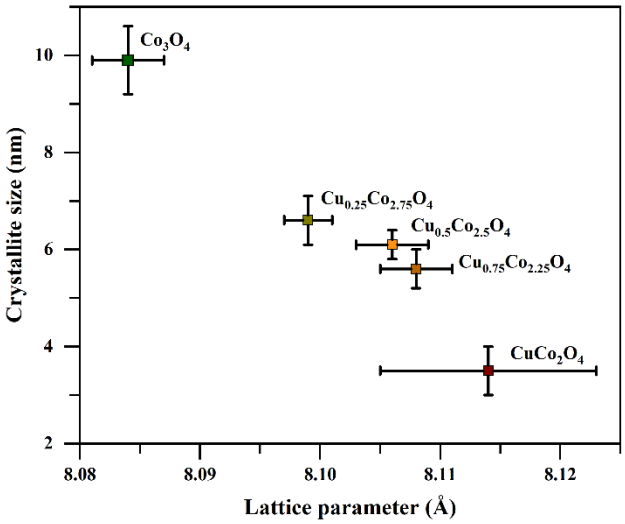

Figure 6.1. Crystallite size plotted as a function of the lattice parameter of $Cu_xCo_{3-x}O_4$.

6.3. Correlation between current density (corrected for real surface area) and lattice parameter

In Figure 6.2, the current density (measured at 1V vs. SCE) corrected for real surface area is plotted as a function of the lattice parameter. The current density decreased as the lattice parameter increased for $Cu_xCo_{3-x}O_4$ and $Ni_xCu_{1-x}Co_2O_4$. However, a gradual decrease in the current density (at 1V) with an increase of lattice parameter was observed only in the case of $Cu_xCo_{3-x}O_4$, such an effect was not observed for $Ni_xCu_{1-x}Co_2O_4$ electrodes. The change in lattice parameter might affect the electronic properties of $Cu_xCo_{3-x}O_4$ and $Ni_xCu_{1-x}Co_2O_4$, which lead to the modifications in the adsorption and desorption of the oxygen intermediates species during the OER, hence the catalytic properties [3].

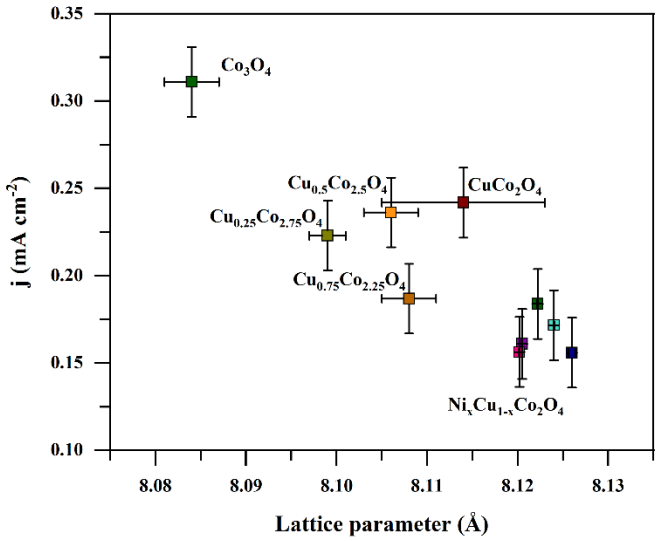

Figure 6.2. Graph of the current density corrected for real surface area as a function of lattice parameters of $Cu_xCo_{3-x}O_4$ and $Ni_xCu_{1-x}Co_2O_4$.

6.4. Correlation between electron binding energy of lattice oxide and Co^{2+}(or Co^{3+}) of spinel oxides

In Figure 6.3, the binding energy of lattice oxide is plotted as a function of the binding energy of Co^{2+} (or Co^{3+}) incorporated in the spinel species, we observed an almost linear correlation. The composition and defects influence the chemical state of each atom in the composition. In general, our study indicates that Co^{2+} or Co^{3+} of (spinel oxide species) Cu and/or Ni-containing cobalt oxides have lower electron binding energy compared to that of Fe-substituted cobalt oxides. Co^{2+} or Co^{3+} of pure cobalt oxides also possesses a higher binding energy compared to Cu and/or Ni-substituted spinel oxides. We also observed that the increase of binding energy of Co^{2+} or Co^{3+} is accompanied by an increase of electron binding energy of lattice oxide, the higher oxidation state of cobalt probably shifting the oxygen electron density towards cobalt and subsequent increase of the electron binding energy of lattice oxygen [6, 7].

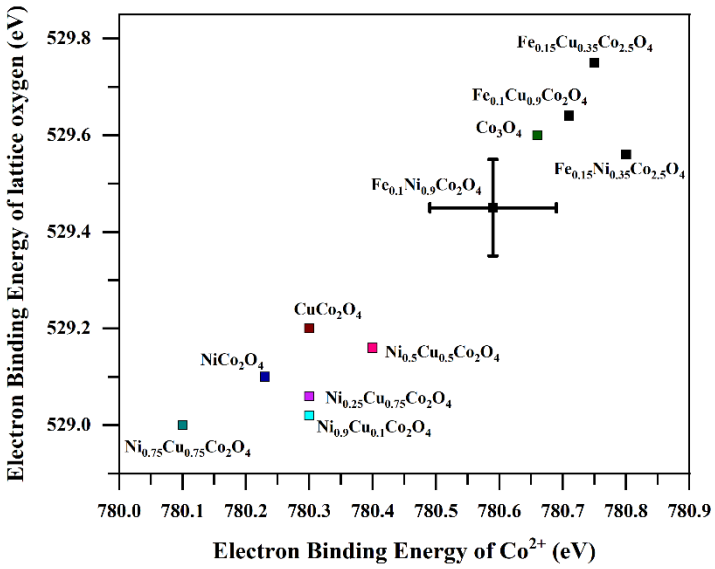

Figure 6.3. The electron binding energy of lattice oxygen is plotted as a function of the electron binding energy of Co^{2+}. Error bar is shown for $Fe_{0.1}Ni_{0.9}Co_2O_4$.

6.5. Correlation between the apparent current density and double-layer capacitance of crystalline and amorphous samples

In Figure 6.4a, a correlation graph between the apparent current density of the amorphous samples at 1V (vs. SCE) and their double-layer capacitance is given, the current density linearly increases with capacitance. This reveals that for amorphous samples, the surface area of the sample is the major contributing factor for increasing the current density rather than its composition. However, this trend is not observed in the case of spinel oxides (see Figure 6.4b), where the factors affecting their catalytic activity are different from the amorphous samples. As mentioned in the literature, abundant active sites and surface exposed defects drive the catalytic performance of amorphous metal oxides [8, 9, 10] and hence surface area can be viewed as the main source for the OER current. When the OER current is corrected for differences in the surface area of the materials an interesting correlation is observed (see section 6.6).

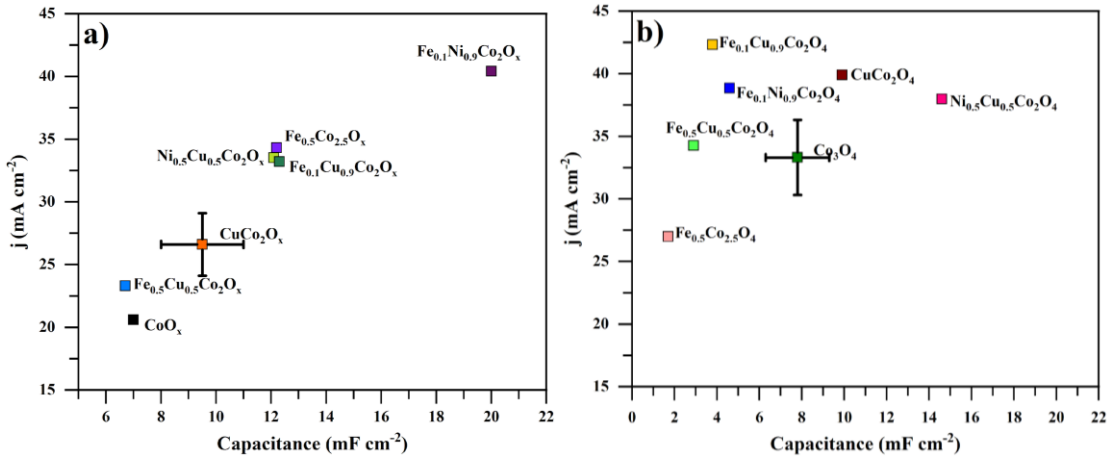

Figure 6.4. The current density obtained from the unit geometric area is plotted as a function of the double-layer capacitance of samples. a) amorphous metal oxides b) spinel oxides

6.6. Correlation between current density (corrected for real surface area) and the electron binding energy of Co^{2+} (or Co^{3+})

From the XPS data analysis and cyclic voltammetry measurements, we observed a correlation between the current density corrected for the real surface area and the electron binding energy of cobalt (Co^{2+} and Co^{3+}) of spinel oxides. The current density increased with the increase of the electron binding energy of Co (Co^{2+} and Co^{3+}) as shown in Figure 6.5b. The assumption that an increase in surface area is the main reason for the good performance of amorphous mixed transition metal oxide materials is further supported by the absence of correlation between the electron binding energy of Co and the OER current for these materials (Figure 6.5a). We also noticed that the presence of Fe increased the binding energy of the cobalt ions in spinel oxides, as the amount of Fe increased, the binding energy of cobalt ions also increased, which also resulted in an increase of current density. This could be associated with a more suitable bond strength in the presence of Fe. Following the Sabatier principle, the shorter Co-O bonds would yield stronger Co-O* and Co-OH* bonds and this would more readily result in the successful protonation of the Co-O* intermediate in the rate-determining step of the spinel oxides (see Section 5.2.2. for discussion about the OER mechanism on the spinel oxides studied here [11].

The studies indicate that the incorporation of Fe introduces changes in the oxidation state of Ni and Co that influence the OER catalytic activity [12, 13]. Lu *et al* prepared

$M_{0.1}Ni_{0.9}Co_2O_4$ (M= Mn, Fe, Cu, Zn). They observed higher Co^{2+}/Co^{3+} and lower Ni^{2+}/Ni^{3+} ratio for $Fe_{0.1}Ni_{0.9}Co_2O_4$ sample and is found to be an excellent bifunctional catalyst, where the higher number of Ni^{3+} and Co^{2+} sites facilitate the OER and ORR (oxygen reduction reaction) respectively [12]. Friebel *et al* observed a high OER catalytic activity (500 fold) with mixed (Ni, Fe) oxyhydroxides over their NiOOH or FeOOH parent compounds. This high catalytic activity was attributed to the unusually short bond distance of the Fe-O bond as it provides optimal adsorption energies to OER intermediates [11].

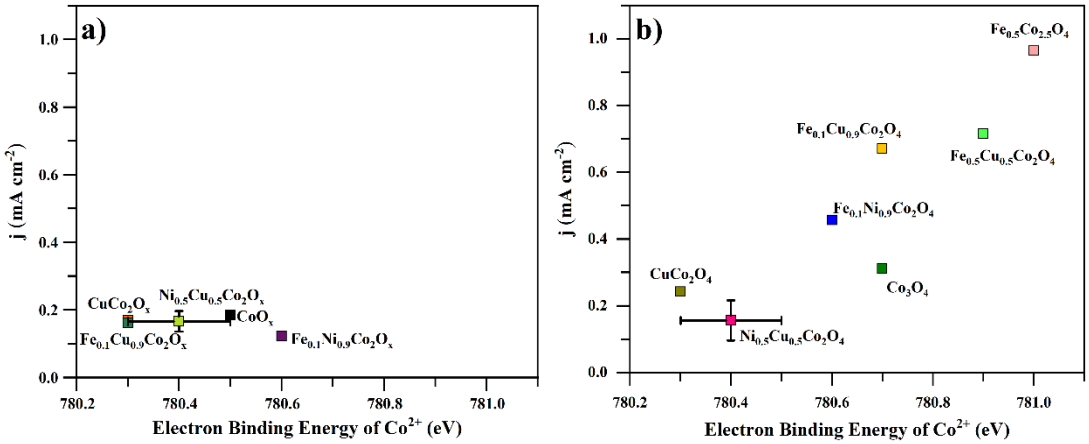

Figure 6.5. The current density obtained from the unit real surface area is plotted as a function of electron binding energy of Co^{2+}. a) amorphous metal oxide and b) spinel oxide.

Several studies correlated the high OER performance of materials to the observed high Co^{2+} to Co^{3+} ratio [12]. The XPS analysis of all our spinel oxide samples indicates that the Co^{2+} to Co^{3+} ratio is higher than the stoichiometric ratio (0.5). Co_3O_4 possessed the highest Co^{2+} to Co^{3+} ratio and has comparatively a higher current density than Cu and Ni-substituted cobalt oxides. Fe-containing spinel oxides also possessed a lower Co^{2+} to Co^{3+} ratio than Co_3O_4 but displayed a higher current density. A direct correlation between the Co^{2+} to Co^{3+} ratio and their catalytic performance was not observed in this study (see Figure 6.6).

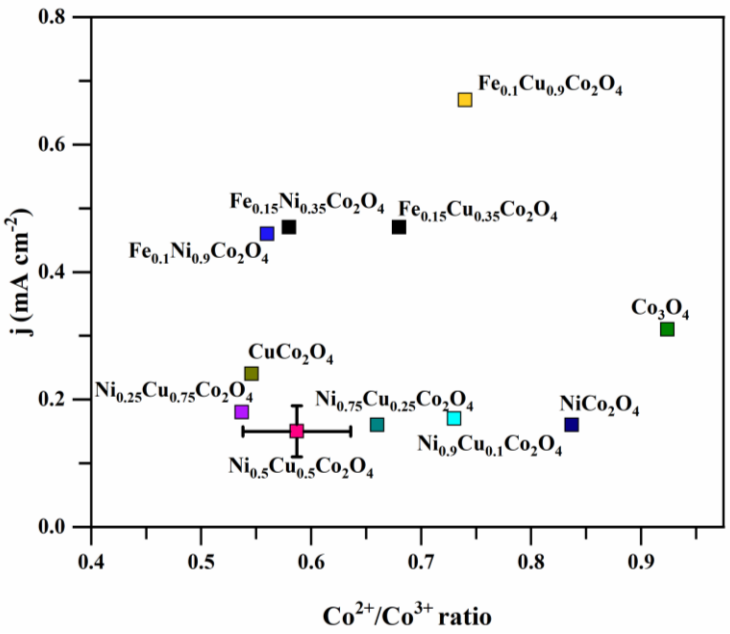

Figure 6.6. The current density obtained from the unit real surface area of spinel oxides is plotted as a function Co^{2+}/Co^{3+} ratio.

In the case of our compounds, Fe is negligible on the surface of crystalline materials. using XPS. In amorphous materials, the observed current density is mainly a function of the surface area of the sample, while this effect is not very significant in the case of crystalline materials. Even though the surface of amorphous samples and spinel oxides have similar surface structural features. Our study indicates that the crystal structure of the materials plays an important role in catalytic activity. This effect is more evident in the case of Fe-substituted cobalt oxides. Fe-substituted cobalt spinel oxides outperformed other spinel oxides. Meanwhile, within the error, Fe-substitution in amorphous cobalt oxides does not show a significant impact on the catalytic activity. Therefore, we conclude that the composition (including doping) and crystallinity play a very important role in the catalytic activity, possibly due to better charge transfer kinetics and favorable electronic effect in these crystalline materials. In spinel oxides, a synergic effect of composition and structure is an important controlling factor deciding the catalytic activity of these materials [8, 14, 15].

6.7. References

[1] J. Li, Oxygen evolution reaction in energy conversion and storage: Design strategies under and beyond the energy scaling relationship, Nano-Micro Lett. 14 (2022) 112.
[2] H. Ghayour, M. Abdellahi, A brief review of the effect of grain size variation on the electrical properties of $BaTiO_3$-based ceramics, J. Power Technol., 292 (2016) 84.
[3] A.I.Y. Tok, S.W. Du, F.Y.C. Boey, W.K. Chong, Hydrothermal synthesis and characterization of rare earth doped ceria nanoparticles, J. Mater. Sci. Eng. A, 466 (2007) 223.
[4] D. Prieur, W. Bonani, K. Popa, O. Walter, K. W. Kriegsman, M. H. Engelhard, X. Guo, R. Eloirdi, T. Gouder, A. Beck, T. Vitova, A. C. Scheinost, K. Kvashnina, P. Martin, Size dependence of lattice parameter and electronic structure in CeO_2 nanoparticles, J. Inorg. Chem. 59 (2020) 5760.
[5] K. Chakrapani, G. Bendt, H. Hajiyani, I. Schwarzrock,T. Lunkenbein, S. Salamon, J. Landers, H. Wende, R. Schlçgl, R. Pentcheva, M. Behrens, S. Schulz, Role of Composition and size of cobalt ferrite nanocrystals in the oxygen evolution reaction, ChemCatChem., 9 (2017) 2988.
[6] N. J. Henson, P. J. Hey, A. Redondo, Density functional theory studies of binding of molecular oxygen with Schiff's base complexes of cobalt, Inorg. Chem. 38 (1999) 1618.
[7] C.F. Windisch Jr., G. J. Exarhos, K. F. Ferris, M. H. Engelhard, D.C. Stewart, Infrared transparent spinel films with p-type conductivity, Thin Solid Films, 45 (2001) 398.
[8] J. S. Kim, B. Kim, , H. Kim, K. Kang, (2018). Recent Progress on Multimetal Oxide Catalysts for the Oxygen Evolution Reaction. Adv. Energy Mater., 8, 11 (2018) 1702774
[9] C. Zhang, C. P. Berlinguette, S. Trudel, (2016). Water oxidation catalysis: An amorphous quaternary Ba-Sr-Co-Fe oxide as a promising electrocatalyst for the oxygen-evolution reaction. Chem. Commun. 52, (2016) 1513
[10] A. Irshad, N. Munichandraiah, (2015). High catalytic activity of amorphous Ir-Pi for oxygen evolution reaction. ACS Appl. Mater. Interfaces, 7 (2015) 15765.
[11] D. Friebel, M. W. Louie, M. Bajdich, K. E. Sanwald, Y. Cai, A. M. Wise, M. J. Cheng, D. Sokaras, T. C. Weng, R. A. Mori, R. C. Davis, J. R. Bargar, J. K. Norskov, A. Nilsson, A. T. Bell, Identification of highly active Fe sites in (Ni,Fe)OOH for electrocatalytic water splitting, J. Am. Chem. Soc. 137 (2015) 1305.

[12] Y. T. Lu, Y. J. Chien, C. F. Liu, T. H. You, C. C. Hu, Active site-engineered bifunctional electrocatalysts of ternary spinel oxides, $M_{0.1}Ni_{0.9}Co_2O_4$ (M: Mn, Fe, Cu, Zn) for the air electrode of rechargeable zinc–air batteries, J. Mater. Chem. A, 5 (2017) 21016
[13] Anantharaj, S., Kundu, S., & Noda, S. (2021). "The Fe Effect": A review unveiling the critical roles of Fe in enhancing OER activity of Ni and Co based catalysts. Nano Energy 80 (2021)105514
[14] A.C. Tavares, M.A.M. Cartaxo, M.I. da Silva Pereira, F.M. Costa J. Electroanal. Chem. 464 (1999) 187.
[15] X. M. Liu, X. Cui, K. Dastafkan, H. F. Wang, C. Tang, C. Zhao, A. Chen, C. He, M. Han, Q. Zhang, Recent advances in spinel-type electrocatalysts for bifunctional oxygen reduction and oxygen evolution reactions. J. Energy Chemistry, 53 (2020) 290

Chapter 7. Conclusion and future work

7.1. Conclusion

Hydrogen is a promising clean energy source that can be produced sustainably by water electrolysis. Both HER and OER are associated with large energy barriers, however, the OER at the anode has very sluggish kinetics which reduces the overall efficiency of the water electrolysis process. The lack of understanding of the controlling factors governing the performance of electrocatalyst materials has greatly hindered the development of highly active catalysts for the OER. Our research work was aimed at investigating the correlation between structure, composition, and performance of materials (cobalt-based amorphous metal oxides and spinel oxides) for the OER, with the objective of establishing guidelines to design highly efficient electrocatalysts for the OER so that high current density can be achieved at lower overpotentials.

To achieve our goal, we have prepared spinel oxides $Cu_xCo_{3-x}O_4$ ($0 \leq x \leq 1$), $Ni_xCu_{1-x}Co_2O_4$ ($0 \leq x \leq 0.75$) and $Fe_yCu_{x-y}Co_xO_4$ (x=1, 1.5 and y = 0.1, 0.15) and performed XPS analysis to study the surface structure and composition. We have also prepared cobalt-based amorphous materials (CoO_x, $CuCo_2O_x$, $Ni_{0.5}Cu_{0.5}Co_2O_x$, $Fe_{0.1}Cu_{0.9}Co_2O_x$ and $Fe_{0.1}Ni_{0.9}Co_2O_x$), the counterparts of spinel oxides prepared in the Morin's group, to understand how the structure of materials influences their observed catalytic activity towards OER. These materials were characterized by SEM, EDX, XRD, TEM, and XPS. The electrochemical measurements were performed using CV and EIS. We have also investigated the underlying kinetics of the catalyzed reactions for spinel oxides and amorphous metal oxides. The surface area measurements were performed on $Cu_xCo_{3-x}O_4$ ($0 \leq x \leq 1$), $Ni_xCu_{1-x}Co_2O_4$ ($0 \leq x \leq 0.75$), and amorphous samples using cyclic voltammetry, and verified using EIS and differential capacitance measurements.

One of the important achievements of our research work is the successful synthesis of ternary amorphous metal oxides that have been rarely studied for OER. The XRD analysis confirmed the formation of an amorphous phase, and we observed a very close agreement between the EDX and stoichiometric compositions. SEM analysis showed a smooth compact structure for all the compositions, and no crystallites were formed on the surface of amorphous samples as opposed to spinel oxides, which further supports the formation of the amorphous phase.

We were able to investigate a very detailed surface analysis of crystalline and amorphous samples. The surface structure and composition analyses are highly useful in our studies as the

electrode reactions are happening on the surface of the electrodes. The binding energy of each element uniquely represents the chemical state of that element on the surface of the sample. Even though XRD analysis confirmed the formation of spinel structure, the XPS analysis indicated that metal atoms of different binding energies exist on the sample surface, which can be assigned to different species such as oxides, hydroxides, and hydroxy oxides. The surface analysis of amorphous metal oxides also displayed similar surface structural features, where the surface has metal atoms of different binding energies indicating the formation of different species. XPS analysis also provided information about the oxidation state of metal ions on the sample's surface, the metal ions in both amorphous and spinel oxides exist in different oxidation states.

XPS analysis also allowed us to study the variation of the binding energy of elements under the influence of other metal ions in the composition. The analysis reveals that cobalt ions (Co^{2+} or Co^{3+}) in Ni and Cu-containing samples possess low binding energy compared to pure cobalt oxide, while Fe-containing samples have higher binding energy. It is also evident from our study that the binding energy of cobalt ions increased with an increase in Fe content in the composition. Moreover, the increase in the binding energy of cobalt ions is also accompanied by an increase in the binding energy of lattice oxygen, the electron density of oxygen ions probably shifts towards cobalt ions due to its increased oxidation state. These variations in the binding energy of elements would also affect the adsorption and desorption of OER intermediates. However, the site occupation of metal ions cannot be completely understood from XPS analysis.

From our understanding, a systematic and detailed study of a series of metal oxides has not been done before. This allowed us to obtain consistent material property correlations between various parameters. This will also allow us to scale material properties based on their structure (bulk and surface) and composition. The material property correlation of different parameters between a few samples leads to inconsistent trends in the material property correlations.

In order to find an optimal electrocatalyst, the intrinsic electrocatalytic activity of the samples was evaluated by normalizing the current density by the real surface area of the corresponding sample. The accurate evaluation of the surface area of the samples confirms the reliable assessment of optimal electrocatalysts. The Brunauer–Emmett–Teller (BET) method is a commonly used method for surface area measurements. However, this method requires a fairly large amount of catalyst for an accurate measurement. Since we have a very thin film deposited

on the substrate with loading < 1 mg, the BET method is not suitable to evaluate the surface area of our samples.

The validity of the surface area measurement using the CV method is still contested by some scientists in part due to the large error associated with these measurements and the large variability in surface area between samples prepared using different preparation methods. We performed surface area measurements using electrochemical methods such as CV, differential capacitance, and electrochemical EIS. These measurements show good agreement between the double-layer capacitance values measured for amorphous and crystalline materials, which indicates that electrochemical methods are an effective tool for measuring the surface area of the electrodes. This provided us with the confidence to use these values for normalizing the current density obtained from the electrodes during CV.

The electrocatalytic activity of the spinel oxides was evaluated by CV. Even though Ni and Cu substituted samples showed high apparent current density, when corrected for real surface area, pure cobalt oxides possessed the higher current density which indicates that Co is the active site for OER. Furthermore, as indicated by XPS analysis, Fe is not present on the surface of the sample, however, Fe-containing spinel oxides are highly active for OER which further supports the fact that the cobalt ions are responsible for the adsorption and desorption of OER reaction intermediates on the surface. The presence of Fe in the composition provided a suitable binding energy to cobalt ions which substantially enhanced the catalytic activity of these materials for OER.

Another important finding of our research includes several interesting correlations between various structural and chemical parameters as well as the structural and electrochemical characteristics of our samples. These correlations help us to scale the material properties based on their structure and composition. X-ray diffraction data analysis of $Cu_xCo_{3-x}O_4$ revealed that the lattice parameter and crystallite size of the samples were correlated inversely. The substitution of Co with Cu increased the lattice parameter of the sample due to the higher ionic radius of copper, while the presence of secondary metal ions in the cobalt lattice decreased the crystallinity of the samples. We also observed an inverse correlation between the lattice parameter and the current density of the spinel oxides. The changes in the lattice parameter will affect the adsorption and desorption of OER intermediates. This will affect the catalytic activity of the samples.

An in-depth XPS analysis provided us with highly useful information regarding material property correlations. We observed that Cu, Ni, and Fe doping affects the binding energy of cobalt; Cu and Ni substitution lowered the binding energy of cobalt, while Fe substitution resulted in a higher binding energy of cobalt. We also found that the binding energy of cobalt and lattice oxide correlated; as the binding energy of cobalt increased, the binding energy of lattice oxide also increased. These binding energy correlations are useful to optimize suitable bonding strength between the metal ion and OER intermediates to achieve high catalytic activity. In our study, when the current density corrected for real surface area was plotted as a function of the binding energy of Co^{2+} and Co^{3+}, a direct correlation was observed; current density increased with the increase of binding energy of cobalt ions. We also noticed that as the amount of Fe in the composition increased the binding energy of cobalt also increased, and hence the current density. By suitable modification of the binding energy of cobalt, high catalytic activity for OER can be achieved. We believe a volcano-type correlation can be derived, where the most suitable binding energy of cobalt ions can give the highest activity for OER. This correlation was not observed in amorphous samples, where, probably due to the lack of crystalline structure, doping of cobalt oxide materials has no influence on the material properties.

This observation is further supported by another correlation that we observed in our study. We found an interesting correlation between the apparent current density of amorphous samples and corresponding double-layer capacitance. This implies that the observed current density of amorphous samples is mainly the function of surface area rather than the intrinsic catalytic activity of the catalysts. This trend is not observed in the case of spinel oxides where the intrinsic catalytic activity of the samples is determined by different factors such as structure and composition. For amorphous materials, we observed that the apparent current density increased when Cu, Ni, and Fe were incorporated in the cobalt oxide lattice. However, when corrected for their real surface area, these samples did not possess a remarkable difference in current density within the error. In addition, this current density is much lower than the corresponding current density obtained from spinel oxides. Unlike amorphous materials, spinel oxides have the advantage of tuning the properties of materials by suitable compositions.

Tafel slopes were obtained for spinel oxides using a rotating disc experiment; pure cobalt oxide and Fe-substituted cobalt oxides have comparatively lower Tafel slopes than Ni and Cu-substituted cobalt oxides which indicate the better catalytic performance of spinel oxides. Our

CV measurements also support this information. Meanwhile, the Tafel slope of amorphous metal oxides is higher than that of spinel oxides, which is also reflected in their catalytic activity towards OER. Kinetic measurements revealed that for crystalline and amorphous materials, the order of the reaction is one and follows preferably a four-electron transfer during OER. However, the rate-determining step is different for these materials. Overall, spinel oxides outperform the corresponding amorphous metal oxides for OER. Our studies reveal that cobalt-based spinel oxides have a highly tunable structure which allows us to optimize highly efficient materials for OER by appropriate doping and structure modification of the cobalt spinel lattice.

The goal of this research work is to outline a strategy to predict a highly efficient electrocatalyst based on the suitable stoichiometric selection of mixed transition metal oxides and provide insight into other metal oxide combinations. The findings of our research work will be highly useful in establishing the guidelines for developing efficient materials for OER. These results are also relevant to the implementation of spinel oxide materials in other technologies, such as energy storage systems, photocatalytic reactors, fuel cells, sensors, and metal-air batteries. This work would address the current energy crisis by developing efficient electrocatalysts for water electrolysis and in turn, would be beneficial in the field of materials.

7.2. Future work

In future work, X-ray absorption studies (XAS) will be performed on amorphous and crystalline materials that we prepared in this work. Extended X-ray absorption fine (EXAFS) and X-ray absorption near-edge structure (XANES) can provide insight into the local bond length and geometry of elements in the lattice. This study will also help to understand the site occupancy of metal ions in the spinel structure so that active sites for the OER can be identified. In situ XAS studies will also be performed to get a deeper understanding of active sites and phases involved in the OER. The effect of the preparation method on the distribution of active sites on the samples can also be identified through this method.

As the Fe-containing spinel oxides are found to be highly active for OER, both binary and ternary spinel oxides containing higher amounts of Fe will be prepared and their influence on catalytic activity will be studied. Mössbauer spectroscopy analysis will also be performed on Fe-containing samples to understand the effect of Fe in the composition. This study will help to

obtain information about the oxidation state and spin state of metal atoms and thereby their effect on catalytic activity.

Appendix 1. Supporting documents for Chapter 3. Material Characterization

To keep the length of the Chapter manageable, additional data for Chapter 3 is shown below. All these Figures and/or Tables are referred to in respective Chapters.

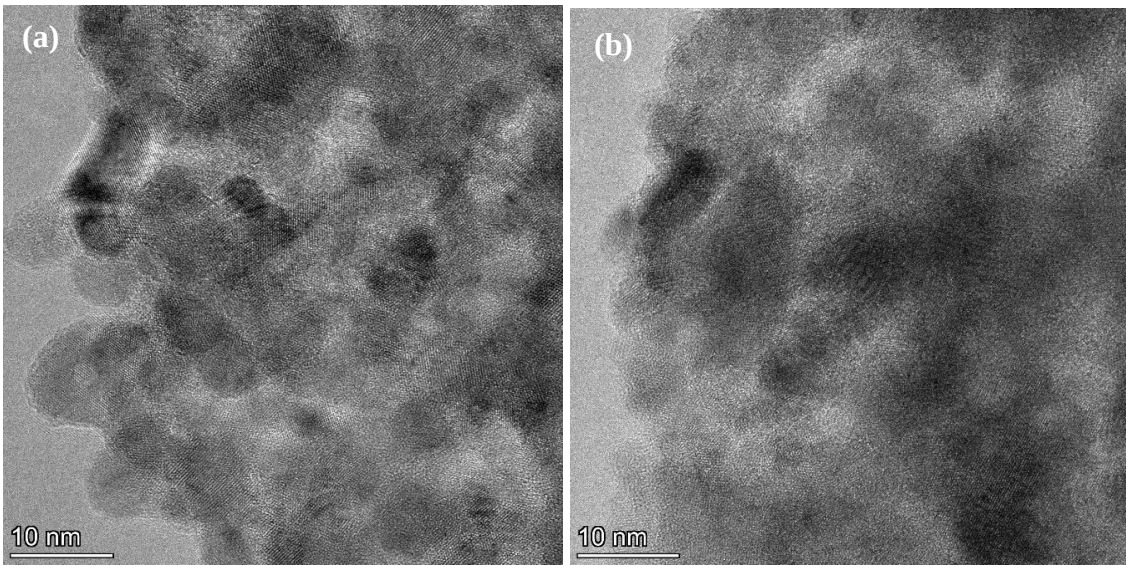

Figure A1.1. HR-TEM images of a) $CuCo_2O_4$ nonpolarized b) $CuCo_2O_4$ polarized

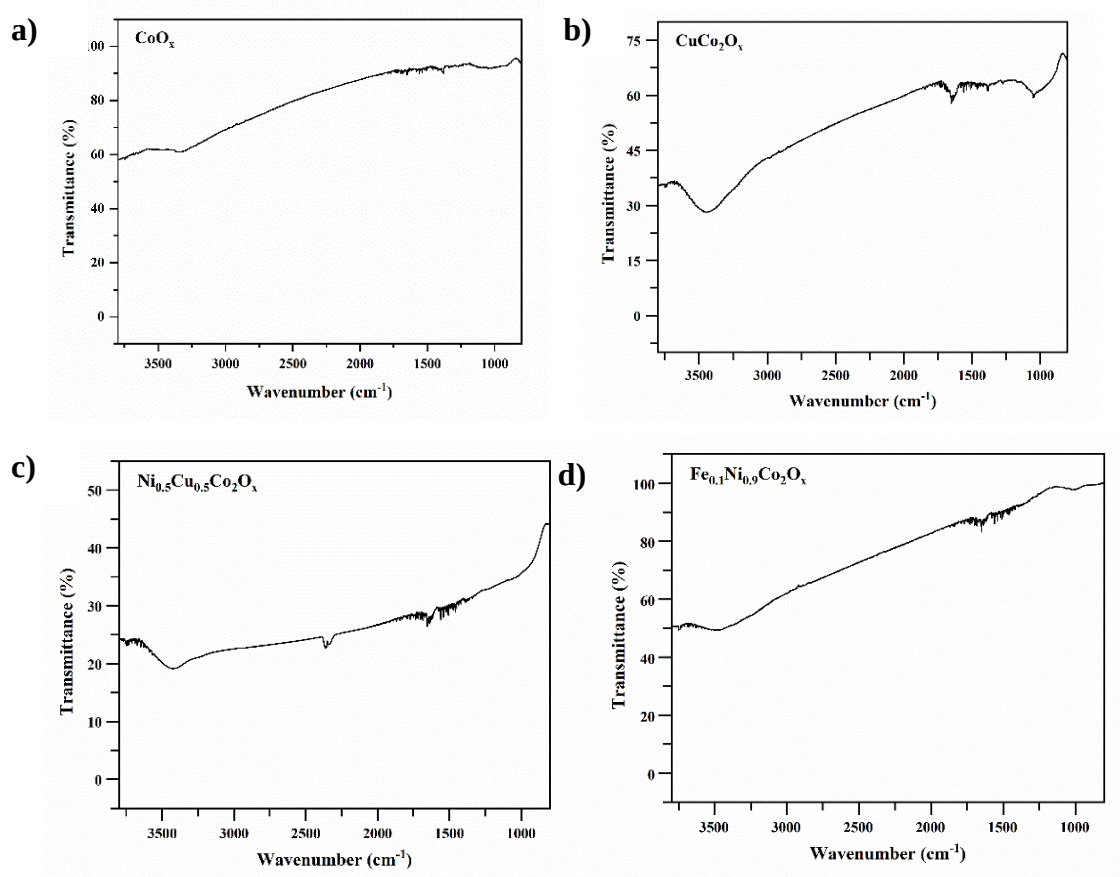

Figure A1. 2. FTIR spectra of a) CoO_x b)$CuCo_2O_4$ c) $Ni_{0.5}Co_{0.5}Co_2O_4$ d) $Fe_{0.1}Ni_{0.9}Co_2O_4$

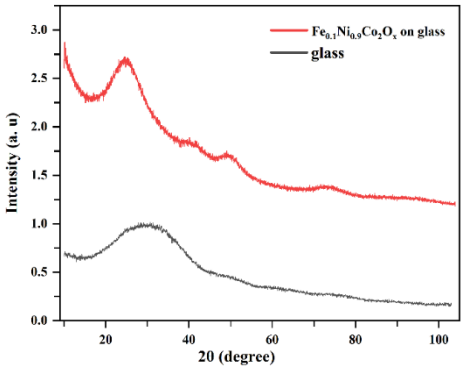

Figure A1. 3. XRD pattern of $Fe_{0.1}Ni_{0.9}Co_2O_4$ deposited on glass (red) and that of normal glass (black)

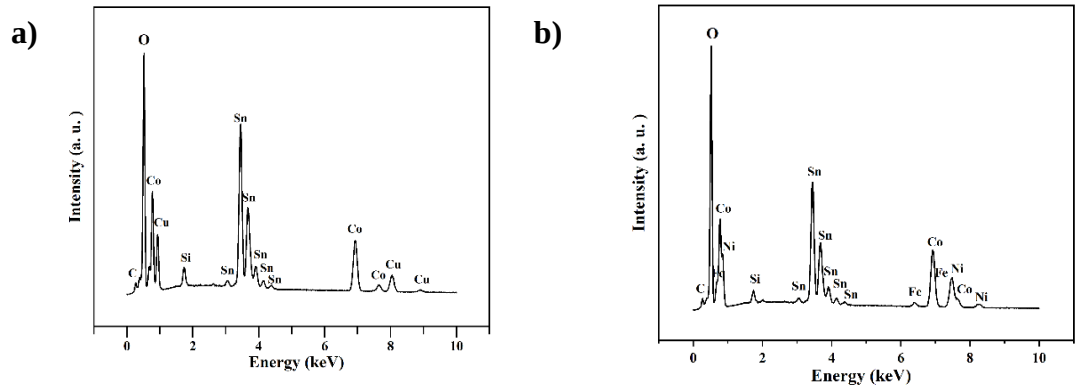

Figure A1. 4. EDX spectra of amorphous a) $CuCo_2O_x$ b) $Fe_{0.1}Ni_{0.9}Co_2O_x$

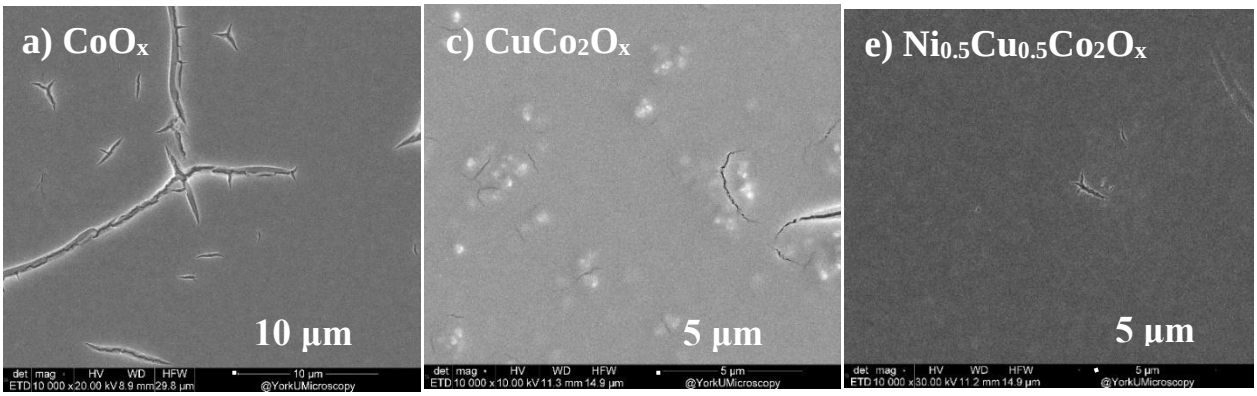

Figure A1. 5. SEM pictures of a) CoO_x b) $CuCo_2O_x$ c) $Ni_{0.5}Cu_{0.5}Co_2O_x$ on FTO glass at 10,000× magnification.

Appendix 2. Supporting documents for Chapter 4. Transition metal oxide surface composition determination by X-ray Photoelectron Spectroscopy analysis

To keep the length of the Chapter manageable, additional data for Chapter 4 is shown below. All these Figures and/or Tables are referred to in respective Chapters.

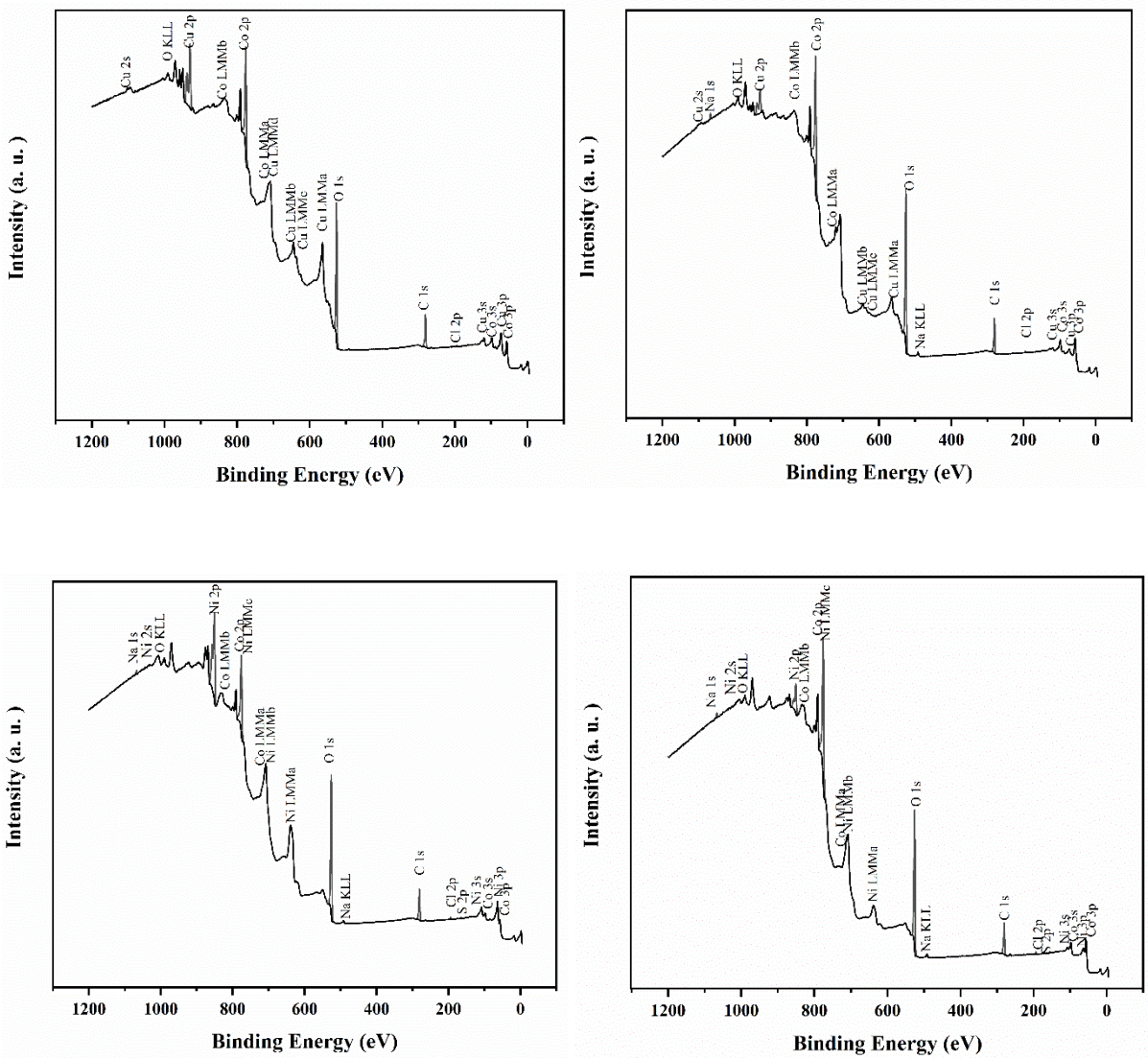

Figure A2. 1. XPS survey spectra of a) XPS survey spectra of $Fe_{0.1}Cu_{0.9}Co_2O_4$ b) $Fe_{0.15}Cu_{0.35}Co_{2.5}O_4$ c) $Fe_{0.1}Ni_{0.9}Co_2O_4$ d) $Fe_{0.15}Ni_{0.35}Co_{2.5}O_4$

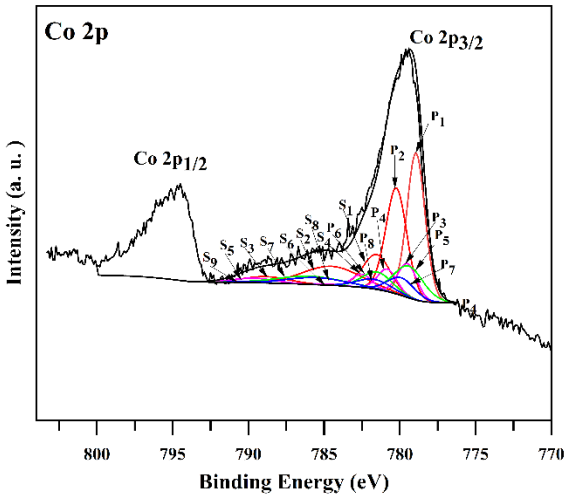

Figure A2. 2a. High resolution spectra Co 2p of $NiCo_2O_4$. P_1 and P_2 = photoelectron peaks of Co_3O_4, P_3 and P_4 = photoelectron peaks of CoOOH, P_5 and P_6 = photoelectron peaks of CoO. P_7 and P_8 = photoelectron peak of $Co(OH)_2S_1$, S_2 and S_3 = satellite peaks of Co_3O_4. S_4 and S_5 = satellite peak of CoOOH, and S_6 and S_7 = satellite peak of CoO and S_8 and S_9 = satellite peaks of $Co(OH)_2$.

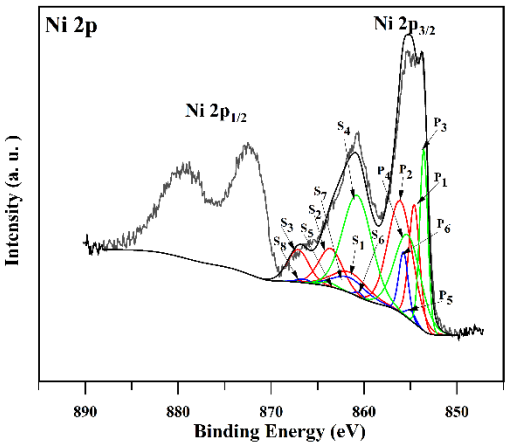

Figure A2.2b. High resolution spectra of Ni 2p of $NiCo_2O_4$. P_1 and P_2 = photoelectron peaks of Ni^{2+} and Ni^{3+} in spinel. P_3 and P_4 = photoelectron peaks of NiO, P_5 and P_6 = photoelectron peaks of $Ni(OH)_2$. S_1, S_2 and S_3 = satellite peak of spinel peaks, S_3 and S_4 = satellite peak of NiO, S_5, S_6 and S_7 = satellite peaks of $Ni(OH)_2$

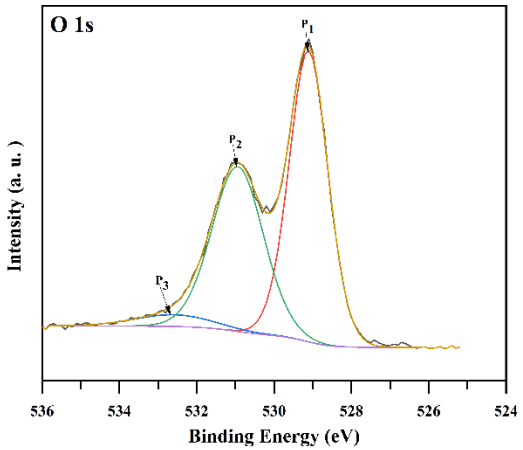

Figure A2. 2c. High resolution spectra of O 1s of $NiCo_2O_4$. P_1 = photoelectron peak of lattice oxygen, P_2 = photoelectron peak of hydroxide, P_3 = photoelectron peak corresponds to surface water.

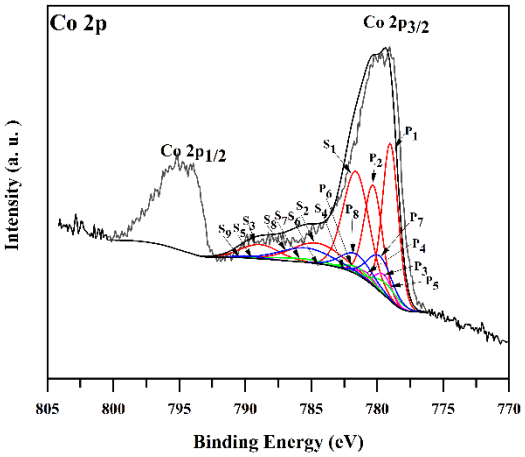

Figure A2. 3a. High resolution spectra Co 2p of $Ni_{0.9}Cu_{0.1}Co_2O_4$. P_1 and P_2 = photoelectron peaks of Co_3O_4, P_3 and P_4 = photoelectron peaks of CoOOH, P_5 and P_6 = photoelectron peaks of CoO and P_7 and P_8 = photoelectron peak of $Co(OH)_2$. S_1, S_2 and S_3 = satellite peaks of Co_3O_4, S_4 and S_5 = satellite peaks of CoOOH, S_6 and S_7 = satellite peaks of CoO and S_8 and S_9 = satellite peaks of $Co(OH)_2$.

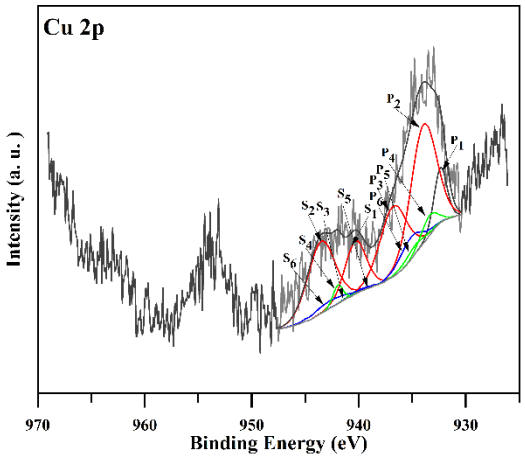

Figure A2. 3b. High resolution spectra of Cu 2p of $Ni_{0.9}Cu_{0.1}Co_2O_4$. P_1 = Photoelectron peak of Cu_2O, P_2 = photoelectron peak of Cu^{2+} in octahedral site of spinel. P_3 = photoelectron peak of Cu^{2+} in tetrahedral site of spinel. P_4 and P_5 are photoelectron peaks of CuO, P_6 = photoelectron peak of $Cu(OH)_2$. S_1 and S_2 = satellite peak of Cu^{2+} in spinel, S_3 and S_4 = satellite peaks of CuO. S_5 and S_6 = satellite peaks of $Cu(OH)_2$.

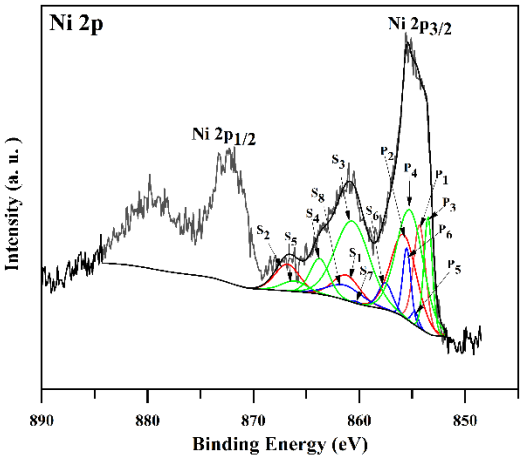

Figure A2. 3c. High resolution spectra of Ni 2p of $Ni_{0.9}Cu_{0.1}Co_2O_4$. P_1 and P_2 = photoelectron peaks of Ni^{2+} and Ni^{3+} in spinel. P_3 and P_4 = photoelectron peaks of NiO, P_5 and P_6 = photoelectron peaks of $Ni(OH)_2$. S_1 and S_2 = satellite peak of spinel peaks, S_3, S_4 and S_5 = satellite peak of NiO, S_6, S_7 and S_8 = satellite peaks of $Ni(OH)_2$

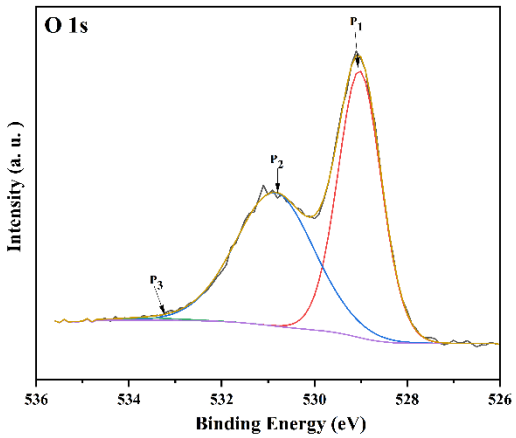

Figure A2. 3d. High resolution spectra of O 1s of $Ni_{0.9}Cu_{0.1}Co_2O_4$. P_1 = photoelectron peak of lattice oxygen, P_2 = photoelectron peak of hydroxide, P_3 = photoelectron peak corresponds to surface water.

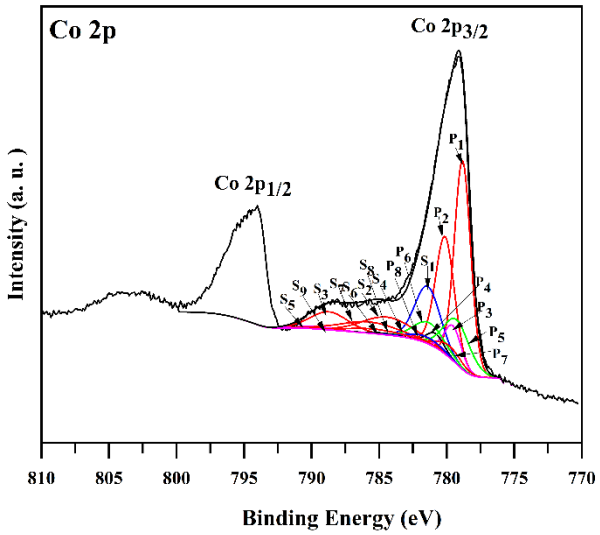

Figure A2. 4a. High resolution spectra Co 2p of $Ni_{0.75}Cu_{0.25}Co_2O_4$. P_1 and P_2 = photoelectron peaks of Co_3O_4, P_3 and P_4 = photoelectron peaks of CoOOH, P_5 and P_6 = photoelectron peaks of CoO and P_7 and P_8 = photoelectron peak of $Co(OH)_2$. S_1, S_2 and S_3 = satellite peaks of Co_3O_4, S_4 and S_5 = satellite peaks of CoOOH, S_6 and S_7 = satellite peaks of CoO and S_8 and S_9 = satellite peaks of $Co(OH)_2$.

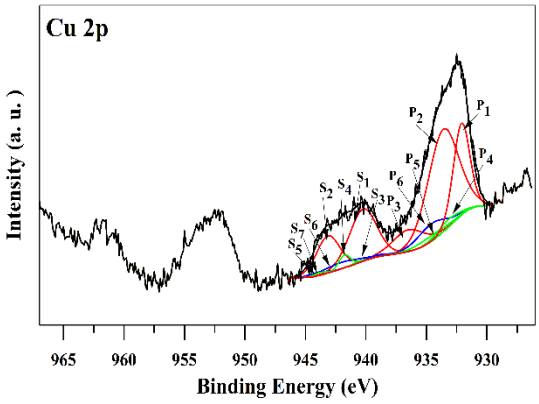

Figure A2. 4b. High resolution spectra of Cu 2p of $Ni_{0.75}Cu_{0.25}Co_2O_4$. P_1 = photoelectron peak of Cu_2O, P_2 = photoelectron peak of Cu^{2+} in octahedral site of spinel. P_3 = photoelectron peak of Cu^{2+} in tetrahedral site of spinel. P_4 and P_5 are photoelectron peaks of CuO, P_6 = photoelectron peak of $Cu(OH)_2$. S_1 and S_2 = satellite peak of Cu^{2+} in spinel, S_3, S_4 and S_5 = satellite peaks of CuO. S_6 and S_7 = satellite peaks of $Cu(OH)_2$.

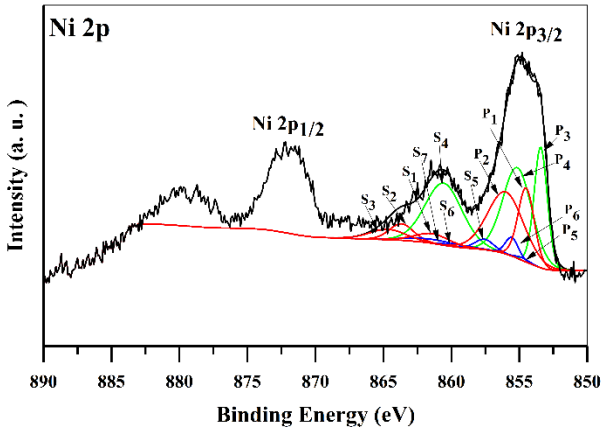

Figure A2. 4c. High resolution spectra of Ni 2p of $Ni_{0.75}Cu_{0.25}Co_2O_4$. P_1 and P_2 = photoelectron peaks of Ni^{2+} and Ni^{3+} in spinel. P_3 and P_4 = photoelectron peaks of NiO, P_5 and P_6 = photoelectron peaks of $Ni(OH)_2$. S_1, S_2 and S_3 = satellite peak of spinel peaks, S_4 = satellite peak of NiO, S_5, S_6 and S_7 = satellite peaks of $Ni(OH)_2$

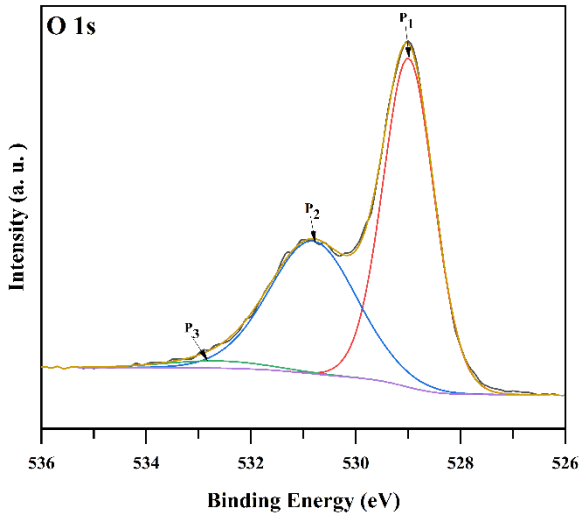

Figure A2. 4d. High resolution spectra of O 1s of $Ni_{0.75}Cu_{0.25}Co_2O_4$. P_1 = photoelectron peak of lattice oxygen, P_2 = photoelectron peak of hydroxide, P_3 = photoelectron peak corresponds to surface water.

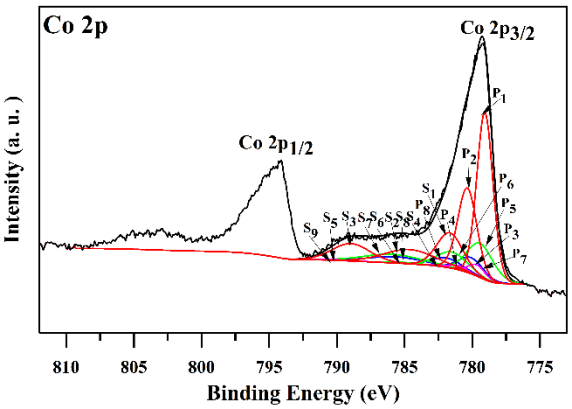

Figure A2. 5a. High resolution spectra Co 2p of $Ni_{0.5}Cu_{0.5}Co_2O_4$. P_1 and P_2 = photoelectron peaks of Co_3O_4, P_3 and P_4 = photoelectron peaks of CoOOH, P_5 and P_6 = photoelectron peaks of CoO and P_7 and P_8 = photoelectron peak of $Co(OH)_2$. S_1, S_2 and S_3 = satellite peaks of Co_3O_4, S_4 and S_5 = satellite peaks of CoOOH, S_6 and S_7 = satellite peaks of CoO and S_8 and S_9 = satellite peaks of $Co(OH)_2$.

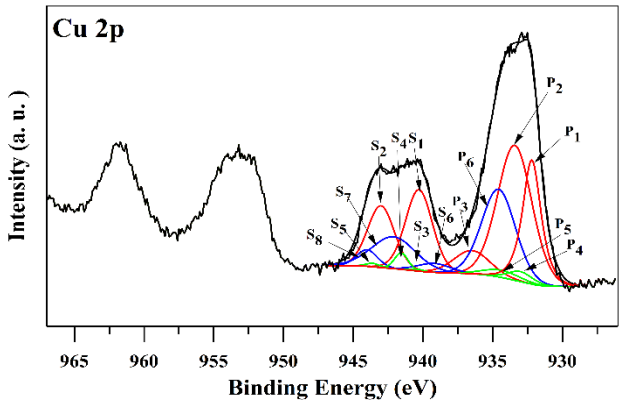

Figure A2. 5b. High resolution spectra of Cu 2p of $Ni_{0.5}Cu_{0.5}Co_2O_4$. P_1 = photoelectron peak of Cu_2O, P_2 = photoelectron peak of Cu^{2+} in octahedral site of spinel. P_3 = photoelectron peak of Cu^{2+} in tetrahedral site of spinel. P_4 and P_5 are photoelectron peaks of CuO, P_6 = photoelectron peak of $Cu(OH)_2$. S_1 and S_2 = satellite peak of Cu^{2+} in spinel, S_3, S_4 and S_5 = satellite peaks of CuO. S_6 and S_7 = satellite peaks of $Cu(OH)_2$.

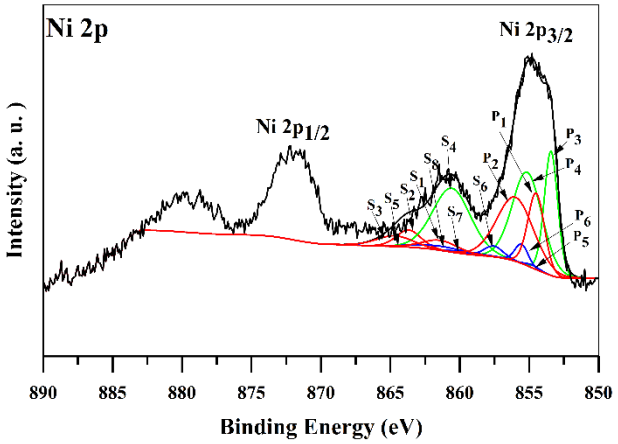

Figure A2. 5c. High resolution spectra of Ni 2p of $Ni_{0.5}Cu_{0.5}Co_2O_4$. P_1 and P_2 = photoelectron peaks of Ni^{2+} and Ni^{3+} in spinel. P_3 and P_4 = photoelectron peaks of NiO, P_5 and P_6 = photoelectron peaks of $Ni(OH)_2$. S_1,S_2 and S_2 = satellite peak of spinel peaks, S_4 and S_5 = satellite pak of NiO, S_6, S_7 and S_8 = satellite peaks of $Ni(OH)_2$

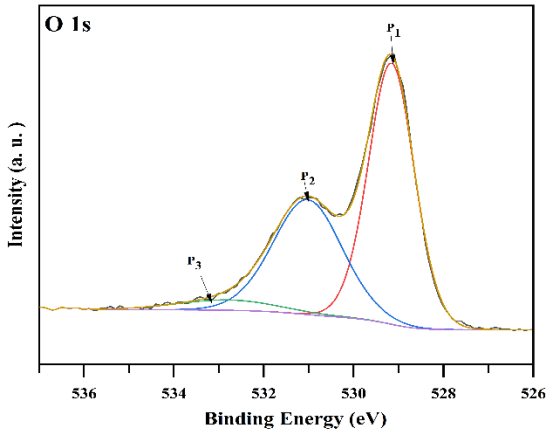

Figure A2. 5d. High resolution spectra of O 1s of $Ni_{0.5}Cu_{0.5}Co_2O_4$. P_1 = photoelectron peak of lattice oxygen, P_2 = photoelectron peak of hydroxide, P_3 = photoelectron peak corresponds to surface water.

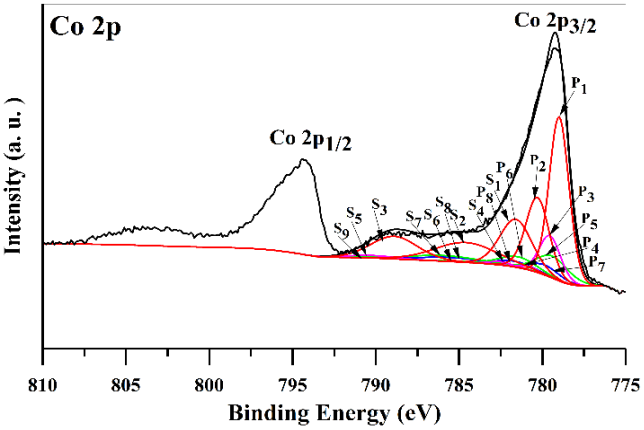

Figure A2. 6a. High resolution spectra Co 2p of $Ni_{0.25}Cu_{0.75}Co_2O_4$. P_1 and P_2 = photoelectron peaks of Co_3O_4, P_3 and P_4 = photoelectron peaks of CoOOH, P_5 and P_6 = photoelectron peaks of CoO and P_7 and P_8 = photoelectron peak of $Co(OH)_2$. S_1, S_2 and S_3 = satellite peaks of Co_3O_4, S_4 and S_5 = satellite peaks of CoOOH, S_6 and S_7 = satellite peaks of CoO and S_8 and S_9 = satellite peaks of $Co(OH)_2$.

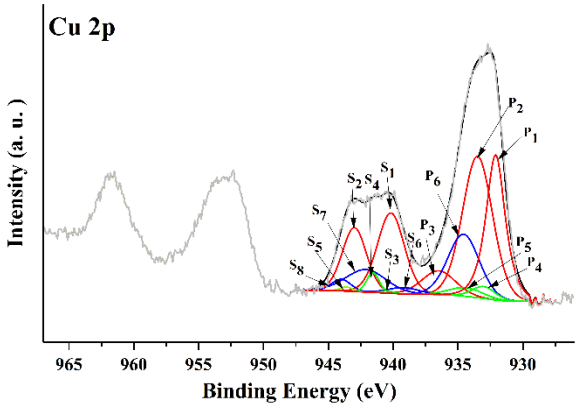

Figure A2. 6b. High resolution spectra of Cu 2p of $Ni_{0.25}Cu_{0.75}Co_2O_4$. P_1 = photoelectron peak of Cu_2O, P_2 = photoelectron peak of Cu^{2+} in octahedral site of spinel. P_3 = photoelectron peak of Cu^{2+} in tetrahedral site of spinel. P_4 and P_5 are photoelectron peaks of CuO, P_6 = photoelectron peak of $Cu(OH)_2$. S_1 and S_2 = satellite peak of Cu^{2+} in spinel, S_3, S_4 and S_5 = satellite peaks of CuO. S_6 and S_7 = satellite peaks of $Cu(OH)_2$.

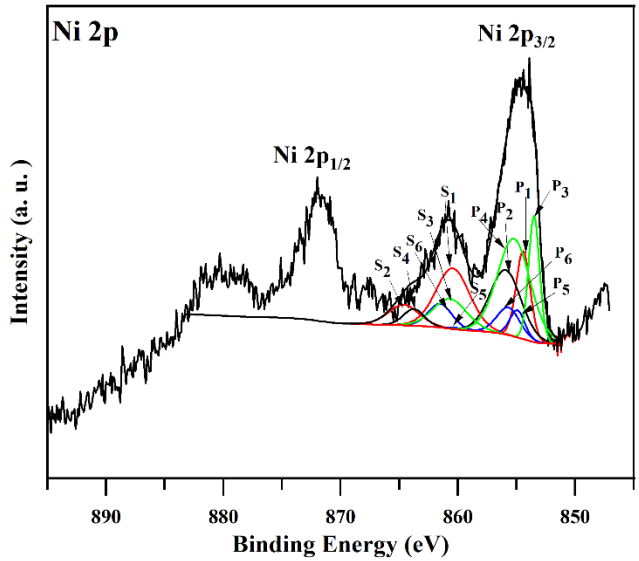

Figure A2. 6c. High resolution spectra of Ni 2p of $Ni_{0.25}Cu_{0.75}Co_2O_4$. P_1 and P_2 = photoelectron peaks of Ni^{2+} and Ni^{3+} in spinel. P_3 and P_4 = photoelectron peaks of NiO, P_5 and P_6 = photoelectron peaks of $Ni(OH)_2$. S_1 and S_2 = satellite peak of spinel peaks, S_3 and S_4 = satellite peak of NiO, S_5 and S_6 = satellite peaks of $Ni(OH)_2$

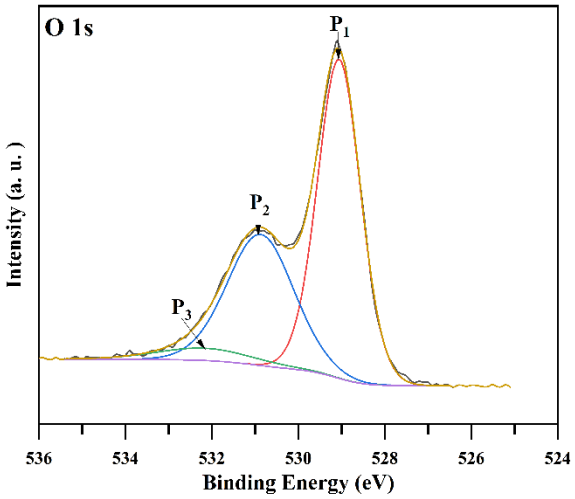

Figure A2. 6d. High resolution spectra of O 1s of $Ni_{0.25}Cu_{0.75}Co_2O_4$. P_1 = photoelectron peak of lattice oxygen, P_2 = photoelectron peak of hydroxide, P_3 = photoelectron peak corresponding to surface water.

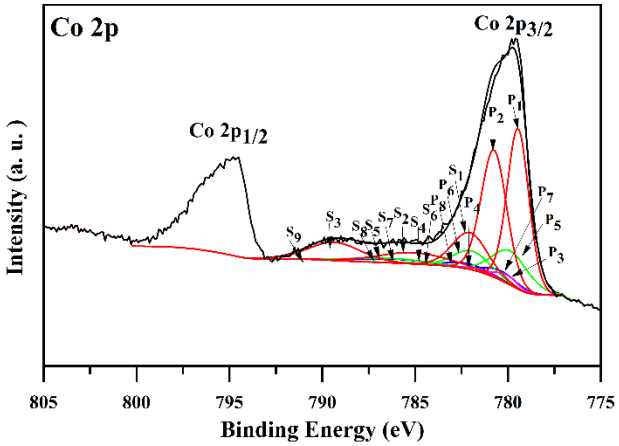

Figure A2. 7a. High resolution spectra Co 2p of Co_3O_4. P_1 and P_2 = photoelectron peaks of Co_3O_4, P_3 and P_4 = photoelectron peaks of CoOOH, P_5 and P_6 = photoelectron peaks of CoO and P_7 and P_8 = photoelectron peak of $Co(OH)_2$. S_1, S_2 and S_3 = satellite peaks of Co_3O_4, S_4 and S_5 = satellite peaks of CoOOH, S_6 and S_7 = satellite peaks of CoO and S_8 and S_9 = satellite peaks of $Co(OH)_2$.

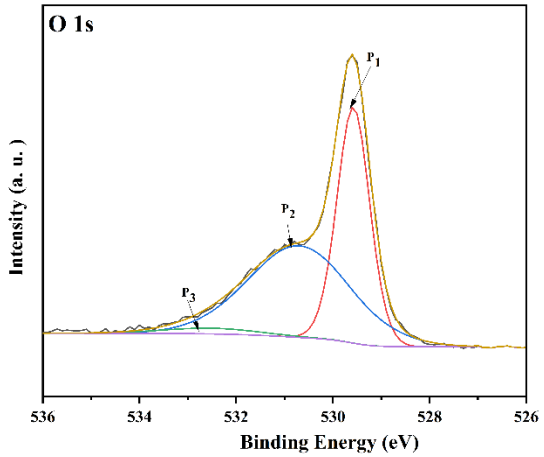

Figure A2. 7b. High resolution spectra of O 1s of Co_3O_4. P_1 = photoelectron peak of lattice oxygen, P_2 = photoelectron peak of hydroxide, P_3 = photoelectron peak corresponds to surface water.

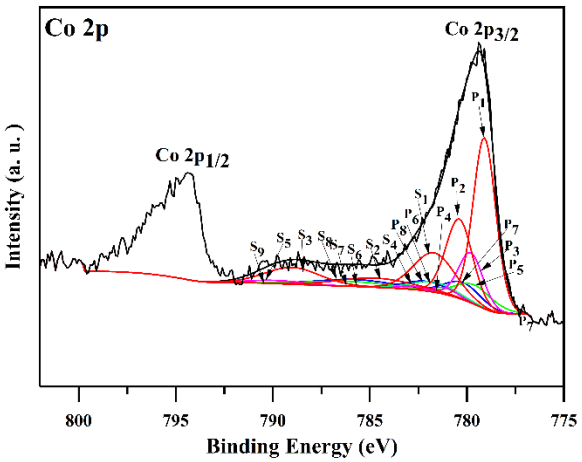

Figure A2. 8a. High resolution spectra Co 2p of Co_3O_4. P_1 and P_2 = photoelectron peaks of $CuCo_2O_4$, P_3 and P_4 = photoelectron peaks of CoOOH, P_5 and P_6 = photoelectron peaks of CoO and P_7 and P_8 = photoelectron peak of $Co(OH)_2$. S_1, S_2 and S_3 = satellite peaks of Co_3O_4, S_4 and S_5 = satellite peaks of CoOOH, S_6 and S_7 = satellite peaks of CoO and S_8 and S_9 = satellite peaks of $Co(OH)_2$.

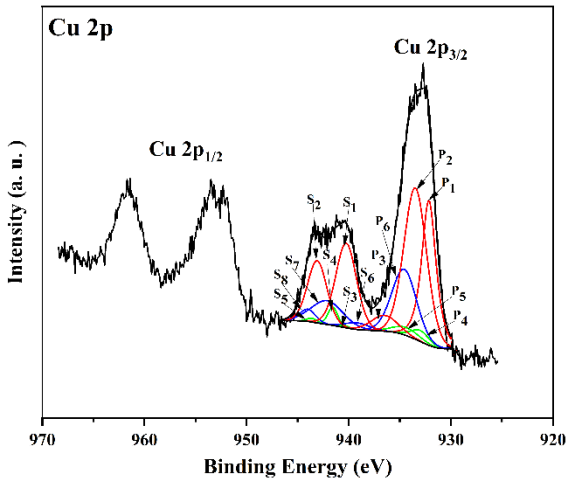

Figure A2. 8b. High resolution spectra of Cu 2p of $CuCo_2O_4$. P_1 = photoelectron peak of Cu_2O, P_2 = photoelectron peak of Cu^{2+} in octahedral site of spinel. P_3 = photoelectron peak of Cu^{2+} in tetrahedral site of spinel. P_4 and P_5 are photoelectron peaks of CuO, P_6 = photoelectron peak of $Cu(OH)_2$. S_1 and S_2 = satellite peak of Cu^{2+} in spinel, S_3, S_4 and S_5 = satellite peaks of CuO. S_6, S_7 and S_8= satellite peaks of $Cu(OH)_2$.

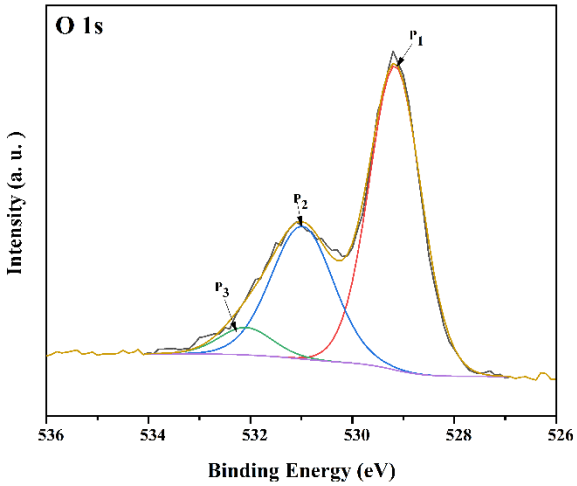

Figure A2. 8c. High resolution spectra of O 1s of $CuCo_2O_4$. P_1 = photoelectron peak of lattice oxygen, P_2 = photoelectron peak of hydroxide, P_3 = photoelectron peak corresponding to surface water.

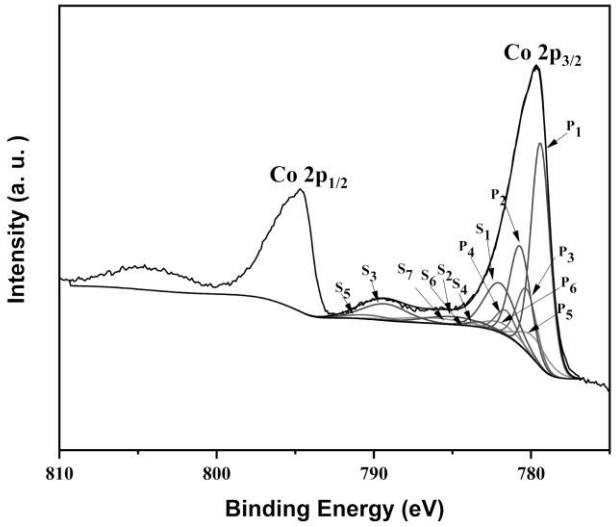

Figure A2. 9a. High resolution spectra of Co 2p of $Fe_{0.1}Cu_{0.9}Co_2O_4$. P and S represent photoelectron peak and satellite peak respectively. P_1 and P_2 = photoelectron peaks of Co_3O_4, P_3 and P_4 = photoelectron peaks of CoOOH, P_5 and P_6 = photoelectron peaks of CoO. S_1, S_2 and S_3 = the satellite peaks of Co_3O_4. S_4 and S_5 = the satellite peak of CoOOH, and S_6 and S_7 = the satellite peak of CoO.

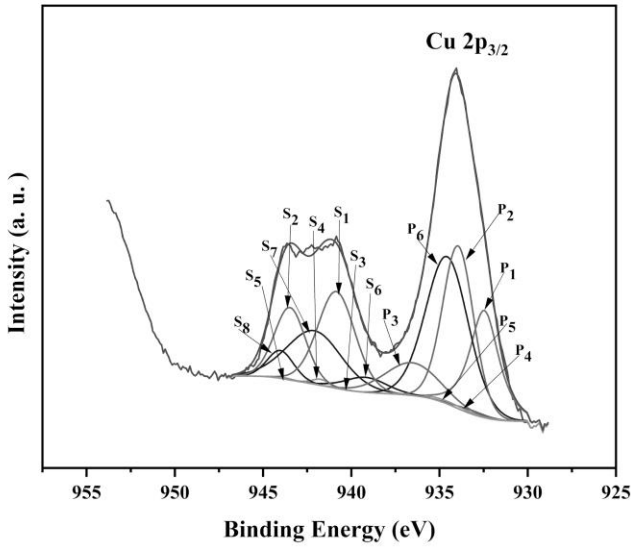

Figure A2. 9b. High resolution spectra of Cu 2p of $Fe_{0.1}Cu_{0.9}Co_2O_4$. P_1 = photoelectron peak of Cu_2O, P_2 = photoelectron peak of Cu^{2+} in Octahedral site of spinel. P_3 = photoelectron peak of

Cu^{2+} in tetrahedral site of spinel. P_4 and P_5 are photoelectron peaks of CuO, P_6 = photoelectron peak of $Cu(OH)_2$. S_1 and S_2 = satellite peak of Cu^{2+} in spinel, S_3, S_4 and S_5 = satellite peaks of CuO. S_6, S_7 and S_8 = satellite peaks of $Cu(OH)_2$.

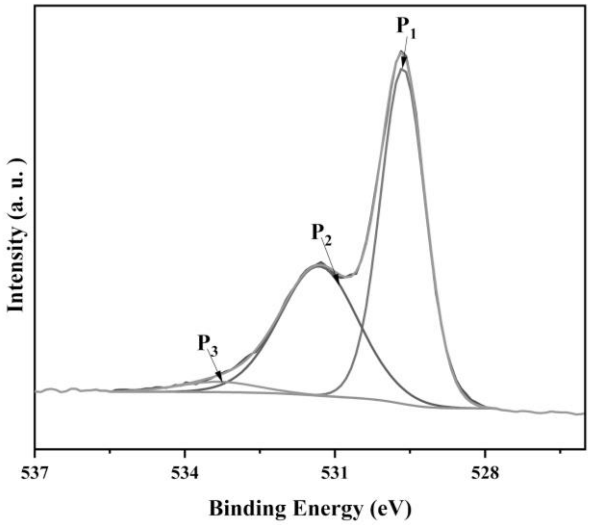

Figure A2. 9c.. High resolution spectra O 1s of $Fe_{0.1}Cu_{0.9}Co_2O_4$. P_1 = photoelectron peak of lattice oxygen, P_2 = photoelectron peak of hydroxide, P_3 = photoelectron peak corresponds to surface water.

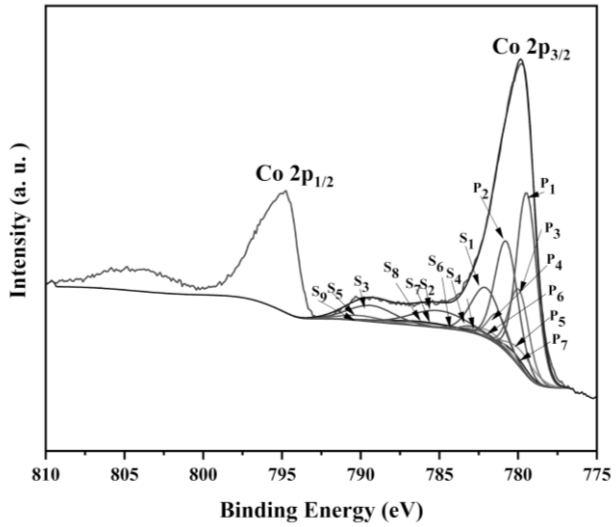

Figure A2. 10a.. High resolution spectra Co 2p of $Fe_{0.15}Cu_{0.35}Co_{2.5}O_4$. P_1 and P_2 = photoelectron peaks of Co_3O_4, P_3 and P_4 = photoelectron peaks of CoOOH, P_5 and P_6 = photoelectron peaks of CoO, P_7 = photoelectron peak of $Co(OH)_2$. S_1, S_2 and S_3 = the satellite peaks of Co_3O_4. S_4 and S_5 = satellite peak of CoOOH, and S_6 and S_7 = satellite peak of CoO, S_8 and S_9 = satellite peaks of $Co(OH)_2$

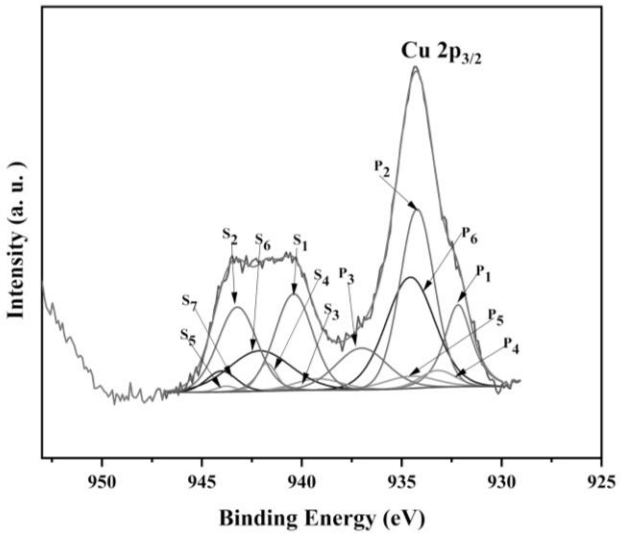

Figure A2. 10b. High resolution spectra Cu 2p of $Fe_{0.15}Cu_{0.35}Co_{2.5}O_4$. P_1 = photoelectron peak of Cu_2O, P_2 = photoelectron peak of Cu^{2+} in Octahedral site of spinel. P_3 = photoelectron peak of Cu^{2+} in tetrahedral site of spinel. P_4 and P_5 = photoelectron peak of CuO, P_6 = photoelectron peak of $Cu(OH)_2$. S_1 and S_2 = satellite peak of Cu^{2+} in spinel, S_3, S_4 and S_5 = satellite peaks of CuO. S_6 and S_7 = satellite peaks of $Cu(OH)_2$.

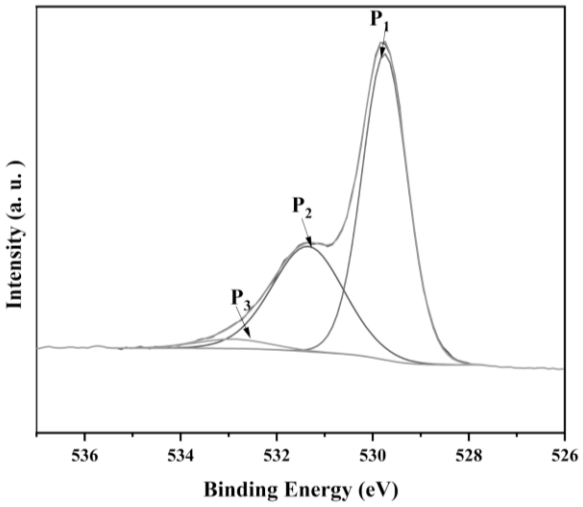

Figure A2. 10c. High resolution spectra O1s of $Fe_{0.15}Cu_{0.35}Co_{2.5}O_4$. P_1 = photoelectron peak of lattice oxygen, P_2 = photoelectron peak of hydroxide, P_3 = photoelectron peak corresponds to surface water.

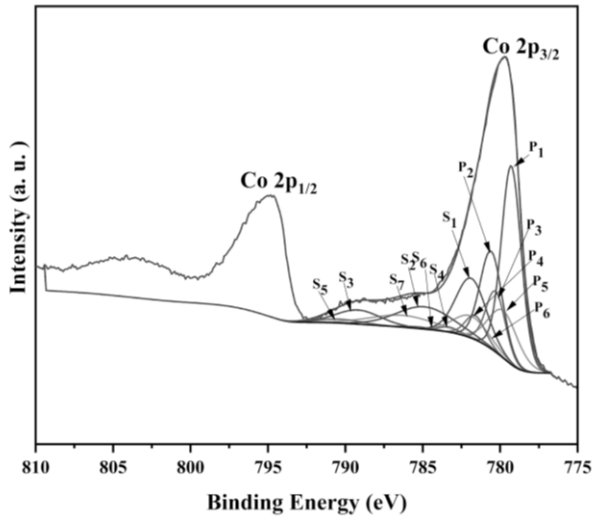

Figure A2. 11a. High resolution spectra Co 2p of $Fe_{0.15}Ni_{0.35}Co_{2.5}O_4$. P_1 and P_2 = photoelectron peaks of Co_3O_4, P_3 and P_4 = photoelectron peaks of CoOOH, P_5 and P_6 = photoelectron peaks of CoO. S_1, S_2 and S_3 = satellite peaks of Co_3O_4. S_4 and S_5 = the satellite peak of CoOOH, and S_6 and S_7 = the satellite peak of CoO.

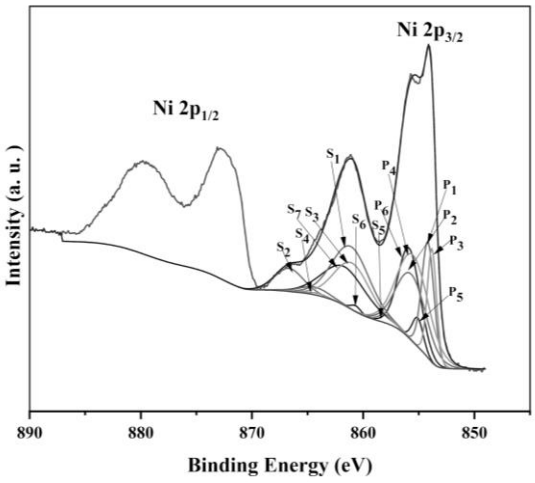

Figure A2. 11b. High resolution spectra of Ni 2p of $Fe_{0.1}Ni_{0.9}Co_2O_4$. P_1 and P_2 = photoelectron peaks of Ni^{2+} and Ni^{3+} in spinel. P_3 and P_4 = photoelectron peaks of NiO, P_5 and P_6 = photoelectron peaks of $Ni(OH)_2$. S_1 and S_2 = satellite peak of spinel peaks, S_3 and S_4 = satellite peak of NiO, S_5 and S_6 = satellite peaks of $Ni(OH)_2$

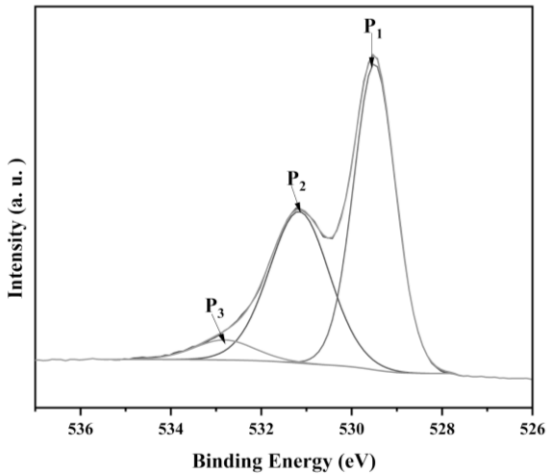

Figure A2. 11c. High resolution spectra O 1s of $Fe_{0.1}Ni_{0.9}Co_2O_4$. P_1 = photoelectron peak of lattice oxygen, P_2 = photoelectron peak of hydroxide, P_3 = photoelectron peak corresponds to surface water.

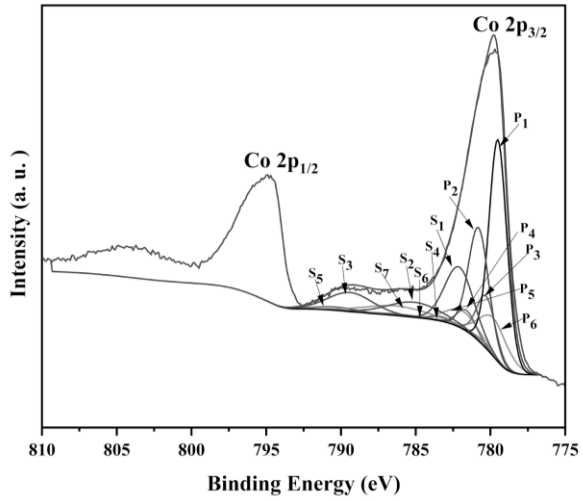

Figure A2. 12a. High resolution spectra Co 2p of $Fe_{0.15}Ni_{0.35}Co_{2.5}O_4$. P_1 and P_2 = photoelectron peaks of Co_3O_4, P_3 and P_4 = photoelectron peaks of CoOOH, P_5 and P_6 = photoelectron peaks of CoO. S_1, S_2 and S_3 = satellite peaks of Co_3O_4. S_4 and S_5 = the satellite peak of CoOOH, and S_6 and S_7 = the satellite peak of CoO.

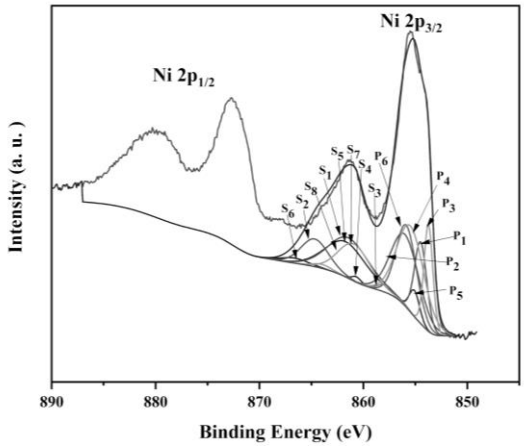

Figure A2. 12b. High resolution spectra Ni 2p of $Fe_{0.15}Ni_{0.35}Co_{2.5}O_4$. P_1 and P_2 = photoelectron peaks of Ni^{2+} and Ni^{3+} in spinel. P_3 and P_4 = photoelectron peaks of NiO, P_5 and P_6 = photoelectron peaks of $Ni(OH)_2$. S_1 and S_2 = satellite peak of spinel peaks, S_3, S_4, S_5 and S_6 = satellite peak of $Ni(OH)_2$, S_7 and S_8 = satellite peaks of NiO

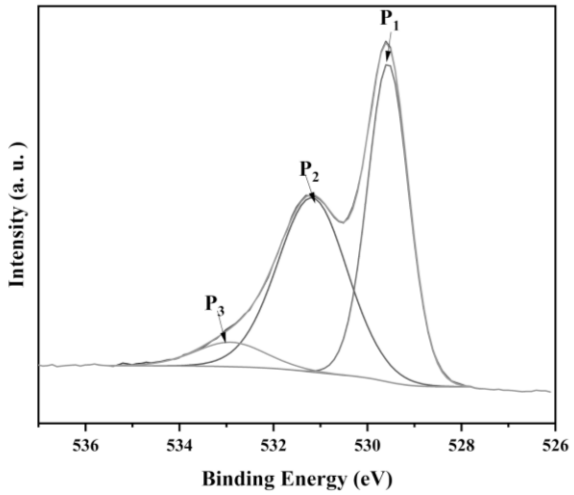

Figure A2. 12c. High resolution spectra O1s of $Fe_{0.15}Ni_{0.35}Co_{2.5}O_4$. P_1 = photoelectron peak of lattice oxygen, P_2 = photoelectron peak of hydroxide, P_3 = photoelectron peak corresponding to surface water.

Table A2. 1. Percentage of various components of O1s peak in spinel oxides

#	sample	Lattice oxygen	Hydroxide	Surface water
1	$NiCo_2O_4$	54.5	41.1	4.4
2	$Ni_{0.9}Cu_{0.1}Co_2O_4$	52.4	47.6	0.0
3	$Ni_{0.75}Cu_{0.25}Co_2O_4$	51.1	35.4	13.5
4	$Ni_{0.5}Cu_{0.5}Co_{2.24}O_4$	57.2	37.9	4.9
5	$Ni_{0.25}Cu_{0.75}Co_2O_4$	58.0	37	5.0
6	Co_3O_4	43.9	53.1	3.0
7	$CuCo_2O_4$	61.9	32.4	5.7
8	$Fe_{0.1}Cu_{0.9}Co_2O_4$	58.1	38.8	3.1
9	$Fe_{0.15}Cu_{0.35}Co_{2.5}O_4$	62.8	34.1	3.1
10	$Fe_{0.1}Ni_{0.9}Co_2O_4$	55.5	39.3	5.2
11	$Fe_{0.1}Ni_{0.9}Co_2O_4$	48.7	45.0	6.3

Table A2. .2. Binding energy values of cations in the spinel oxides (Appendix)-data will be discussed in chapter 6.

#	Sample	Co^{3+}(eV)	Co^{2+}(eV)	Cu^{1+}(Td) (eV)	Cu^{2+}(Oh) (eV)	Cu^{2+}(Td) (eV)	Ni^{2+}(eV)	Ni^{3+}(eV)
1	$NiCo_2O_4$	778.9	780.2	-	-	-	854.6	856.1
2	$Ni_{0.95}Cu_{0.05}Co_2O_4$	779.0	780.3				854.6	856.1
3	$Ni_{0.9}Cu_{0.1}Co_2O_4$	779.0	780.3	932.4	934.0	936.8	854.3	855.8
4	$Ni_{0.75}Cu_{0.25}Co_2O_4$	778.8	780.1	932.1	933.6	936.5	854.5	856.0
5	$Ni_{0.5}Cu_{0.5}Co_2O_4$	779.1	780.4	932.2	933.4	936.5	854.2	855.7

6	$Ni_{0.25}Cu_{0.75}Co_2O_4$	779.0	780.3	932.1	933.5	936.5	854.4	855.9
7	Co_3O_4	779.4	780.7					
8	$CuCo_2O_4$	779.0	780.3	932.2	933.5	936.5		
9	$Cu_{0.9}Fe_{0.1}Co_2O_4$	779.4	780.7	932.5	934.0	936.6		
10	$Fe_{0.15}Cu_{0.35}Co_{2.5}O_4$	779.5	780.8	932.2	934.2	937.0		
11	$Fe_{0.1}Ni_{0.9}Co_2O_4$	779.3	780.6	-	-	-	854.2	855.7
12	$Fe_{0.15}Ni_{0.35}Co_{2.5}O_4$	779.5	780.8				854.5	856.0

Table A2. 3. The percentage of various species present at the surface of amorphous metal oxide

Peak	Phase	Percentage	Peak	Phase	Percentage
Co 2p	Co-Spinel	39.94 – 70.79	Ni 2p	NiO	71.07 – 73.71
	CoOOH	12.33 – 31.17			
	$Co(OH)_2$	16.88 - 34.93		$Ni(OH)_2$	26.29 – 28.93
Cu 2p	Cu -spinel	57.07 - 75.76	O 1s	Metal oxide	44.0 – 62.8
				Hydroxide	32.4 – 56.1
	$Cu(OH)_2$	16.22 – 38.63		Surface water	1.0 – 6.3
	CuO	4.3 – 8.02			

Table A2. 4. Percentage of various components of O1s peak in amorphous samples

#	sample	Lattice oxygen	Hydroxide	Surface water
1	Co_3O_x	43.5	56.5	0.0
2	$Cu_1Co_2O_x$	58.0	42.0	0.0

3	$Ni_{0.5}Cu_{0.5}Co_2O_x$	50.2	47.7	2.1
4	$Fe_{0.1}Cu_{0.9}Co_2O_x$	54.2	45.8	0.0
5	$Fe_{0.1}Ni_{0.9}Co_2O_x$	38.4	43.3	18.3

Table A2. 5. Binding energy values of cations in the amorphous metal oxides

#	Sample	Co^{3+}(eV)	Co^{2+}(eV)	Cu^{1+}(Td) (eV)	Cu^{2+}(Oh) (eV)	Cu^{2+}(Td) (eV)	Ni^{2+}(eV)	Ni^{3+}(eV)
1	CoO_x	779.2	780.5					
2	$CuCo_2O_x$	779.0	780.3	932.3	933.7	936.9		
3	$Ni_{0.5}Cu_{0.5}Co_2O_x$	779.1	780.4	932.0	933.7	936.5		
4	$Fe_{0.1}Cu_{0.9}Co_2O_x$	779.0	780.3	932.3	933.8	937.3		
5	$Fe_{0.1}Ni_{0.9}Co_2O_x$	779.3	780.6	-	-	-		

Appendix 3.1. Supporting documents for Chapter 5.1. Electrochemical properties - Double layer capacitance measurements on crystalline and amorphous transition metal oxides

To keep the length of the Chapter manageable, additional data for Chapter 5.1. is shown below. All these Figures and/or Tables are referred to in respective Chapters.

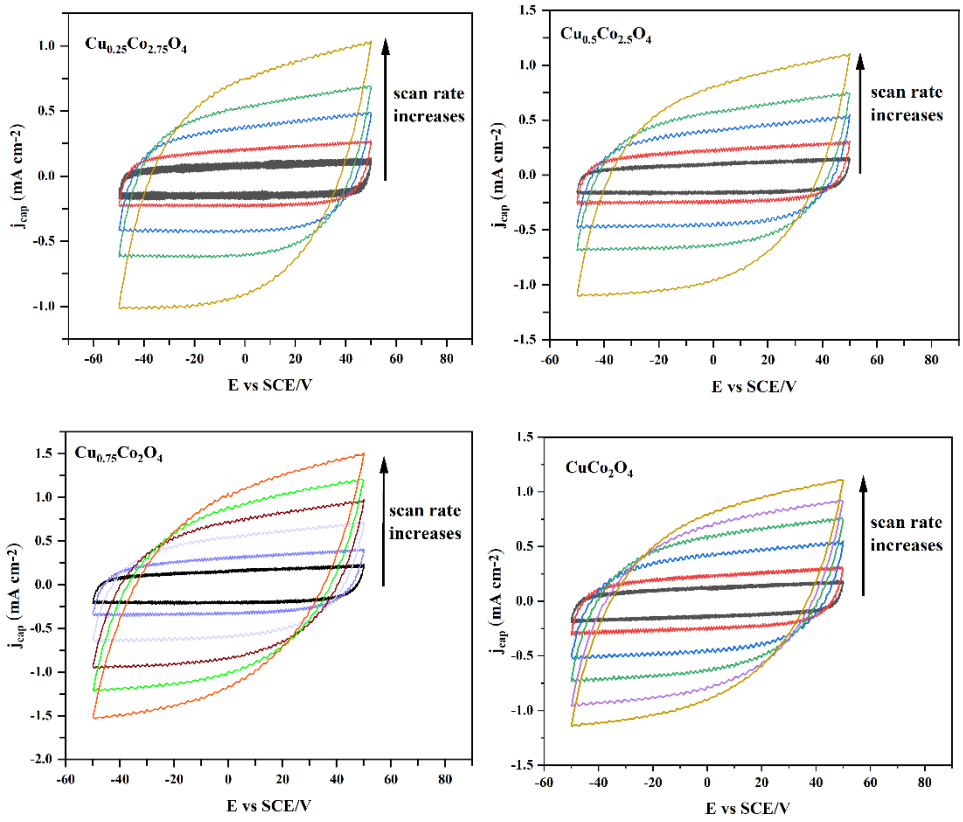

Figure A3.1.1. Cyclic voltammograms of the $Cu_xCo_{3-x}O_4$ electrodes in 1M KOH for scans recorded in a potential range of -50 mV to 50 mV (SCE) at various sweep rates of 10, 20, 40, 60, 80 and 100 mV s^{-1}.

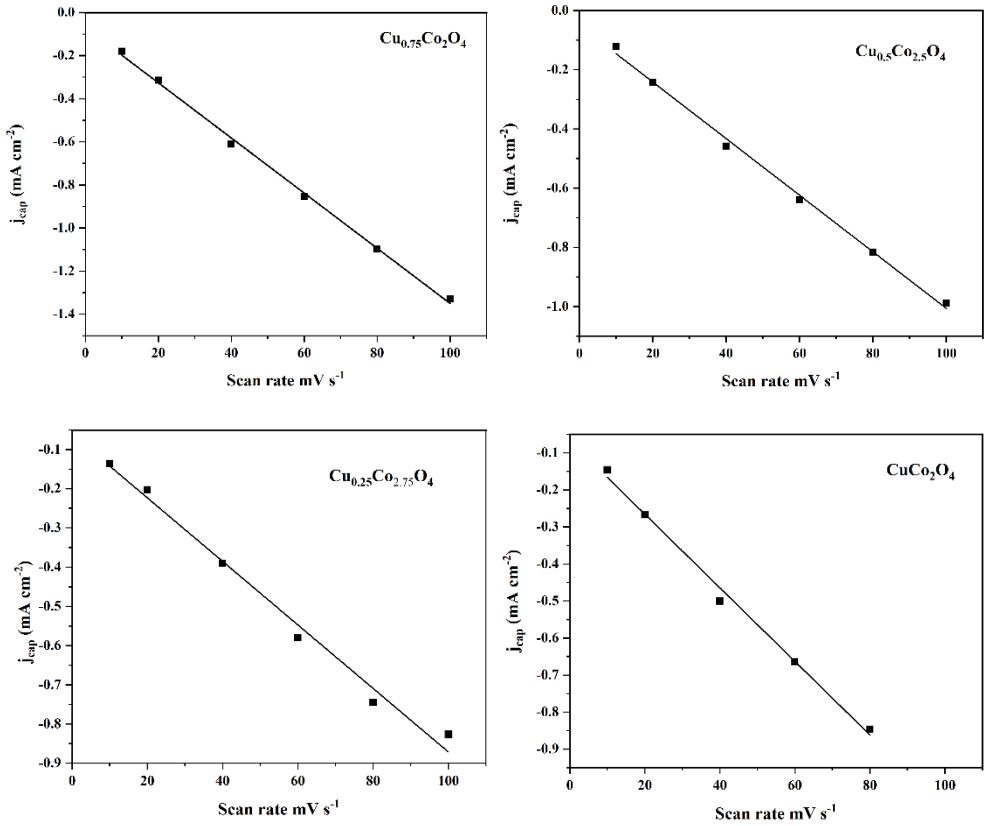

Figure A3.1.2. Graphs of the double layer charging current density at -25 mV as a function of scan rates towards negative potentials for $Cu_xCo_{3-x}O_4$ electrodes.

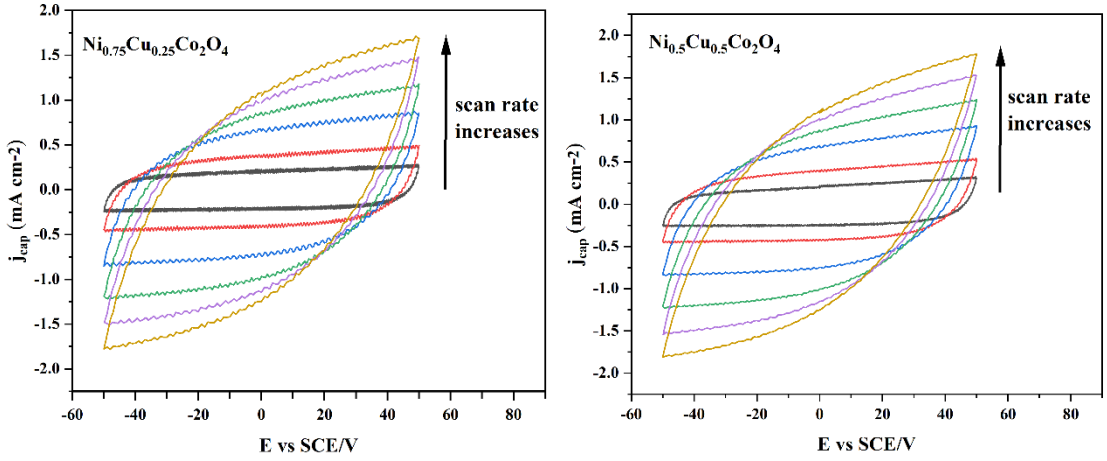

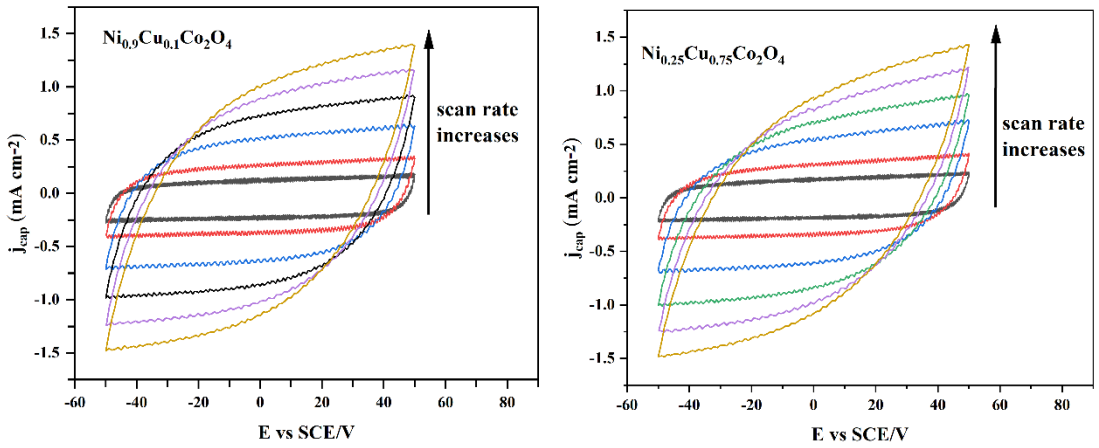

Figure A3.1.3. Cyclic voltammograms of $Ni_xCu_{1-x}Co_2O_4$ electrodes in 1M KOH for scans recorded in a potential range of -100 mV to 100 mV (SCE) at various sweep rates.

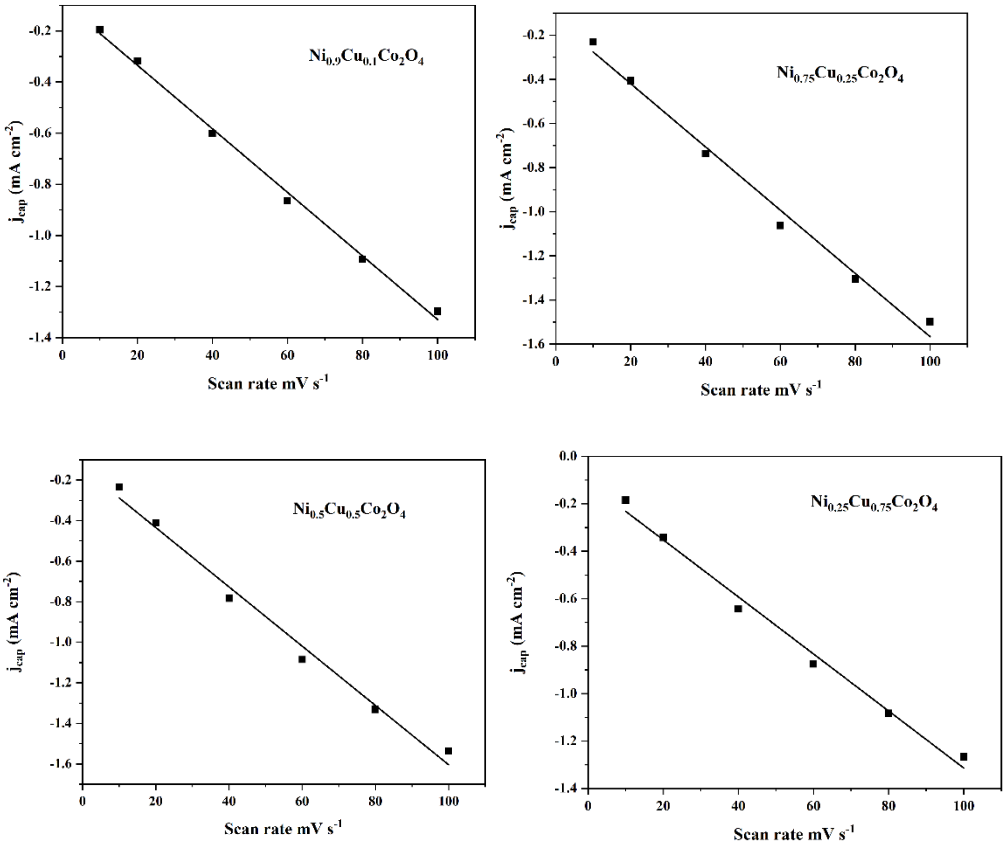

Figure A3.1.4. Graphs of the double layer charging current density at -25mV as a function of scan rates towards negative potentials for $Ni_xCu_{1-x}Co_{3-x}O_4$ electrodes

Table A3.1.1 Circuit parameters obtained for $Cu_xCo_{3-x}O_4$ and $Ni_{1-x}Cu_xCo_2O_4$ prepared by the thermal decomposition method

samples	R_{ct}	R_{ϕ}
Co_3O_4	26.4 ± 4.7	424 ± 47
$Cu_{0.25}Co_{2.75}O_4$	17.4 ± 2.0	476 ± 43
$Cu_{0.5}Co_{2.5}O_4$	21.0 ± 4.4	374 ± 40
$Cu_{0.75}Co_{2.25}O_4$	25.5 ± 1.0	630 ± 111
$CuCo_2O_4$	28.4 ± 3.6	404 ± 66
$NiCo_2O_4$	17.4 ± 3.4	231 ± 57
$Ni_{0.9}Cu_{0.1}Co_2O_4$	25.7 ± 4.3	830 ± 49
$Ni_{0.75}Cu_{0.25}Co_2O_4$	17.9 ± 3.4	196 ± 32
$Ni_{0.5}Cu_{0.5}Co_2O_4$	19.9 ± 3.3	207 ± 12
$Ni_{0.25}Cu_{0.75}Co_2O_4$	24.1 ± 5.6	310 ± 28

Appendix 3.2. Supporting documents for Chapter 5.2. Electrochemical properties – Catalytic activity of crystalline and amorphous transition metal oxides towards the OER and OER kinetics

To keep the length of the Chapter manageable, additional data for Chapter 5.2. is shown below. All these Figures and/or Tables are referred to in respective Chapters.

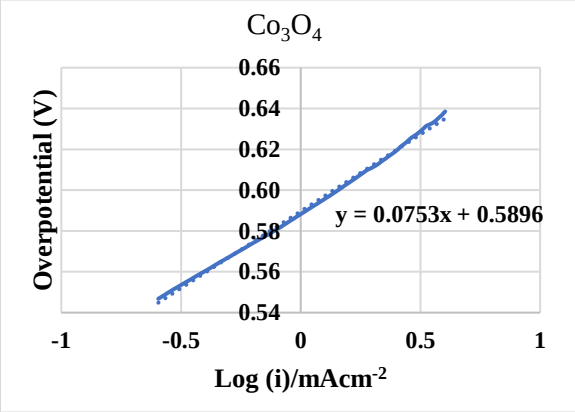

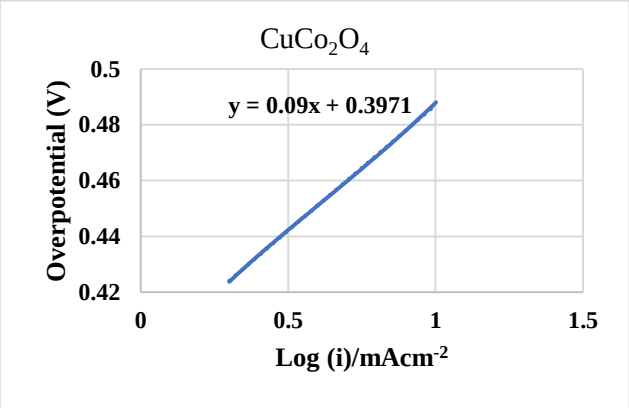

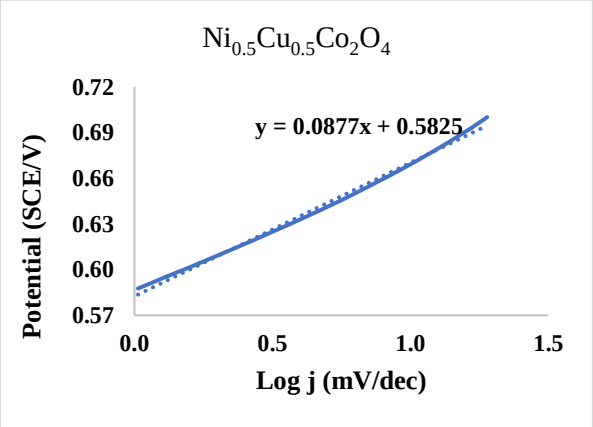

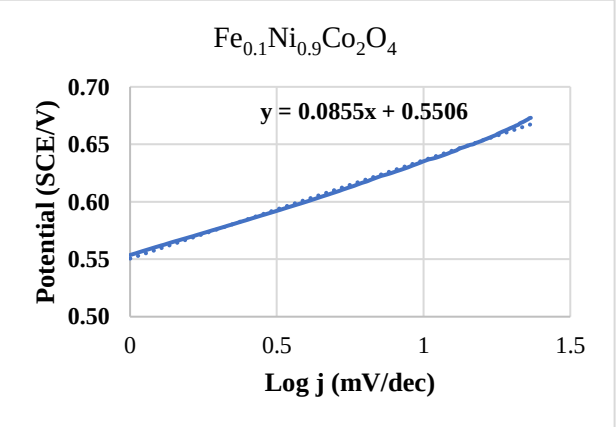

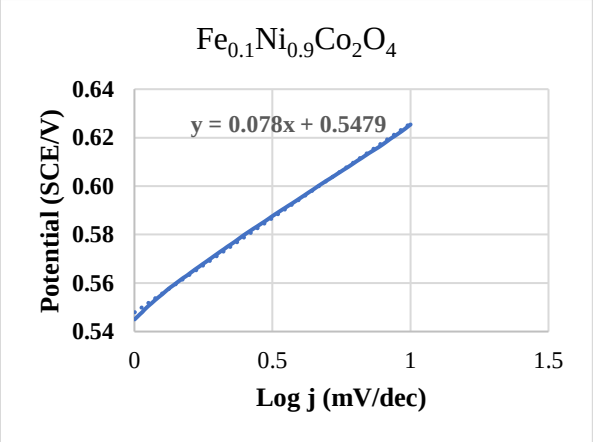

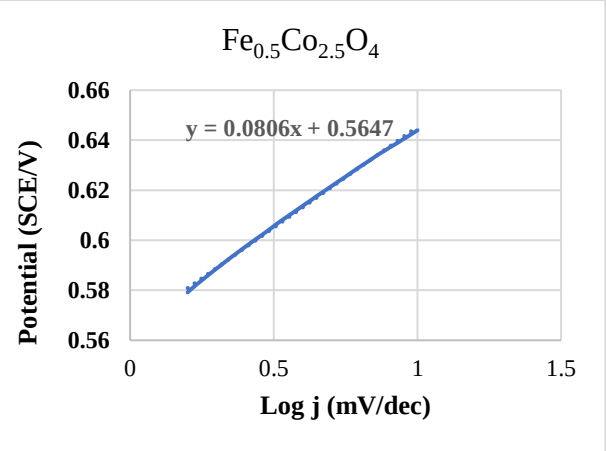

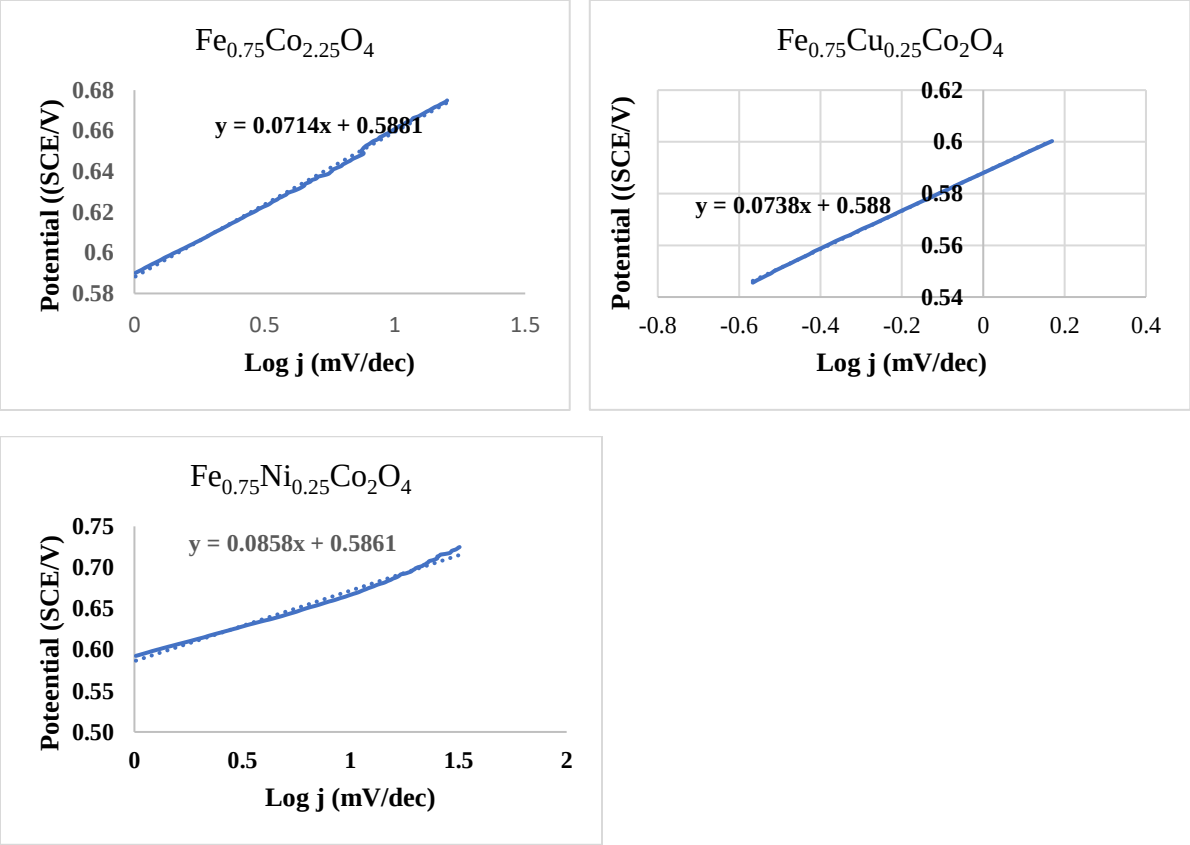

Figure A3.2.1. Tafel slope of spinel oxides in 0.1 M KOH solution at 3000 rpm

Appendix 4. Supporting documents for Chapter 6. Important materials science correlations for the mixed transition metal oxides

To keep the length of the Chapter manageable, additional data for Chapter 6. is shown below. All these Figures and/or Tables are referred to in respective Chapters.

Table A4.1. Co^{2+}/Co^{3+} ratio and current density corrected for the real surface area of spinel oxides

Sample	Co^{2+}/Co^{3+} ± 0.049	Current density corrected for real surface area (mA cm^{-2})
$NiCo_2O_4$	0.837	0.16
$Ni_{0.9}Cu_{0.1}Co_2O_4$	0.730	0.17
$Ni_{0.75}Cu_{0.25}Co_2O_4$	0.660	0.16
$Ni_{0.5}Cu_{0.5}Co_2O_4$	0.587	0.15
$Ni_{0.25}Cu_{0.75}Co_2O_4$	0.537	0.18
Co_3O_4	0.924	0.31
$CuCo_2O_4$	0.546	0.24
$Fe_{0.1}Cu_{0.9}Co_2O_4$	0.74	0.67
$Fe_{0.15}Cu_{0.35}Co_{2.5}O_4$	0.68	0.47
$Fe_{0.1}Ni_{0.9}Co_2O_4$	0.56	0.46
$Fe_{0.15}Ni_{0.35}Co_{2.5}O_4$	0.58	0.47